From local topography to global morphology : origins and consequences on the activity of comets

Selma Benseguane

Université Claude Bernard Lyon 1

THÈSE de DOCTORAT DE
L'UNIVERSITÉ CLAUDE BERNARD LYON 1

Ecole Doctorale N° 52
Physique et Astrophysique

Discipline : Astrophysique

Soutenue publiquement le 25/09/2023, par :
Selma Benseguane

From local topography to global morphology: origins and consequences on the activity of comets

---

Devant le jury composé de :

Cathy Quantin-Nataf Professeure, LGL-TPE	**Présidente**
Sonia Fornasier Professeure, Observatoire de Paris	**Rapporteure**
Jean-Baptiste Vincent Chercheur, DLR	**Rapporteur**
Olivier Groussin Astronome, LAM	**Examinateur**
Aurélie Guilbert-Lepoutre Chargée de Recherche, LGL-TPE	**Directrice de thèse**
Jérémie Lasue Astronome Adjoint, IRAP	**Co-Directeur de thèse**

Abstract

Cometary nuclei exhibit considerable complexity on both local and global scales. Circular depressions, or 'pits,' have been observed on all Jupiter Family Comets visited by spacecrafts, sparking interest in their formation and evolution via thermally-driven activity and erosion under present illumination conditions. Moreover, the global irregularity of these nuclei has led us to examine their potential impact on overall comet activity and the importance of shape data for precisely fitting ground-based activity curves.

To investigate these questions, we have modeled the thermally-driven activity, both on the level of local topographic features or pits, and the whole nucleus – depending on the focus of each study – taking into account the intricate shape model and the surface illumination conditions associated with it. For each facet of the local or global shape model, we compute the solar energy, including shadowing and self-heating effects, that we include as a surface condition of a thermal evolution model. This model, in turn, generates activity outputs, such as gas or dust production rates and local erosion.

We studied the pits present on the surface of 67P/C-G, 9P/Tempel 1, 81P/Wild 2 and 103P/Hartley 2, for which we have high resolution 3D shape models. We ran simulations over a time frame corresponding to the duration each comet has spent in its current inner Solar System orbit (e.g., 10 orbits for 67P). We found that erosion of pits achieved after all the orbital revolutions cannot adequately explain the current morphology of these pits. This holds true both in terms of the quantity of material eroded and the pattern of shape evolution resulting from such a process. Therefore, pits are unlikely to be formed by gradual erosion.

For our study of the global activity, our focus was on comets 67P, 9P, and 103P. These comets have 3D shape models and sufficient observed production rates covering the perihelion period. By using these data, we were able to compare observed and simulated water production rates. Our simulations incorporated both low-resolution shape models that maintain the overall comet shape and spherical models with equivalent surface areas. We also adjusted for various initial structural and thermal parameters. Our study found that understanding secular comet activity requires considering thermal or mechanical heterogeneities as much as shape or more. Ground-based observations alone cannot clear up the ambiguity among these characteristics, thereby justifying a spherical approximation for initial understanding of comet activity.

Acknowledgements

I am immensely grateful to my supervisors, Aurélie Guilbert-Lepoutre and Jérémie Lasue, for their invaluable guidance, patience, and expert insights throughout this PhD journey. Your mentorship has not only shaped this thesis but has also profoundly influenced my personal and professional development. I truly never imagined that supervisors could be this amazing – you rock!

I would also like to express my sincere thanks to my defense jury for their constructive feedback and challenging questions, which have greatly contributed to enhancing the quality of this work.

I extend my genuine thanks to all who offered expert support in the complex technical aspects, particularly with the PSMN (ENS-Lyon) and the Spice kernels (JPL). My gratitude also goes to colleagues from the European Space Agency (ESA), US Naval Academy, and Imperial College London, whose collaborative efforts were instrumental in refining my work.

A special acknowledgment goes to the THEMISS team, the heart of the "petit corps" community. They say you truly get to know people during travels, and I had the pleasure of learning more about each of you, especially during the international conferences. The memories we've created together, from insightful discussions to shared laughter, are invaluable and will always be cherished. Okay, let's be honest, it was maybe 20% science, and the rest was enjoying the company and evaluating foreign cuisine.

To my friends that I knew in the lab, thank you for your unwavering bienveillance, understanding, and companionship. The moments of laughter and relaxation we shared, punctuated by our multiple daily coffee breaks, have been a treasured respite from the rigours of academic life. Cheers to those countless cups of coffee that fuelled our friendship and discussions!

Of course, in the lab, there are also colleagues in front of whom we appear so serious. I have come to appreciate each of you as well!

To my friends outside the lab, you know how much each of you is special to me. Even though I might have sounded like an extraterrestrial at times, your efforts to understand my PhD-induced "mental disability" are priceless.

Lastly, to my dearest ones: my family! You have been my constant source of love and encouragement. Your belief in me and your sacrifices have been the foundation upon which I have built my aspirations and achievements. This accomplishment is as much yours as it is mine.

Contents

Introduction

Comets, potentially the least altered bodies within the Solar System, provide invaluable insights into its origins and evolution. One of the most striking aspects of these comets, made evident thanks to spacecraft images, is their notably complex morphology. From localized surface features such as fractures, boulders, and depressions, to the intricate global configurations of their nuclei (bilobate, elongated, etc), these comets carry the marks of their complex formation histories and the physical processes they've encountered since. Their diverse structures offer a captivating glimpse into the profound phenomena of our Solar System. This thesis aims to unravel the nuanced relationship between the unique morphology of Jupiter Family Comets (JFCs) and their thermally-driven activity, considering both local and global scales.

A characteristic local feature of cometary nuclei, observable in all visited JFCs, is the presence of large scale circular depressions ranging from a few tens to hundreds of meters, often referred to as 'pits' (e.g., Vincent et al., 2015a; Ip et al., 2016). The potential formation and evolution of these pits, through thermal activity and erosion occurring in the recent phase of comets, represent a pivotal area of investigation in this research: we will undertake an exhaustive study into the thermal and morphological evolution of pits present on the surfaces of 67P/C-G, 81P/Wild 2, 9P/Tempel 1 and 103P/Hartley 2, with careful consideration of the effects of local illumination conditions. The goal is to determine if gradual erosion could be at the origin of these features.

Expanding our investigation to a macroscopic scale, we will explore how the diverse and irregular forms of cometary nuclei affect overall cometary activity and their role in interpreting ground-based activity curves appropriately. Our study specifically involves comets 67P, 9P, and 103P. Through simulations using low-resolution and spherical shape models, as well as examining the impact of composition and heterogeneity on global activity, we aim to assess the respective contributions of these factors to observed comet activity in relation to the effect of the intrinsic shape.

To address these goals, our approach focuses on modeling the thermally-driven activity at local (pits) and global (nucleus) levels, considering shape effects. By incorporating surface shape geometry into energy balance calculations using 3D shape models, we account for surface illumination conditions, including shadowing and self-heating. The thermal simulations yield two key outputs: erosion analysis across different sides of the pits and the total water production rates released by the nucleus as a whole.

This manuscript consists of six chapters and a conclusion part:

- Chapter 1 introduces comets, their exploration, their complex shapes and thermal evolution mechanisms. It sets up the thesis's focus on how a comet's shape influences its thermal evolution and activity.
- Chapter 2 outlines the methodology used in the various studies to investigate the thermal evolution, with a particular focus on incorporating the shape. It is crucial for our study to properly account for the shadowing and self-heating effects on the surface, as these processes can influence the distribution of energy and the activity in consequence.
- Chapter 3 delves into the thermal evolution of a specific 67P/C-G's pit, probing its evolution due to activity. We also examine the impact of: porosity, dust-to-ice mass ratio, presence of a dust mantle, and super volatiles like CO and CO_2, as well as local shape complexities, on this pit's evolution. The aim is to retrieve pits' primordial traits to help decipher their formation mechanism.
- Chapter 4 quantifies the erosion undergone by 30 depressions, including circular and elongated pits and alcoves, on 67P/C-G's surface under current illumination conditions, covering periodic, daily, and seasonal cycles. This assists in reproducing their evolution and investigating their possible formation through this process.
- Chapter 5 probes pits on the surfaces of comets 81P/Wild 2, 9P/Tempel 1, and 103P/Hartley 2, investigating potential similarities in their evolution and origin to those observed on 67P/C-G.
- Chapter 6 seeks to determine the influence of the global nucleus shape and composition on the water production rates of comets 67P/C-G, 103P/Hartley 2, and 9P/Tempel 1, using available data from ground-based and spacecraft observations. The goal is to ascertain if the activity curves reflect shape information and if any potential underlying complex shapes could bias our interpretation of these curves.
- Finally, we summarize the conclusions drawn from all our work and outline the perspectives for future research.

Chapter 1

Comets: small active bodies with complex shape

1.1 Why are comets interesting?

About 4.6 billion years ago, a cloud of dust and gas known as the solar nebula began to collapse due to its own gravity. As it collapsed, it began to heat up and spin faster, and the center of the nebula became hot enough to ignite nuclear fusion, forming the protosun. As the solar nebula cooled, solid particles began to condense and stick together, forming small objects: planetesimals, that collided and merged to form the Solar System's planets. The planets continued to grow by accreting more planetesimals and other material, until they reached their current sizes. Many of the solar system's planets have moons, which formed either through accretion or through the gravitational capture of smaller objects. Dynamical rearrangements then likely took place resulting in planetesimals being scattered, expelled, or redirected to outer Solar System regions considered as dynamical reservoirs. Here, shielded from intense thermal and collisional activity, these preserved planetesimals evolved into icy objects most of which evolved to comets we study today.

The synergy between theoretical models, observations, and laboratory experiments has greatly enriched our understanding of planetesimal and comet formation processes (Simon et al., 2022). It is now recognized that comets are not just remnants of the Solar System, but potentially harbor pristine material and represent the least altered objects within it. This is evident in the observation of substantial amounts of highly volatile species on comets. For instance, CO, a significant icy constituent that sublimates at around $\sim$25 K, is observed on comets (Biver et al., 2022). The detection of such components indicates the presence of untouched material in the comet, suggesting it has likely been shielded from significant alterations. Their study has thus been at the center of our interest because it leads to a deeper understanding of the formation and evolution of the Solar System and the solar nebula.

This chapter provides an essential background for the thesis. It starts with an overview of comets, followed by an exploration of the various existing ways to study them. We start with ground-based observations, discussing their limitations in understanding cometary activity, especially regarding constraining the complex shape of cometary nuclei. Next, we highlight the ground-breaking observations from space missions, aimed at Jupiter Family Comets. Special emphasis is placed on the *Rosetta* mission and comet 67P/C-G, the central object of this work. We then present the insights and models constrained by these investigations, which have helped define the current understanding of cometary nuclei structure and mechanisms. This leads finally to the core issues addressed in this thesis regarding the role of cometary shape and topography in the thermal evolution and the observed cometary activity.

1.2 General description

The nucleus of a comet, typically a few kilometers in diameter, forms its central part. This nucleus contains various types of ices, predominantly water ice (by 80%, see Figure 2 of Bockelée-Morvan and Biver, 2017), followed by other ices, chiefly CO and CO_2, among others. In addition, the nucleus contains refractory materials, including minerals, organics, and salts (Filacchione et al., 2022, and references therein) As the comet orbits the Sun, the increase in solar radiation triggers the sublimation of ices within the nucleus, leading to the development of a coma, the halo (cloud) of gas and dust particles -ranging in size from a few micrometers to over a centimeter- surrounding the nucleus (Merouane et al., 2016). Solar radiation pressure and solar wind then shape this material into two distinct tails pointing away from the Sun: the ion tail and the dust tail. The ion tail consists of ionized gases, predominantly water vapor, CO, CO_2, CH_4, and NH_3, which are photoionized or dissociated by solar ultraviolet radiation. These ionized particles are highly responsive to the magnetic field embedded in the solar wind, and are thus blown directly away from the Sun. The dust tail, on the other hand, consists of small dust particles that are driven off by sublimating gases and slightly lag behind. Dust particles are less affected by the solar wind but are pushed away from the Sun by radiation pressure. The dust tail often appears curved as it follows the comet's trajectory.

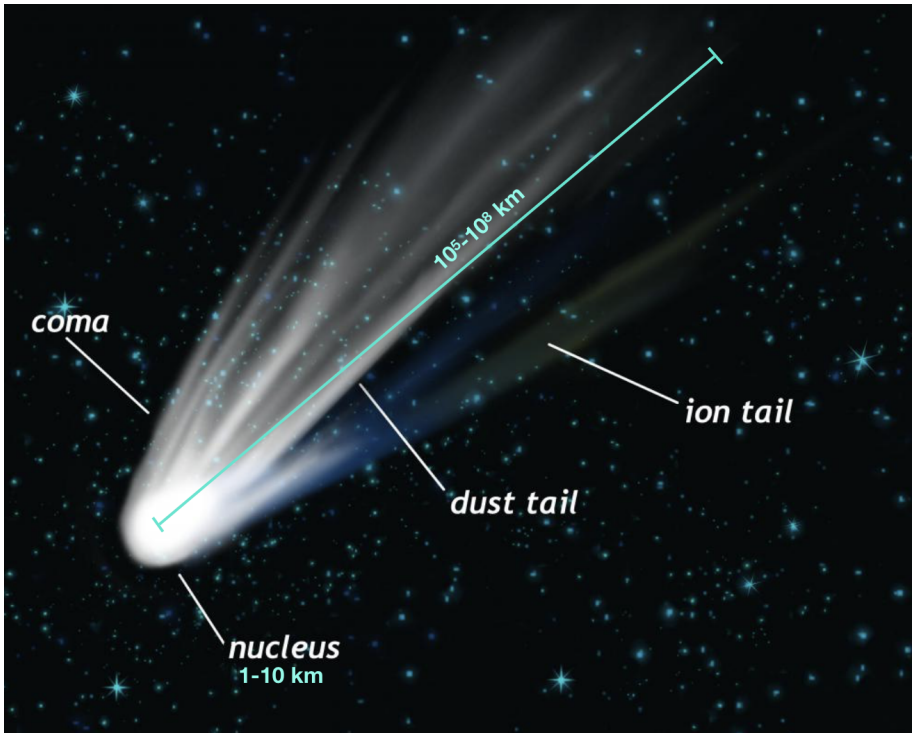

Figure 1.1: Key features of a comet activated by solar heating: the nucleus, the luminous coma, and the distinct dust and ion tails that trail behind, all shaped and illuminated by the solar energy. Adapted from image by *Christopher Witt*.

As the comet moves away from the Sun and cools after its perihelion passage, the coma and tails dissipate, leaving just the nucleus, until its next approach to the Sun.

1.3 Where do they come from?

1.3.1 Dynamical reservoirs

Since its creation, the Solar System has continued to evolve over time, with comets colliding with the planets and moons, and the outer planets migrating to their current positions. Models describing these dynamical re-arrangements are detailed in (Davidsson et al., 2016, and references therin). As a result of these dynamical re-arrangements, comets are predominantly stored in two primary reservoirs within the Solar System: the Oort Cloud and the Kuiper Belt.

The Oort cloud: theorized by Jan Oort in 1950, it is an immense, roughly spherical shell surrounding the Solar System at approximately 20,000 to 150,000 AU (Brasser and Morbidelli, 2013). Although direct observation remains impossible due to the vast distances and the sparse density of the cloud, it is inferred to be the source of long period comets (Kaib and Quinn, 2009).

The Kuiper belt and the Scattered disk: these structures span the trans-neptunian region beyond the orbit of Neptune (Brasser and Morbidelli, 2013). Along with resonant objects like Pluto, they contribute to a gravitational cascade toward Centaurs in the giant planet region and Jupiter-Family Comets towards the inner parts of the Solar System (Nesvorný et al., 2017; Steckloff et al., 2020).

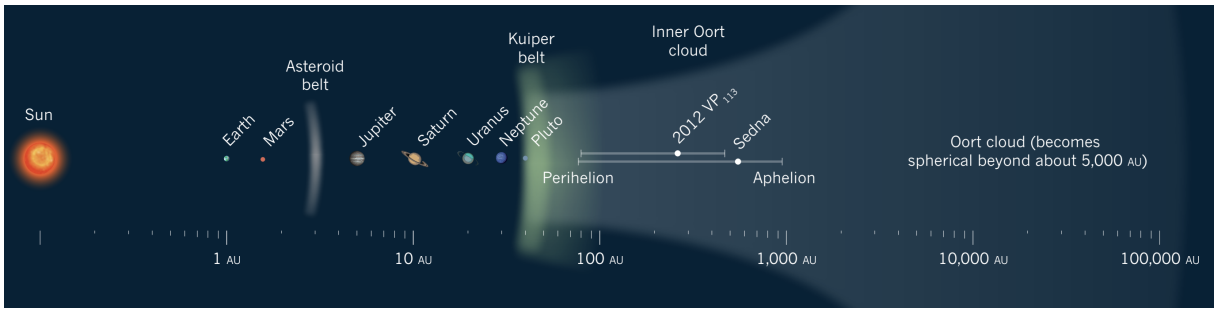

Figure 1.2: Illustrative overview of the Solar System highlighting the main reservoirs of comets: the Oort cloud and the Kuiper belt. The Asteroid belt is also shown. Positioned from far outer Solar System to near the Sun, they house an abundance of comets and provide key insights into the composition and history of our Solar System. Credits: Schwamb (2014).

1.3.2 Populations of comets

Comets remain within their reservoirs until they are gravitationally disturbed. Comets in the Oort cloud are predominantly disturbed by gravitational interaction with massive objects such as stars, passing nebulae and galactic structures, while comets in the Kuiper belt and and Asteroid belt are affected mainly by small kicks from gravitational interactions with giant planets (Ruzicka, 2019). As a result of these perturbations, comets may be disrupted from their orbits in their respective reservoirs and set on a trajectory

towards the inner Solar System.

Short-period comets: they typically have orbital periods of less than 200 years, and can be classified into two families, Jupiter-Family Comets (JFCs) and Halley-type comets. JFCs have orbits characterised by low eccentricity, and typically low inclination ($< 30°$), they have periods of less than 20 years, they are thought to come mainly from the Kuiper belt, where they got destabilized due to interactions with Neptune. They are called Jupiter-family comets because their orbits are influenced by the gravity of Jupiter. Comet 67P/Churyumov-Gerasimenko is an example of a JFC. After being expelled from its reservoir, a JFC typically has a median dynamical lifetime of almost a billion years, starting from the moment it becomes a JFC until it is either ejected from the Solar System or enters an orbit close enough to the Sun for us to observe its brightness (Nesvorný et al., 2017, and references therein). Halley-type comets have orbital periods ranging from 20 to 200 years, and orbital inclinations ranging from very low to being retrograde exceeding 90 °. They are thought to originate from either the Kuiper belt or the Oort Cloud. These comets are named Halley-type due to their orbits resembling that of comet 1P/Halley.

Long-period comets: identified by orbital periods largely exceeding 200 years, they are originating from the Oort Cloud. Large planets, such as Jupiter, have the capacity to capture long-period comets, reducing their orbits and consequently leading to their transformation into JFCs (Ruzicka, 2019). An example of a long-period comet is C/1995 O1 (Hale-Bopp), characterized by an orbital period between 2300 and 2500 years. Dynamically new comets, a subset of long-period comets also originating in the Oort cloud, probably carry the best preserved characteristics. They have experienced minimal thermal or mechanical alterations compared to other comet populations. Indeed, though periodic comets, including both Jupiter-Family Comets (JFCs) and Halley-type comets also carry some primitive fingerprints, they do show signs of past alteration, sustained after they traveled through the Solar System from their reservoirs to inner Solar System orbits (Roth et al., 2020).

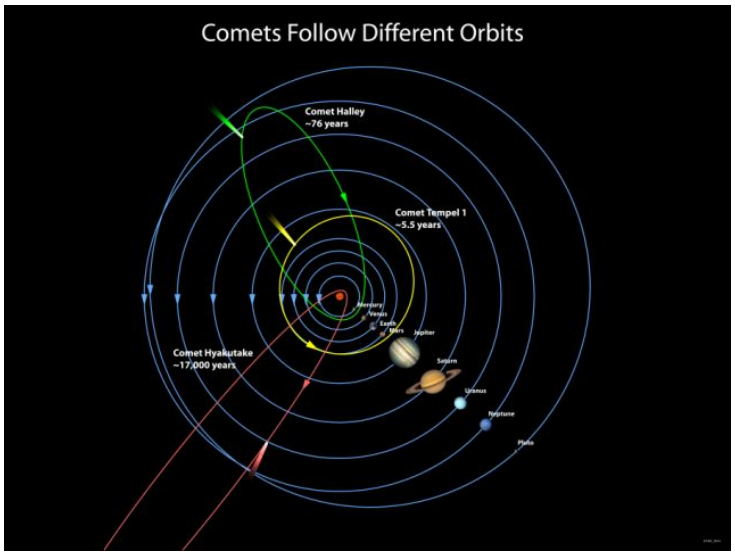

Figure 1.3: Illustration of distinct orbits for three notable comets, representative of the different cometary populations: 9P/Tempel 1 for short-period JFCs, 1P/Halley for short-period Halley-type comets, and C/1996 B2 (Hyakutake) for long-period comets. Credits: *Kay Gibson*, Ball Aerospace & Technologies Corp.

1.4 Ground-based observations of comets

Comets have been observed with the naked eye and through ground-based facilities for many centuries before the advent of space exploration. Ground-based observations have been able to provide considerable amounts of data, enabling robust statistical and population level analyses on essential physical characteristics of comets, such as their orbital parameters, size, rotational properties or their composition (Knight et al., 2023). Moreover, these observations prove to be cost-effective when compared to their space-based alternatives. Comets are known for their inherent variability, which necessitates regular and repeated observations, only feasible from ground-based facilities. Considering that only a limited number of comets have been examined by spacecrafts, and given that comets contain a diverse range of volatile and refractory elements, our comprehensive understanding of the properties of comets largely stems from such remote sensing techniques. Therefore, telescope observations, conducted over a wide wavelength range from visible, near-infrared, and mm/sub-mm wavelengths, have proven to be crucial. They enhance our scientific understanding and complement ongoing and prospective space missions (Snodgrass et al., 2022). Remote sensing of cometary gases and dust unveils the primitive components of comets and sheds light on their evolution through the preservation and loss of volatiles.

1.4.1 Coma and nucleus observations

1.4.1.1 Coma gases

Ground-based spectroscopy across different wavelengths allow the observation of different compositional properties of the cometary comae, and variability in native ices abundance ratios.

At the visible and ultraviolet (UV) wavelengths, atomic and molecular species, such as ions and radicals, including daughter molecules (e.g., OH, CN, C_2, and C_3) formed from photochemical reactions of more complex molecules, can be detected (Roth et al., 2020). Observatories like the Hubble Space Telescope offer capabilities in these wavelengths (e.g., Lamy et al., 2009, 2011), but ground-based facilities such as the Keck Observatory and the European Southern Observatory's Very Large Telescope also contribute valuable data (e.g., Meech et al., 2004; Stinson et al., 2014). Infrared (IR) spectroscopy identifies larger molecules, solid-phase materials, and volatiles, like H_2O, CO, and CO_2, that sublimate directly from the nucleus during outgassing. Notably, the Keck Observatory and the Subaru Telescope are equipped with IR capabilities (e.g., Bonev et al., 2021; Kobayashi and Kawakita, 2010). Radio and microwave spectroscopy, offered by facilities like the Atacama Large Mm/sub-mm Array (ALMA), allows the detection of larger parent molecules like HCN, H_2O, NH_3, and CH_3OH, often providing insights into the comet's interior regions (Bockelée-Morvan, 2008). From these observations, we can identify molecules and measure their ratios, usually with respect to water as it is typically the most abundant volatile species. These have provided insights into the original composition of the cometary nucleus ((albeit with a number of caveat, e.g. Prialnik, 2006) and the photochemical processes in the coma. Analysis of such data has led to the identification of abundance patterns. For instance, Lippi et al. (2021) suggest two main cometary chemi-

cal classes: one less processed than another indicating a distinct formation site or nuclei material evolution. However, compositional trends allowing a taxonomical classification, species detectable at all wavelengths need to be characterized for an extensive number of comets.

1.4.1.2 Coma dust

Observations of dust in comae also provides essential clues to comet activity and behavior.

Ground-based observations primarily focus on monitoring a comet's brightness over an extended period of time to create a secular light curve. This technique reveals information about the dust production rate and overall cometary activity, offering critical insights into its behavior and evolution (Ferrín, 2010). An additional critical tool is the Afρ (A'Hearn et al., 1984), representing the sunlight scattered by the dust particles in the coma. It serves as a reliable proxy for determining the variation of dust flux (Fink and Rubin, 2012). Changes in Afρ values indicate variations in cometary activity, making it a critical tool for calculation and interpreting the activity of comets. Results from Sárneczky et al. (2016) for example, have shown that dynamically new comets, – making their first come back close to the Sun – often exhibit symmetric comae and higher Afρ values compared to returning comets, suggesting high levels of activity. The more modest rise in Afρ values as these comets approach the Sun could is interpreted as changes in dust production or nucleus properties. Studying these comets would therefore provide valuable information about the original, unaltered state of cometary activity, and their initial conditions before they undergo the changes associated with entering the inner Solar System. The photometric study of dust also offers insights into comet composition (Bauer et al., 2022). Visible wavelength observations provide color indices, measures of light scattering off comet dust grains. This scattering provides critical compositional information, such as the particle size and ice-to-refractory ratio. For instance, Solontoi et al. (2012) and Jewitt (2015) investigated a wide array of comets, and have not found significant compositional differences between short and long-period comets, suggesting shared formation conditions in the protoplanetary disk. These studies also noted no clear trend between dust color and heliocentric distance, leading to conjectures about particle size and ice-to-dust ratios, which enhance our understanding of cometary evolution.

1.4.1.3 Nucleus properties

Ground-based telescopes across multiple wavelengths often serve as the initial observational approach facilitating the determination of orbital parameters, physical properties such as size, general shape, spin state, and thermal properties of comet nuclei.

Optical and near-infrared photometry and spectroscopy, carried out using large telescopes such as Keck and ESO's VLT, can be used to infer a comet's color and determine its composition and size. Rotational lightcurves are an invaluable resource for comet's physical traits such as the spin rate, global shape, density, and composition. Kokotanekova et al. (2017) used lightcurves to investigate the physical characteristics of JFCs and KBOs. They established trends regarding bulk density and tensile strength of these bodies, providing a groundwork for evaluating different hypotheses concerning their origin and evolution. Moreover, they refined the understanding of JFCs through detailed analysis of

albedo and phase functions. Radar observations, previously conducted at facilities like Arecibo and currently the Goldstone Complex, can derive size, shape, rotation period, and give insights into surface roughness and reflectivity (e.g., Kamoun et al., 2014; Howell et al., 2014). Long baseline interferometry, combining signals from multiple telescopes across various wavelengths, can help resolve small-scale nucleus features (Boissier et al., 2009). Finally, spectropolarimetry offers clues about the size, shape, and composition of grains on the surface of the nucleus (e.g., Kwon et al., 2022).

For a detailed review of nucleus physical properties such as sizes, shapes, spin states, and thermal properties, refer to Knight et al. (2023).

1.4.2 Limitations with regards to nucleus studies

The inherent limitations of observations from the ground arise from the constraints imposed by the Earth's atmosphere and the substantial distances to the comets. Atmospheric interference occurs when the Earth's atmosphere distorts or obstructs incoming light from comets, thereby complicating the capture of clear images or spectra. The Earth's atmosphere also absorbs certain wavelengths, which limits access to certain wavelengths such as UV making it difficult to observe comets in these wavelengths. Additionally, when inactive, nuclei are small and faint and impossible to capture. The telescope's resolution is restrained by the mirror or lens size, causing an impossiblity in discerning the nucleus shape or features on comet surfaces. Typically a few km wide, nuclei are mostly unresolvable via remote observations due to this limitation. For substantive size constraints, the object must be several times nearer, which is a rare occurrence. Only four comets have been observed this close thanks to HST, with high-resolution imaging capturing just 252P/LINEAR. As a result, comet nucleus sizes and physical properties are predominantly inferred, not directly measured (Knight et al., 2023). Finally, the elliptical orbits of comets result in infrequent appearances in the inner Solar System, with individual comets only well-studied during close encounters with Earth. Additionally, the limited field of view of ground-based telescopes allows to only observe a small portion of the sky at any given time, so it can be difficult to track comets for long periods of time.

1.5 Space missions before Rosetta

Ground- and space-based observations taken together offer a comprehensive approach to comet investigation, each providing unique benefits and challenges: while ground-based observations enrich our understanding of the general comet population, space-based investigations afford unparalleled opportunities to examine individual comets in depth, once contextualized within the larger frame of knowledge derived from ground studies. The International Cometary Explorer (ICE), launched in 1978, was the pioneering spacecraft to encounter a comet, specifically 21P/Giacobini-Zinner. Originally intended to investigate the interaction between the solar wind and Earth's magnetic field as part of the International Sun-Earth Explorer mission, ICE's onboard instruments were not specifically designed for close-up comet studies, which limited the scope and quantity of data gathered. Nonetheless, ICE successfully obtained the first *in situ* data from a comet

(Brandt et al., 1985). The game changer for the space exploration of comet nuclei has come from the encounters of comet 1P/Halley in 1986. This section highlights the crucial insights obtained from major space missions that explored short-period comets prior to the *Rosetta* mission.

1.5.1 From 1P/Halley to 103P/Hartley

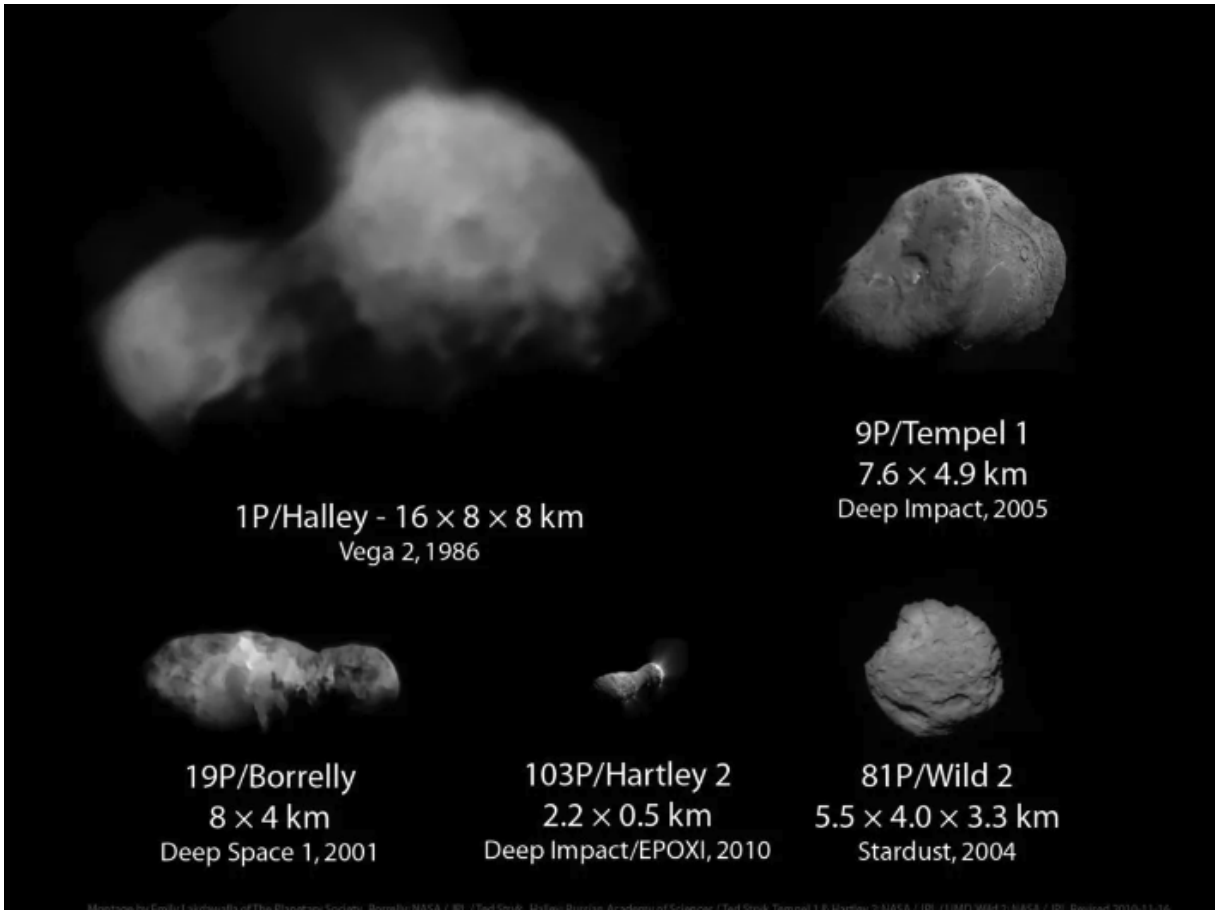

Figure 1.4: Comets visited by spacecrafts before *Rosetta*. Montage by *Emily Lakdawalla*. Halley: Russian Academy of Sciences / Ted Stryk. Tempel 1 and Hartley 2: NASA / JPL / UMD. Borrelly: NASA / JPL / Ted Stryk. Wild 2: NASA / JPL.

The latest perihelion passage of comet 1P/Halley in 1986 posed an important landmark in cometary study. Several missions were sent to visit the comet: the Soviet Union's Vega 1 and 2 (Sagdeev et al., 1986), Japan's Sakigake and Suisei (Hirao and Itoh, 1988), and the European Space Agency's *Giotto* (Reinhard, 1986).

Giotto

Launched in 1985, the *Giotto* spacecraft was the first to closely encounter comet 1P, coming within just 596 km of its surface. This proximity enabled comprehensive composi-

tional analysis of the comet's coma and the gas and dust particles in its tails. Interestingly, the surface displayed a remarkably low geometric albedo of 4%, suggesting a high surface temperature. The dominant volatiles in the coma were found to be H_2O (predominantly), CO, and CO_2. Contrary to the expectation from global ground-based activity, *Giotto*'s observations revealed that only about a third of the comet's surface was active (Keller et al., 1988). *Giotto* also allowed to capture the first-ever close-up images of a comet's surface, revealing dimensions of the nucleus of 16×8×8 km, and a complex surface topography. *Giotto*'s data remains an important resource for studying molecular distributions, even three decades after the mission. The discovery of O_2 in 67P/C-G was a significant breakthrough Bieler et al. (2015), prompting a re-evaluation of *Giotto*'s mass spectrometer readings. When the data was recalibrated for an O_2 abundance relative to water, comparable to that observed in 67P/C-G, the results were notably more accurate. This suggests that comet 67P/C-G is not unique in its abundance of O_2, and that molecular oxygen may be a common parent molecule in comets. Furthermore, *Giotto*'s data was contrasted with other findings from *Rosetta*, including ion composition and plasma processes (review by Snodgrass et al., 2022, and references therein).

Deep Space 1

In 2001, the *Deep Space 1* explored comet 19P/Borrelly, revealing a bilobate-shaped nucleus, which was roughly half the size of comet Halley (measuring ∼8×3×3 km), and a dark surface with a low albedo, ranging between 0.01 and 0.03. The comet's surface was also found to be dry, lacking in water and hydrated minerals. Additionally, the presence of active jets on the comet was observed (Soderblom et al., 2002). Images enabled the identification of a rich surface geology with the existence of various terrains on the comet's surface. The accomplishment, marked by the mission's images, represented a significant advancement in the study of the cometary geology. Compared to Halley, which is considered an intermediate-period comet thought to represent the composition of distant long-period comets, comet 19P/Borrelly exhibits an evolved surface as a result of its activity during previous orbits within the inner Solar System (Li et al., 2007). Compared to most long-period comets and comet Halley, Borrelly seems to have a deficiency in carbon-chain molecules (A'Hearn et al., 1995). This characteristic is believed to reflect its distinct formation region.

Stardust

Launched in 1999, *Stardust* was a pioneering spacecraft that achieved the remarkable feat of collecting grain samples from a comet's coma and returning them to Earth for analysis. The spacecraft visited comet 81P/Wild 2 in 2004 at a distance of 236 km, and successfully returned cometary samples to Earth in 2006 (Brownlee et al., 2004). Analyses of the collected refractory elements revealed they had formed at different temperatures and locations within the primordial disk (Zolensky et al., 2006), providing evidence for radial mixing at the Solar System scale during their formation and suggesting a large diversity among cometary nuclei. Water ice was detected on the surface of 81P, and complex organic molecules were found in its coma, thereby offering invaluable insights into

the composition and evolution of the early Solar System. The mission also provided a link between cometary dust and the interplanetary dust particles collected in the Earth's atmosphere (Palma et al., 2019). Also, dust structures showed the mixture of very compact and very fluffy dust particles in the coma, playing an important role in observations and comet activity (Burchell et al., 2008). Detailed imagery of the comet's nucleus revealed its oblate shape of about 5.5×4×3.3 km, showed a variety of depressions, and highlighted active collimated jets (review by Snodgrass et al., 2022, and references therein).

Deep Impact

Launched in 2005, *Deep Impact* sent a spacecraft to collide with comet 9P/Tempel 1, creating an impact crater and allowing the study of the comet's ejected materials revealing the mechanical properties and composition in the aim to explore the interior of the comet (A'Hearn et al., 2005). The mission consisted of a flyby that carried high-resolution cameras and an IR imaging spectrometer, and an impactor, designed to excavate less altered material at depth and compare it with surface components, and that captured images of the impact site with the highest resolution ever achieved on a cometary nucleus at the time (10 m/px Snodgrass et al., 2022, and references therein). The impact generated a self-luminous flash, and the ejecta analysis provided information about the nucleus's material properties: a high porosity, low strength, and gravity-controlled cratering (review by Snodgrass et al., 2022, and references therein). Water was the dominant component in the gases and in dust ejected from the impact, indicating the presence of water ice beneath the surface. In 2011, the spacecraft *Stardust-NExT*, revisited 9P/Tempel 1, allowing the comparison of surface changes after one orbit of the comet. Images showed a 50 m crater surrounded by a rim of 180 m in diameter, degradation of pre-impact surface features, and ejecta curtain disruption. Two possible scenarios may explain the observation: either a large 200 m crater collapsed into a 50 m pit, or a nested crater structure was formed, featuring a small 50 m inner pit within a shallow 180 m excavation crater (Schultz et al., 2013). Comet 9P/Tempel 1, measuring about 7×5×5 km, exhibits a simple global shape. Yet its surface displays a remarkable diversity characterized by the significant presence of surface depressions.

EPOXI

In 2010, the *Deep Impact* spacecraft was recycled under an extended mission named *EPOXI*, visited comet 103P/Hartley 2 at a distance of ∼700 km (A'Hearn et al., 2011). The properties of the comet's nucleus were intriguing and diverse. The comet presented a hyperactivity that was linked to the sublimation of its water ice grains (review by Snodgrass et al., 2022, and references therein). The activity was not homogeneous across the surface showing likely a heterogeneous composition, with the active surface area constituting about 10% of the total surface. The *EPOXI* mission reported a Deuterium-Hydrogen (D/H) ratio in the comet that matched that of Earth's oceans, providing a significant insight related to the questions of Earth's water origins. Furthermore, it detected considerable disparities in the distribution of volatiles originating from different parts of the comet (A'Hearn et al., 2011). The nucleus, measuring 2.3 km in length and with a di-

ameter of 0.7 km for each lobe, exhibits an elongated, bilobate structure with a surface characterized by rugged terrain.

1.5.2 Nucleus shape and surface topography

Before space exploration, comets were thought to be simple, spherical bodies. All comets visited by spacecrafts showed irregular, non-spherical shapes: 81P/Wild 2 is characterized by a flattened oblate shape; 9P/Tempel 1 resembles a potato; the shapes of 1P/Halley and 103P/Hartley 2 were more complex, with 1P/Halley having a peanut-like form while 103P/Hartley 2 showcases a notably elongated shape with a smooth waist and rigged small and big lobes (see Figure 1.4). The advent of space missions has revealed a surprising highly irregular and diverse shapes, showcasing the complexity of formation and evolution of these objects. It is believed that such shapes reflect mostly the formation mechanism of comet nuclei. If not remnants of a larger objects fragmented over time, these irregularities must have originated during the comet's formation process itself. This suggests that the intricate structures we observe today could provide invaluable insights into the early Solar System's conditions and processes (Guilbert-lepoutre et al., in comet III). The shapes of cometary nuclei can greatly differ, and these variations significantly influence the comet's spin and activity. Particularly during periods of high activity, when gas and dust are expelled, the shape affects how sunlight warms the comet, triggering inhomogeneous sublimation. This, in turn, can alter the comet's rotation and trajectory.

Concerning the local topography, JFCs visited by spacecrafts, 81P/Wild 2, 9P/Tempel 1, 19P/Borrelly, and 103P/Hartley 2, were imaged at a resolution of few tens of m/px Vincent et al. (2015b), and have presented clear evidence of active geology manifesting as complex topography, which is of particular interest for our work as you will notice as we delve further into this manuscript. The diverse morphological features present on their surfaces have been extensively studied and catalogued in the literature (Basilevsky and Keller, 2006; Cheng et al., 2013; Pajola et al.). We only provide an overview of the most common features, but we recommend readers refer to the cited references for a detailed analysis. Dark spots have been identified on both 19P/Borrelly and 103P/Hartley 2 (Soderblom et al., 2002; Syal et al., 2013); bright terrains were observed on 9P/Tempel 1 and 103P/Hartley 2 (Belton et al., 2013a; Syal et al., 2013); mesas, which are elevated circular areas of land with a flat top and sides that are usually steep cliffs, were identified on 9P/Tempel 1, 19P/Borrelly, and 81P/Wild 2 (Belton et al., 2013a; Soderblom et al., 2002; Brownlee et al., 2004); ridges are found on 19P/Borrelly, 103P/Hartley 2, and 81P/Wild 2 (Soderblom et al., 2002; Syal et al., 2013; Brownlee et al., 2004). All four comets feature smooth terrains in some areas, as well as circular depressions, which are common across their surfaces. On comet 81P/Wild 2, the circular depressions can be steep walled and flat-floored, while on the other comets, they are rather smoother (Cheng et al., 2013). These features are indicative of an active geology and their modification with time is believed to be provoked by the sublimation process (Pajola et al.). See examples of the cited features in Figure 1.5.
Among the various depressions observed, large circular features and alcoves are frequently found on the surfaces of numerous comets. These features exhibit a wide range of shapes

and sizes, spanning from a few tens to several hundreds of meters (Ip et al., 2016).

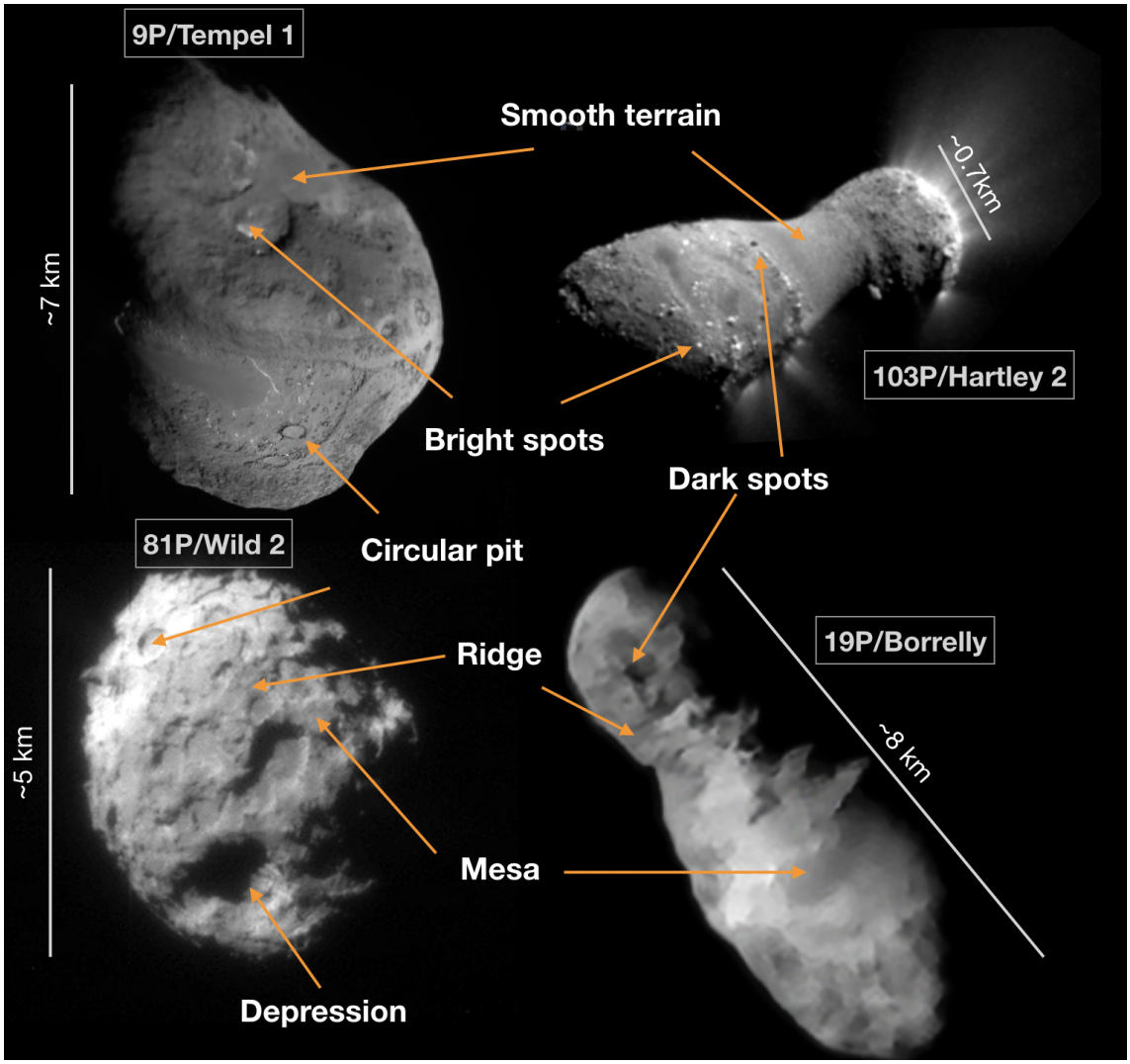

Figure 1.5: Examples of key morphological features on cometary surfaces, including dark and bright spots, mesas, ridges, smooth terrains, circular depressions, and pits, observed on comets 19P/Borrelly, 103P/Hartley 2, 9P/Tempel 1, and 81P/Wild 2.

1.6 Rosetta: a revolutionary mission

The European Space Agency's (ESA) *Rosetta* mission[1] made history as the first spacecraft to escort and rendez-vous a comet on its orbit around the Sun, ultimately deploying the Philae lander. This unprecedented accomplishment offered precious insights into the nature of comets, as well as the conditions and processes that shaped them. The *Rosetta* mission was named after the Rosetta Stone, an artifact discovered in Egypt that helped the French scholar and polymath Jean-Francois Champollion decipher ancient hieroglyphics.

[1]https://www.esa.int/Science_Exploration/Space_Science/Rosetta

Similarly, the mission aimed at unlocking the mysteries of our Solar System's oldest building blocks: comets.

1.6.1 Scientific objectives

The *Rosetta* orbiter's 11 instruments [2] aimed to capture high-resolution data about the nucleus' shape, density, temperature, and the chemical composition of both nucleus and coma different components. The Philae lander's 10 instruments [3] aimed to analyze the surface and sub-surface material, collecting samples and determining their chemical composition.
The main goal of the *Rosetta* mission is to enhance our understanding of the Solar System's origins and development. Since the composition of comet 67P/Churyumov-Gerasimenko was thought to mirror that of the pre-solar nebula from which the Sun and planets emerged over 4.6 billion years ago, a comprehensive examination by *Rosetta* and its lander would offer crucial insights into the processes that shaped the Solar System. To achieve this, the measurement goals consisted of (Schwehm and Schulz, 1999; Glassmeier et al., 2007):

- Global characterization of the nucleus and its dynamic properties.
- Its surface morphology and composition.
- Determination of compositions of volatiles and refractories in the nucleus and their interrelation.
- Studies of cometary activity and related surface layer and inner coma processes.
- Studies of the interaction between the solar wind and the outgassing comet during perihelion.

The detailed scientific objectives for each instrument on the orbiter and lander are presented in Glassmeier et al. (2007).

1.6.2 10 year trip to target

In December 2002, just a month before *Rosetta*'s scheduled launch, a major setback occurred when a similar Ariane 5 rocket failed during a satellite launch. As a result, *Rosetta*'s launch was postponed until the issue was addressed, causing the mission to lose its initial target: comet 46P/Wirtanen. Researchers identified a new target, the larger comet 67P/Churyumov-Gerasimenko. In 2004, the *Rosetta* spacecraft successfully launched from Kourou, French Guiana, and orbited Comet 67P/Churyumov-Gerasimenko for over two years, studying it extensively. Before reaching the orbit of 67P/Churyumov-Gerasimenko, *Rosetta* underwent several phases and successfully gathered intriguing data about other bodies. One year after its launch, the spacecraft's imaging instruments witnessed the collision between comet 9P/Tempel 1 and the impactor from the *Deep Impact* mission. In 2008, *Rosetta* had a flyby of the main belt asteroid 2867 Steins, passing within 800 km of

[2] https://sci.esa.int/web/rosetta/-/35061-instruments
[3] https://sci.esa.int/web/rosetta/-/31445-instruments

it. *Rosetta* also conducted a flyby and captured images of asteroid 21 Lutetia, providing valuable insights into both asteroids (Barucci et al., 2015).

From May to July 2014, *Rosetta* executed a series of orbital adjustments to establish its orbit around comet 67P/Churyumov-Gerasimenko. Throughout the mission, which lasted until 2016, *Rosetta* closely accompanied the comet during its journey around the Sun, conducting extensive investigations that enabled detailed analysis of the comet. This resulted in a wealth of significant data on the comet, that will be concisely presented in the following section. Details about the journey of *Rosetta* are presented in Figure 1.6.

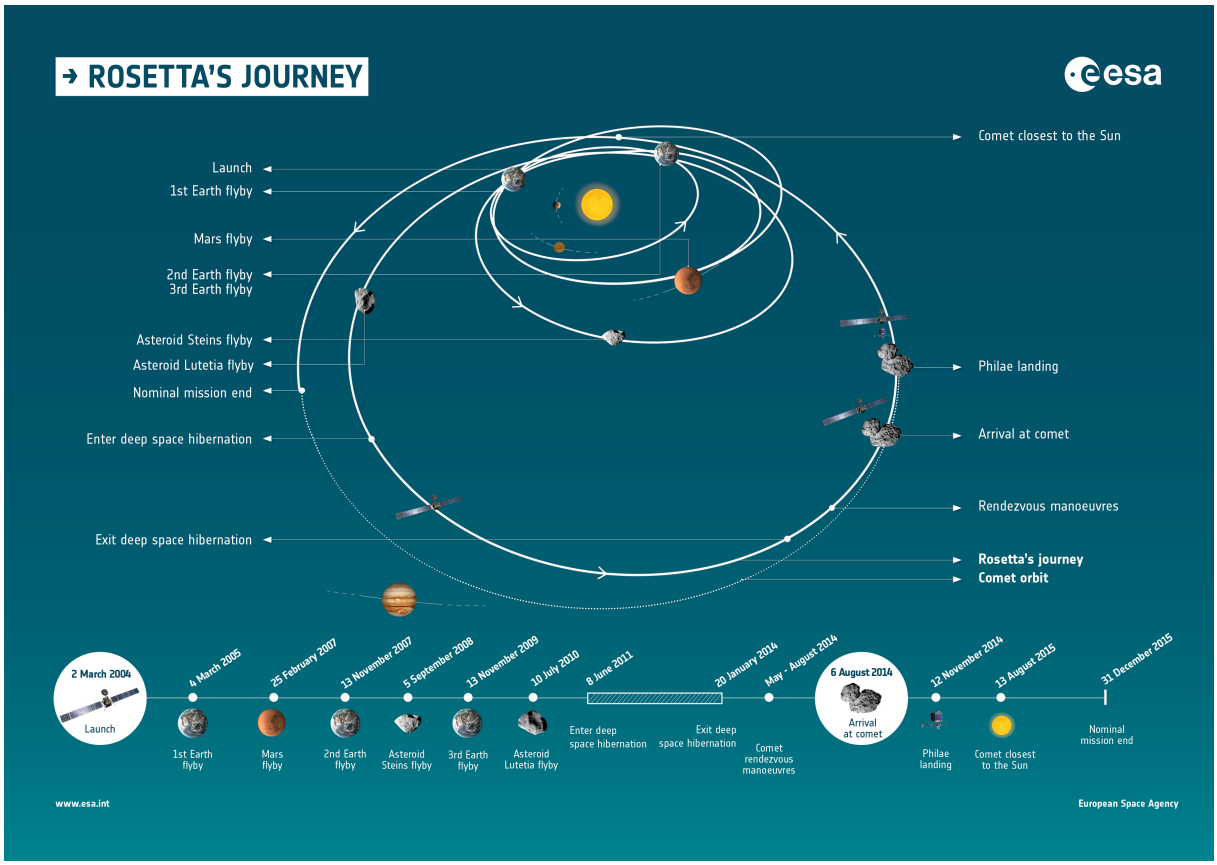

Figure 1.6: The trajectory of the *Rosetta* probe towards 67P/Churyumov-Gerasimenko and the key stages of the mission. ©ESA

1.6.3 Rendez-vous with 67P/Churyumov-Gerasimenko

67P/Churyumov-Gerasimenko, hereafter: 67P/C-G, is a periodic comet with an unusual recent history. One of its previous orbits had a perihelion distance of ∼4 AU, but after an encounter with Jupiter, it decreased to ∼3 AU and shifted inwards. Gradually, it further declined to 2.77 AU before another Jupiter encounter in 1959 placed it in its current orbit (Maquet, 2015). Discovered in 1969, it has been intensely observed by ground-based and space-based telescopes once it became the target of a space mission. The comet has an orbital period of ∼6.45 years, a semi-major axis of 3.46 AU, a rotation period between 12.0 and 12.8 hours, and a high rotation axis obliquity (52°) that results in strong seasonal

effects (Keller et al., 2015b).
The *Rosetta* mission closely studied 67P/C-G during two years and observed its perihelion passage on 13 August 2015, at a distance of 1.24 AU from the Sun, and the lander Philae was able to land on its surface and take measurements and images from the surface during only 2.5 days (Biele et al., 2015). The mission contributed significantly to our understanding of 67P/C-G and of comets in general, revealing important information about their composition, isotopic levels, and morphology.

1.6.3.1 Surprising complex shape

In July 2014, the OSIRIS imaging system onboard *Rosetta* returned interesting images of comet 67P/C-G. Instead of the expected 'potato' form (see Figure 1.7), 67P/C-G was revealed to have an irregular shape: the nucleus is made of two lobes (bilobate) like a rubber duck, composed of a big lobe and a small lobe connected by a neck (Sierks et al., 2015; Jorda et al., 2016). It exhibits overall dimensions of ∼4.3×2.6×2.1 km along its principal axes, (Jorda et al., 2016). The large lobe measures ∼4.1×3.5×1.6 km, and the small lobe ∼2.5×2.1×1.6 km. The comet's axis of rotation is almost parallel to the long axes of the lobes and perpendicular to the neck (Sierks et al., 2015; Preusker et al., 2017).

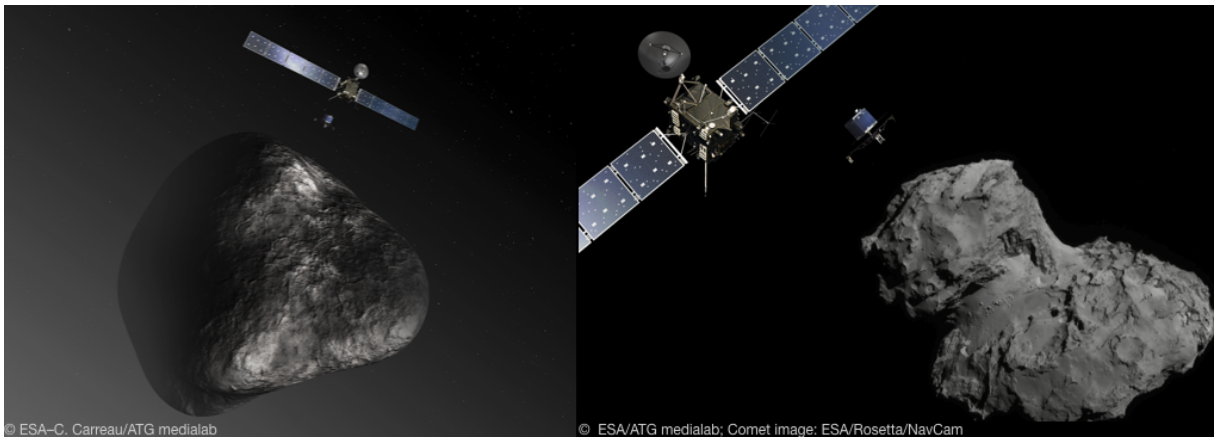

Figure 1.7: An artist image presenting: on the left, the 'potato-shaped' nucleus of 67P/C-G as predicted from pre-Rosetta ground-based observations; on the right, the actual bilobate shape as revealed by *Rosetta*'s images.

The intricate structure of the comet, combined with a rotational axis tilt of 52°, exerts a noteworthy influence on its behavior. This configuration results in substantial variations in daily exposure to sunlight between the lobes and the connecting region due to shadowing. Additionally, it leads to pronounced seasonal thermal changes between the northern and southern hemispheres. The northern hemisphere, when the comet is located further away from the Sun, experiences mostly illuminated conditions, while the southern hemisphere receives intense irradiation during a brief period of the few months around perihelion (Keller et al., 2015a).

The complex shape can also induce changes in the nucleus spin rate, the spatial distribution of the cometary material on its surface, and the way the nucleus releases gas and

dust (Thomas et al., 2015a). Gutiérrez et al. (2005) have made predictions regarding the anticipated alterations in the spin axis direction and spin period for 67P/C-G. Indeed, a discernible change in the spin period of comet 67P/C-G has been observed between the perihelion passages in 2009 and 2015 (Mottola et al., 2014), based on initial images obtained by the OSIRIS camera aboard the *Rosetta* spacecraft. Keller et al. (2015a) demonstrated that the variation curve of 67P's spin period is primarily influenced by the complex bilobate shape of its nucleus. The outgassing can produce acceleration of the nucleus and, depending on its shape, a net torque altering its rotation state (Attree et al., 2019). Additionally, seasonal effects linked to the orientation of the spin axis play a key role in the formation, stability and evolution of dust mantles (Rickman et al., 1990; De Sanctis et al., 2010b), and in turn largely control the temporal variations of the gas flux (Attree et al., 2019).

1.6.3.2 A very rich geology

> "*Rosetta has completely changed our picture of comets.*" "*Previously, they were pictured as dirty ice balls – or, as some prefer, icy dust balls – but now we know them, or at least this one, to be geologically complex worlds where a myriad of processes are at work creating the incredible surface structure and activity of the comet,*" said Eberhard Grün, a scientist that worked on the *Rosetta* mission at the Max Planck Institute for Nuclear Physics in Heidelberg.

OSIRIS camera providing highly detailed images of the surface of comet 67P/C-G centimeter-to-millimeter scale resolution, revealed its complex morphology including dynamic surface features (Thomas et al., 2015b). Significant surface and subsurface processes play crucial roles in determining this complex appearance. This can be primarily attributed to mechanisms leading to erosion on its surface, including changes in local solar radiation, thermal fracturing, and sublimation (Birch et al., 2017).

The surface of 67P/C-G displays signs of stratification, notably through clearly visible terraces and strata (Massironi et al., 2015; Ruzicka et al., 2019). Numerous other geomorphological features are present on its surface including mainly: fractures, goose-bump and wind-tail-like features, boulders and pancake features, scarps, cliffs and depressions of varying shapes and sizes: large, deep pits, shallow thermokarst depressions that demonstrate obvious scarp retreat, and a bowl-shaped crater (Sierks et al., 2015; Vincent et al., 2015a; El-Maarry et al., 2019; Bouquety et al., 2021a; Fornasier et al., 2021). See examples of the main features in Figure 1.8.

The surface of comet 67P/C-G has been categorized into 26 distinct regions based on their geomorphological and topographical characteristics (Thomas et al., 2015a; El-Maarry et al., 2016, 2019). The northern hemisphere and equatorial regions are characterized by rough terrain, featuring cliffs and pits. On the other hand, the southern hemisphere appears flatter with a higher erosion rate, primarily influenced by the intense activity close to perihelion (El-Maarry et al., 2016). The northern hemisphere is covered by sedimentary materials, while the southern hemisphere exposes the bedrock nucleus. The process of sediment transport and erosion might have obscured any original differences between the two lobes, as suggested by Birch et al. (2017). A study by Barrington et al. (2022)

focusing mainly on smooth terrains confirms that sediment transfer from the active south to the north occurs around the comet's perihelion. This process, which happens both within and between regions, is influenced by the topography of the comet. Some regions exhibit little signs of erosion or deposition and could potentially serve as the final repositories for sediment. Understanding these sediment pathways on comet 67P is critical for gaining insights into the activity and evolution of cometary surfaces. The presence of a non-uniform dust layer could explain the observed rates of water production from comet 67P (Attree et al., 2019). However, it was found that more dust falls back to the nucleus than previously thought (Thomas et al., 2015a; Keller et al., 2017; Hu et al., 2017), indicating that the nucleus surface has been significantly eroded or covered by cometary activity. Finally, the stability of the mantle is shown to be dependent on the obliquity of the nucleus spin axis (Attree et al., 2019; De Sanctis et al., 2010b).

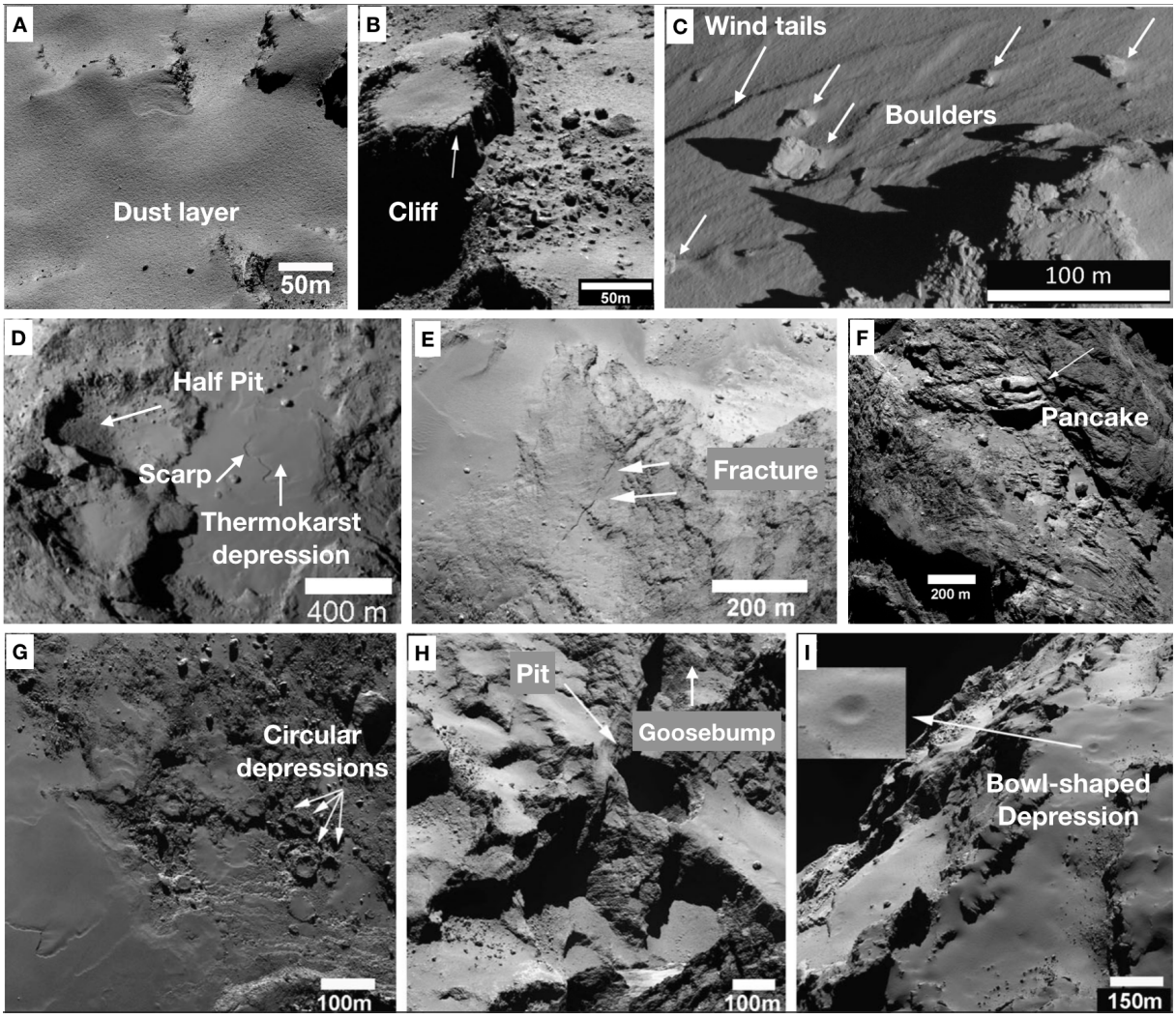

Figure 1.8: Main geomorphological features observed on the surface of 67P/C-G. Image A is adapted from El-Maarry et al. (2015); images B, C, D, E, G, H, and I are adapted from El-Maarry et al. (2019); and image F is adapted from El-Maarry et al. (2016).

Overall, understanding the mechanisms that shape and evolve the surface remains a significant challenge. Thermal models, accompanied with observations aim to constrain the underlying processes and timescales that govern the complex evolution of the surface topography.

1.6.3.3 Coma and surface composition

The composition of 67P/C-G's coma is dominated by H_2O. It is followed by CO_2 and CO, then O_2 (Bieler et al., 2015; Läuter et al., 2020b). The coma composition was observed to be very diverse. The detection of complex organics like amino acid (glycine, Altwegg et al., 2016), salts (Altwegg et al., 2020), noble gases (Rubin et al., 2018), and molecular nitrogen provided insights into the Solar System formation models, Earth's atmosphere, and the possibility of life blocks. One significant result regarding the composition of comet 67P/C-G is the discovery of abundant molecular oxygen (O_2) and its correlation with water (Bieler et al., 2015; Keeney et al., 2019; Luspay-Kuti et al., 2022). DFMS recorded in-situ data and found high levels of molecular oxygen around 67P/C-G, with local abundances of $\sim$3.80$\pm$0.85 relative to H_2O (Bieler et al., 2015). It was the first detection of molecular O_2 on a comet. The O_2/H_2O ratio is isotropic and doesn't change with heliocentric distance, suggesting primordial O_2 was incorporated during the comet's formation (Bieler et al., 2015). The D/H measured by ROSINA is notably different from other comets suggesting Jupiter family comets have diverse origins. It is more than three times that on Earth, meaning that Earth's water is unlikely to have originated from comets like 67P/C-G (Altwegg et al., 2015).

The mission also yielded valuable insights into the properties of dust grains present in the comet. The detected dust grains exhibited a flaky aggregate structure even at the smallest scales observed. The constituent grains making up these aggregates were found to have dimensions on the order of 0.1 μm. Interestingly, this size range corresponds to the expected size of interstellar solid particles that played a crucial role in the formation of bodies in the early Solar System through the process of accretion (Güttler et al., 2019).

Comprehensive analysis of data gathered on the coma and the surface of the nucleus provided valuable insights into the nucleus composition and characteristics. The surface of 67P/C-G is covered by organic-rich dark material with low geometric albedo of $\sim$6% (Fornasier et al., 2015), and is characterised by a lack of considerable water-icy regions (Capaccioni et al., 2015). Only a small number of ice patches in the northern hemisphere were however identified by OSIRIS and VIRTIS (Barucci et al., 2016; Fornasier et al., 2016; Filacchione et al., 2016). Some of them are suggested to be sources of activity and outbursts (Vincent et al., 2016a). Water and CO_2 spatial distributions were investigated, with water production originating from illuminated areas and CO_2 sublimating below the diurnal skin depth. Moreover, VIRTIS observations revealed cyclic patterns in activity and water ice production rate, with maximum outgassing occurring approximately 20 days after perihelion (Hansen et al., 2016). Additionally, temperature profiles of the near surface provided by MIRO highlight the clear presence of seasonal and diurnal tendencies, with a low thermal inertia ranging from $\sim$10 to 50 J $K^{-1}m^{-2}s^{-0.5}$ (Gulkis et al., 2015b; Davidsson et al., 2021b, 2022c). Filacchione et al. (2022) reviewed our current under-

standing of the composition of 67P/C-G's nucleus: a mixture of ices, minerals, organic matter, and salts, resulting in dark and red-colored surfaces. The surface is covered by a variable dust layer, primarily made up of dehydrated dust grains comprising minerals, organic matter, and salts. The composition and physical properties of the nucleus evolve with heliocentric distance and seasonal cycling, with increased solar flux near perihelion leading to heightened activity, erosion of surface layers, exposure of ices, and mobilization and redistribution of dust. These processes result in color, composition, and texture changes across different regions of the nucleus.

1.6.4 Nucleus mysteries persist

Philae was designed to conduct measurements on the composition, physical and electrical properties, temperature, and magnetic field of the nucleus of comet 67P/C-G, with an intended operational period of 5 days on battery and more if illuminated. However, due to its unfortunate crash landing, it was unable to complete its planned measurements and operated for only 64 hours. Despite this setback, some of the data collected during Philae's short-lived operations were still able to be analyzed and provided valuable insights on the nucleus surface and interior. For instance, CONSERT operated for around 9 h after Philae's landing. The radio waves transmitted by CONSERT specifically probed a limited area corresponding to the upper part of the small lobe of the comet, with an expected penetration depth of up to 100 m and a propagation length of around 1 km (Herique et al., 2019). The measurements indicated a very low dielectric permittivity value $\sim$1.27 in the shallow subsurface ($<$25 m Kofman et al., 2020), consistent with a material composed of water ice, dust enriched with organic materials, and exhibiting a porosity of 70% to 80% (Herique et al., 2019).

While the *Rosetta* mission provided extensive data on the coma and surface features of comet 67P/C-G, there remain unresolved questions and areas for future research on the various properties of the nucleus. This is primarily due to the short operational period of the Philae lander. Remote sensing techniques, despite offering general evaluations of nucleus composition, cannot provide detailed information on the fine-scale structure and composition of the nucleus surface (Capaccioni et al., 2015). Crucial questions that could significantly improve thermal models involve determining the volatile-to-refractory (or dust-to-ice mass) ratio within particles and the nucleus (Choukroun et al., 2020), as well as understanding compositional heterogeneity as ice distribution (Fornasier et al., 2023), conductivity, and the forms of water ice. Addressing these questions may necessitate accessing more pristine material, such as obtaining information about subsurface layers using ground-penetrating radars (Asphaug and Thangavelautham, 2015; Hérique et al., 2018), or exploring a less-altered comet (Snodgrass et al., 2022), which aligns with the future mission *Comet Interceptor*[4].

[4]https://www.cometinterceptor.space/

1.7 Thermal evolution models of comets

The idea of solid comet nuclei was widely doubted before the 1950s. The "flying sandbank" model, first introduced in the late 19th century, imagines a comet not as a single solid entity but as a cluster of individual bodies. According to this model, comet activity results from both the loss of volatile components and the dispersion of constituent particles (Rickman, 2018). Lyttleton (1948) notably supported this model, claiming that certain observations contradict the widely accepted model of a solid nucleus comet. They pointed to phenomena such as contracting comas and remote comet activity to argue that a solid nucleus is not the sole explanation for observed comet features. They asserted that any space mission aimed at researching an active comet should carry cameras capable of verifying the existence of a solid nucleus on a km scale within the comet. The introduction of Whipple's theory in the 50s, proposing the cometary nucleus as an icy conglomerate based on the effect of non-gravitational forces, sparked a vigorous discussion about the solidity of a comet's nucleus (Whipple, 1950). Despite his proposition, many scientists continued to support Lyttleton's concept of a 'sandbank nucleus', and the debate would persist until the decisive spacecraft encounters with Halley comet in 1986 provided more concrete evidence.

Since their origin in the 1950s, models simulating cometary nucleus activity have substantially evolved aiming to understand the underlying processes that determine the behavior of comets and identify the factors impacting their activity. Initially, simple energy balance models were used to estimate the surface temperature of a comet based on the balance between incoming solar radiation and outgoing thermal radiation. Over time, these models began to incorporate the process of ice sublimation and focused on reproducing gas production from the surface layer and did not consider heat diffusion in the internal layers. After Whipple (1950)'s model of the cometary nucleus, the first quantitative study of gas production from ices was by Squires and Beard (1961). We note that at this step, the outgassing is considered in the solar direction only.

Huebner (1965) introduced then the first model to consider a spherical nucleus, addressing a significant limitation of previous models. Further improvements were made by studying the relationship between enthalpy of sublimation and temperature (e.g., Delsemme and Miller, 1971), and the consideration of the specific angular dependency of surface elements in relation to the Sun by Cowan and A'Hearn (1979). This led to the model of energy balance at a surface unit:

$$\frac{F_{\odot}\,(1-\mathcal{A}_R)\;cos\;\zeta}{r_H^2} = \varepsilon\sigma T^4 + \Delta H_{\alpha}\;Q_{\alpha}, \tag{1}$$

where $F_{\odot}$ is the solar flux at 1 AU from the Sun, $\mathcal{A}_R$ the Bond albedo, ζ the local solar zenith angle, r_H the heliocentric distance, ε the emissivity, σ the Stefan–Boltzmann constant; T the surface equilibrium temperature, ΔH_{α} the latent heat of sublimation of ice species α, and Q_{α} the corresponding sublimation rate.

Heat diffusion in the internal layers of the nucleus was added to the surface models at a later point (e.g., Kührt, 1984). As a result, researchers began to uncover interest-

ing subsurface phenomena, such as the thermal gradient in the deep layers. Panale and Salvail (1984) included heat and gas diffusion and dust mantling, and studied the effects of the rotational state of the comet by considering its period and spin axis, as well as the latitudinal dependency that expresses seasonal effects (Prialnik et al., 2004; Huebner et al., 2006). Shortly later, the observation of comet 1P/Halley during its 1986 perihelion passage, revealed some physical properties prompting the next step in the study of comet nuclei through numerical models, such as the very low bulk density and the high porosity (Rickman, 1989).

Prialnik and Bar-Nun (1987) developed a model to examine the crystallization of amorphous ice in the nucleus subsurface, which is an important heat source to consider in thermal processes. The proposed model assumed that the subsurface of a cometary nucleus is made up of a combination of amorphous and crystalline ice. The proportion of amorphous ice decreases as the depth increases. Through this model, they were able to estimate the rate of amorphous ice crystallization at different depths, temperatures and water vapor levels in the subsurface. The crystallization of amorphous ice releases a significant amount of heat ($9{\times}10^4$ J/kg, Ghormley, 1968), which can affect the temperature distribution in the subsurface and the overall thermal budget of the comet. Based on experimental data, Schmitt et al. (1989) showed that this transition is exothermic and determined the rate of this phase transition as a function of temperature.

The KOSI experiments (Kometensimulation, Grün et al., 1989) significantly helped constrain physical characteristics of comets and thereby, models. The experiments aimed to examine sublimation and heat transfer in porous mixtures of ice and dust. The experiments involved a cooled, low-pressure chamber housing a tank of water ice and carbon dioxide mixed with mineral and carbon particles. Ten xenon lamps simulated solar radiation, inducing ice sublimation (Sears et al., 1999). Comprehensive data collection was facilitated by various sensors, including a mass spectrometer and dust collectors, and different measurements were taken before and after illumination (see details on experiement equipments in Seidensticker and Kochan, 1992). The simulation experiments varied in insolation duration and intensity, and sample composition. The KOSI experiments significantly advanced our understanding of physical processes related to comet activity: dust mantle formation, stratification, dust ejection, and the ratio of ejected gas to dust. The resulting theoretical model formed the basis of the thermal comet nucleus model by Benkhoff and Huebner (1995). For a comprehensive overview of the KOSI experiments' results, we recommend referring to Sears et al. (1999).

Espinasse et al. (1991) developed a model of a porous comet nucleus of feeble density and investigated its thermal behavior and chemical differentiation. The model considered heat conduction, mass transfer, sublimation of multiple volatile species and crystallization of amorphous ice. The study revealed the stratigraphy of the nucleus evolved with the heliocentric distance, and volatiles depleted in the subsurface layers while enriched in deeper layers. The importance of CO and CO_2 in controlling the phase transition propagation and the relation between nucleus composition and gas production rates were highlighted.

Incorporating the role of radioactive decay as a heat source in comets, later models accounted for its more significant influence when comets are in the outer Solar System, distant from the Sun (Prialnik and Podolak, 1995). Despite being relatively weak, this heat source can be more consequential in larger bodies as suggested by Guilbert-Lepoutre

et al. (2011). While currently not substantial enough to be observed, it may have influenced the thermal history of comets during the early stages of the Solar System and planetary formation (Huebner et al., 2006). The radiogenic heat produced by radioactive isotopes (e.g., ^{26}Al, ^{60}Fe and ^{53}Mn) may have been used in the cometary core for the crystallization or sublimation of ices. The short-lived isotope ^{26}Al has a half-life of only 7.2×10^5 years and represents an important source to consider in the thermal modeling of TNOs or comets in the centaur phase.

Subsequent development in modeling techniques led to a shift from 1.5D to more complex 3D models. Additionally, models started to take into account the actual shape of the comet instead of representing it as a simple sphere.

Despite significant advancements in cometary models over the years, spurred by extensive observations and theoretical work, certain limitations persist. These include time-intensive complex calculations requiring substantial computational power, lack of detailed observations on composition and shape, and incomplete understanding of cometary material properties. To manage, models often resort to assumptions and simplifications, leading to uncertainties in the results. Critical parameters like density, porosity, conductivity, composition of ices, and dust-to-ice ratio are yet to be firmly established. Adding to the complexity is the broad variety of behaviors and characteristics exhibited by comets, which challenges the establishment of a standard set of parameters for model constraints. Finally, many of the current models typically default to the assumption of a spherical comet nucleus. This simplification is often made when we lack the comprehensive, high-resolution data necessary to determine the actual shape of the nucleus. However, it's important to acknowledge that the true shape of a comet can significantly influence its activity, presenting a notable constraint within these models.

Overall, despite the challenges that can affect their reliability, thermal models are an important tool for understanding the behavior of comets. In the last few decades, there has been increasing interest in using them to predict the behavior of comets during close encounters with the Sun, and to understand the effects of these encounters on the comet's thermal and structural properties (e.g., Capria et al., 2012; Guilbert-Lepoutre et al., 2014). Also, there has been a growing focus on using thermal models to understand the processes of the formation and evolution of surface features, and the role of subsurface processes in driving these changes, especially after the *Rosetta* space mission which provided us with the largest database of data from an active nucleus over more than 2 years of in-situ observations (e.g., Mousis et al., 2015; Guilbert-Lepoutre et al., 2016; Bouquety et al., 2022).

The combination of observations and models helped us constrain the structure of the thermal processes likely to occur within the nucleus, that we will see in the next sections.

1.8 How does the nucleus work?

Qualitative description of the different processes occurring in the cometary nucleus

1.8.1 Solar energy absorbed at the surface

The nucleus interior, while not fully understood, is generally supposed homogeneous at a macro-scale. Dust grains and rocky materials primarily form the matrix, with water ice and other frozen gases serving as a filling agent (Prialnik et al., 2004).
As the comet approaches the sun, it is exposed to incident solar radiation that heats up its surface, and varying with the nucleus's spin. Solar flux absorbed on the surface is partially re-radiated in the infrared wavelength range, partially spent on sublimating surface volatile species if there are any, and partially conducted into the nucleus's interior. When this heat propagates through the nucleus interior, it triggers various physical and thermal processes leading to the observed activity.

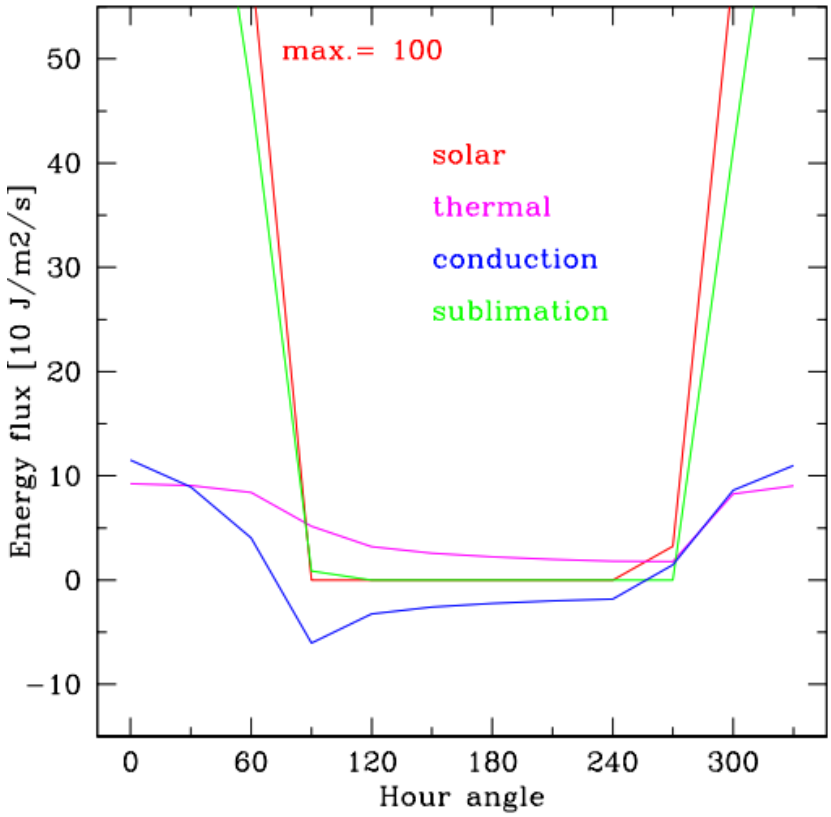

Figure 1.9: Energy flux at a nucleus surface: insolation, infrared reradiation, water ice sublimation, and conduction into the interior, as a function of the subsolar angle at a heliocentric distance of 1.1 AU. Credits: Huebner et al. (2006).

Cometary nuclei are highly absorptive of insolation. They typically exhibit a low albedo ranging from 2% to 10% (Shubina et al., 2023), with the extent depending on the presence of water ice and other volatiles or organic molecules. In rare cases, the albedo can reach up to 33%, as observed in centaurs (Barucci et al., 2004; Shubina et al., 2023).

During the night, when solar heating is absent, comet activity significantly decreases, and even recondensation of volatiles can occur, as observed by *Rosetta* (De Sanctis et al., 2015). The spin of the nucleus primarily affects surface water ice sublimation, while more volatile species sublimate from the nucleus's interior, depending on its internal structure and compositional stratification. Thermal conductivity plays a crucial role in the penetration of heat into the nucleus. Ongoing sublimation of volatile ices from some depth and chemical differentiation are expected in the nucleus. Consequently, emissions of more volatile ices vary slightly over the nucleus's spin, while less volatile species like water are highly influenced by the spin period. In cases of complex internal structure, where volatiles are trapped in amorphous ice, their release may occur during the transition from amorphous to crystalline ice. We detail in the next sections the physical and thermal processes occurring as a result of heat propagation inside the cometary material.

1.8.2 Heat propagation in the subsurface

For a comet to exhibit thermal activity in its subsurface, leading to the ejection of dust and the formation of a coma, it must contain a sufficient amount of internal heat. This internal heat drives the sublimation of volatiles within the nucleus, which in turn leads to the ejection of dust and gas from the surface. The main heat source is external, induced by solar radiation absorbed at the surface -depending on the nature of the surface grains, in terms of composition and reflection capacities. Additionally, heat can also be generated internally, such as through the condensation of vapor gases or from a radiogenic source in the early formation of the comet. The heat wave propagates within the interior mainly via thermal conduction in the solid matrix, and with the gas vapor flow through the pores driven by a pressure gradient, which can transport a significant amount of heat. At temperatures below 200 K, radiation within the smaller pores can be neglected (Huebner et al., 2006).

The heat diffusion through the radial direction is expressed by:

$$\rho_{bulk} c \frac{\partial T}{\partial t} = \text{div}\left(\kappa \overrightarrow{\text{grad}}\, T\right) + \sum_{\alpha} \mathcal{Q}_{\alpha}, \tag{2}$$

where T is the temperature; t the time, ρ_{bulk} the material's bulk density and c its heat capacity; κ its thermal conductivity coefficient; $\sum_{\alpha} \mathcal{Q}_{\alpha}$ is the energy gained due to condensation or used in the sublimation process for each ice α.

The thermal conductivity of dust and ice mixtures plays thus a crucial role in determining the speed and depth of heat penetration into the nucleus. These values can vary widely. The thermal conductivity of the icy matrix is lower compared to compact water ice, which is attributed to the reduced contact area between particles, quantified by the Hertz factor (Huebner et al., 2006). Thus, the heat transport depends on the nature and quantity of ices present in the nucleus and diffused in the different layers, porosity, and also the nature and the size of dust particles and their contacts. The orbital skin depth of a few meters demonstrates the significant impact of such a porous material on heat propagation, effectively insulating surface layers from internal ones (Prialnik et al., 2004).

1.8.3 Ice sublimation and recondensation

The process of ice sublimation results in the retreat of the ice fronts in the radial direction, away from the surface, in function on the enthalpy of vaporization of each species. The sublimation fronts, present between the solid and gaseous phases of the ices, keep moving inward away from the surface of the comet, as the gaseous ices expand. The sublimation front retreat facilitates the mass loss from the surface through erosion. It also leads to the concentration of ices in the deep interior. As the sublimation rates are highly influenced by temperature, they vary significantly between gas species and can lead to the formation of multiple sublimation fronts and layers of refrozen gases (Huebner et al., 2006). Therefore, having the information about the sublimation fronts gives insight on the properties of the cometary interior. The sublimation can also occur from surface ice patches and grains containing ice like the boulders, even if they represent a minimal contribution to the global activity (Fornasier et al., 2023). A schematic representation is given in Figure 1.10.

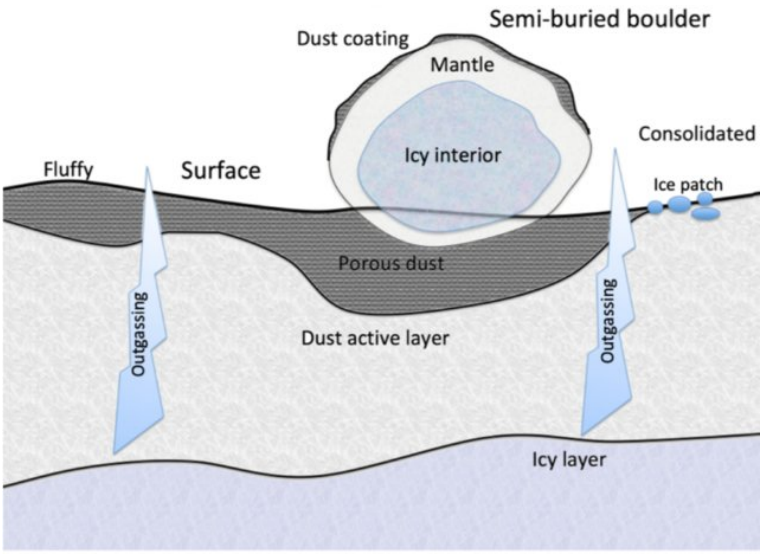

Figure 1.10: Schematic illustration of ice sources in the top layers of a nucleus. Outgassing can originate from the sublimation of deep icy layers through the overlying dust layers or from small fissures or patches of near-surface and surface ice. Credits: Lisse et al. (2021). Please note, this is a generalized representation and may not apply uniformly across the entire surface of a comet.

Alternatively, within the night period or when the comet travels sufficiently further from the sun, the temperature in the near-surface decreases, leading to the condensation of a portion of the gases on the walls of the pores within the comet's structure. This condensation results in the formation of new ice particles, that accumulate within the pores. The sublimation and recondensation processes also depend on the local pressure, and involve the exchange of latent heat.

1.8.4 Amorphous–crystalline transition

The structure of ice depends on the temperature and pressure at its formation. Ice can take one of three forms: crystalline, amorphous, or a combination of both. Crystalline ice is characterized by a more ordered structure than amorphous ice. The most familiar form of ice is generally the crystalline structure —but if the temperature of the surrounding medium is low (below $\sim$ 120 K, Huebner et al., 2006) and the rate of condensation is sufficiently rapid, H_2O molecules will not have time to reorient themselves into crystals; instead they will remain in a disordered form known as amorphous ice. Cometary interiors are expected to contain amorphous ice that crystallize when sufficiently heated (Prialnik and Jewitt, 2022). The transition to crystalline ice, allows to create a separate front for the phase transition. This process is exothermic and allows to release gases, such as CO and CO_2, previously trapped in the amorphous ice.

1.8.5 Gas diffusion in the porous matrix

The gas released from the interior of the comet through sublimation of ices or as a result of amorphous ice crystallization (mainly H_2O ice) diffuses through the pores to the surface. The gas flow from the interior of a comet to the surrounding coma is driven by a pressure gradient between the two regions. The high pressure inside the comet causes gas to flow towards the surface, where the pressure is typically low or nonexistent. This pressure gradient creates a driving force that causes the gas to flow from the interior to the surface of the comet, contributing to the formation and evolution of the coma. The rate at which the gas flows through the pores, the gas flux, is affected by various factors such as the size and shape of the pores and especially the temperature of sublimation of the gas molecules.

The gas flow through the porous matrix following the mass conservation equation:

$$\frac{\partial \varrho_\alpha}{\partial t} + \text{div } \overrightarrow{\phi_\alpha} = q_\alpha, \tag{3}$$

where ϱ_α is the mass per unit volume of each gas species; ϕ_α is the flux; and q_α is the gas source term due to sublimation or recondensation.

1.8.6 Erosion and mantle formation

To understand the process that eject gas and dust from a comet, as well as the structure and evolution of the coma, it is crucial to accurately model the coma-nucleus boundary. This involves consideration of factors such as the comet's size and shape, local topography, and the presence of dust and volatile gases –which are pulled out from both the nucleus and the ejected dust grains.

When outgassing triggers erosion, dust is propelled into the coma. However, some of this dust, particularly the heavier particles, are not pushed away by gas particles in the coma. Instead, they eventually resettle on the surface, forming a dust mantle. Conversely, lighter dust grains are more readily transported if the gas pressure is sufficiently high, leading to surface erosion (Prialnik et al., 2004). Dust mantle can also be created the devolatilization of surface layers due to sublimating ices where the dust is not ejected due to heavy grains or through cosmic bombardment (Huebner et al., 2006).

The sizes of the dust particles that both leave and redeposit on the comet are well predicted by models. These simulate various forces acting on individual dust grains, including centrifugal forces and the gravitational attraction force of the nucleus (Capria et al., 1996; De Sanctis et al., 1999). The critical dust grain radius, is the size of the largest particle that can be carried away from the comet due to the equilibrium of forces acting on it. This process is influenced by the state of the comet's rotation axis (Prialnik et al., 2004), as well as the mass distribution in the interior of the nucleus.

The presence of dust on the surface of a comet can change its reflective properties and thermal inertia in the first layers and thus the subsequent thermal processes, making it an important factor to consider in thermal models. The presence of dust on the surface of a comet can change its activity over time and could quench it if a big part of the surface is covered by a thick layer of dust grains (close to 100% Prialnik and Bar-nun, 1988).

The KOSI-9 experiment examined the dust mantle evolution on a ice-dust mixture: a mixture of water ice and 10% olivine grains, was exposed to varying insolation. The first phase saw an increase in surface temperature and a decrease in gas and dust emissions, indicating dust mantle formation. The second phase had avalanches disrupting the mantle, leading to an increase in ice and dust emissions. In the third phase, without reaching critical gas flux, no increased emissions occurred, and a few mm-thick dry dust mantle formed (Grün et al., 1993).

A dust coating was observed on several comets including 67P, where OSIRIS observations revealed the presence of dust deposits in the northern regions, which are believed to have been ejected from the highly active southern hemisphere during the comet's previous perihelion (Thomas et al., 2015b; El-Maarry et al., 2019). This mantle is almost certainly nonuniform on the surface of 67P (Hu et al., 2017; Davidsson et al., 2021a), but typically ranging from some mm up to few cm in the northern hemisphere (Davidsson et al., 2022a). Some regions were observed to have a significantly thicker dust mantle, reaching more than 1 m (see Fornasier et al., 2021, and references therin).

1.8.7 Layered nucleus: a consequence of activity

The thermophysical processes present within cometary nuclei, as detailed above, have been key in shaping our understanding of the structure of the comet nucleus, at least within the surface layers. As a result of sublimation, the originally homogeneous nucleus evolves into a stratified structure in the active layers, with the separation between various layers is marked by a sublimation front. Sublimation fronts are typically located near the surface. These fronts trigger the release of gases and dust into the comet's coma, thus after an important activity, different materials are supposed to exist at various depths. A schematic representation of the probable structure of the near-surface layers is shown in Figure 1.11.

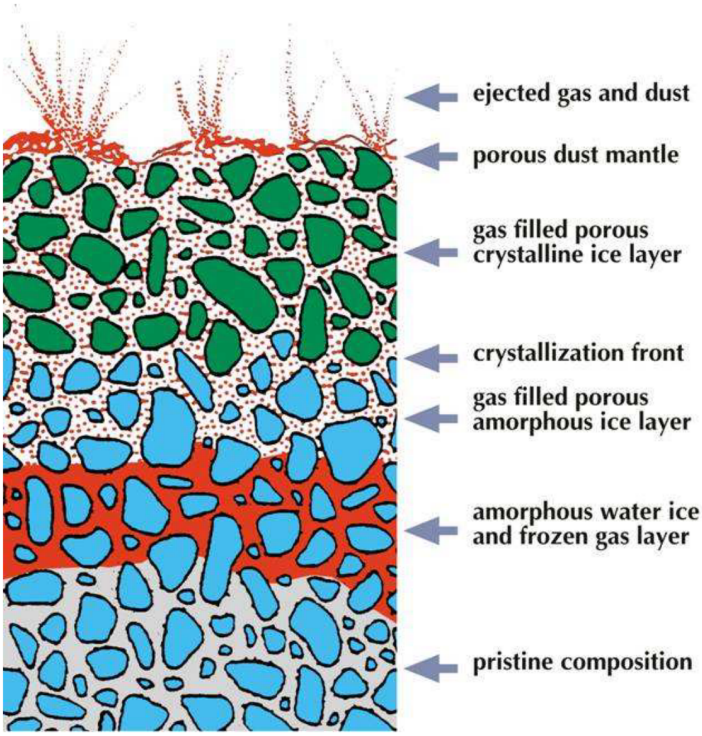

Figure 1.11:
Stratified layers of a comet with an arbitrary scale. Different depths of ices are represented corresponding to their respective temperature of sublimation. (Prialnik, 1997; Huebner et al., 2006).

The proportions of the different materials are observed to be different among different comets, suggesting possible lack of uniformity in their structure. There's also potential for cometary nuclei to possess more complex structures, with varied materials or regions existing at different depths or mixed together in unconventional manners. This further accentuates the need for continued research to unveil the hidden complexities of cometary nuclei structures. The internal structure of a comet is highly shaped by elements such as internal temperature and pressure, potential heat sources, and the cohesive strength of the nucleus. These elements can impact the overall cometary activity. Consequently, a deeper comprehension of the internal structure could yield crucial insights into cometary behaviors, and vice versa.

1.9 Factors influencing surface energy balance

On the surface of the comet, a balance is maintained between the net incoming solar flux, thermal radiation losses, heat required for ice sublimation, and heat transport into or out of the nucleus. Thus, the nucleus structure and composition, along with the various internal processes previously discussed, play a major role in the energy balance at the surface. Sublimation at the surface is directly linked to the active fraction, the portion of the surface that is actively releasing gas and dust. The presence of ice on the surface of a comet is ultimately influenced by its distance to the Sun and its position relative to the point at which ice sublimates. For water ice, sublimation becomes increasingly significant at approximately 3 AU from the Sun.

Other surface properties contribute to the overall surface balance. The composition of the refractory material that, in combination with the ice, influences the albedo that

directly affects the amounts of solar energy absorbed. Lastly, comet nuclei, in addition to having a complex overall shape, are rugged and present at their surface small-scale features such as cliffs, pits, and fractures, as detailed in Sections 1.5.2 and 1.6.3.2. This complex shape and topography influences the distribution of energy on the surface, as well as the release and redeposition of dust and gas, which could lead to significant variations beneath the surface and changes in surface morphology in consequence. Hence, 3D models serve a significant role not just in geological studies, but also in accurately modeling the thermal activity.

1.10 My work: influence of shape

This research work was primarily focused on two central scientific inquiries, specifically related to the impact of the complex shape on the thermal activity of Jupiter Family Comets.

First, we conducted an extensive study on the thermal evolution and morphological changes of the large depressions observed on these comets under current illumination conditions, with further considerations given to the influence of initial structural and thermal parameters. This work would take us a step closer in the investigation of the origins of these depressions.
The second objective examined how a comet's distinctive global shape, along with its surface and internal composition, influence its overall activity. The purpose was to decode the complex relationships between the properties of a comet's nucleus and its observable behavior.

To achieve these goals, we incorporate the surface shape into the calculations of the energy balance and model thermal activity. Gas flux released and erosion resulting from thermal simulations are explored for the different purposes.

Chapter 2

Thermal evolution model – accounting for the nucleus shape

This chapter outlines our methodology for investigating the thermal evolution accounting for the shape effects at both local and global scales. We begin by providing an overview on the evolution of existing thermal model, from fast rotator consideration to sophisticated 3D models, and justify our choice of model. We then describe our methodology in detail, which will be referred to throughout the manuscript with any necessary adjustments to physical and compositional parameters or application for specific purposes.

2.1 Choice of a 1D numerical scheme

Thermal evolution models typically assume that comet nuclei can be modeled by a spherical shape. This assumption considerably simplifies the physical and numerical models, by reducing a number of shape-related free parameters to compute the energy balance at the surface. The first and the simplest assumption is to consider the comet as a fast rotator. This assumption is valid when the rotation period of the comet is much shorter than the timescale of typical thermal processes being considered, and leads to the simplifying assumption of a constant incidence angle ζ for all surface elements (in this case though, we typically assume one surface element). This results in a uniform distribution of solar energy received at the surface and thus a uniform distribution of heat diffused in the subsurface. However, when studying diurnal or seasonal thermal phenomena, the assumption of a fast rotator is not only limiting, but also wrong because it does not account for variations in the distribution of heat over longitude and latitude. Therefore, considering a slow rotator is necessary to compute the surface distribution of energy.

Thermal evolution models have expanded to multiple space dimensions, starting with 1.5D models that consider only one point at the equator, allowing to reproduce diurnal variations of the surface temperature at the equator (Benkhoff and Boice, 1996; Capria et al., 1996; De Sanctis et al., 1999). These simpler models were followed by 2.5D models that accounted for variations of the energy along a meridian (Enzian et al., 1997, 1999), and a quasi-3D model which consider both longitudinal and latitudinal variations of surface energy, allowing the study of both diurnal and seasonal effects on the surface. In these

cases, the internal radial heat transfer and gas flow is considered only in one dimension (Gutiérrez et al., 2000; Cohen et al., 2003). Some subsequent developments have focused on improving thermal evolution models, particularly with regard to the lateral conduction of heat that was lacking in the previous models, and the three-dimensional resolution of equations for spherical bodies (Rosenberg and Prialnik, 2009; Guilbert-Lepoutre et al., 2011). Although the effect of lateral heat transfer is typically negligible, it can become significant over very large time scales. Finally, there has also been a focus on improving models to account for the effect of non-spherical shapes of cometary nuclei. A first attempt was made by Lasue et al. (2008) using a 1000 facet model of 67P/C-G derived from HST observations (Lamy et al., 2007) to calculate the energy balance at its surface. In general, more elaborate models (with multiple dimensions, and/or accounting for many internal processes) are complex and time-consuming to solve numerically, requiring advanced numerical techniques to solve a large number of equations. In contrast, simpler models are easier to implement, versatile and computationally efficient. However, they may lack the accuracy of more complete models.

For our study, we aim to investigate the influence of the energy input on the thermal evolution of comet nuclei, specifically focusing on surface erosion and production rates, while accounting for local topography and the global morphology of the nucleus. Thus, we require a thermal evolution model that remains relatively simple in terms of geometry, but accounts for "standard" physical processes sufficient to describe cometary activity. Choosing the appropriate model is critical, and we consider the following aspects in selecting our numerical scheme:

1- Each surface element is assigned its own boundary condition at the surface, making a one-dimensional thermal evolution model the optimal choice. This is further supported by results from Macher et al. (2019), who found that temperature differences at the surface of 67P between a 1D and a 3D thermal simulation (which considers lateral heat fluxes) are only around 0.1%. This is due to the fact that lateral heat fluxes remain very small over the timescales we will have to consider, because the thermal conductivity of the cometary material is very low.

2- Physical processes included in the model should be consistent with the standard set in recent decades (Prialnik et al., 2004; Huebner et al., 2006). These processes include heat and gas diffusion, phase transitions for volatile species, the drag of dust particles by the escaping vapor phase, and the formation of a dust mantle at the surface (detailed in Section 1.8 of Chapter 1).

3- Thermal evolution models typically require a number of free thermo-physical parameters that might be poorly constrained, either by observations or laboratory experiments. We want the exploration of the parameter space from a computational standpoint to be efficient, as it is necessary to gain a better understanding of the robustness of our results. As a result, it is preferable to use simple expressions for thermo-physical parameters such as the thermal conductivity, to avoid the introduction of additional parameters (e.g., Davidsson, 2021).

Taking these factors into consideration, we have chosen a well-established one-dimensional numerical scheme (De Sanctis et al., 2005, 2010b; Lasue et al., 2008). This approach offers the numerical flexibility we seek, while including all necessary thermal processes for our study.

2.2 Thermal evolution model

The thermal model used in our study is derived from a number of physical and numerical developments stemming from the original work of Espinasse et al. (1991). The subsequent improvements are described in various works (e.g., Espinasse et al., 1993; Capria et al., 1996, 2001; De Sanctis et al., 2005; Lasue et al., 2008; De Sanctis et al., 2010b,a). In the following, we provide a summary of the main features of this model, which is based on the simultaneous solving of the mass and energy conservation equations in one dimensional space. For one facet of the nucleus shape model, the heat conduction and gas diffusion equations are thus solved in 1D, following the radial direction of this facet. The material is considered to be a porous mixture of H_2O ice, but also CO_2 and CO in proportions described below, and dust grains incorporated in the icy matrix. Water ice is initially considered to be in the amorphous form (Prialnik and Jewitt, 2022). The model thus accounts for the phase transition from amorphous to crystalline ice, as well as for the sublimation and recondensation of water, CO and CO_2 ices. The drag and release of dust grains due to the pressure exerted by escaping gas flux is computed, as is the possibility of accumulation of dust grains to form a dust mantle at the surface based on their size and mass relative to a "critical radius" (see Section 2.2.3). Finally, erosion of the surface is also computed.

2.2.1 Energy conservation equation

Heat diffusion through the nucleus is expressed by:

$$\rho_{bulk} c \frac{\partial T}{\partial t} = \mathrm{div}\left(\kappa \overrightarrow{\mathrm{grad}}\ T\right) + \sum_{\alpha} \mathcal{Q}_{\alpha} + \mathcal{Q}_{cr}, \tag{1}$$

where T [K] is the temperature; t [s] is the time, ρ_{bulk} [kg m^{-3}] is the material's bulk density and c [J kg^{-1} K^{-1}] its heat capacity (the product is the average of the specific heats of the various components weighted by their masses in a volume unit); κ [W m^{-1} K^{-1}] its thermal conductivity coefficient; $\sum_\alpha \mathcal{Q}_\alpha$ is the energy gained due to condensation or used in the sublimation process for each ice (α representing each of the ice components, i.e. H_2O, CO, CO_2); and $\mathcal{Q}_{cr}$ is the energy source released during the crystallization of H_2O amorphous ice (Ghormley, 1968). The model does not consider the energy related to the convection of gases in the pores, because it is much smaller than the energy from phase transitions, according to Steiner et al. (1991) and De Sanctis et al. (1999).

We describe now two mechanisms at the origin of energy sources or sinks. The first is the energy loss or gain due to sublimation or recondensation, respectively, of the various ice species present in the matrix. We assume that the matrix consists of a mixture of dust

and ices, with H_2O, CO, and CO_2 present as pure compounds in the initial ice. For each ice, the energy source term is:

$$\mathcal{Q}_\alpha = -\psi \ \Delta H_\alpha \ q_\alpha, \tag{2}$$

where ψ is the porosity; ΔH_α [J kg^{-1}] is the latent heat of sublimation of ice species α (H_2O, CO, or CO_2); and q_α is the corresponding gas source term, which is obtained through mass conservation equations as we will see later on. The second source is the energy released during the crystallization of amorphous water ice, which is assumed to be exothermic and is expressed by:

$$\mathcal{Q}_{cr} = \lambda(T) \ \varrho_{am} \ \Delta H_{ac}, \tag{3}$$

where ϱ_{am} [kg m^{-3}] is the mass of amorphous water ice per unit volume. The phase transition releases a latent heat $\Delta H_{ac} = 9{\times}10^4$ J kg^{-1} (Klinger, 1981) at a rate of $\lambda(T) = 1.05 \times 10^{13} \ e^{-5370/T}$ s^{-1}, determined by Schmitt et al. (1989).

2.2.2 Mass conservation equation

Gases released from the sublimation of the initially icy material flow through the porous matrix: the process follows the mass conservation equation:

$$\frac{\partial \varrho_\alpha}{\partial t} + \text{div} \ \overrightarrow{\phi_\alpha} = q_\alpha, \tag{4}$$

where ϱ_α [kg m^{-3}] is the mass per unit volume of each gas species; ϕ_α[molec m^{-2} s^{-1}] is the flux; and q_α is the gas source term due to sublimation or recondensation. By assuming that vapor and solid phases are in local thermodynamic equilibrium, and the vapor phase behaves as an ideal gas (i.e., no interaction between species), we can express each gas flux $\overrightarrow{\phi_\alpha}$ as:

$$\overrightarrow{\phi_\alpha} = -\mathcal{G}_\alpha \ \overrightarrow{\text{grad}} \ \mathcal{P}_\alpha, \tag{5}$$

with $\mathcal{P}_\alpha$ the partial pressure of each gas; and $\mathcal{G}_\alpha$ a gas diffusion coefficient that expresses how easily a gas can diffuse through a solid material and depends on the structural parameters of the solid matrix (such as the porosity, the size of pores, or the tortuosity), and temperature (see Prialnik et al. 2004 or Huebner et al. 2006 for details). The gas temperature is assumed to be the same as the temperature of the matrix through which the gas diffuses (De Sanctis et al., 1999). This assumption simplifies the model by eliminating the need to consider the effect of gas pressure on temperature. Therefore, for each volatile species, the gas source term (from equation 4) can be written as:

$$q_\alpha = \frac{1}{\mathcal{R}T} \frac{\partial \mathcal{P}_\alpha}{\partial t} - \text{div} \left(\mathcal{G}_\alpha \ \overrightarrow{\text{grad}} \ \mathcal{P}_\alpha \right), \tag{6}$$

where $\mathcal{R} = 8.3145$ J k $^{-1}$mol^{-1} is the ideal gas constant.

2.2.3 Dust mantle and critical grain radius

Modeling the flow of gas through the mantle involves analyzing the diffusion of gas through the porous medium (Huebner et al., 2006). The formation of a dust crust on the surface is a result of gas and dust activity. As water ice on the surface of the nucleus sublimates, dust particles are assumed to become free and no longer interact with each other (Huebner et al., 2006). Some particles will be blown off by the gas and some, heavier, may accumulate on the surface. In our model, we assume a range of dust distribution size from 10^{-6} to 10^{-2} m. The model computes the forces acting on each individual dust grain: gas drag, centrifugal force, and gravitational attraction force of the nucleus (De Sanctis et al., 2010b). The balance between these forces is used to define the behavior of dust grains. In case a dust mantle is formed by accumulating grains at the surface, the production of gas can progressively decline, or the gas pressure can subsequently overcome the action of the dust cover, by removing the mantle and re-initiating a new cycle (Huebner et al., 2006).

The critical grain radius is a measure of the size of the largest dust particle that is able to escape from the nucleus. It can be expressed using the following equation (De Sanctis et al., 1999):

$$a^* = \frac{3}{4} \frac{\phi_{H_2O} \cdot V_{H_2O} + \phi_{CO_2} \cdot V_{CO_2} + \phi_{CO} \cdot V_{CO}}{\rho_{dust} \left[G \, \frac{M_n}{R_n^2} - R_n \, \omega^2 \, cos^2\xi \right]} \quad [m] \tag{7}$$

where G = 6.6743×10 $^{-11}$[m^3 kg^{-1} s^{-2}] is the universal gravitational constant; M_n [kg] and R_n [m] the mass and radius of the nucleus; ω [rad s^{-1}] its angular rotation velocity; ρ_{dust}[kg m^{-3}] the dust grains density; V_{H_2O}, V_{CO_2} and V_{CO} [m s^{-1}] velocities of the gas fluxes. The numerator term represents the lifting force exerted by the outflowing gases, while the denominator represents the gravitational attraction corrected by the centrifugal force. Particles with a radius $a < a^*$ are blown off the surface and contribute to the dust flux in the coma, while those with $a \geq a^*$ accumulate on the surface and contribute to the formation of the dust mantle. Depending on the heliocentric distance, a^* can vary from 10^{-5} to 0.04 m (De Sanctis et al., 2010a). Larger heavier grains accumulating on the surface can create small hollow spaces, allowing to trap smaller particles. This enables a large number of smaller grains to contribute to dust mantle formation. This trapping process is efficiently implemented in the code.

2.3 Surface boundary condition

The energy received at the surface of the nucleus is the boundary condition for the thermal evolution model. Therefore, we need to properly determine this quantity before assessing the amount of heat transferred to the subsurface layers. For our purpose, we make use of a 3D shape model for each nucleus of interest. The spatial resolution of this shape model is such that we can compute the energy balance for each of its facets, accounting not only for the global shape of the nucleus, but also the local topography of the surface: i.e. a flat area compared to a cliff, each with distinct insolation properties. Comet 67P/C-G will serve as our primary example to showcase and demonstrate our surface energy model: 67P

is indeed well known, with the best determinations of many physical characteristics, made possible by the extensive data collected by the *Rosetta* mission. However, in Chapter 5, we will also present and analyze simulation outputs for other comet nuclei.

2.3.1 Shape model

Shape model reconstruction techniques primarily use 3D modeling algorithms such as Stereography, Photogrammetry, Stereophotogrammetry, and Photoclinometry. These models are predominantly derived from 2D images acquired by space missions targeting comet nuclei. For a more comprehensive understanding of these reconstruction algorithms and their applications in the shape modeling of comets and other small bodies, we refer to (Stooke, 1992; Jorda et al., 2010; Capanna et al., 2012; Preusker et al., 2017) and the references therein. Overall, having a detailed information about the surface morphological characteristics of a comet nuclei can be useful for a variety of purposes, including determining its volume, rotational state, morphometrical characterization, and an improved surface energy balance which can in turn improve the assessment of subsurface processes and coma studies.

All comets studied in our work have 3D shape models for their nuclei, made of triangular meshes generated using reconstruction from 2D images. When available, we specify the reconstruction technique used in the results chapters. However, in this section, we provide a detailed description of the shape model of 67P, which is the primary focus of our study and has the most finely resolved shape model among the comets we examined. Owing to the high quality images obtained by *Rosetta*, comet 67P's nucleus was reconstructed using several techniques such as Stereophotoclinometry (SPC, Gaskell et al., 2008; Jorda et al., 2012) and Stereophotogrammetry (SPG, Oberst et al., 2004; Preusker et al., 2012). These techniques provided detailed information on the global shape of 67P and its surface features, including the smallest boulders. The model we use was reconstructed using the SPG technique on high-resolution images taken by the *Rosetta*/OSIRIS instrument (Preusker et al., 2015). The latest SPG model (SHAP7) reaches a very high spatial resolution, with 44 million facets of an average spacing of 1.0-1.5 m, reconstructed from 1500 OSIRIS' NAC images of a resolution reaching the range of 0.2-3 m/pixel (Preusker et al., 2017) [1]. From this model, several lower-resolution models were derived[2].

In our study, we use various versions of this shape model, primarily 124,938 facets, 1,000, and 500 facets, depending on the specific feature studied. As a rough estimate, the typical average distance between two nodes of a facet of the ∼125k facet shape model is around 20 m. As a result, we do not consider local topography and roughness on a smaller scale. We show in Figure 2.1 different resolutions of the SPG shape model SHAP7 used in our different studies. Since our thermal evolution modeling can be computationally demanding, we adapt the resolution of the shape model with the aim of obtaining the optimal equilibrium between calculation time and outcome accuracy for each study case. For instance, for the analysis of the evolution of pits in Chapters 3 and 4, the shape

[1] http://europlanet.dlr.de/Rosetta/

[2] http://comsim.esac.esa.int/rossim/SHAPE_MODEL_DRAFTS/SHAP7_8/SPG/shap7_model_info.asc

model of ∼125k facets was the most appropriate, as it provided a detailed representation of each pit studied, and several facets for each geometric portion of a pit could be selected. Similarly, for the global study in Chapter 5, the 500 facets model was sufficient to capture the effect of the global, bilobate shape of the nucleus. The energy balance is calculated at each triangular facet of the shape model, as described in the next section.

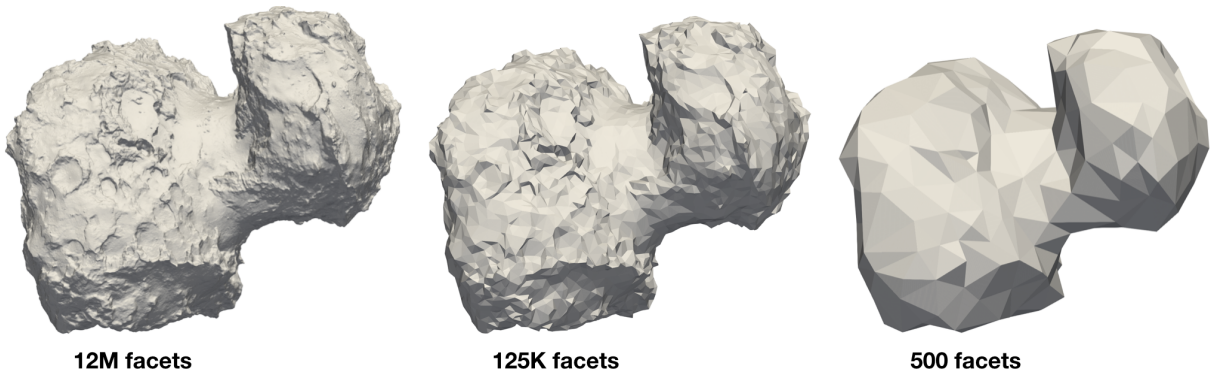

Figure 2.1: The shape model of 67P at different resolutions, obtained from the 44M SPG model (Preusker et al., 2017). High-resolution models are suitable for investigating local surface features such as valleys, cliffs, and pits, while lower resolution models are typically sufficient for global analyses.

2.3.2 Energy balance equation

The temperature at the surface is retrieved from a balance between the solar energy received on the surface point and the energy used for sublimation of surface ice. The boundary condition describing the energy equilibrium at the surface is given for each facet by:

$$(1 - \mathcal{A}_R)\ \mathcal{E} = \varepsilon\sigma T^4 + \kappa\frac{\partial T}{\partial r} + \sum_{\alpha} f_\alpha \Delta H_\alpha Q_\alpha, \tag{8}$$

where $\mathcal{A}_R$ is the Bond albedo of each facet for which we compute the energy balance; ε is the emissivity, σ = 5,67051 x 10^{-8} [W m^{-2} K^{-4}] is the Stefan–Boltzmann constant; and T [K] is the surface equilibrium temperature. We allow for the presence of volatile species at the surface, so that sublimation is possible: f_α represents the fraction of the facet's surface covered by these ices, and Q_α [kg m^{-2} s^{-1}] is the corresponding sublimation rate. Finally, $\mathcal{E} = E_\odot + E_{IR} + E_{VIS}$ [W m^{-2}] is the total energy flux received by the facet of interest. It is adapted to the specific facet and takes into account the contributions from direct insolation $E_\odot$, accounting for **Shadowing** due to the complex global morphology of 67P's nucleus or the local morphology, and from **Self-heating** E_{IR}+E_{VIS}: the energy flux received by reflection and emission from neighboring facets in the visible and infrared, respectively. See Figure. 2.2 for an illustration of the shadowing and self-heating on a given region of comet 67P's surface.

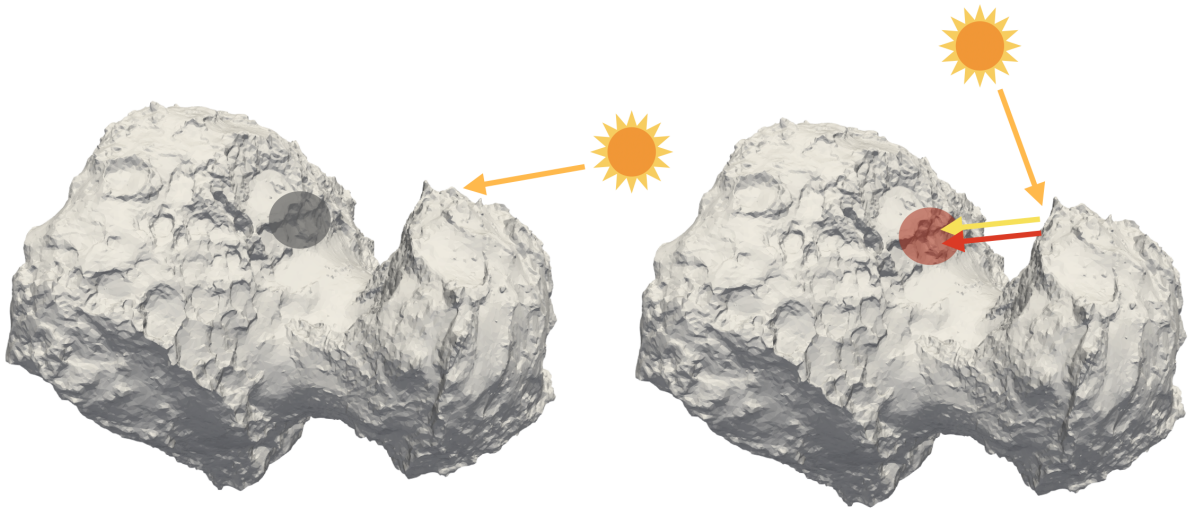

Figure 2.2: Schematic representation of direct insolation, shadowing, and self-hating on comet 67P's surface.

Direct insolation energy:

It is given by:

$$E_{\odot} = \frac{F_{\odot}}{r_H^2} \cos\xi, \tag{9}$$

where $F_{\odot} = 1368$ [W m^{-2}] is the solar flux at 1 AU. The heliocentric distance r_H [AU] and the local zenith angle ξ depend on the nucleus orbital evolution and its rotational state. For each time step across the orbit, the coordinates of the subsolar point on the nucleus are retrieved using SPICE database kernels available on the WebGeocalc platform (WGC)[3,4]. These kernels contain information on both the rotation state of 67P's nucleus and its orbital parameters. Using the coordinates of the subsolar point, the local zenith angle is computed for each facet at each time step of the orbit. Additional criteria are applied to account for facets located on the night side of the nucleus: if $\cos\xi$ <0, then $E_{\odot}$= 0. Direct insolation can be intercepted at some location on the surface due to the complex shape of the nucleus, as well as the small scale roughness. Therefore, shadow criteria are also applied.

Shadowing effect:

Assessing whether a facet is shadowed by other facets of the shape model is very delicate technically, and can be computationally expensive, depending on the spatial resolution of the shape model. The most straightforward way to perform such a calculation would be testing the shadowing for each node of the facet with all the facets of the shape model. As in practice the number of facets is of the order of the number of nodes, this operation scales as $\mathcal{O}(N^2)$. The procedure adopted to overcome this issue and minimize

[3]https://wgc.jpl.nasa.gov:8443/webgeocalc/#NewCalculation
[4]http://spice.esac.esa.int/webgeocalc/#NewCalculation

the computing time is to project the nodes of the shape model orthogonally on a 2D plane normal to the zenith direction of the subsolar point. This plane is divided into L cells along both directions (see top panel of Figure. 2.3). Each node of the mesh is then associated with a square, and each facet is associated with one or more squares depending on which nodes it contains, and each facet is associated with all the cells it overlaps (see bottom of Figure. 2.3, the facet, is associated with the red cells). Only nodes and facets belonging to the same square are tested together. We calculate the projected position of each node along the direction to the sun on the plane defined by the facet. If this projected position is within the facet and the node is below the plane, the node is shadowed, the Sun being above the plane. A facet is shadowed if its 3 nodes are shadowed. The parameter L needs to be optimized (Figure. 2.3). A small value of L means that many tests are performed per square as many nodes and facets belong to the same square. On the other hand, if L is too large (too many cells), facets overlap on too many cells, and some cells are free of nodes, resulting in the storage of unnecessary information, which is computationally expensive. A balance must be found between the allocation time and computing time.

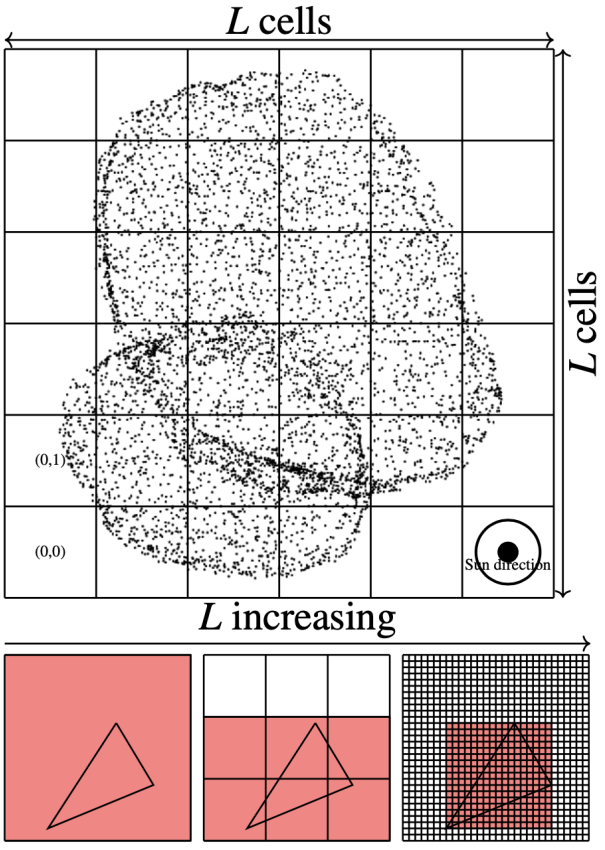

Figure 2.3:
Schematic of of how shadowing is determined over the nucleus with an optimizing technique aiming to reduce verification time.
Top panel shows the projection of nodes onto a chessboard of L x L cells. Bottom panel illustrates how the parameter L affects the assignation of a facet to the different cells of the chessboard. The red squares indicate the cells to which the corresponding facet is assigned. Allocation time (i.e. associating nodes and facets to a square) dominates for large L while testing (i.e. a node is shadowed or not by a facet) does for small L.
(Courtesy of A. Beth)

Self-heating contribution to energy:

Self-heating is the process by which energy is received through either reflection or emission of energy from neighboring surface elements. This process can be particularly significant for nuclei with complex morphology, such as 67P, where it has been observed both on a global and local scale (e.g., El-Maarry et al., 2015). Self-heating can be a significant additional source of energy, and it can affect the strength and duration of outgassing by contributing to an increase in surface temperature. It is composed of two contributions: a visible component, which is radiation reflected by mutually facing facets (E_{VIS}), and a thermal infrared emission (E_{IR}). The infrared contribution from radiation reflected by facing facets is typically negligible compared to the other two self-heating contributions, and is not taken into account in our model. The amount of self-heating received by a surface element from its surrounding environment depends on the self-viewing geometry between the different facets. This geometry within a pair of emitting and receiving facets is determined by the orientation of both facets, the size of the emitting facet, and the distance between the two.

The visible contribution of self-heating received by the facet of interest, which we aim to evaluate in the energy balance, can be expressed as follows:

$$E_{VIS} = \sum_{T} \mathcal{A}_T \frac{F_\odot}{r_H^2} \cos\xi_T \frac{S_T}{\pi} \frac{\cos\zeta_T \cos\zeta_R}{\delta_T^2}, \tag{10}$$

where $\mathcal{A}_T$ is the Bond albedo of an emitting facet T; ξ_T is its local zenith angle; S_T is its surface; ζ_T is the angle between the normal of the transmitter and the receiver facets; ζ_R is the angle between the normal of the receiving and the emitting facets, and δ_T is the distance between the two facets (see Figure 2.4).

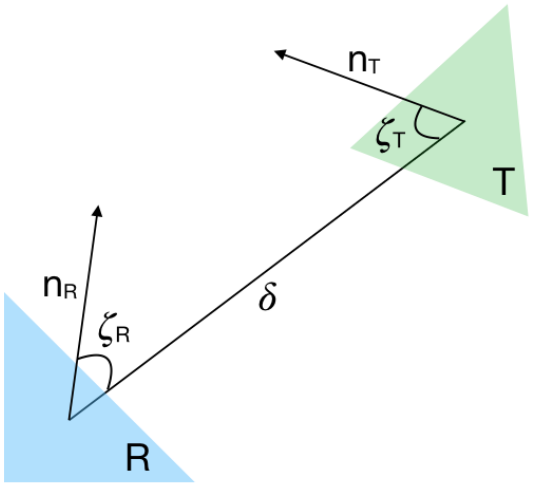

Figure 2.4: Illustration of the geometry involved in self-heating and the parameters used in equation 10.

The infrared contribution is expressed by:

$$E_{IR} = \sum_{T} \varepsilon\sigma T_T^4 \frac{S_T}{\pi} \frac{\cos\zeta_T \cos\zeta_R}{\delta_T^2}. \tag{11}$$

The temperature of each emitting facet T_T is calculated using the energy balance (Eq. 12) which only takes into account the direct insolation and does not consider the self-heating contributions. A minimum threshold of $T_T = 20$ K has been established for emitting facets when located on the night side. This value was thoroughly evaluated against a variety of alternative options, however it was determined that it did not significantly impact the overall results.

$$(1 - \mathcal{A}_T)\frac{F_\odot \cos \xi_T}{r_H^2} = \varepsilon \sigma T_T^4, \tag{12}$$

The self-heating reflections and emissions are also subject to shadowing caused to intercepting facets, and it is handled in the same manner as the shadowing of direct insolation. In this case, instead of considering the geometry between the Sun, facets, and nodes of the facet in question, we take into account the geometry of a potential emitting facet, the other facets, and nodes of the facet in question.

2.4 Numerical considerations

2.4.1 Radial grid

The nucleus is simulated with a 1D grid in the direction perpendicular to the facet. The resolution of this radial grid is chosen by considering the diurnal and orbital skin depths, of about few cm to several meters respectively (Huebner et al., 2006). The mass loss rate and expected lifespan of the active comet also play a role in determining the appropriate size of the grid (Prialnik et al., 2004). A higher mass loss rate and shorter lifespan may require a finer grid to capture more detailed information, while a lower mass loss rate and longer lifespan may allow for a coarser grid. Taking these information into consideration, the radial grid is divided into 500 layers of increasing thickness from the surface to the center. The first 150 layers are 1 cm thick, followed by 150 layers that are 10 cm thick, and the inner layers range from meters to tens of meters in thickness. The equations for the calculation of ice sublimation and recondensation at each time step are solved for each individual layer of the grid. A specified threshold is set for the amount of ice in a layer, and if it falls below that threshold, the layer is merged with the layer below it, and a new layer is created with a different temperature, thickness, and composition. Moreover, the model evaluates the presence of dust particles at the surface layer, and the removal of these particles leads to a decrease in layer thickness and surface erosion.

2.4.2 Timestep and orbital considerations

Energy flux calculations at the surface are performed with a timestep of 8 minutes over a full recent orbital revolution of the comet (i.e., ∼6.44 years for 67P). Correspondingly, the thermal evolution model is run with a timestep of 8 minutes. For the study of Pits in Chapters 3 and 4, the simulations are run for the number of orbits that the comet has undergone under the current illumination conditions. For 67P, this corresponds to approximately 10 orbits since its last significant orbital change, and until it was visited by the *Rosetta* spacecraft (Maquet, 2015). For the study of global effects, calculations

are run in correspondence to the observations of water or dust production rates. To simulate the thermal evolution of the comet nuclei under current illumination conditions, we first need to take into account its journey from the Kuiper Belt to the inner Solar System through the use of a standard multistage injection process (Capria et al., 2001; De Sanctis et al., 2005). Through these early orbits, we intend to create a more realistic subsurface composition by simulating the thermal processing sustained prior to its current orbit. This standard procedure does not capture the complexity of the actual coupled thermal and dynamical evolution of comets (e.g., Gkotsinas et al., 2022), but it allows to account for the gradual retreat of ice due to sublimation, and the boundary between amorphous and crystalline water ice, beneath the surface before being placed in its current orbital configuration. This process involves several "insertion orbits", each with specific semimajor axis and eccentricity values, listed in Table 2.1. These orbits are generic for 67P's dynamical history (Carusi et al., 1985; De Sanctis et al., 2005).

Table 2.1: Parameters of the multistage injection orbits.

Orbit	a [AU]	e	q [AU]
Multistage 1	50	0.5	25
Multistage 2	25	0.4	25
Multistage 3	8	0.5	4

a: semimajor axis; e: eccentricity; q: perihelion distance.

2.5 Initial parameters used in the model

To solve time-dependent equations for a comet nucleus, initial conditions such as temperature, composition (mass fractions of ices and dust), structure (porosity, pore size, and water ice properties) must be assumed. We use standard values for several parameters in our thermal evolution model. These values are representative of the typical range of values for Jupiter Family Comets (JFCs) that were retrieved from observational data as well as theoretical models. They serve as a foundation for all comets in our model.

We refer to Huebner et al. (2006) for more details about the generic parameters. Nevertheless, some parameters have been well constrained thanks to the *Rosetta* measurements that have helped to shed light on the composition and internal structure of cometary nuclei and contribute significantly to the knowledge we had on comets. The values of the main parameters used in our simulations are given in Table 2.2.

Table 2.2: Initial parameters for the thermal evolution model.

Parameter		Symbol	Value	Unit
Bond albedo		$\mathcal{A}$, $\mathcal{A}_R$, $\mathcal{A}_T$	0.06	-
Emissivity		ε	0.95	-
Initial temperature		T_i	30	K
Hertz factor		f_H	0.005	-
Pore radius		r_{pore}	10^{-4}	m
Porosity		ψ	75	%
Mass per unit volume	Dust	ρ_d	1000	kg m^{-3}
	H_2O ice	ρ_{am}, ρ_{cr}	917	kg m^{-3}
	CO ice	ρ_{H_2O}	1250	kg m^{-3}
	CO_2 ice	ρ_{H_2O}	1977	kg m^{-3}
Mass fraction	Dust/H_2O	X_d/X_{H_2O}	1	-
	CO/H_2O	X_{CO}/X_{H_2O}	0	-
	CO_2/H_2O	X_{CO_2}/X_{H_2O}	0	-
Thermal conductivity	Dust	κ_d	3	W m^{-1}K^{-1}
	H_2O cr	κ_{cr}	567/T	W m^{-1}K^{-1}
	H_2O am	κ_{am}	2.34×10^{-3} T $+ 2.8 \times 10^{-2}$	W m^{-1}K^{-1}
Heat capacity	Dust	c_d	1300	J kg^{-1}K^{-1}
	H_2O ice	c_{H_2O}	1610	J kg^{-1}K^{-1}
	CO ice	c_{CO}	2010	J kg^{-1}K^{-1}
	CO_2 ice	c_{CO_2}	1610	J kg^{-1}K^{-1}
Latent heat of sublimation	H_2O	ΔH_{H_2O}	2.83×10^6	J kg^{-1}
	CO	ΔH_{CO}	0.29×10^6	J kg^{-1}
	CO_2	ΔH_{CO_2}	0.58×10^6	J kg^{-1}

It is important to carefully consider the different thermophysical parameters included in the model. Some have a mutual dependency and require thoughtful examination. The conductivity is highly influenced by composition and porosity:

$$\kappa = f_\psi \; f_H \; \frac{\sum_i M_i \kappa_i}{\sum_i M_i}, \tag{13}$$

where f_ψ and f_H are respectively the correction factors to account for the porosity and the reduced contact between solid grains, also known as the Hertz factor which represents more concretely the area of contact between material grains relative to the cross-sectional area (Prialnik et al., 2004); M_i is the mass per unit volume of each constituent i; and κ_i is their respective thermal conductivity (see Table 2.2). This formula is the most convenient in order to be able to describe the conductivity of the crust.

Similarly, the heat capacity of a cometary nucleus is expressed as:

$$c = \frac{\sum_i M_i c_i}{\sum_i M_i}, \tag{14}$$

c_i being the heat capacity of each component (see Table 2.2 for respective values).
The bulk density of a cometary nucleus is also highly dependent on the porosity:

$$\rho_{bulk} = (1 - \psi) \left(\sum_i \frac{X_i}{\rho_i} \right)^{-1}, \tag{15}$$

where ψ is the porosity, X_i is the mass fraction of each individual component in the cometary material mixture, and ρ_i [kg m^{-3}] is the corresponding solid density of each constituent.
One of the difficulties in investigating thermal processes that take place in the top layers of a comet's nucleus is that these layers may have different properties compared to the rest of the nucleus. Porosity, which can impact the overall density, is a crucial aspect to take into account in this regard. The density of 67P's nucleus, as derived from the *Rosetta* measurements, is 533±6 kg m^{-3} (Pätzold et al., 2016). However, this value can be represented by multiple sets of values for composition and porosity. To better understand the thermal processes in the first layers of the nucleus, we have used values that produce a bulk density similar to the observed bulk density of the comet.

2.6 Model algorithm summary

In our work, we have developed a surface energy model that uses subsolar coordinates obtained from the comet's kernels, which describe the general state of the comet in its orbit, to calculate the energy received at each facet of the shape model at each time step of the orbit. The energy model takes into account the Sun-Comet, shadowing, and self-illumination geometries in its calculations. The total energy, including the self-heating contribution, is then linked to the thermal calculations as the surface conditions of each facet. We summarize in Figure 2.5 the algorithm of our model.

This method is applied to investigate in great detail a specific pit of 67P's surface in Chapter 3, by evaluating the extent to which the local shape could impact thermal activity and if such activity in the recent phase of a JFC could contribute to forming such features. We also conduct a detailed study of the effect of key initial parameters: porosity, dust-to-ice mass ratio, the presence of super volatiles CO and CO_2, and the presence of a dust mantle, on the thermal activity occurring in this feature. In Chapter 4, we extend our study to other pits present on the surface of 67P in order to explore different illumination conditions and the role of location and shape in their thermal and erosional behavior. In Chapter 5, we apply our method to pits observed on other JFCs that were visited by spacecraft: 81P/Wild 2, 9P/Tempel 1, and 103P/Hartley 2. This allows to explore the thermal behavior for different orbital characteristics and very different nucleus shapes. Finally, in Chapter 6, we apply this method to study the effects of the global shape of a nucleus on its activity, focusing on comets 67P, 103P, and 9P.

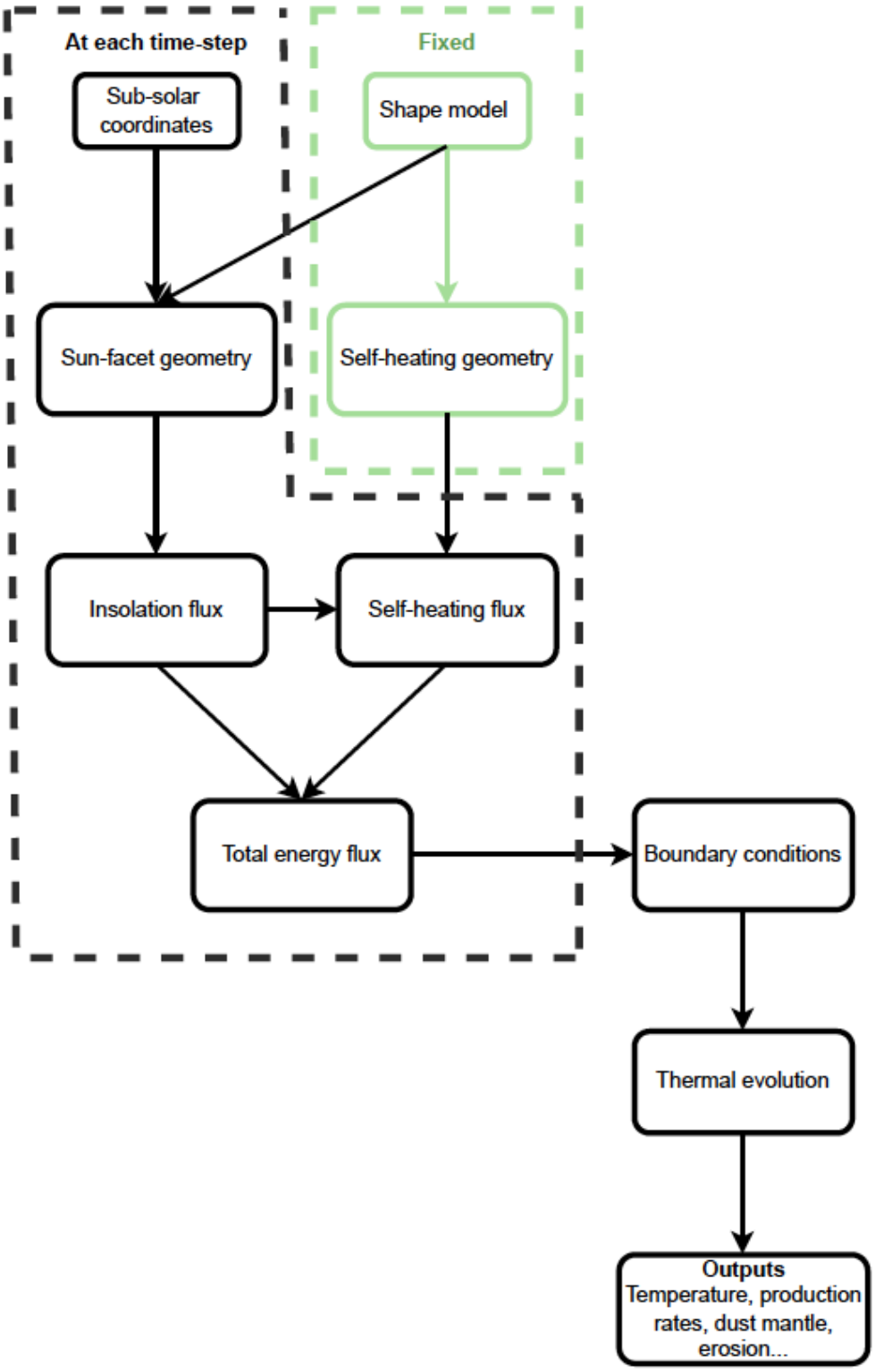

Figure 2.5: Diagram illustrating the integrated approach used in this study to model the energy balance and thermal evolution of cometary surfaces, incorporating the shadowing and self-heating related to the shape model.

Chapter 3

In depth: Thermal evolution of one pit at the surface of 67P

A significant geological diversity is observed on the surface of 67P/C-G. We refer to Chapter 1 for a summarized overview. The observation of depressions on 67P/C-G, linked with cometary activity, offers the opportunity to glimpse at the characteristics of the subsurface, and thermophysical processes actively modifying them, and consequently the mechanisms that shape a nucleus through cometary activity (Sierks et al., 2015; Besse et al., 2015; Vincent et al., 2015a).

Two main types of depressions can be distinguished on the surface of 67P based on their dimensions, i.e. their diameter but mainly their depth: shallow depressions and deep depressions (see Figure 3.1, where both types are represented in the Imhotep region).

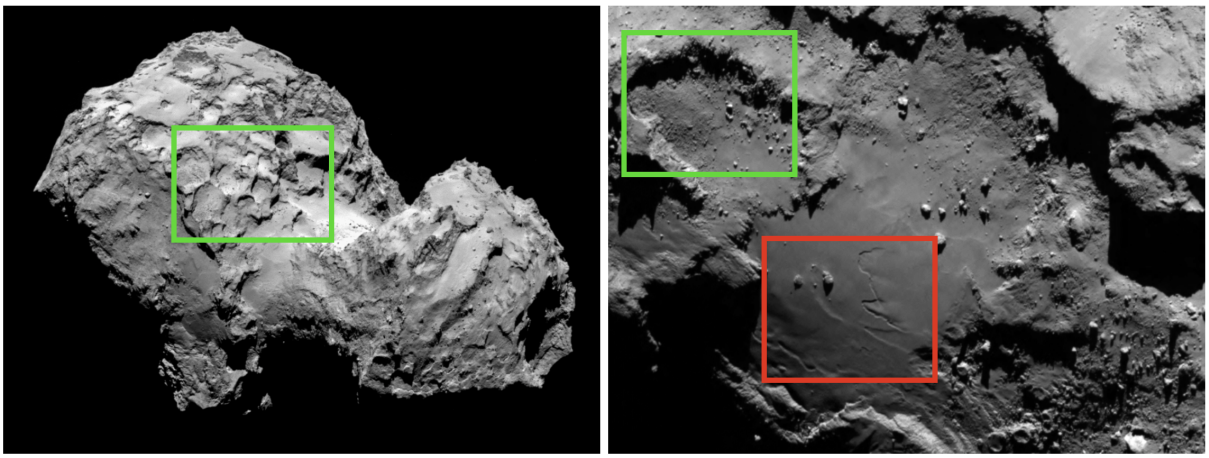

Figure 3.1: Rosetta images revealing the surface of comet 67P, highlighting two distinct types of depressions. The red quadrant highlights shallow depressions with depths of only a few meters, while the green quadrant show deep depressions, generally representing the so called pits and alcoves, characterized by steep walls ranging from 10 to 100 meters in depth. Credits: ESA/Rosetta/MPS for OSIRIS Team MPS/UPD/LAM/IAA/SSO/INTA/UPM/DASP/IDA.

In this study, we are interested in deep depressions characterized by steep walls with a depth of 10-100s of meters (Massironi et al., 2014; El-Maarry et al., 2015; Thomas et al., 2015b; El-Maarry et al., 2019). These large scale structures include pits, as well as cliffs or alcoves. Besse et al. (2015) used OSIRIS images to identify and describe the pits, drawing attention to the accumulation of boulders at the base of some depressions. This suggests that the pits are dynamic, undergoing changes over time, possibly indicating varied formation mechanisms or different timelines of formation and evolution.

The origin and evolution of these depressions is intriguing and still not fully understood since their first observations. Because they are unlikely to be primordial (Schwartz et al., 2018), several formation scenarios were proposed to explain their formation. Owing to *Rosetta*'s extensive dataset on the shape and activity of 67P, a number of detailed studies have aimed at understanding the origin and evolution of pits on its surface.
Holsapple and Housen (2007) and Vincent et al. (2015a) argue that impacts on cometary surfaces are expected to produce features with a morphology distinct from these observed pits, so that they should be a signature of some process related to cometary activity rather than the result of collisions. However, it is important to distinguish the few small circular features that can be interpreted as impact craters (see Figure 5 from El-Maarry et al., 2015), likely resulting from low-velocity impacts such as the fall of boulders.
Many other studies suggest that pits on 67P are considered to be indicative of endogenic activity. Vincent et al. (2015a), Kossacki and Czechowski (2018) and Leliwa-Kopystynski (2018) propose a formation by sinkhole collapse[1]: the collapse of the surface on a subsurface cavity, which can either be primordial or formed as a result of subsurface depletion of volatiles by ice sublimation. Vincent et al. (2015a) proposes that sinkhole collapse would be accompanied by outbursts. Moreover, they suggest that pits expand slowly over time due to erosion of their walls as a result of sublimation, providing a measure of the surface's erosion state. Further, they propose that the size and spatial distribution of these pits point towards substantial heterogeneity in the physical, structural, or compositional properties within the first few hundred meters beneath the nucleus surface. Similarly, Massironi et al. (2014) suggest that the sublimation process leads to slope retreats, material ablation at the pit's location and the degradation of depressions.
Mousis et al. (2015) investigated the potential of pits formation through phase transitions such as sublimation or amorphous water ice crystallization, showing that the formation time for such features is extensive, around a thousand years. Guilbert-Lepoutre et al. (2016) further demonstrated the improbability of pit formation under current illumination conditions, as no known mechanism can produce such large pits quickly.
Thomas et al. (2015a) postulate that neither ice sublimation nor sinkhole collapse are possible scenarios for the formation of such depressions. They suggest that the quasi-circular aspect of the observed pits necessitates an order that is not inherently expected in either mechanism.

In this chapter, we investigate in detail the thermal evolution of a specific pit on 67P. Without any a priori knowledge of their origin, our goal is to understand how these surface

[1]https://blogs.esa.int/rosetta/2015/07/01/comet-sinkholes-generate-jets/

features evolve due to the unavoidable cometary activity of the nuclei,. One objective is that primordial characteristics of pits might be retrieved, in order to help identify the mechanism that formed them.

Additionally, we seek to explore the influence of physical parameters and local complex shape on pits evolution. Indeed, a variety of physical parameters can influence the outcome of thermal evolution models of comets (e.g., conductivity, albedo, porosity...). Nevertheless, the uncertainty surrounding these parameters presents a significant challenge, as direct measurements are lacking. While certain parameters have minimal effects on simulation outcomes, others are of utmost importance and need meticulous examination. Therefore, examining the role of these parameters in the thermal activity is critical for improving our comprehension of the physical processes regulating cometary behavior. The physical parameters we investigate include porosity, dust-to-ice ratio, CO and CO_2 relative abundance to H_2O, and the presence of an initial dust mantle at the surface of the nucleus. To isolate the effects of each parameter, they are evaluated independently of one another. The significance of these parameters in affecting the thermal behavior of the nucleus in some cases has been demonstrated in previous studies (e.g., Espinasse et al., 1993; Prialnik et al., 2004; Kossacki and Jasiak, 2019; Hoang et al., 2020). Our study aims to extend this knowledge by examining their effects on a longer timescale that could have an important impact on the subsurface structure and the morphology of the surface. We thus conduct several simulations during all the recent phase of the comet in the inner Solar System (yet, under the illumination conditions provided by the current orbit), using different values of the aforementioned parameters. The surface complex shape may also represent a key element in the energy balance and therefore the thermal evolution over the different sides of a surface feature (Keller et al., 2015a; Marshall et al., 2018; Tosi et al., 2019; Zhao et al., 2020). However, no study has been made on the evolution of such a deep feature as pits on such a long timescale considering the shape effects. Therefore, we investigate the relative influence of local complex shape on the evolution of the studied pit, by considering shadowing and self-heating effects on the energy balance and thermal activity through the inclusion of the comet's shape model containing local and global surface geometry, as described in Chapter 2.

3.1 Pit selected for this study

We select a pit in the Seth geological unit of 67P's northern hemisphere, with a latitude of approximately 35 ° N. The pit has a diameter of 210 m and a depth of 60 m and in shown in Figure 3.2. It is labeled as "Pit 5" in Table 4.1 within the context of the generalized pit analysis conducted in Chapter 4. It is situated on the large lobe of the nucleus, facing the sky and away from the shadowing and self-heating that may occur from the small lobe, allowing us to solely study the impact of shadowing and self-heating caused by the local topography of the pit. The shape model used in this study is the SPG model (detailed in Chapter 2), composed of a ∼125,000 triangular facets (Figure 3.2). With this model, the average distance between two nodes of a facet is ∼20 m, which provides a balance between sufficient spatial resolution to capture the shape effects of the pit, with several facets for each morphological area of interest of the pit, while also mitigating the

computation time. The simulations were performed on 15 facets of the shape model for this surface feature, distributed across various regions of the pit, including the bottom, walls, and surrounding plateau. These simulations cover the past ten orbits of comet 67P so to assess the evolution of this pit since 67P acquired its current orbit. This allows us to analyze the impact of parameter variations on the thermal evolution near the Sun over an extended period of time.

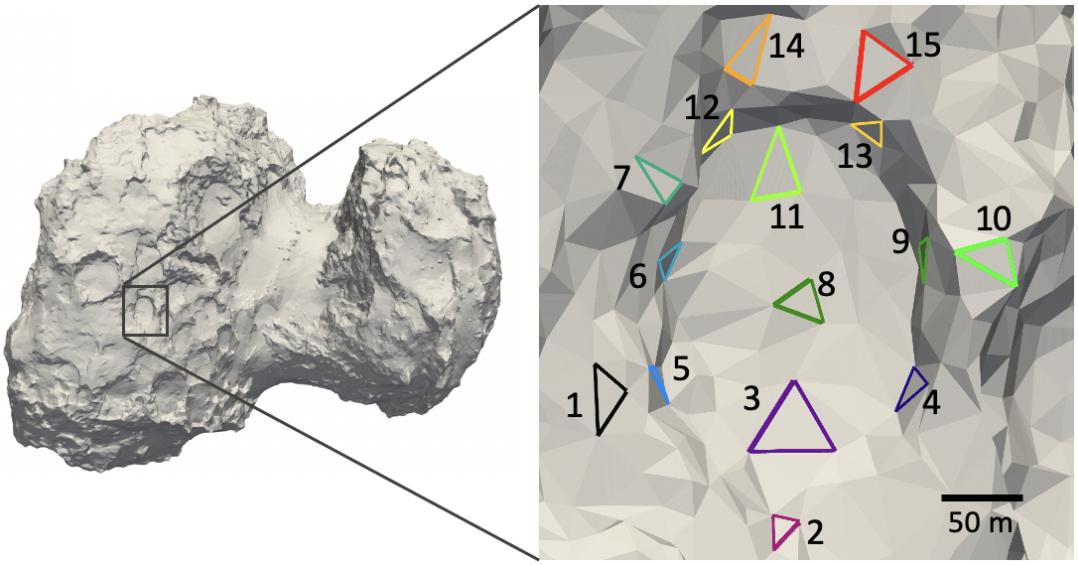

Figure 3.2: Pit selected for study, showing the sampled facets on the plateau, walls, and bottom. The shape model used is an SPG model composed of ∼125,000 facets (Preusker et al., 2017, see Section 2.3.1 of Chapter 2).

3.2 Energy balance at the surface of the pit

The energy received by the 15 facets is calculated at each 8 minute time-step, under current illumination conditions (see Section 2.3 of Chapter 2 for details about the method). To ease the visual analysis of seasonal effects sustained through the orbit, we smooth the plots shown below over a one-day period in the middle panel of Figure 3.3. The energy flux is significant around perihelion, and reaches its maximum around 3 months before perihelion for most of the facets. Due to the comet's high obliquity of $\sim 50°$, the northern hemisphere where the pit is located experiences almost 4 months of darkness during the perihelion passage, when the southern hemisphere is exposed to the Sun. The energy flux exhibits significant variations throughout the orbit, particularly when approaching the perihelion, mainly due to the complex global shape of the nucleus, additionally combined with its complex rotational state. The observed differences between the flux of the different facets can be attributed to the complex local-scale shape. Located at a latitude of approximately 35°, the pit experiences an optimal solar exposure at a heliocentric distance of ∼3 AU, as illustrated in the bottom panel of Figure 3.3, while the maximum energy flux is reached at distances closer to the Sun, right before perihelion.

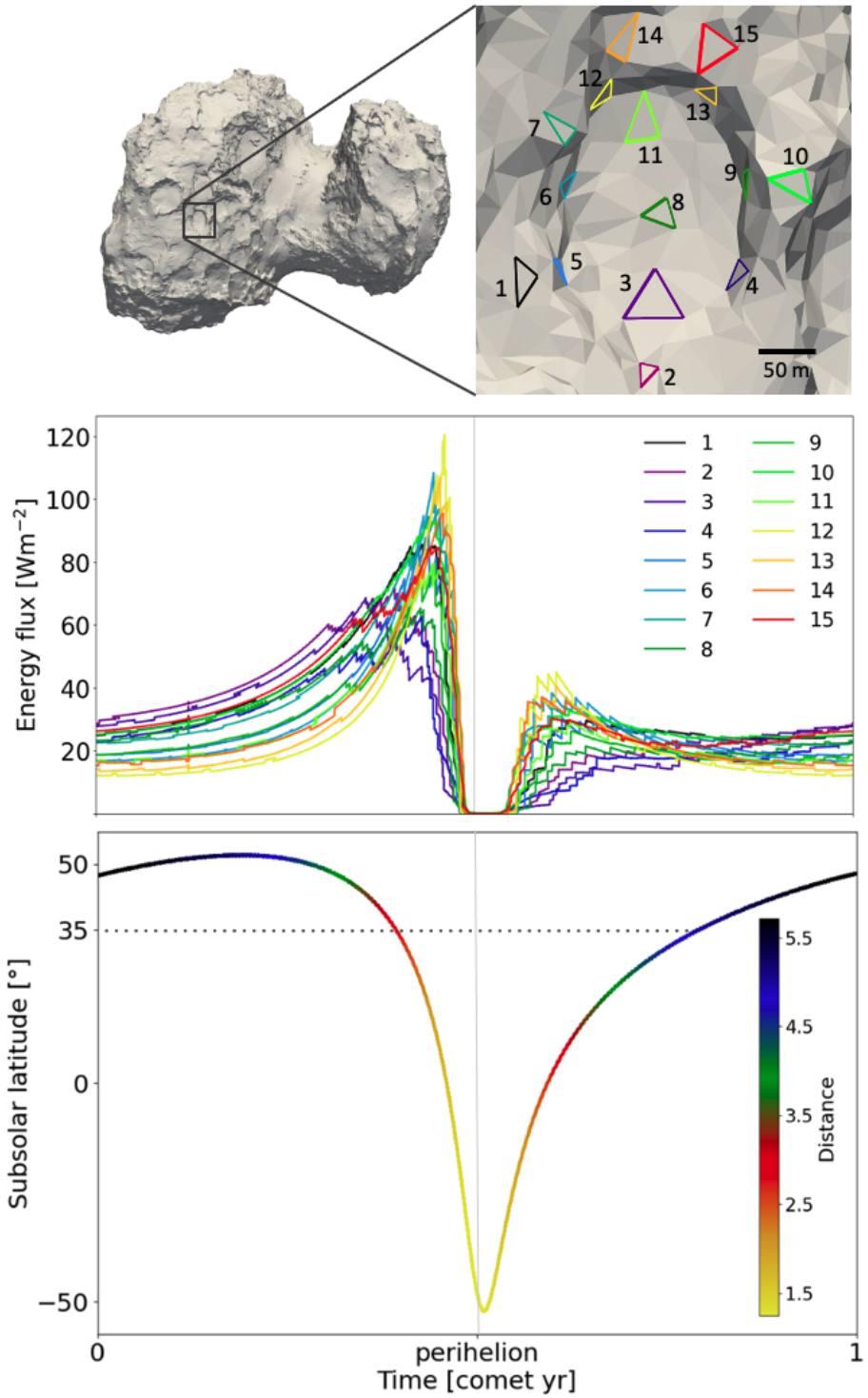

Figure 3.3: Top: Facets sampled for study. Middle: Energy received at the 15 facets during one complete orbit, smoothed over a daily period window. The gray line marks the perihelion. Bottom: Latitude of the subsolar point and the heliocentric distance of 67P during its recent orbit. The pit being located at a latitude of ∼+35, it experiences the highest exposure to the Sun's direction at a distance of ∼3 AU before perihelion and ∼ 5 AU after.

Figure 3.4 illustrates the energy received by the 15 facets at each time-step of the orbit. A closer examination of the diurnal period highlights the distinctive energy fluctuations for each facet. The diurnal energy received by each facet follows a specific pattern, largely dictated by its local orientation relative to the Sun and whether it is shadowed. Consequently, even within a single day, facets can be exposed differently to the Sun, leading to important variations even within a daily period.

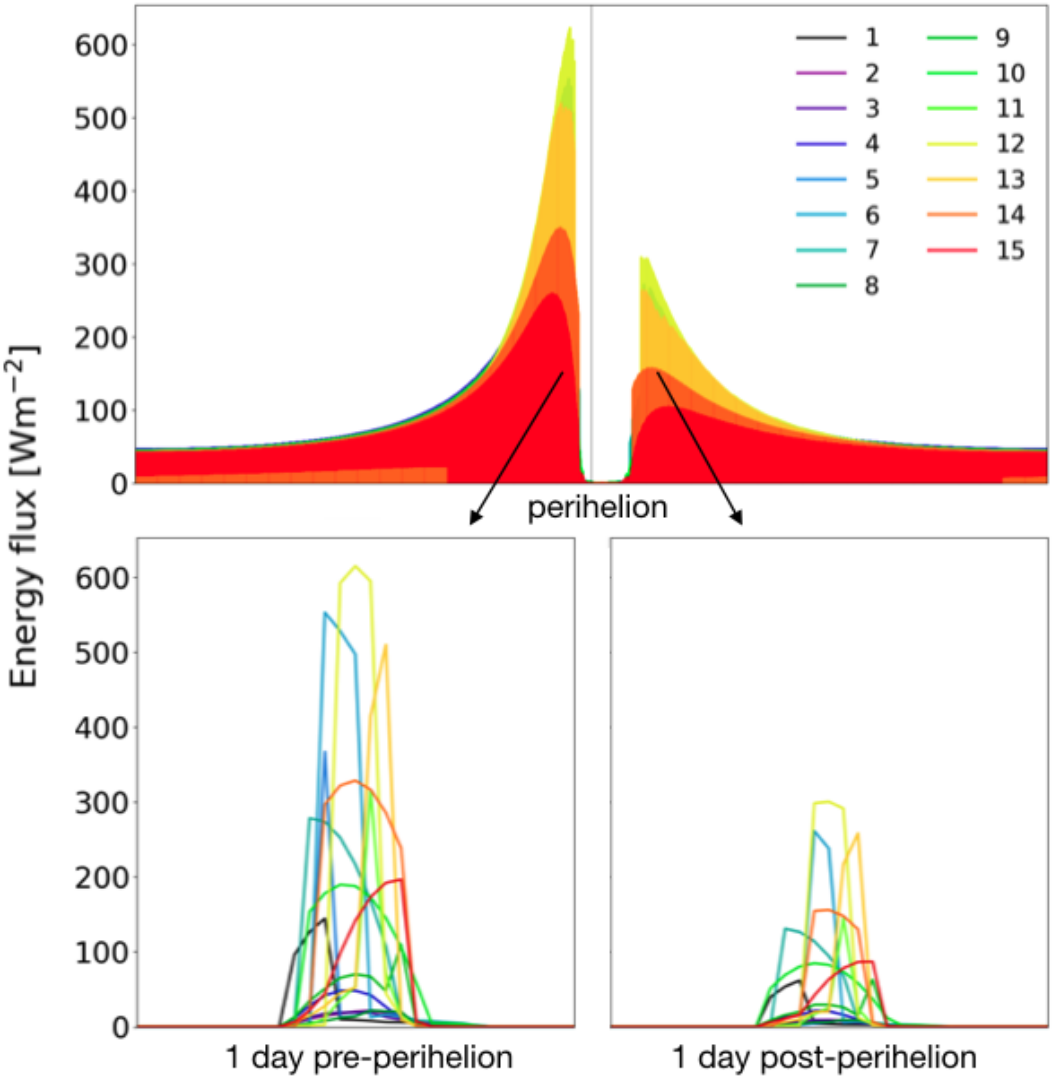

Figure 3.4: Top: energy flux received at the 15 facets of the pit over one full orbit, calculated using our surface model presented in Chapter 2. Bottom: a closer view of the energy diurnal variations, one day before and after perihelion.

Figure 3.5 presents the total energy integrated over the course of the orbit and the maximum energy received near perihelion for the different facets of the pit. The total energy exhibits a significant variation of over 50% between the minimum and maximum value, with the bottom facets receiving the least energy, followed by the wall facets, while the plateau facets receive the highest energy quantities. This difference in energy

distribution is attributed to the fact that the plateau facets are exposed to the Sun for a longer duration than the wall and bottom facets. Generally, facets facing upwards are less affected by the local topography, even some of those located on the bottom, as the depression is relatively shallow. On the other hand, facets that tend to be directed toward the equator receive the highest amounts of energy, with a peak that exceeds the lowest peak by more than three times. These facets are directly facing the Sun during the closest approach and while the pit is still exposed.

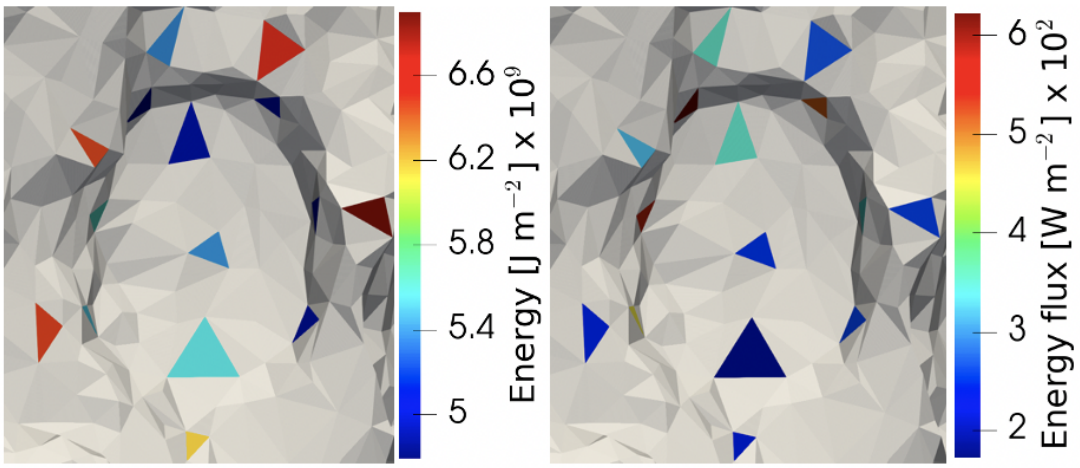

Figure 3.5: Energy received at the 15 studied facets. Left: total quantity of energy integrated over one complete orbit. Right: maximum of energy reached close to perihelion.

The non-uniform distribution of energy across the different facets of the pit emphasizes the significance of incorporating its complex shape into the surface energy balance calculations. The observed heterogeneity, either between the plateau and bottom or along the lateral direction, is mainly attributed to the effect of shadowing. The complex shape of the pit induces shadowing, which decreases the energy received by certain parts of the pit. This complex morphology gives rise to a significant amount of self-heating at certain sides of the pit. The contribution of self-heating to the energy balance at the different facets is shown in Figure 3.6, with the wall facets receiving the highest self-heating contribution, followed by the bottom facets. Conversely, the plateau facets receive the lowest amount of self-heating due to their upward orientation. Facets located on the right side of the pit in Fig. 3.6 receive the highest amounts of self-heating. This is likely attributed to their orientation towards the facets that receive a significant amount of direct insolation, leading to the reflection and emission of a substantial amount of energy. Furthermore, these facets are subject to a larger number of neighboring facets, some of which are located outside of the pit. For instance, while facet 6 is visible to only 152 neighboring facets, facet 9 faces 254 facets. The self-heating contribution can reach up to 50% of the total energy for these facets, indicating its importance in energy balance calculations, particularly to study phenomena occurring within the deepest surface morphological structures. Except for these few facets, direct insolation remains the dominant energy source. The evolution of plateau and bottom facets are primarily driven by direct insolation. The impact of shape on energy distribution is further explored in Chapter 4.

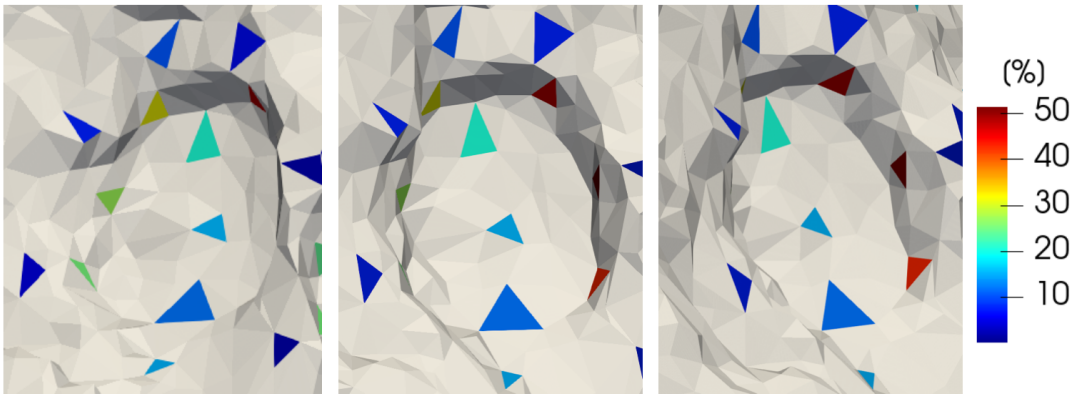

Figure 3.6: Contribution of self-heating to the total energy flux received at the 15 facets over a complete orbit.

The impact of local topography on the energy distribution within a pit is substantial, with the plateau facets receiving almost twice as much energy as the walls and bottom facets. An asymmetry is also observed in the energy distribution along the lateral direction, with facets facing the equator receiving a higher amount of energy near perihelion. For some wall facets, self-heating can also exceed the direct energy input. Hence, it is essential to consider the effects of shadowing and self-heating when studying thermal activity on a local scale such as within a pit.

The energy received at each of the 15 facets is then used as the surface boundary condition to the thermal evolution model as described in Section 2.2 of Chapter 2. The thermal evolution of each facet over ten orbits is simulated through a series of tests, the results of which are presented in sections 3.3 to 3.6. These simulations are conducted for various configurations of the initial parameters, thus testing the main parameter space. When we study the effect of one given physical or thermal parameter, the others are kept at the "baseline" values listed in Table 2.2 of Chapter 2. Table 3.1 displays the various configurations with the values tested for each parameter:

Table 3.1: Critical parameters whose influence has been studied in detail: porosity ψ, dust-to-ice mass ratio X_d/X_{H_2O}, mass fraction of CO (X_{CO}) and CO_2 (X_{CO_2}), and thickness of initial dust mantle δ_{dust}. The specific values tested are denoted in bold. Note: Porosity was limited to 60% for the CO and CO_2 tests to prevent numerical instability.

	ψ (%)	$\frac{X_d}{X_{H_2O}}$	$\frac{X_{CO}}{X_{H_2O}}, \frac{X_{CO_2}}{X_{H_2O}}$ (%)	δ_{dust} [cm]
Porosity test (Sec. 3.3)	**60, 70, 80**	1	[0, 0]	0
Dust/Ice test (Sec. 3.4)	75	**0.5, 1, 2**	[0, 0]	0
CO, CO_2 test (Sec. 3.5)	60	1	**[0, 0], [1, 1], [5, 15]**	0
Mantle test (Sec. 3.6)	75	1	[0, 0]	**0, 5, 10 30, 60, 100**

3.3 Influence of porosity

The *Rosetta* data allowed to estimate porosity values for the nucleus of 67P ranging from 65% to 85%, through the combination of observations and modeling (Kofman et al., 2015; Taylor et al., 2017; Herique et al., 2019; Pätzold et al., 2019). However, some areas of the surface appear to be made of consolidated material (El-Maarry et al., 2019), likely resulting in lower local porosity, even though direct, local measurements have not been conducted. For instance, the Philae lander's MUPUS instrument was unable to break through the material of 67P's nucleus, as a hard layer was encountered just a few centimeters below the surface, with a local porosity reaching low values even less than 60% as determined from the observed characteristics of the refractory material's composition (Spohn et al., 2015). Given the potential significant variability, we investigate the influence of porosity on the outcome of thermal activity and surface erosion at the level of the pit by performing tests using three values of porosity ψ: 60%, 70% and 80%, for the full ten orbital revolutions of 67P (see Table 3.1).

Our simulations provide different types of outputs: the surface temperature of the facet, the gas and dust fluxes, the surface erosion for each time step of the 10 orbits, or the thickness of the dust mantle for instance. While the primary focus of this study is on erosion, we initially present all outputs to construct a overall view of the facets' behavior. This is illustrated by Figure 3.7, where simulation results are shown for the intermediate porosity value: 70%.

The temperature profile of the facets is driven by the local energy received. Prior to perihelion where the energy is at its peak, local temperatures can reach a maximum of approximately 200 K (198 K). The temperature range obtained from our results is consistent with the measurements derived from VIRTIS (Tosi et al., 2019). During the perihelion passage, the surface temperature drops significantly to $\sim$ 55 K as the pit is in the dark side during this period. The H_2O flux trend follows the surface temperature globally throughout the orbit. Even though the H_2O production rate reaches its maximum just before perihelion, owing to the increased solar irradiation leading to enhanced sublimation, the dust flux does not follow a similar pattern. Instead, the peak occurs around 4.5 AU pre-perihelion, with the subsolar point located at latitudes around 50°. At this distance, water outgassing is relatively low, but the sudden important dust ejection is not necessarily linked to the intensity of this volatile outgassing. Indeed, the build up of pressure, even with the presence of low sublimation, leads eventually to sudden dust ejection. This is expected to happen before the maximum water ice sublimation as it is a necessary step for water ice to be able to sublimate, otherwise water-driven activity would be quenched.

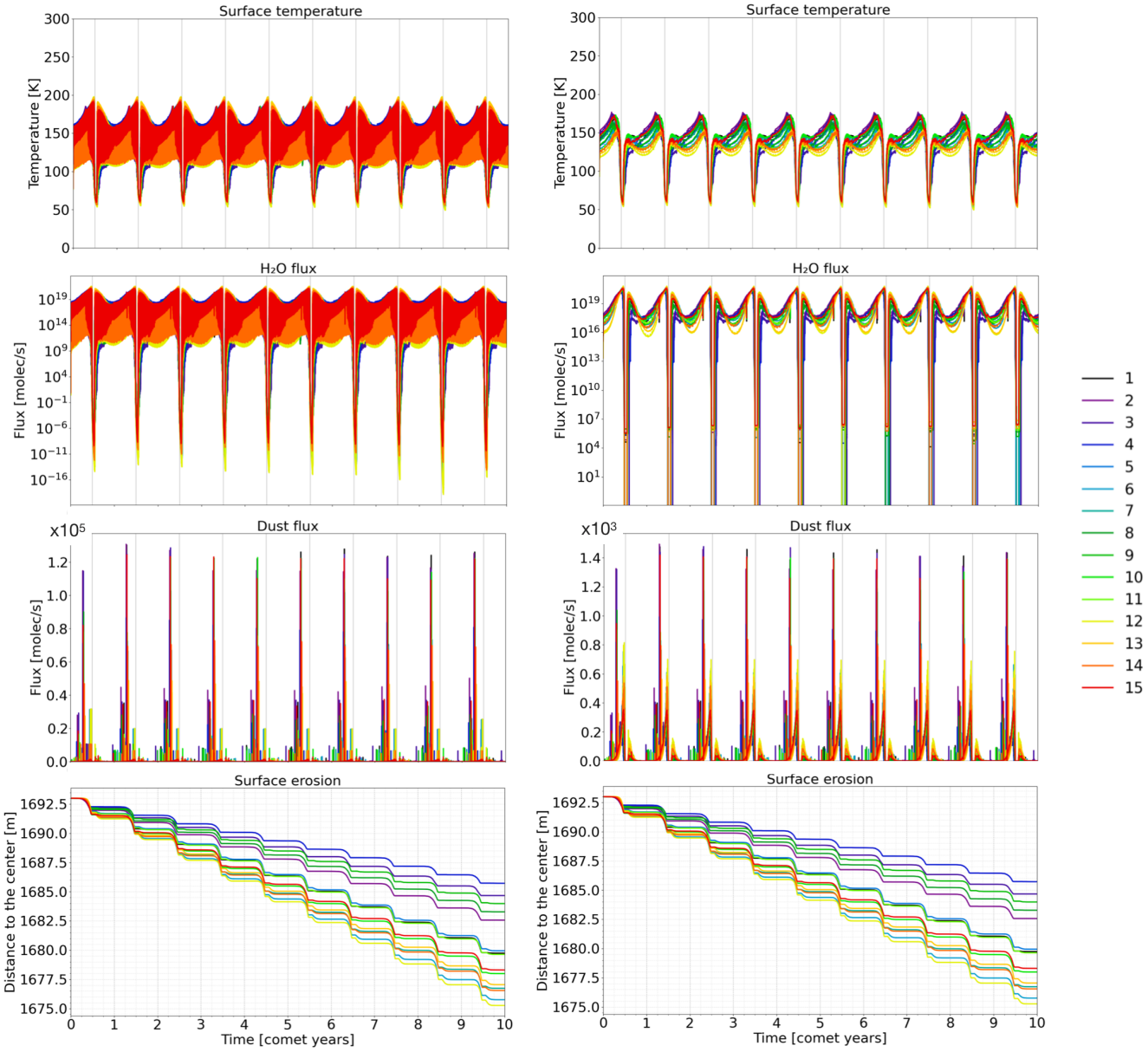

Figure 3.7: Left: variations of surface temperature, H_2O flux, dust flux, and erosion of the 15 studied facets for each time step of the ten full orbits, considering a porosity of 70%. Right: same quantities smoothed over one day to show only seasonal variations for clarity.

We also notice that the observed increase in dust production starting from the second orbit onward is plausibly due to the ejection of the dust mantle of ≤ 11 mm thickness, which formed at slightly earlier on the orbit (see Figure 3.8). This suggests that several factors, such as sublimation, topography, and heliocentric distance variations, contribute to the regulation of dust activity of the nucleus. In addition, it should be noted that a secondary significant dust activity phase is observed during the period of high outgassing near perihelion.

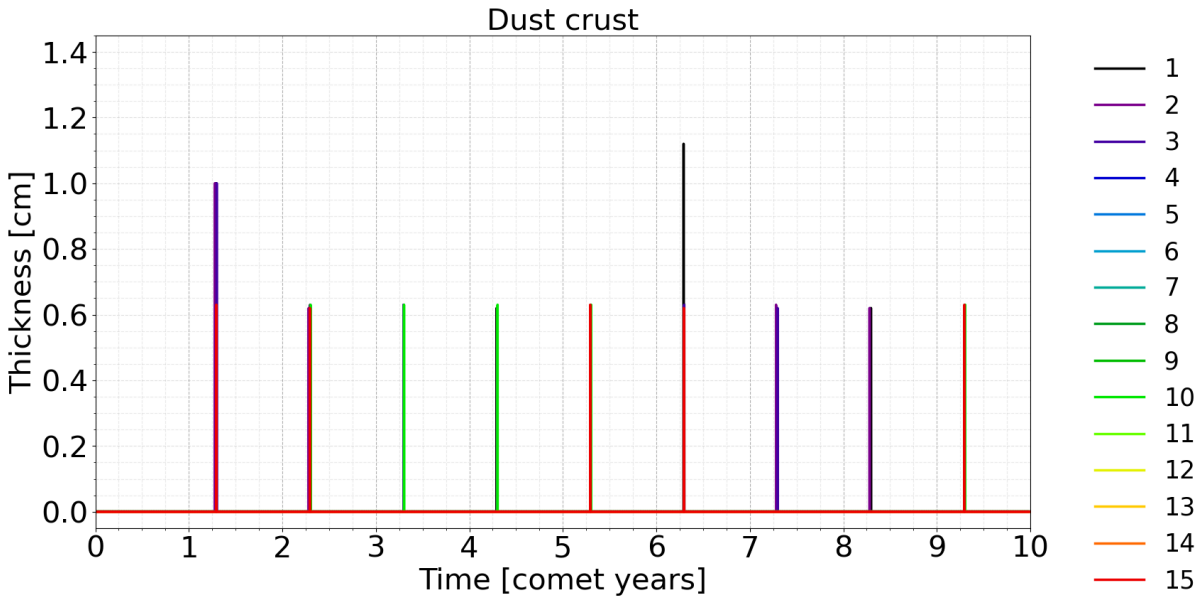

Figure 3.8: Evolution of the dust layer over ten full orbits of 67P for a porosity of 70%.

Although the outgassing does not substantially vary from one orbit to the other (between the 10 orbital revolutions considered), the erosion rate becomes more prominent at each perihelion, particularly for highly active facets eroding by up to 2 m during the last perihelion passage, and reaching a total erosion of almost 18 m after the 10 orbits (see Figure 3.7). This phenomenon could be attributed to the possible correlation between the decreasing amount of ice in the local material, and the increasing porosity, but further investigations are necessary to confirm this.
Finally, the erosion rate is not a gradual process during the orbit, but is largely controlled by the sudden high activity near perihelion and extends until almost the perihelion and restarts right after. In other words, significant erosion can only occur when there is a substantial loss of both gas and dust. Outside of the perihelion passage and at large heliocentric distances, erosion rates remain low and are sustained by cometary activity to a negligible extent.

We now investigate the extent of thermally-induced activity with different values of the internal porosity, over the course of 10 orbits.

The surface temperature exhibits marginal differences between the three porosity scenarios (60%, 70%, and 80%), with high porosity leading to lower surface temperature values, as shown in Figure 3.9. Between a 60% and a 80% porosity, the peak of temperature reached at the perihelion approach decrease by 0 to 2 K for the different facets, while the minimum temperature reached during perihelion period in shadow drops by ∼6 K. This could be attributed to the high porosity actually resulting low thermal inertia in the surface layers. In contrast, the gas flux is higher with high porosity, as shown in Figure 3.10, likely due to more voids facilitating gas transport.

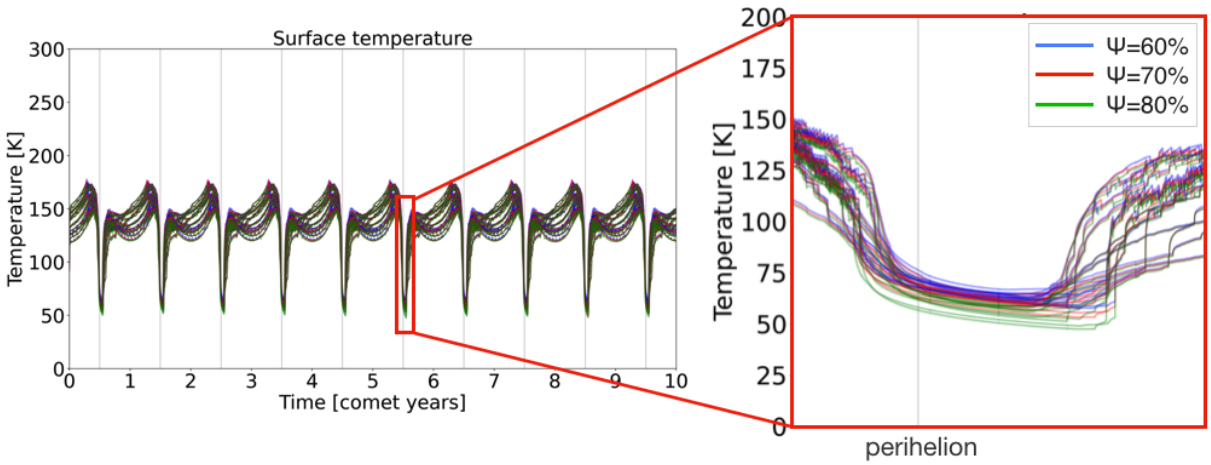

Figure 3.9: Surface temperature during ten full revolutions on 67P's current orbit, for all facets of the pit, and for the three porosity values: 60% (blue), 70% (red), and 80% (green). We zoom in on one perihelion to highlight the temperature differences.

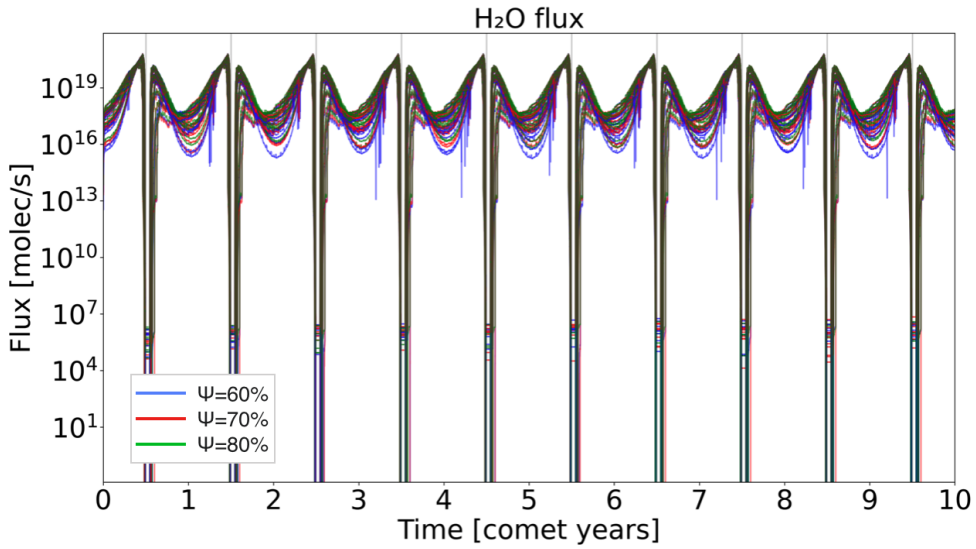

Figure 3.10: H_2O flux during ten full revolutions on 67P's current orbit, for all facets of the pit, and for the three porosity values: 60% (blue), 70% (red), and 80% (green).

The dust flux is on the other hand higher for low values of porosity as shown in Figure 3.11, as there is a greater amount of dust available to be blown off. In fact, the average dust production is 55% higher for the 60% porosity compared to the 80% case.

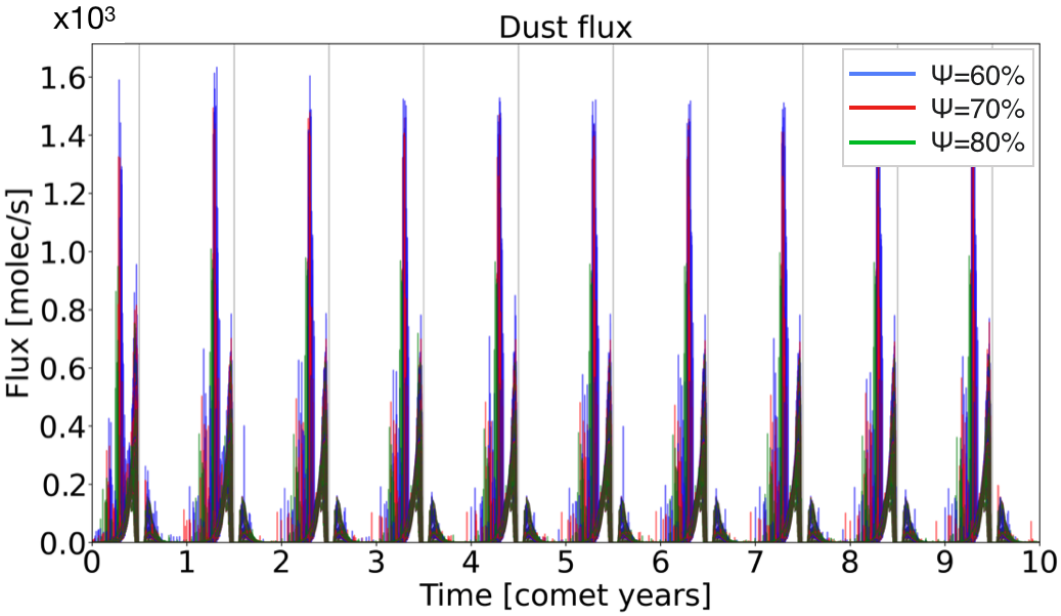

Figure 3.11: Dust flux during ten full revolutions on 67P's current orbit, for all facets of the pit, and for the three porosity values: 60% (blue), 70% (red), and 80% (green).

Moreover, a thin layer of dust, ranging from few mm to 1.4 cm, is temporarily formed in the scenarios with 60% and 70% porosity, whereas no such layer is observed with 80% porosity (see Figure 3.12). The formation of this layer in instances of low porosity could be attributed to the greater amount of dust available to be expelled, or insufficient outgassing to drag this greater amount of dust. However, this layer is rapidly disrupted by the high gas pressure during the perihelion passage. Additionally, this temporary dust layer may have contributed to the substantial production of dust flux (Figure 3.11) and could have played a role in the observed increase in surface temperature.

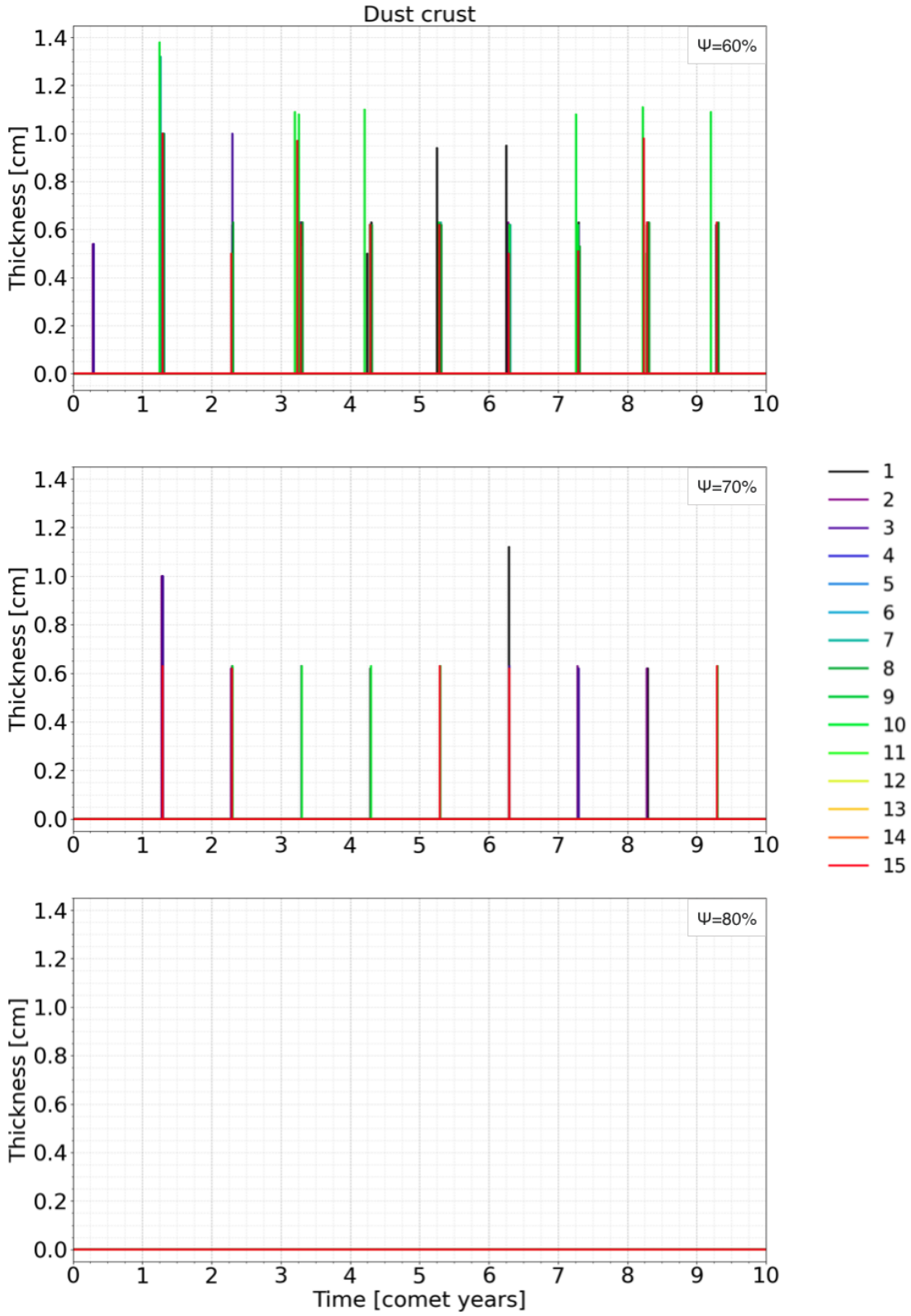

Figure 3.12: Dust layer formed as a result of activity during ten full revolutions on 67P's current orbit, for the three cases of porosity: 60% (upper panel), 70% (middle panel), and 80% (bottom panel).

Finally, higher porosity values lead to increased erosion rates. Although the amount of eroded material (in mass) is higher in cases of low porosity due to the presence of more dust to be expelled by the outgassing, the volume of this material increases with increasing porosity, resulting in a greater extent of erosion throughout the thermal evolution. For instance, the average erosion sustained with a porosity of 70% is approximately 30% higher than that with a porosity of 60%, and the erosion with a porosity of 80% is about 50% higher than that with a porosity of 70% for all facets (see Figures 3.13 and 3.14).

However, regardless of the value of porosity, the erosion achieved after 10 orbital revolutions remains very low compared to the observed dimensions of pit, i.e. a diameter of ∼210 m and a depth of ∼60 m.

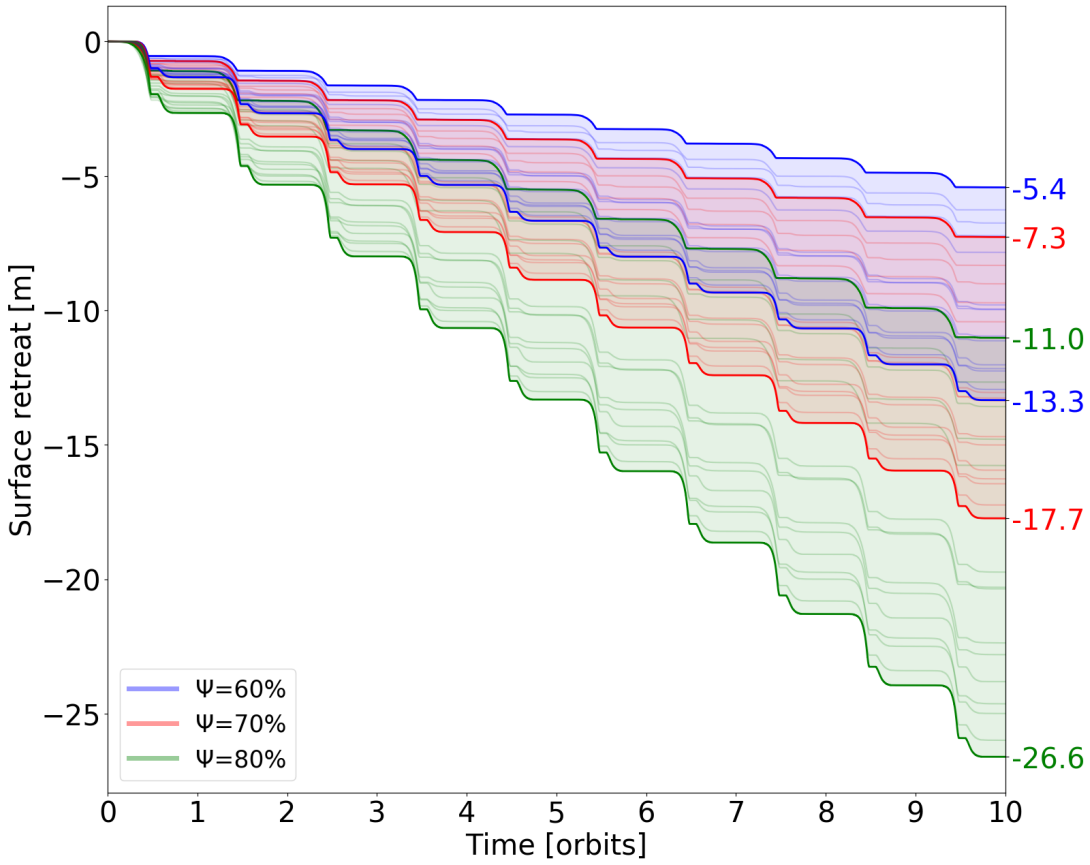

Figure 3.13: Progressive erosion sustained during ten full revolutions on 67P's current orbit, for all facets of the pit, and for the three porosity values: 60% (blue), 70% (red), and 80% (green).

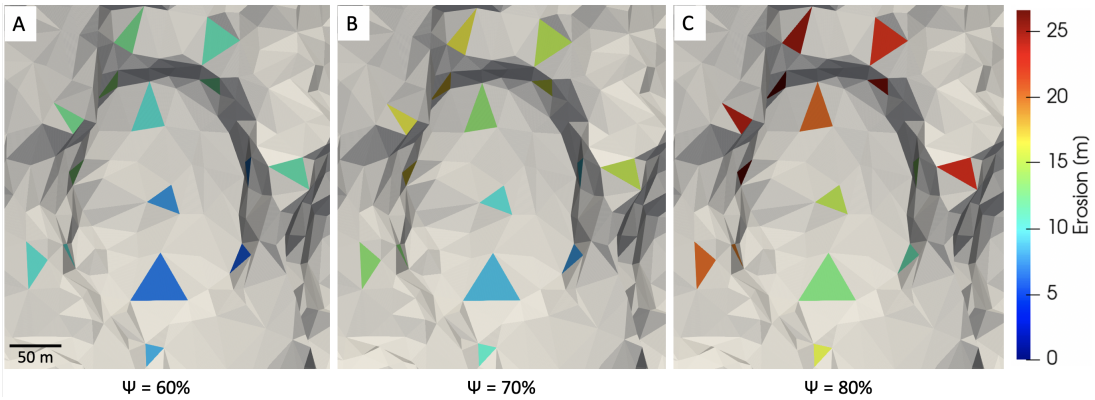

Figure 3.14: Erosion sustained after ten orbits for each facet of the pit, and for the different porosity values: 60% (A), 70% (B), and 80% (C).

Overall, our results show that porosity is a key parameter that can influence both the thermal evolution and the local morphology over multiple orbital revolutions: a nucleus of a high porosity of 80%, despite its low conductivity, can sustain locally twice the erosion obtained with a 60% porosity. However, under current illumination conditions, no reasonable value of the porosity can lead to the carving of the observed pit through time.

3.4 Influence of dust-to-ice ratio

Determining the bulk dust-to-ice mass ratio of a cometary nucleus is challenging, particularly when inferred from the composition of the coma (Choukroun et al., 2020). Studies have attempted to estimate this ratio using models constrained by *Rosetta* data. For example, Marschall et al. (2020) inferred a dust-to-gas ratio of $0.73^{+1.3}_{-0.70}$ for escaping material and $0.84^{+1.6}_{-0.81}$ for ejected material by fitting the ROSINA/COPS data. However, variations in instruments or observation times can yield different values, with certain nucleus regions showing ratios exceeding 2 (Fulle et al., 2017; O'rourke et al., 2020). Overall, Choukroun et al. (2020) suggest that observations of 67P are consistent with a global dust-to-ice ratio of $\sim$1. Based on modeling considerations, Davidsson et al. (2022a) suggest that a relatively pristine nucleus should have a mass ratio of refractories to water ice of 1, and the water abundance of fallback material is slightly lower, with a ratio of 2. Davidsson et al. (2022c) confirm that a water abundance corresponding to a ratio of 1-2 is consistent with the observed thickness and variation over time of the dust mantle, as inferred from MIRO observations (Gulkis et al., 2015a). Because of the uncertainty related to this physical characteristic, investigating its impact on the thermal evolution is crucial. We have thus conducted tests using three different values of this ratio to examine its influence on the thermal evolution of our pits, as summarized in Table 3.1.

Increasing the dust-to-ice mass ratio from 0.5 to 2 results in a small increase, by $\sim$2-3 K on average, of the surface temperature throughout the orbit. However, the differences are not significant enough to confidently attribute them to a direct impact of the ratio.

A difference of ∼8-9 K is observed during the period of heightened activity at perihelion, probably as a result of the increased thermal conductivity. However, during the perihelion phase, the temperature drops by up to 6 K. At the same time, the average water production increases by ∼75%, and the average dust flux is almost 6 times higher. Thus the temperature drop might be a result of an increased rate of phase transition, which is a heat sink. It should be noted that expressing the differences in fluxes based solely on peak values may not accurately reflect the underlying processes, which can be complex and not fully understood. We show the different outputs in Figures: 3.15, 3.16, and 3.17.

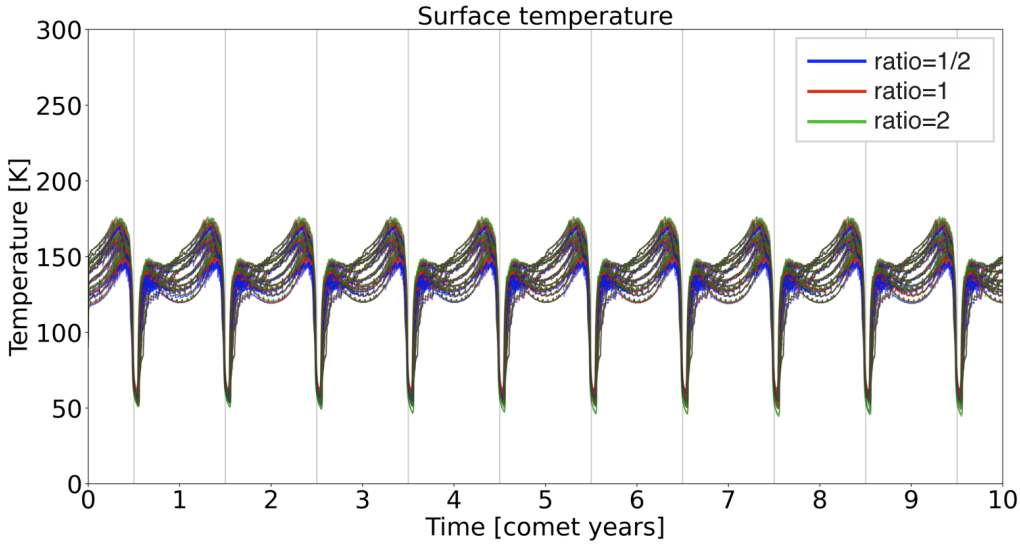

Figure 3.15: Surface temperature during ten revolutions on 67P's current orbit, for all facets of the pit, and for the three dust/ice ratio cases: 0.5 (blue), 1 (red), and 2 (green).

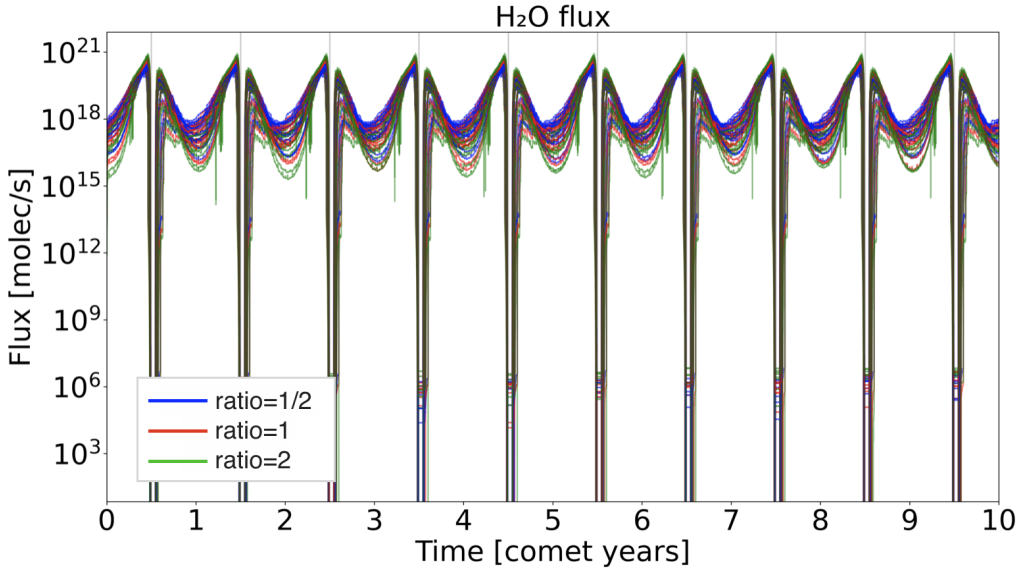

Figure 3.16: H_2O flux during ten full revolutions on 67P's current orbit, for all facets of the pit, and for the three dust/ice ratio cases: 0.5 (blue), 1 (red), and 2 (green).

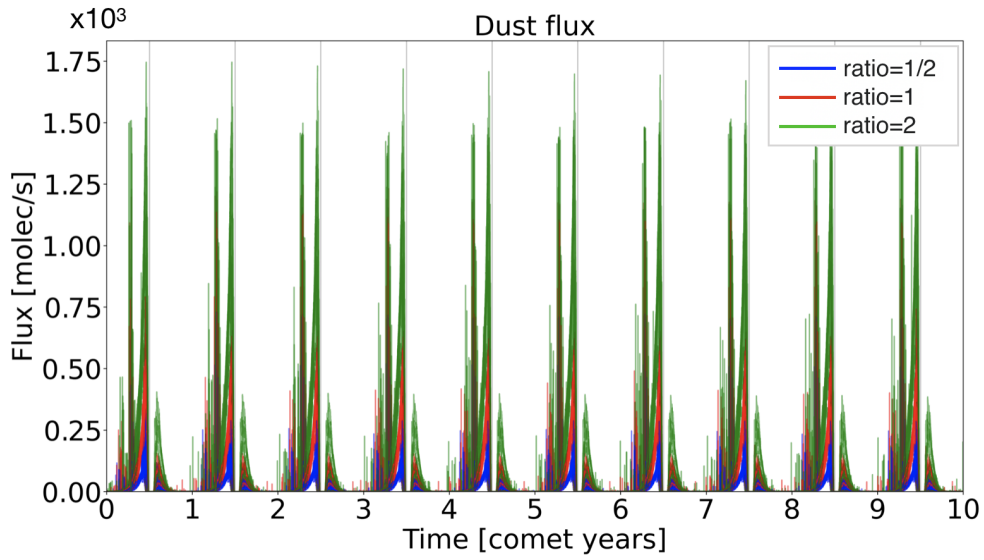

Figure 3.17: Dust flux during ten full revolutions on 67P's current orbit, for all facets of the pit, and for the three dust/ice ratio cases: 0.5 (blue), 1 (red), and 2 (green).

As a result of this increased activity, erosion significantly increases, almost doubling when the ratio is doubled as shown in Figures 3.18 and 3.19.

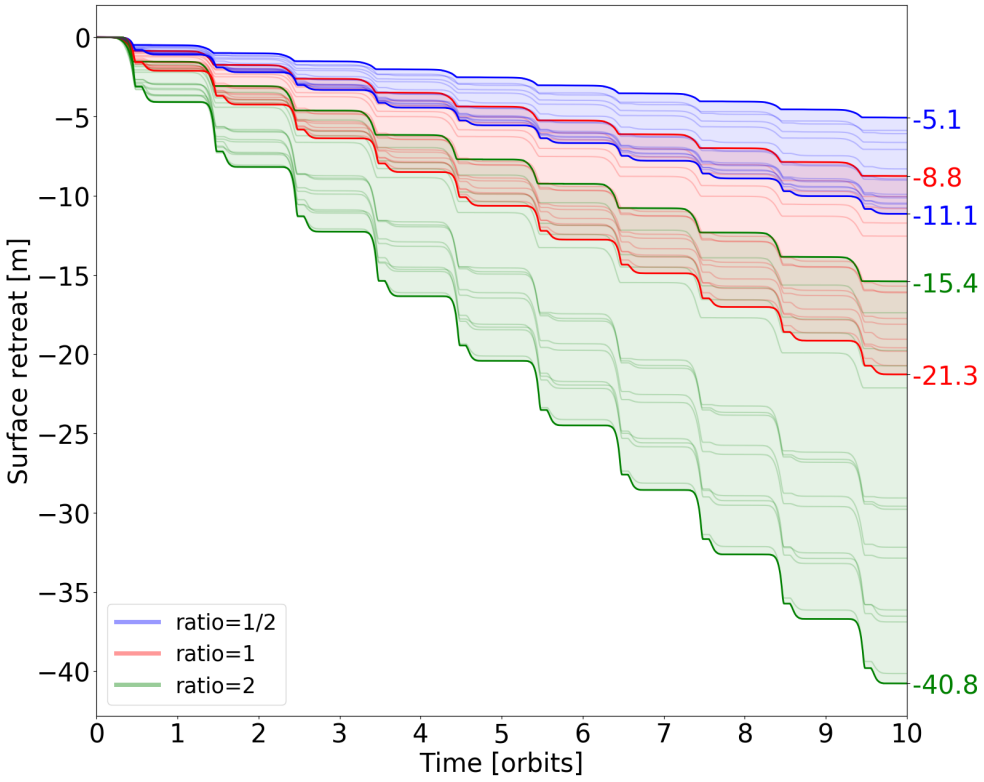

Figure 3.18: Progressive erosion sustained during ten full revolutions on 67P's current orbit, for all facets of the pit, and three values of the dust/ice mass ratio: 0.5 (blue), 1 (red), and 2 (green).

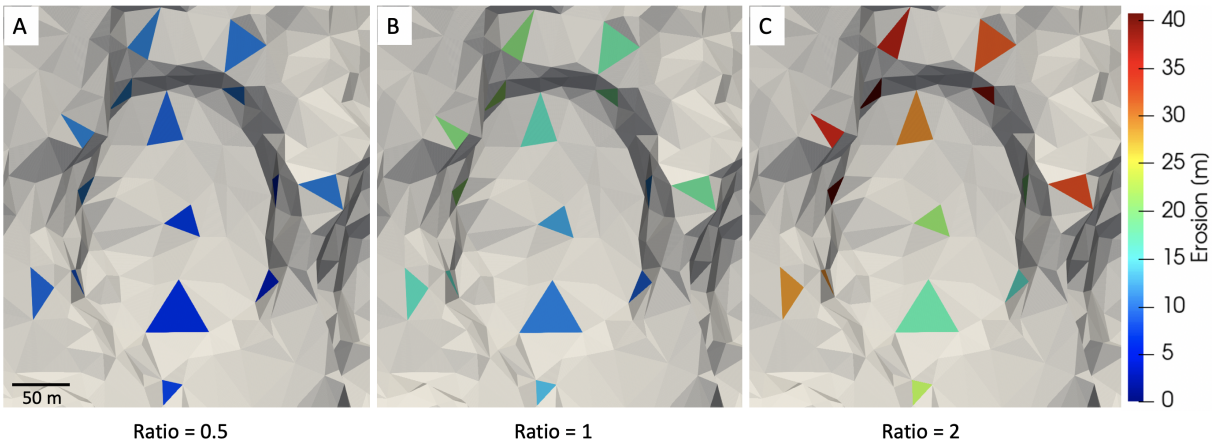

Figure 3.19: Erosion sustained after ten orbits for each facet of the pit, and different values of the dust/ice mass ratio: 0.5 (A), 1 (B), and 2 (C).

Finally, a dust layer forms before each perihelion passage for a dust-to-ice ratio of 2, reaching up to 1.2 cm for several facets located on different sides of the pit, but is quickly removed by subsequent activity (Figure 3.20). The transient aspect of this dust layer might have contributed to the observed higher production of gas (in the simulation outputs), by temporarily increasing the local thermal inertia (as already seen in the case of low porosity in Section 3.3). Notably, for each orbital revolution, the first significant ejection of dust (which only occurs at a ratio of 2) coincides with the period where this transient dust layer is being formed at the surface. This observation suggests that the formation and removal of this dust layer is correlated with dust and gas ejection, potentially as a result of an increased thermal inertia.

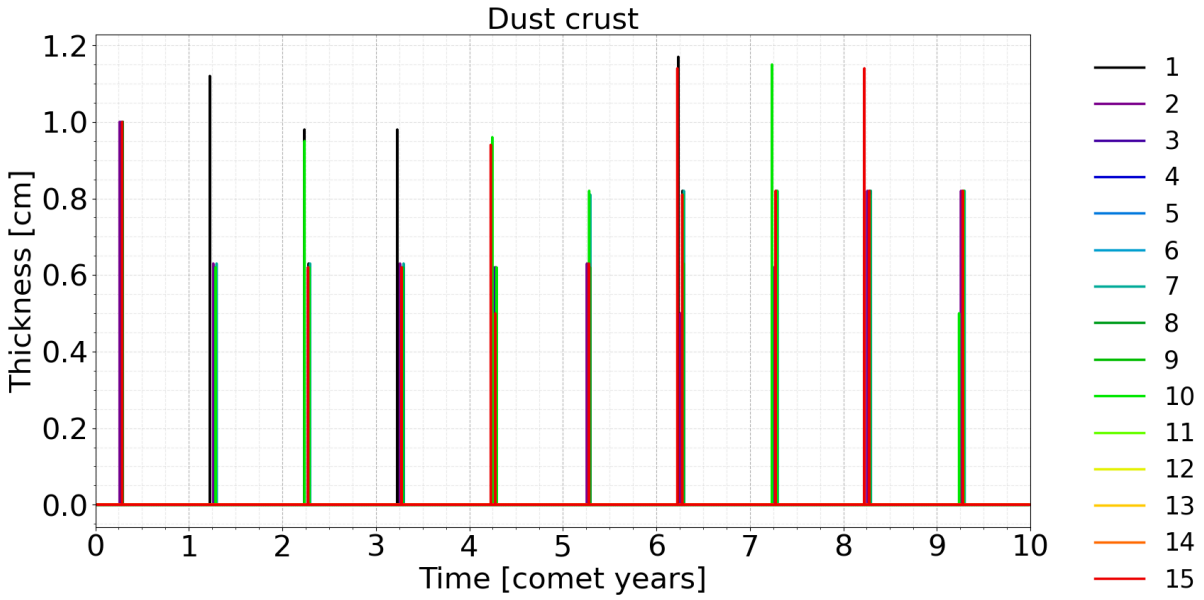

Figure 3.20: Dust layer formed as a result of activity during ten full revolutions on 67P's current orbit, with a dust/ice ratio of 2.

As for porosity, the initial dust-to-ice mass ratio can have a significant effect on the modeled cometary activity. For the values tested, a higher ratio leads to increased activity and erosion: doubling the ratio results in a doubling of the erosion achieved after ten orbital revolutions. This emphasizes the importance of properly setting the dust-to-ice ratio in thermal evolution models, to obtain a realistic representation of the activity. Yet, for all values tested, the erosion sustained under current illumination conditions does not allow to carve a pit.

3.5 Influence of CO and CO_2 abundance

Measuring the abundance of CO and CO_2 in a cometary nucleus is challenging. These abundances are usually estimated from production rates measured in the coma, but this process is not simple. According to modeling studies such as Prialnik (2006), values obtained by integrating over a long period of time are more accurate than those taken at a single point in the orbit. Herny et al. (2021) showed that the nucleus of 67P can be considered uniform to the first order, the bulk ice being dominated by H_2O (91.4%±4.5%), then CO_2 (6.7%±3.5%) and CO in small amount (1.9%±1.2%). However, they show that to a second order, there is a distinct difference in composition between the northern and southern hemispheres and that varies over the orbit. The northern hemisphere's CO/CO_2 ratio is estimated to be ∼0.6±0.1, while the southern hemisphere's ratio is ∼0.2±0.1. Production rates of CO and CO_2 do vary significantly across the orbit, sometimes by several orders of magnitude, but are mainly insolation driven, where the variations are caused by the tilt of rotation axis and eccentricity of the nucleus (Fougere et al., 2016; Biver et al., 2019; Läuter et al., 2019a; Combi et al., 2020). Besides, these volatile species are very sensitive to cumulative heating; hence, the uppermost surface layers are certainly depleted compared to the bulk values.

To better understand the role of CO and CO_2 in the evolution of our pit of interest, we examine their impact on thermal evolution outputs for three different initial mass fraction scenarios, as summarized in Table 3.1. The introduction of these volatile species in large amounts into the ice composition lead to numerical instabilities, observed for a non-negligible number of facets, even when their sublimation fronts have retreated below the surface during the multi-stage injection phase: the more volatiles present, the higher the number of facets exhibiting instability. It is possible that the sublimation of CO and CO_2 as modeled for these facets could in reality trigger localized outbursts of activity, which our model is unable to simulate. These numerically unstable facets are often found in parts of the depression that experienced the highest activity and erosion rates in previous tests, i.e. regions that receive the most energy near perihelion. Resolving this numerical instability would require significant changes in the initial thermophysical parameters for these facets, which would undermine the validity of our comparisons, or in the resolution of the grid which is computationally expensive. To mitigate this effect, we consider a reduced porosity for these tests in order to minimize the impact of instabilities.

Water outgassing is the main driver of activity around perihelion, while at larger

distances the activity remains controlled by CO and CO_2 due to their higher volatility, as shown in Figure 3.21.

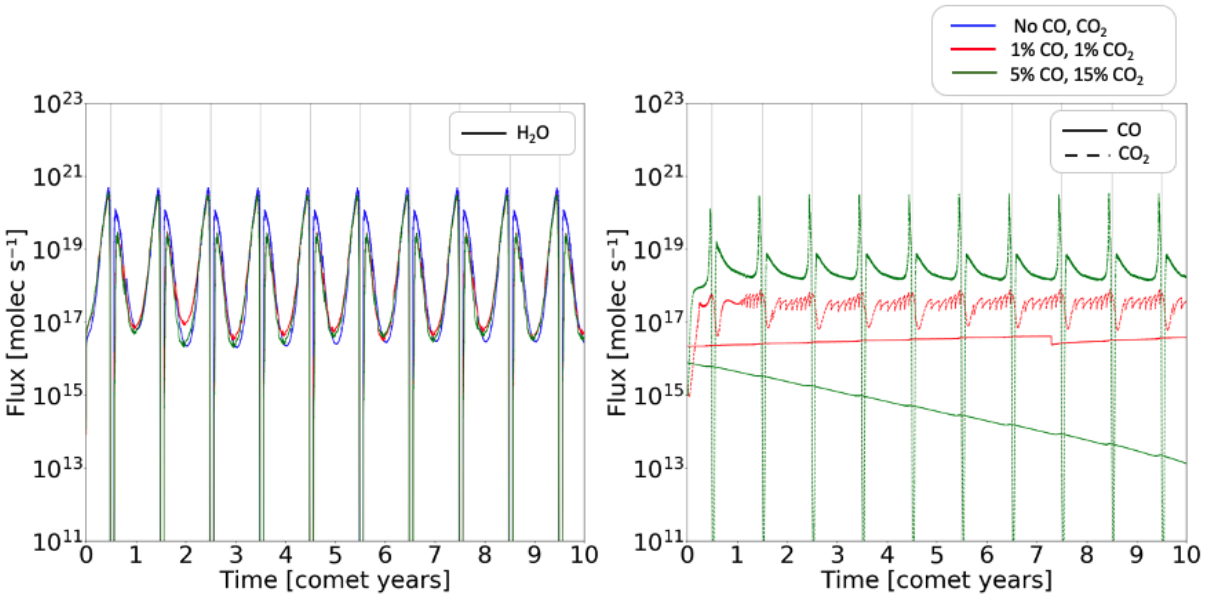

Figure 3.21: Degassing pattern from the active facet 9 during ten full revolutions on 67P's current orbit, for three cases of ice composition: without CO and CO_2, 1% CO and 1% CO_2, and 5% CO and 15% CO_2. Left: H_2O flux; right: CO_2 and CO fluxes.

The presence of 5% CO and 15% CO_2 leads to a significantly higher dust ejection rate for most facets, as shown in Figure 3.22. This effect is due to significant and sustained outgassing of these volatiles at those particular distances.

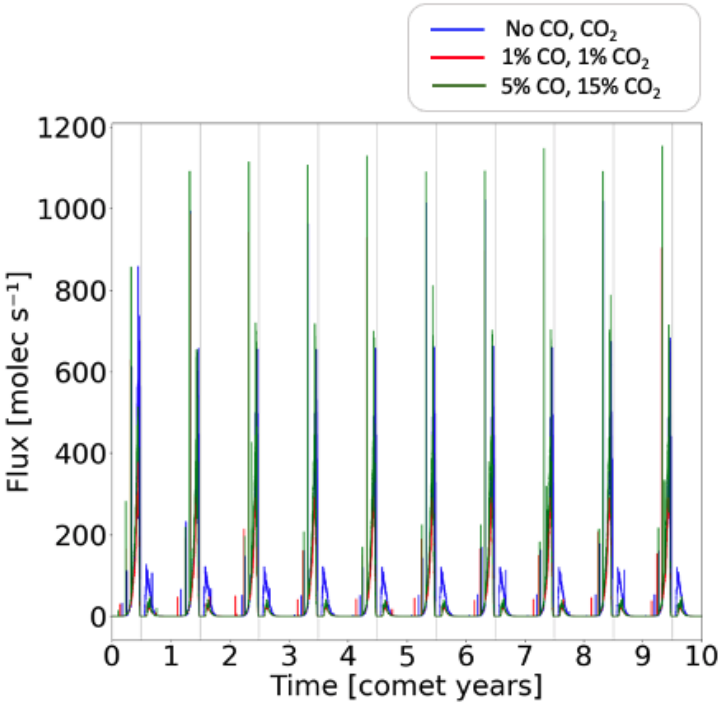

Figure 3.22: Dust flux of the active facet 9 during ten full revolutions on 67P's current orbit, for three cases of ice composition: without CO and CO_2, 1% CO and 1% CO_2, and 5% CO and 15% CO_2.

However, even smaller amounts of CO and CO_2 (1% each) can lead to non-uniform patterns of activity and erosion among different facets, contrary to what was observed in previous simulations. The final erosion shown in Figure 3.23 highlights this deviation.

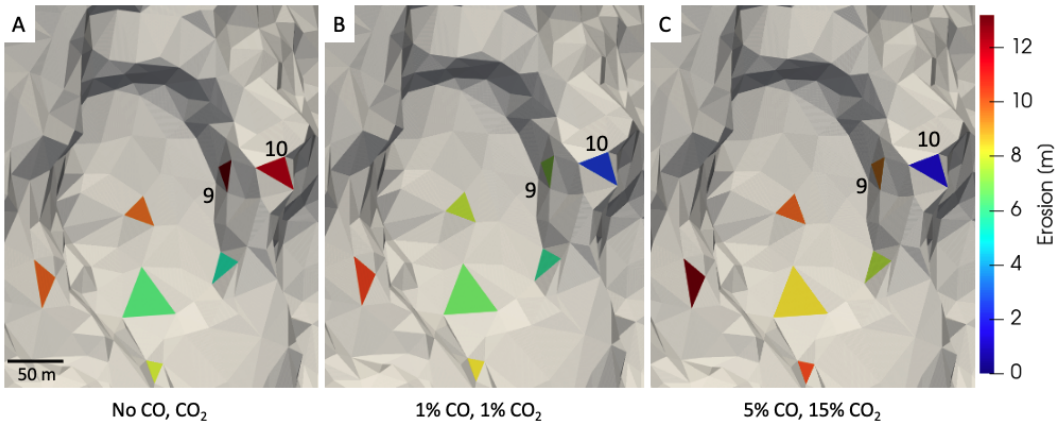

Figure 3.23: Erosion sustained after ten orbits by the seven facets remaining active, for three cases of ice composition: no CO and CO_2, 1% CO and 1% CO_2, and 5% CO and 15% CO_2, from left to right.

In addition to the complex shape of the comet, which leads to complex energy distribution and makes it difficult to infer activity, the presence of additional volatiles can further complicate the pattern of activity throughout the orbit, due to their higher volatility. This can result in distinct dust production patterns (as seen in Figure 3.22) or dust layer properties. Indeed, a temporary dust layer is formed in the three cases. However, it can persist in the presence of volatiles, leading to an increase in surface temperature. It is the case for example for facet 10 as shown in Figures 3.24, 3.25, and 3.26. This facet receives the highest integrated energy flux over the orbit (see Figure 3.5). Its dust mantle starts forming during the second and third orbital revolutions, for the cases of 1%CO 1% CO_2 and 5% CO 15% CO_2 respectively. Additionally, the surface temperatures on this facet can rise to nearly 250 k. Over time, the thickness of this crust reaches around 8 cm, and the presence of the dust layer almost quenches the overall activity, that results in low gas and dust fluxes decreasing orbit after orbit (see Figures 3.27 and 3.28): while a degree of activity is maintained, no substantial erosion is observed (Figure 3.23).

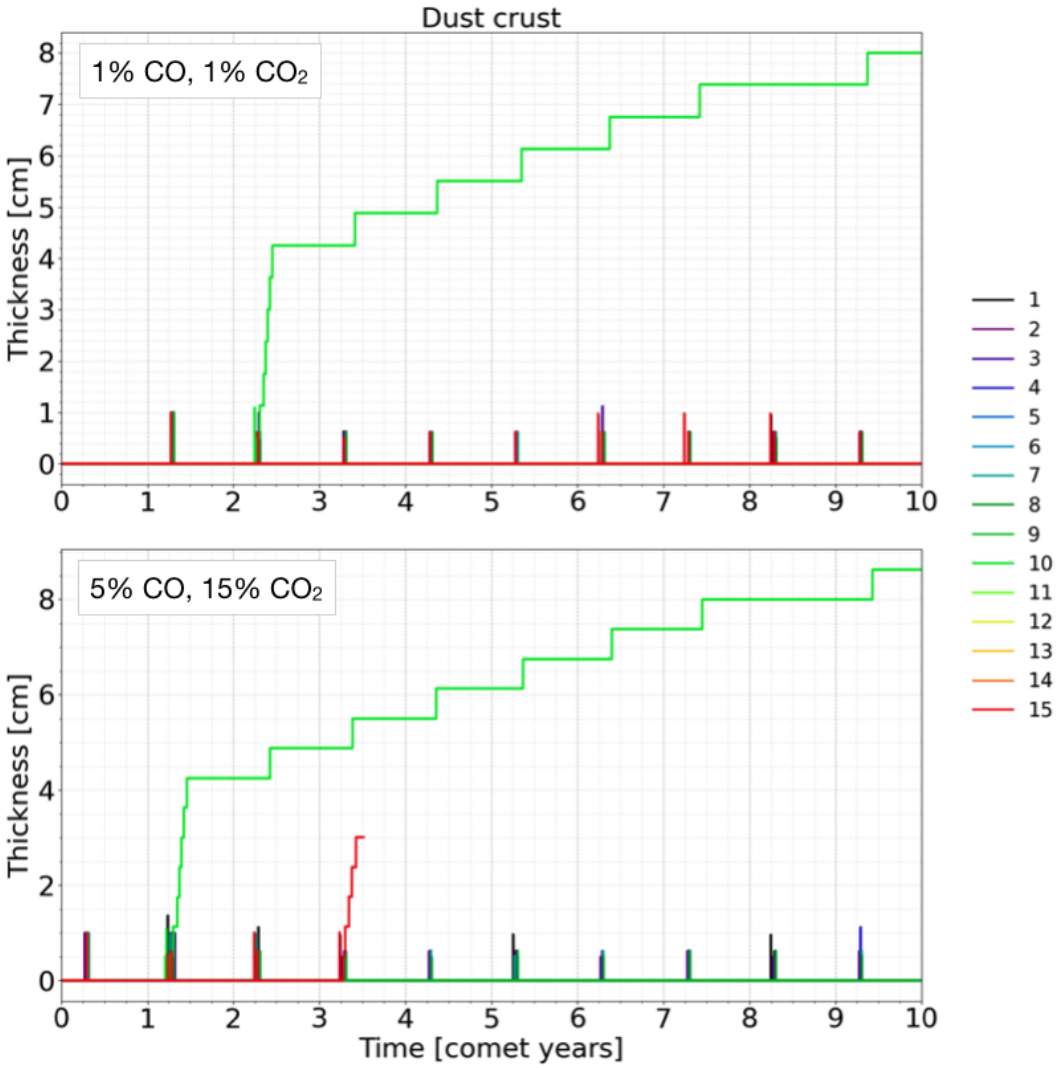

Figure 3.24: Evolution of the dust layer formed as a result of activity, over the ten orbital revolutions of 67P, for 1% CO 1% CO_2 (up) and 5% CO 15% CO_2 (down).

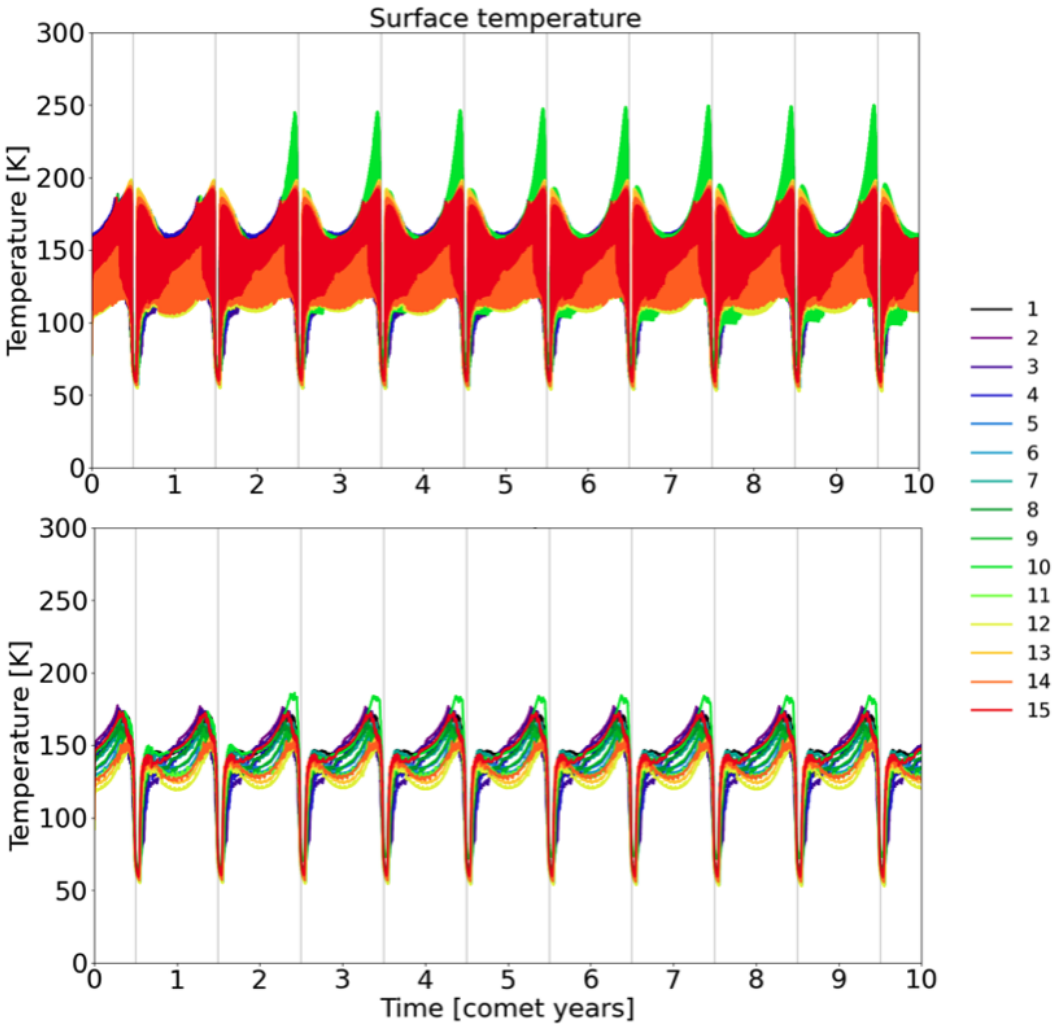

Figure 3.25: Top: surface temperature during ten full revolutions on 67P's current orbit, for the case of 1% CO and 1% CO_2 abundances. Bottom: same data, smoothed over a daily period window.

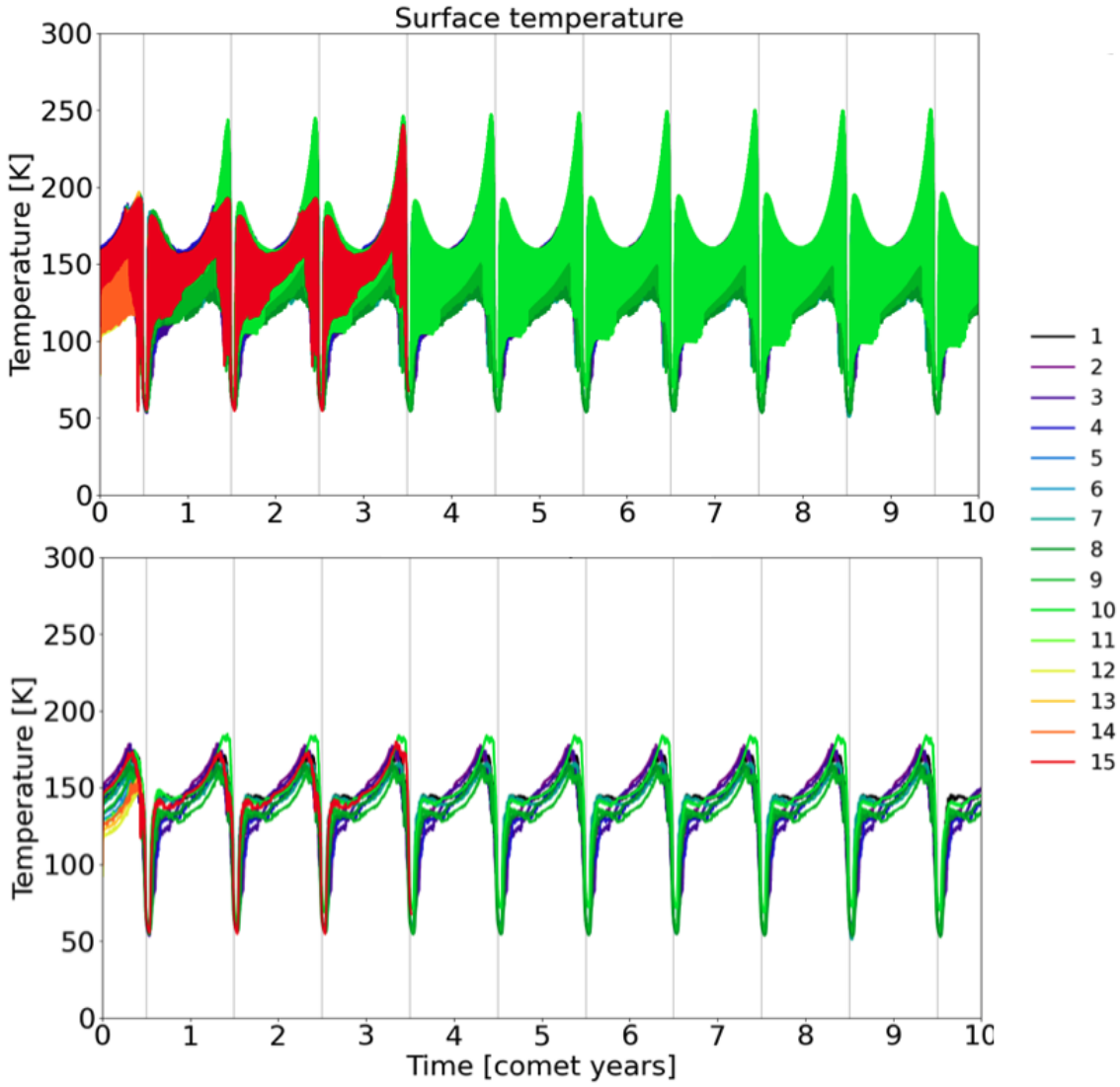

Figure 3.26: Top: surface temperature during ten full revolutions on 67P's current orbit, for the case of 5% CO and 15% CO_2. Bottom: same data, smoothed over a daily period window.

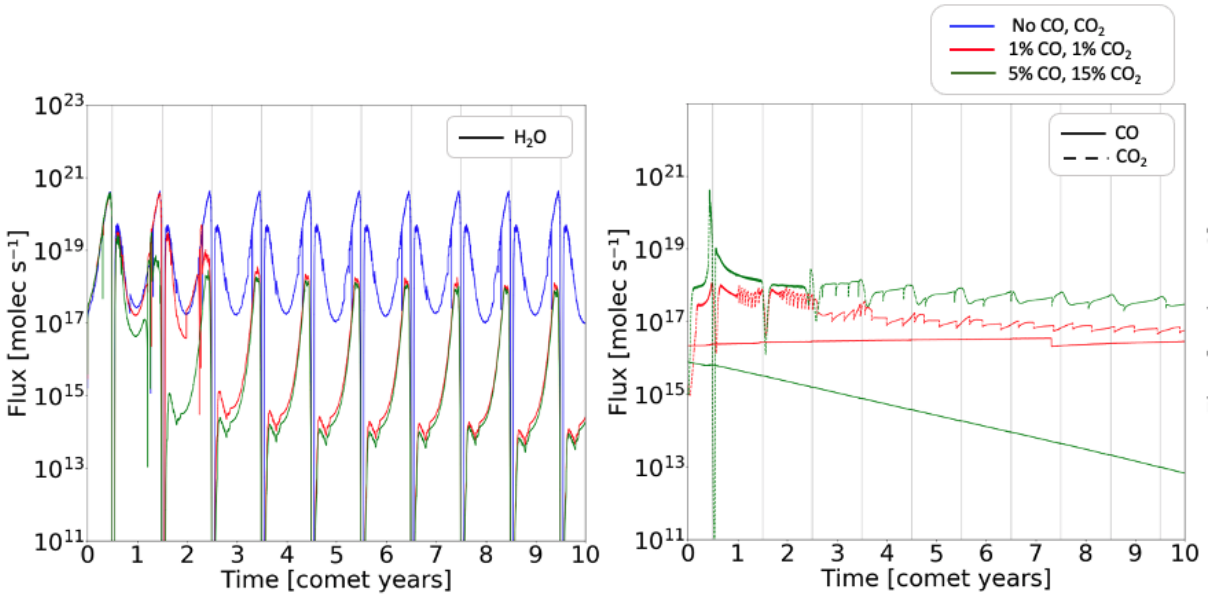

Figure 3.27: Activity pattern of facet 10 that is quenched by the dust layer in the presence of CO and CO_2 (see Figure 3.24), for three cases of ice composition: no CO and CO_2, 1% CO and 1% CO_2, and 5% CO and 15% CO_2. Left panel: H_2O flux, right panel: CO_2 and CO fluxes.

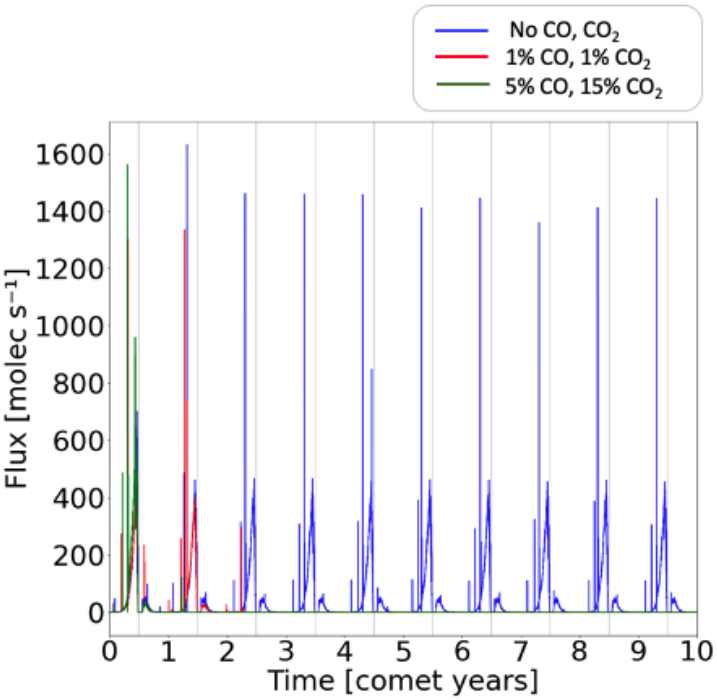

Figure 3.28: Dust flux of the quenched facet 10 during ten full revolutions on 67P's current orbit, for three cases of ice composition: without CO and CO_2, 1% CO and 1% CO_2, and 5% CO and 15% CO_2.

Overall, in the presence of additional volatiles, areas that receive a sudden high energy input at perihelion may exhibit – numerically – a non-linear behavior, which might be related to an actual explosive behavior. In contrast, regions that receive a relatively

constant high energy input over the orbit tend to accumulate a dust layer at the surface after multiple perihelion passages, which suppresses their activity during subsequent perihelion passages. These results have potential implications for the observed dust jets and crust layers observed on the surface of 67P during the encounter, but are beyond the scope of our study. Finally, facets that receive a lower energy input build a dust layer that is not thick enough to quench their activity, and is eventually removed by the ongoing activity. As a result, these facets remain active throughout the ten orbital revolutions.

The inclusion of CO and CO_2 in the initial ice composition adds significant complexity to our thermal evolution simulations, often leading to numerical instabilities and unpredictable behavior. However, our simulations show that these additions have a marginal effect on the surface erosion over the ten full orbital revolutions.

3.6 Influence of an initial dust mantle

The analysis of *Rosetta* long-term observations of 67P's nucleus has revealed the presence of a dust mantle covering large smooth plains in the northern hemisphere. This mantle is believed to originate from the southern hemisphere following the ejection of dust particles during perihelion (Keller et al., 2015a, 2017; Thomas et al., 2015a; Attree et al., 2019). The thickness of the mantle, ranging from few mm to few m locally (Thomas et al., 2015a), remains uncertain and likely nonuniform (Hu et al., 2017; Davidsson et al., 2021a), but a noteworthy result from Herny et al. (2021) is that, in order to fit the ROSINA/DFMS measurements and reproduce the patterns of gas production rates, a thin dust mantle ($\sim$5 mm) all over the nucleus surface is needed. This requirement is particularly evident in measurements taken before the first equinox and after the second equinox. Furthermore, Davidsson et al. (2022a) used the NIMBUS model to simulate the H_2O and CO_2 production rates before and after perihelion, and concluded that the dust mantle in the northern hemisphere of 67P is typically less than 2 cm thick.

In our previous tests, we observed that such a thin layer could naturally form on the comet's surface without affecting the activity and erosion, as it is often removed by activity. This periodic formation and removal of the crust is caused by dust particles being dragged by escaping gas. However, we have also seen that in some cases, the mantle can accumulate up to 10 cm and play a significant, different role in the overall thermal evolution. To further understand the effect of the presence of a dust mantle on the nucleus, we consider a scenario where a dust mantle is present when the comet reaches its current orbit (which occurred in 1959, Maquet, 2015), and test various thicknesses ranging from 5 cm to 1 m (Table 3.1).

Simulation results show that a dust mantle thinner than 5 cm is rapidly removed by cometary activity after the first perihelion passage (see Figure 3.29).

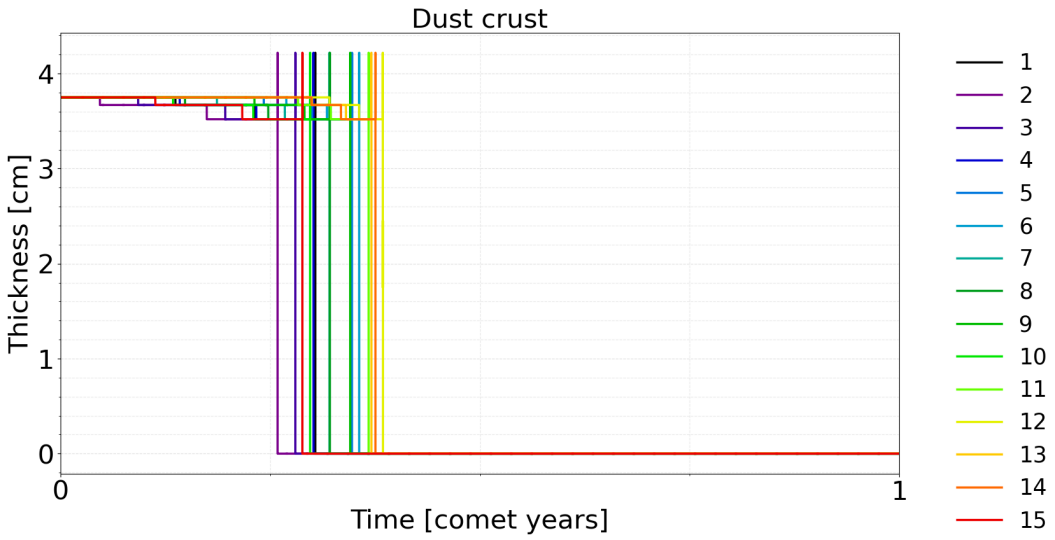

Figure 3.29: Evolution of the dust layer thickness over the first orbit out of the ten total orbits considered, for an initial mantle of 5 cm.

Prior to the mantle's removal, surface temperatures rise significantly at the approach of the first perihelion reaching up to 220 K (Figure 3.30), before decreasing to "normal" levels, i.e. when the mantle is removed (Figure 3.29). This is explained by the higher surface thermal inertia induced by the presence of the dust layer. The crust is removed by the outgassing that is observed to be initially low, then increases at the quarter of the orbit when the crust is still present, and then returns to "normal" levels after mantle removal (Figure 3.31). Correspondingly, dust production is significant during the period of increased activity prior to the first perihelion (Figure 3.32). Once the dust layer is removed, activity continues its "normal" behavior, i.e. as seen in previous tests.

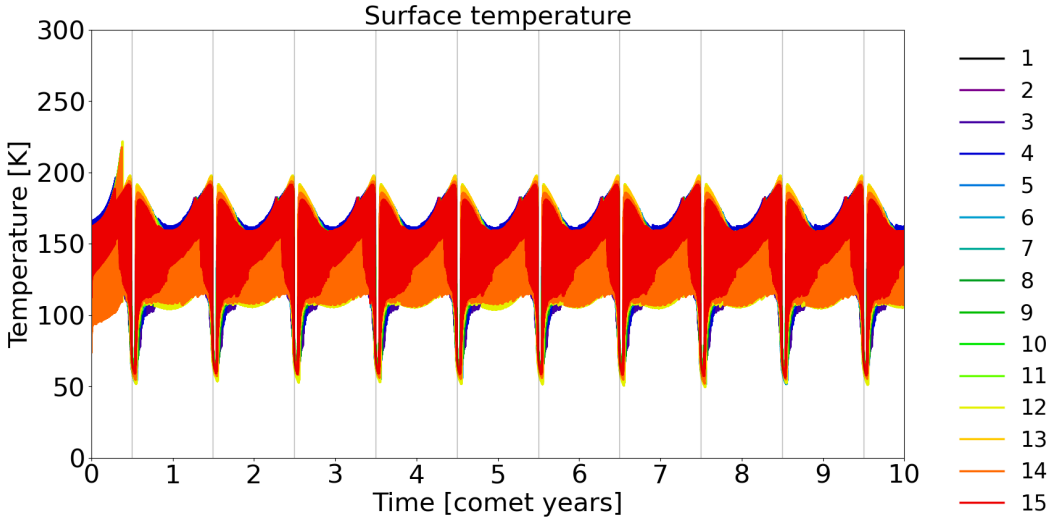

Figure 3.30: Surface temperature during ten full revolutions on 67P's current orbit, for an initial dust mantle of 5 cm.

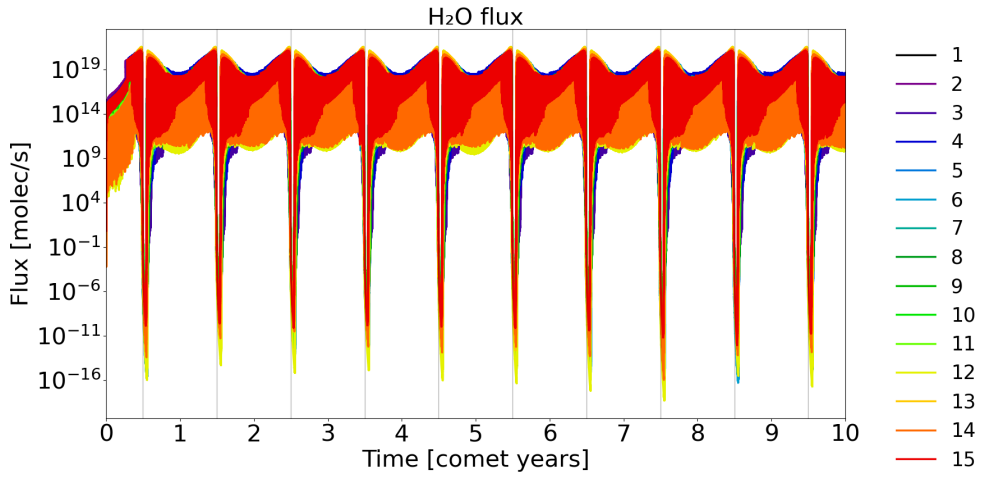

Figure 3.31: H_2O flux during ten full revolutions on 67P's current orbit, for an initial dust mantle of 5 cm.

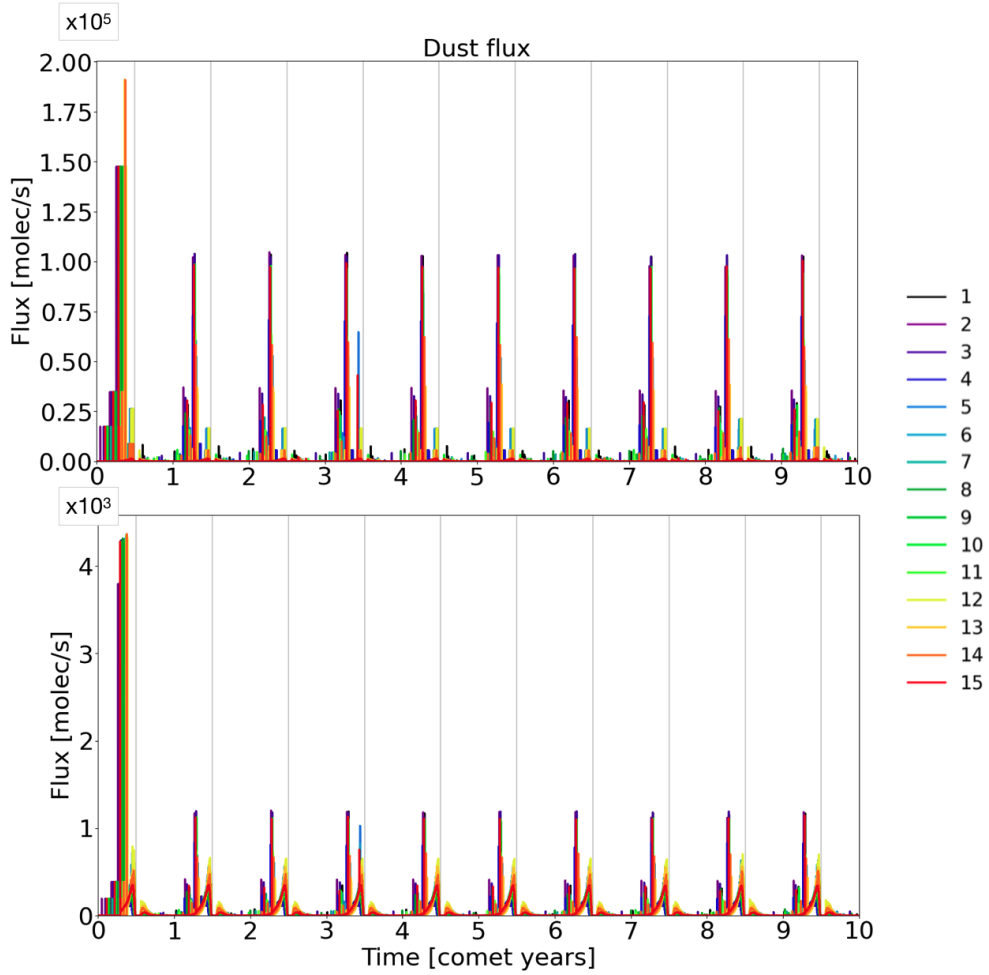

Figure 3.32: Top: dust flux during ten full revolutions on 67P's current orbit, for an initial dust mantle of 5 cm. Bottom: same data, smoothed over a daily period window.

With an initial dust mantle of 10 cm, surface temperatures exceed 250 K for most facets, and reach more than 300 K for some of them (see Figure 3.33).

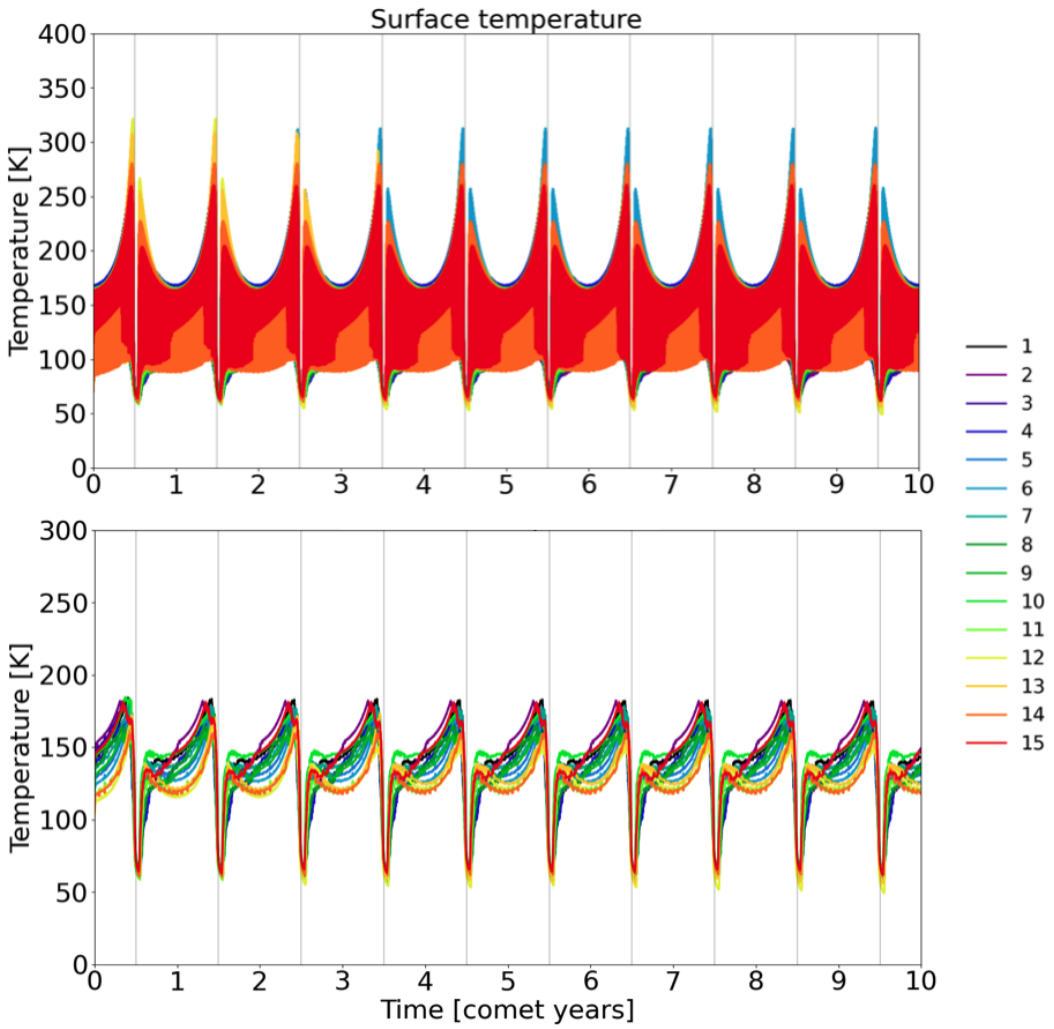

Figure 3.33: Top: surface temperature during ten full revolutions on 67P's current orbit, for an initial dust mantle of 10 cm. Bottom: same data, smoothed over a daily period window.

The rise in temperature could be attributed to the presence of the dust layer, both its insulating effect and the resulting change in surface albedo, as observed in previous simulations. However, some of the most active facets were able to efficiently remove this layer, resulting in a subsequent decrease in temperature at their surfaces after a few perihelion passages (e.g., facets 9, 10, 12, and 13 in Figure 3.34). These facets have either received the most energy close to perihelion resulting in brief but strong activity (i.e facets 12, 13), or received the highest amount of energy integrated over the orbit (i.e facet 10, Figure 3.5), enabling them to remove the dust mantle after several perihelion passages (Figure 3.34). Facet 9 is particularly noteworthy because it does not receive a high peak of energy at perihelion, or a large integrated quantity over the orbit, but instead receives a

significant amount of energy continuously throughout the orbit (as shown in Figure 3.3), which enables the maintenance of activity and mantle removal.

The activity of the remaining facets was quenched, leading to the accumulation of dust on their surfaces, resulting in the thickening of the dust layer to more than 10 cm and reaching nearly 12 cm, as shown in Figure 3.34.

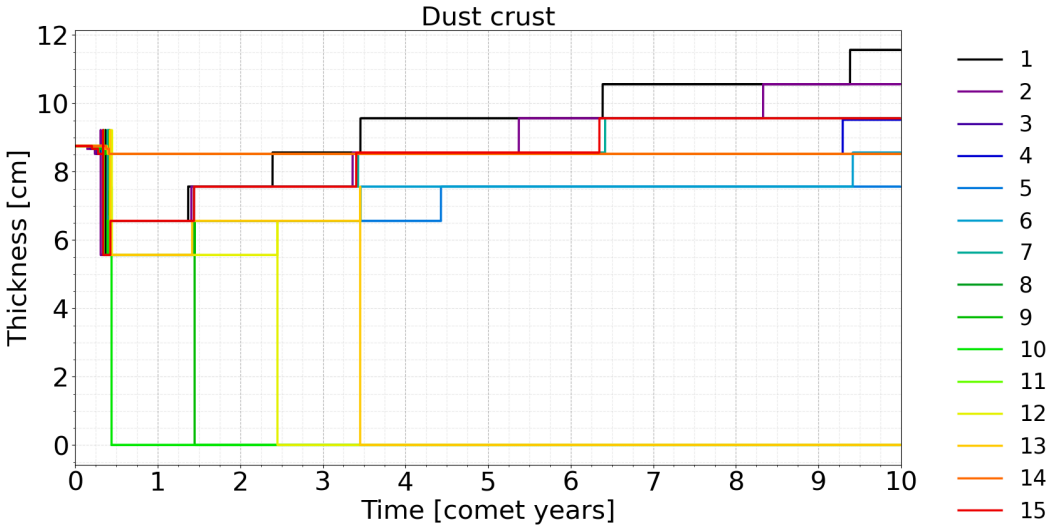

Figure 3.34: Evolution of the dust layer thickness over the first orbit out of the ten total orbits considered, for an initial mantle thickness of 10 cm.

The H_2O and dust production are low for the quenched facets, where sublimation occurs through a deeper layers beneath the surface. In contrast, both quantities increase for the active facets, once the crust was removed during the first orbits, provoking surface erosion reaching up to 17 m for the most active facet. These findings are illustrated in Figures 3.35, 3.36, and 3.37.

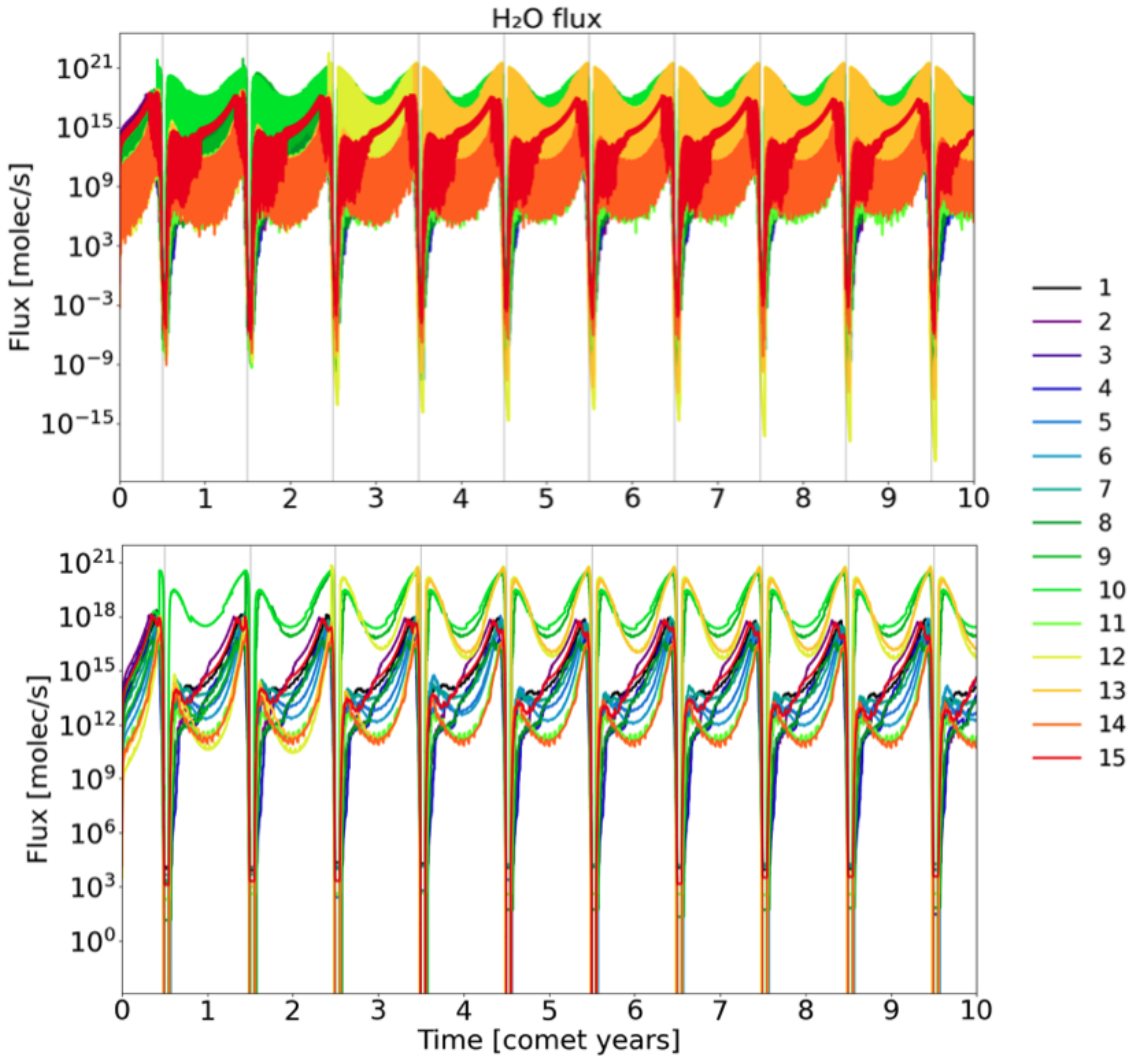

Figure 3.35: Top: H_2O flux during ten full revolutions on 67P's current orbit, for an initial dust mantle of 10 cm. Bottom: same data, smoothed over a daily period window.

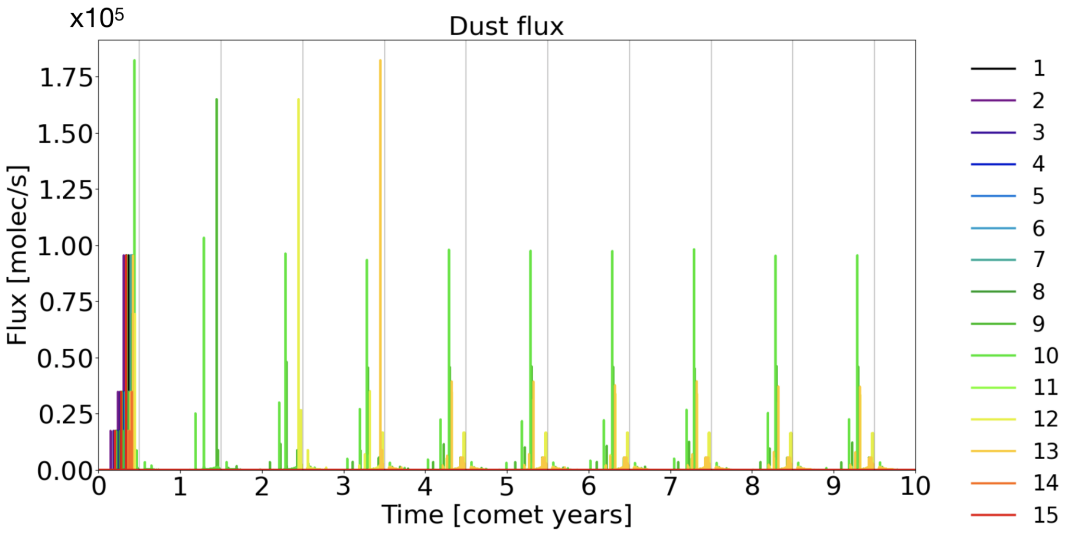

Figure 3.36: Dust flux during ten full revolutions on 67P's current orbit, for an initial dust mantle of 10 cm.

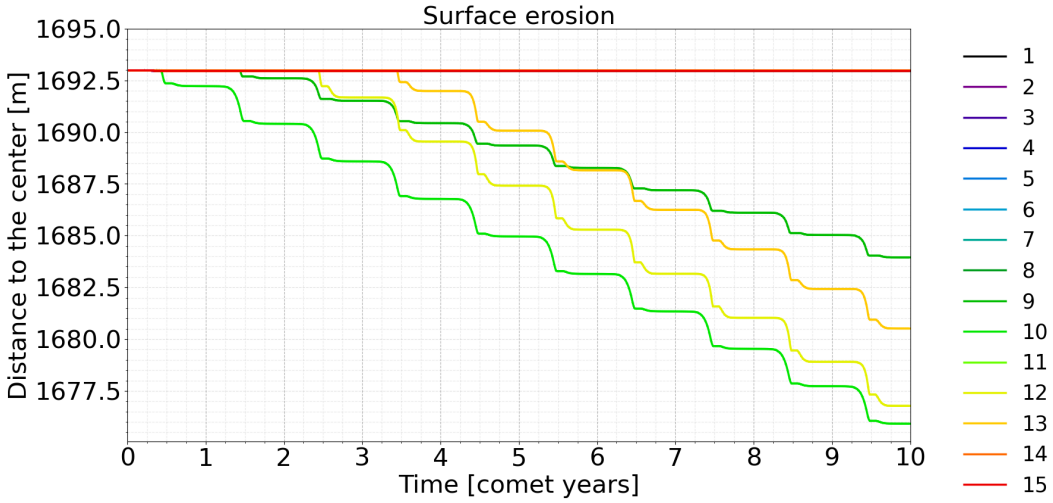

Figure 3.37: Progressive erosion sustained during ten full revolutions on 67P's current orbit, for an initial dust mantle of 10 cm. Only 4 facets remain active.

Finally, a dust mantle thicker than 10 cm (i.e., 30 cm, 60 cm, or 1 m) remains stable on the surface and is unaffected, as outgassing remains quenched during the ten orbital revolutions. Such a thick dust layer may be responsible for the inactivity observed in certain parts of the 67P's nucleus during certain moments of its orbit. For instance, The reduction in energy input after the summer equinox in the southern regions causes a decrease in gas flux and surface temperature, resulting in the formation of a dust mantle that quenches cometary activity by redepositing the dust particles (Attree et al., 2019). Figures 3.38, 3.39, 3.40, 3.41, and 3.42 provide a comparison of the activity outputs in three cases of dust mantle thickness, namely 0 cm, 5 cm, and 10 cm. The erosion achieved by the 15 facets for different initial dust mantles is illustrated in Figure 3.43.

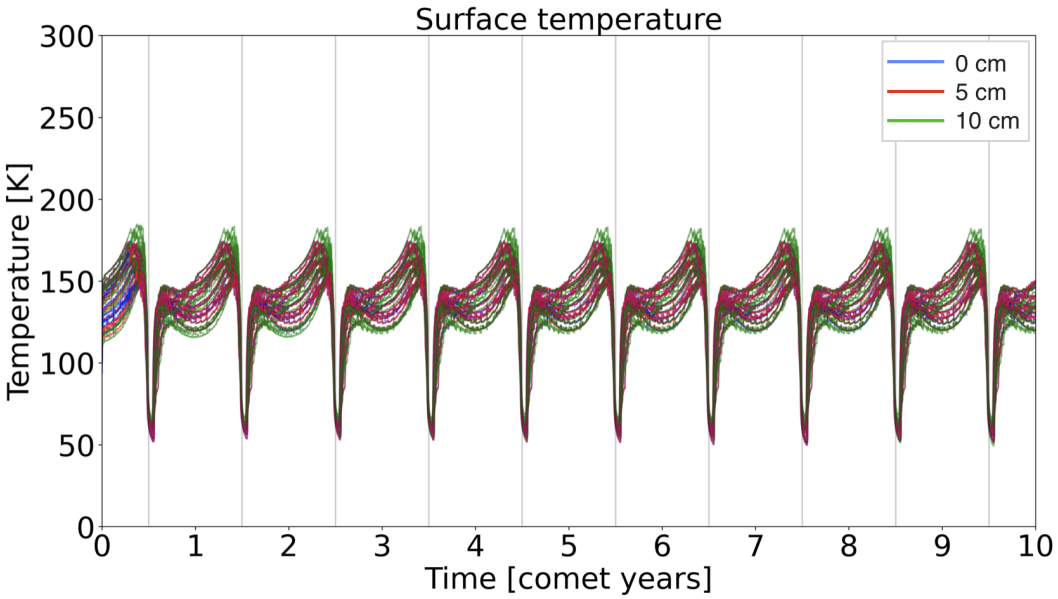

Figure 3.38: Surface temperature during ten full revolutions on 67P's current orbit, for all facets of the pit, and for the three values of mantle thickness: 0 cm (blue), 5 cm (red), and 10 cm (green).

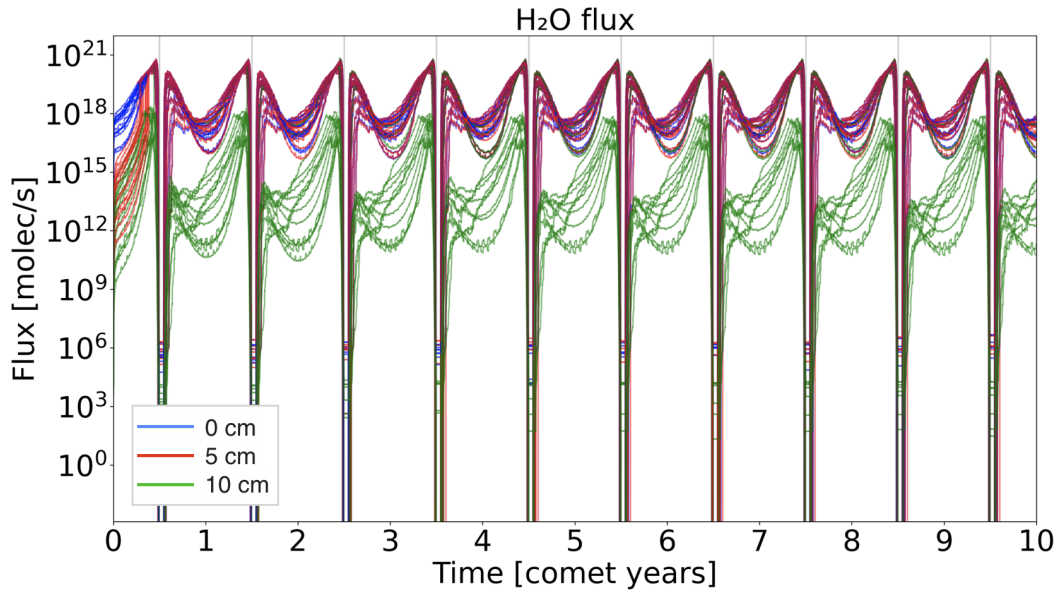

Figure 3.39: H_2O flux during ten full revolutions of 67P's for all facets of the pit, and for the three values of mantle thickness: 0 cm (blue), 5 cm (red), and 10 cm (green).

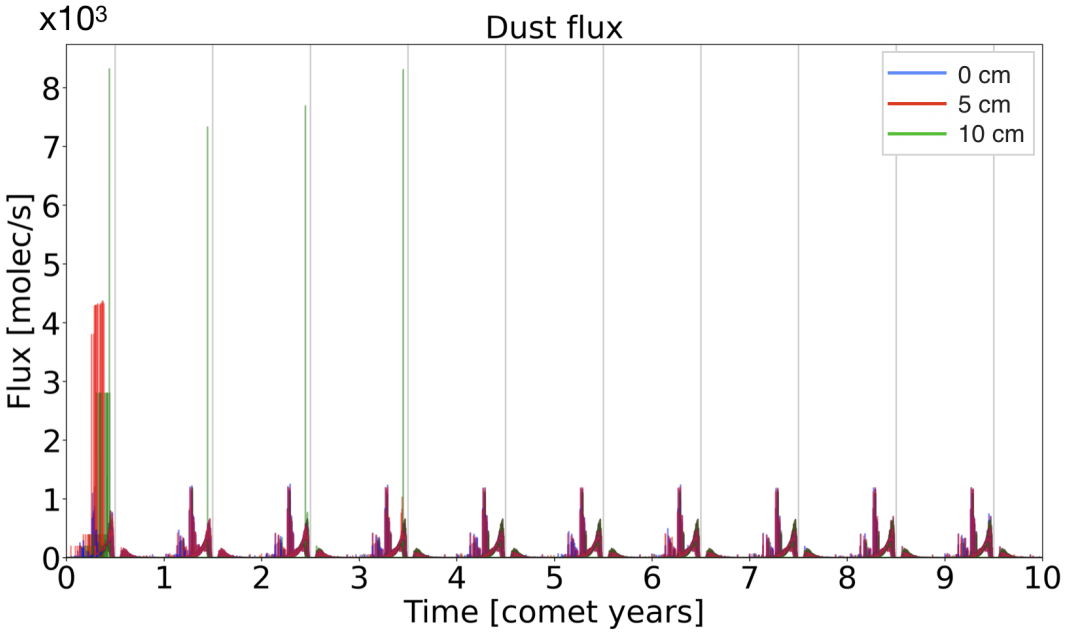

Figure 3.40: Dust flux during ten full revolutions on 67P's current orbit, for all facets of the pit, and for the three values of mantle thickness: 0 cm (blue), 5 cm (red), and 10 cm (green).

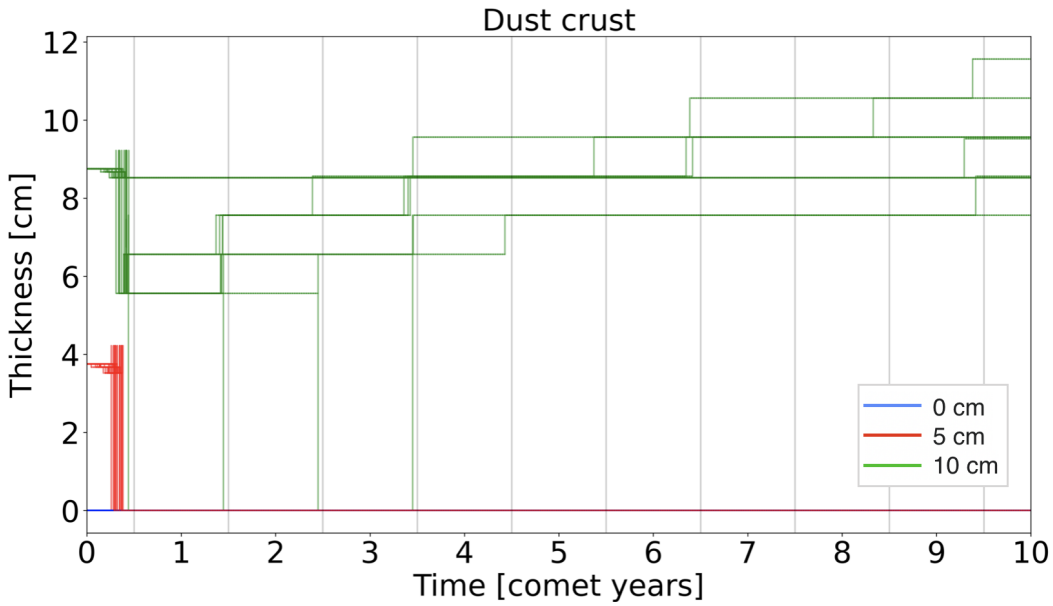

Figure 3.41: Dust layer formed during ten full revolutions on 67P's current orbit, for all facets of the pit, and for the three values of mantle thickness: 0 cm (blue), 5 cm (red), and 10 cm (green).

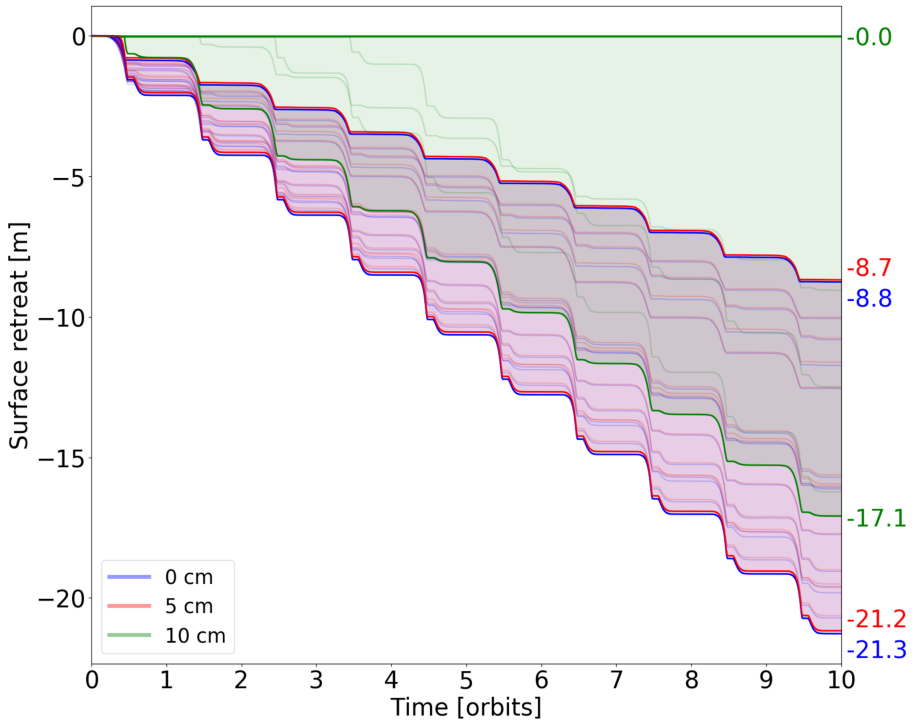

Figure 3.42: Progressive erosion sustained during ten full revolutions on 67P's current orbit, for all facets of the pit, and three values of initial dust mantle's thickness: 0 cm (blue), 5 cm (red), and 10 cm (green).

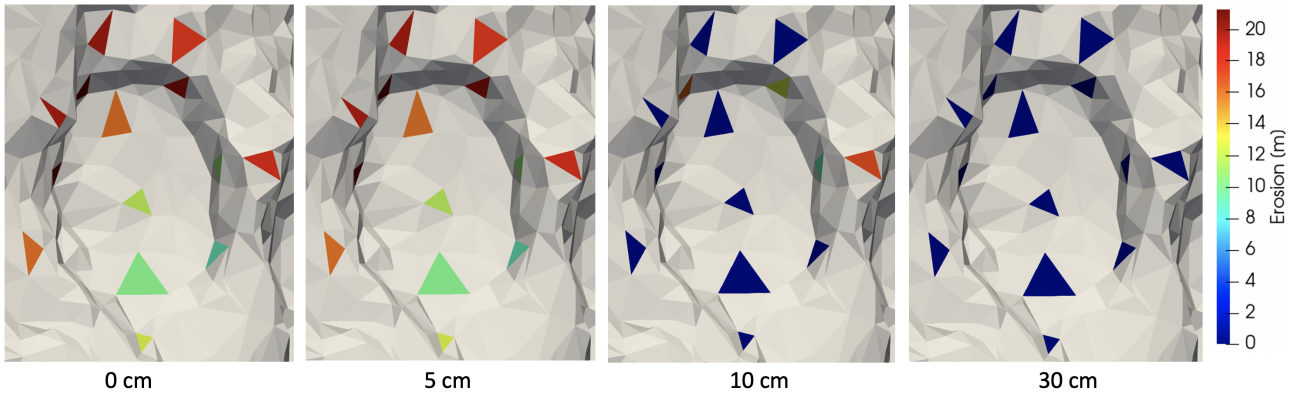

Figure 3.43: Erosion sustained after ten orbits with an initial dust mantle of 0 cm, 5 cm, 10 cm and 30 cm, left to right, respectively

A thin mantle of 5 cm is rapidly removed by cometary activity, while a 10 cm mantle can sometimes quench activity, resulting in the absence of surface erosion. A mantle thickness larger than 10 cm can suppress activity during the full 10 orbital revolutions. These results emphasize the critical role of the dust mantle in setting the level of thermally-induced activity and surface erosion.

3.7 Summary of the main results

Our study of a single pit has provided valuable insights into the significance of initial parameters, and shape effects on the thermal evolution and surface erosion over multiple orbital revolutions. We have thus gained a clearer understanding of the influence of each key parameter, and can make educated hypothesis on the initial values that should be set for further work:

- Local topography plays a substantial role in energy distribution within the pit, with plateau facets receiving nearly twice the energy of walls and bottom facets, indicating the role of considering shadowing. Additionally, an asymmetry is observed in energy distribution along the lateral direction, with facets facing the equator receiving a higher degree of energy near perihelion. Self-heating can be an important additional source of energy in the depths and walls, reaching up to 50% of the total amount of energy within the pit.
- Porosity is a key parameter, with a value of 80% resulting in nearly twice the erosion compared to 60%. Therefore compact areas may behave differently than areas covered in fluffy dust.
- The initial dust-to-ice mass ratio also has a substantial effect on activity, with higher ratios leading to increased activity and erosion.
- Adding CO and CO_2 to the initial composition has a marginal effect on the overall erosion sustained after 10 orbital revolutions. This is because erosion seems to be dominated by water sublimation.
- The thickness of the dust mantle may play a critical role in determining the level of thermal activity and surface erosion: a mantle thinner than $\sim$5 cm is rapidly removed by cometary activity, while a mantle of 10 cm or larger is able to suppress activity, which is consistent with the presence cyclic mantle of few centimeters (Davidsson et al., 2022a).

Beyond these key caveat that we will need to keep in mind, the key take-home message is the following. Regardless of the initial configurations of the nucleus, the erosion achieved after 10 orbits of evolution under current illumination conditions is insufficient to explain the formation of the pit. This indicates that other processes may be responsible for its formation. This raises the question of whether this result is exclusive to the Seth pit, or can be extended to other pits distributed across the 67P's surface. Indeed, different illumination conditions, where the seasons could play a major role in the erosional behavior of each morphological feature, could lead to a different result. Furthermore, pits on 67P display a diversity of shapes and dimensions, resulting in varying local exposition to illumination of the facets. To explore this question, we conduct further simulations of thermal activity on a set of 30 pits distributed on the surface of 67P. To reduce the number of free parameters, we use a uniform set of initial parameters for all the pits, and keep the energy input as the only variable parameter for the thermal simulations, as detailed in the subsequent section.

3.8 Selection of a uniform set of initial parameters

Whether cometary nuclei have homogeneous thermo-physical characteristics remains a topic of debate. Whether any observed heterogeneity is primordial or reflect the past thermal processing of comet nuclei is also a matter of debate. For example, Guilbert-Lepoutre and Jewitt (2011) proposed that heterogeneity can be observed at various spatial scales, potentially stemming from non-uniform initial thermophysical properties, non-uniform insolation, or non-uniform thermally-induced evolutionary processes. As a result, distinct processes associated with non-uniform characteristics may play a significant role in the evolution of a cometary nucleus's interior and surface morphology. However, our goal for this chapter is to model the thermal behavior of the nucleus' surface, arising from the energy received from direct insolation, global and local self-heating, and shadowing effects, alone. Therefore, a consistent of initial values for thermo-physical parameters is needed, which can be used for all facets of interest, regardless of their position on the nucleus. This approximation will not fully capture the localized conditions for all regions of the comet surface, however, it will provide a reasonable estimate for quantifying local and global outgassing, and erosion trends.

- The bulk porosity is set to 75% as it is in good agreement with the different porosity estimates for the bulk of comet 67P reported in previous works (e.g., Herique et al., 2019; Pätzold et al., 2019).

- The dust-to-ice mass ratio is set to 1, the value that has been used historically in modeling the thermal evolution of comets, from the *Giotto* mission measurements at 1P/Halley (see Huebner et al., 2006, and references therein). This value appears to be consistent with ground-based estimates (Kofman et al., 2015) and the *Rosetta* measurements for 67P, within the large range of derived values available in the literature (e.g., Marschall et al., 2020; Choukroun et al., 2020; Davidsson et al., 2022c).

- No CO or CO_2 is included in the ice mixture, to mitigate the possible numerical instabilities. As our results and observations (Hässig et al., 2015) indicate, their absence does not significantly impact the thermal evolution and erosion patterns.

- Finally, a dust mantle is not considered at the beginning of the simulations, because it might not be present in all regions, and typically does not exceed a few centimeters (Davidsson et al., 2022a). Additionally, the formation and destruction of such a layer is a natural consequence of cometary activity, which is fully taken into account in the thermal evolution model.

We use this uniform set of parameters in the next Chapter to investigate the evolution of 30 features (i.e., circular and elongated pits and alcoves) observed on the surface of 67P.

Chapter 4

Thermal evolution of other pits on 67P

4.1 Observation of pits and previous studies

Pits on 67P are mostly located on the northern hemisphere, and are generally concentrated in some regions. For instance, the Maftet geological unit displays irregular-shaped pits of 10 to 20 m deep and 100 to 150 m in diameter (Thomas et al., 2015a). The Seth region is dominated by multiple series of quasi-circular, flat-floored pits (Besse et al., 2015), and contains a pit chain similar to the one observed on Ma'at (Thomas et al., 2015a, see Figure 4.1). It also contains 10–100s of meter-high cliffs, which are also observed in Hathor (El-Maarry et al., 2015). Furthermore, Vincent et al. (2015a) reports the detection of cometary activity in the form of localized dust jets in some of these pits. Additionally, they note that active pits have a high depth-to-diameter ratio compared to inactive ones (Besse et al., 2015). Our study thus specifically considers the following pits: Seth_01, Seth_02, Seth_03, Seth_04, Seth_05, Seth_06, Ma'at_01, Ma'at_02, Ash_03, Ash_04, Ash_05 and Ash_06 (see Figure 1 from Vincent et al., 2015a). We also include additional pits, with similar geomorphological characteristics as the ones studied in Vincent et al. (2015a). We also study cliffs or alcoves (Figure 4.1), as these might be construed as deteriorated pits (Vincent et al., 2015a).

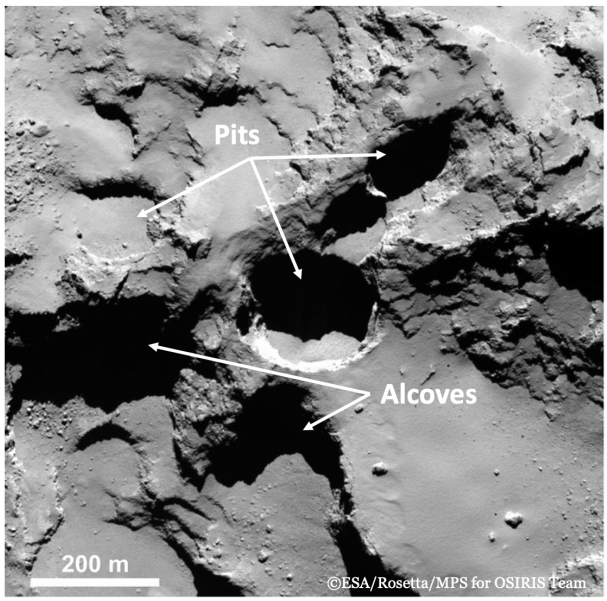

Figure 4.1: OSIRIS/NAC image of a part of the Seth region on which we illustrate the type of depressions we study: pits and alcoves (half circular-pits). ©ESA/Rosetta/MPS for OSIRIS Team.

Consequently, our study focuses on features of at least a few tens of meters in depth, and a few hundreds of meters in diameter: the smallest depth and diameter are ∼35 m and ∼130 m, respectively. In the following, we will indifferently use the term "pit" for the sake of simplicity.

Cometary surfaces are subject to strong erosion and frequent modification due to the sublimation of volatile specis, suggesting that these depressions may be linked to cometary activity. Determining the exact formation process of these depressions remains a challenge (Vincent et al., 2015a). In this chapter, we focus on investigating the evolution and possible formation of pits through outgassing-induced erosion.
Mousis et al. (2015) explored the possibility of forming such structures with phase transitions (i.e. sublimation, amorphous water ice crystallization, and clathrate destabilization). They showed that the time required for producing features of the spatial scale observed by *Rosetta* on the surface of 67P is long, of the order of a thousand years or more, and they require a large scale subsurface heterogeneity. Guilbert-Lepoutre et al. (2016) further showed that the current illumination conditions do not support the formation of pits, as no known mechanism could carve the surface to form pits with a depth of ∼200 m, and a diameter ranging from 100 to 300 m over short timescales. Ip et al. (2016) proposed that pits may have formed through a mechanism operating similarly on many JFCs, which might have occurred before the comets entered the inner Solar System. Finally, Birch et al. (2017) suggest that the outgassing occurring during the recent orbits is likely to lead to a non-uniform erosion, resulting in the transformation of pits into remnants with greater topographic variability. This suggests that outgassing and erosion are unlikely to be the mechanism forming them.

With these arguments in mind, we want to understand how the progressive modification of 67P's surface due to cometary activity might have affected the characteristics of pits and alcoves. In particular, we are interested in understanding whether signatures

of the formation mechanism at the origin of pits can still be found. Our goal is thus to quantify the amount of erosion sustained by pits at the surface of 67P, under the current illumination conditions that periodic, daily and seasonal cycles entail. Based on our modeling method presented in Chapter 2, and applied to the in-depth study of one pit on the Seth geological unit in Chapter 3, we now perform a study of the thermal evolution of multiple pits at the surface of 67P, aimed at understanding the effects of surface energy input.

4.2 Selection of 30 pits for the study

The diversity of local morphological features at the surface of 67P has been recently reviewed by El-Maarry et al. (2019). Most circular depressions can be found in the northern hemisphere, where deep pits and steep cliffs are also observed. Pits in the southern hemisphere are scarcer, typically wider and shallower than the ones found in the northern hemisphere. This dichotomy is explained by the large obliquity of the nucleus (52 °) inducing strong seasons affecting the nucleus, where the southern hemisphere sustains intense heating and erosion during the summer (Keller et al., 2015a). For this study, we select pits with different shapes and dimensions which can be representative of the different illumination conditions at the surface, on both hemispheres and on both lobes, with as much sampling in latitude as possible. We focus on large features, and therefore do not include cometary thermokarst depressions, that represent ground subsidence, provoked by permafrost thawing initiated by ice sublimation (Bouquety et al., 2022).

With these constraints in mind, we have selected 30 pits: their positions on the surface, as well as morphological characteristics such as their approximate diameter and depth, are given in Table 4.1.

We note that not all features are circular or quasi-circular pits. Indeed, we have also selected elongated pits, alcoves, as well as cliffs, in order to achieve our sampling goals, and study possible evolutionary links between those features. We further note that some of the pits selected have shown activity, witnessed by *Rosetta*/OSIRIS (Vincent et al., 2015a). For each pit, facets of the shape model have been selected on the surrounding plateaus, the bottom, and the walls for a detailed study of each energy contribution (direct insolation, self-heating and shadowing), and thermal evolution. One caveat of our method is that we do not account for any shape evolution. Indeed, it is impossible to know what these morphological structures looked like 10 orbits ago, as we still do not know how, when, and through what process they were formed. Therefore, the erosion sustained at each time step is not used to modify the geometry of morphological structures. Instead, erosion after 10 orbital revolutions is assessed from the current shape of 67P's nucleus, as observed by *Rosetta*. A posteriori, we note that the average erosion computed from our simulations remains sufficiently small that this approximation is valid.

Table 4.1: Location and characteristics of the 30 studied pits.

ID	Lat [°]	Lon [°]	R_n [km]	D [m]	d [m]	Hemis-phere	Lobe
1	61	-160	0.936	210	150	N	big
2	53	-159	1.262	150	90	N	big
3	48	-152	1.401	175	130	N	big
4	25	-20	2.262	190	55	N	small
5	35	-153	1.693	210	60	N	big
6	37	-149	1.574	165	85	N	big
7	36	10	1.930	155	50	N	small
8	-12	109	1.570	505	85	S	big
9	24	63	1.128	265	95	N	big
10	53	89	1.203	230	70	N	big
11	26	-14	2.301	185	60	N	small
12	45	5	1.810	130	60	N	small
13	15	-135	1.758	370	120	N	big
14	19	-129	1.414	345	80	N	big
15	25	-123	1.085	240	85	N	big
16	48	-133	1.064	135	50	N	big
17	29	-10	2.314	205	55	N	small
18	53	-139	0.950	265	165	N	big
19	64	-154	0.967	220	125	N	big
20	16	-146	2.137	275	105	N	big
21	17	-148	2.284	140	40	N	big
22	18	-154	2.350	210	35	N	big
23	37	-167	2.072	380	115	N	big
24	-36	121	1.353	355	80	S	big
25	-36	167	1.463	685	80	S	big
26	30	143	1.900	655	90	N	big
27	16	109	1.660	290	90	N	big
28	-63	-143	1.602	215	100	S	big
29	65	122	1.548	165	60	N	big
30	14	99	1.589	240	80	N	big

R_n: average distance to the center of mass of the shape model; D and d: approximate diameter and depth of the depression, respectively.

All facets selected for our study can be localized on the 3D shape model (Figure 4.2 top panel) and a 2D map of the high resolution shape model in an equidistant cylindrical projection (Figure 4.2 bottom panel). We note that this map is based on a 12 million facet version of the SHAP7 shape model: we created a "rubber sheet", or a stretchable surface, by putting each vertex point at an elevation proportional to its distance from the comet center above the plane of evenly spaced latitude and longitude. Shading was then realized through 3D rendering. The equidistant cylindrical projection cannot display the overhung

areas, however we do not study any such feature here. We note that sophisticated map projections that do display the complete surface of the comet have been presented, (e.g., Grieger, 2019; Leon-Dasi et al., 2021).

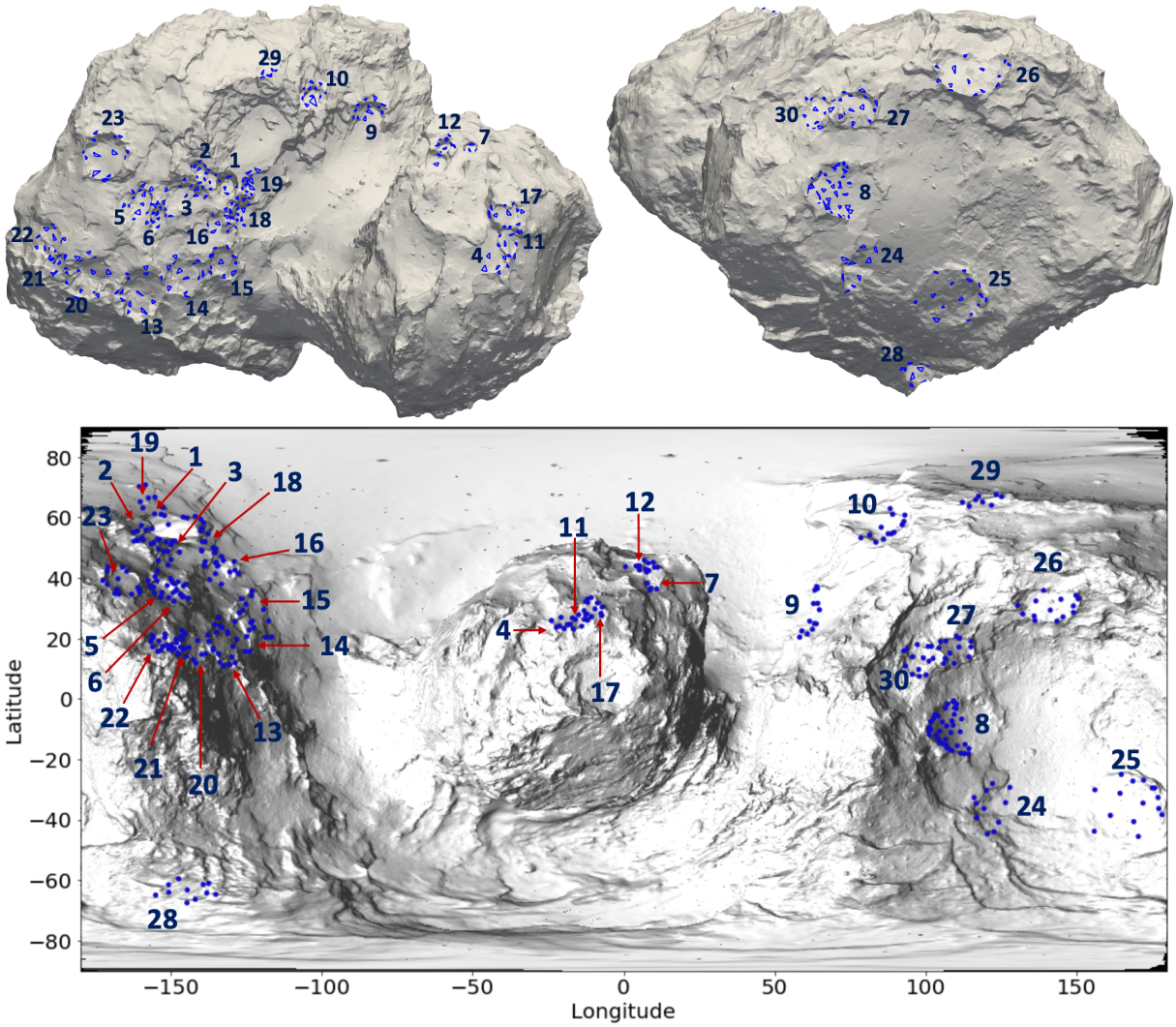

Figure 4.2: Top: Location of the facets selected for the study of the 30 pits on the surface of 67P. The shape model presented is the SPG model composed of 124,938 facets (Preusker et al., 2017) and used for the surface energy calculation. Bottom: Location of the facets selected for the study of the 30 pits on the surface of 67P. The 2D map is a projection of the high-resolution SPG shape model composed of 12 million facets.

4.3 Evolution of the pits over 10 orbits

In this study, as we seek to quantify how energy received at the surface – through direct insolation, local and global self-heating and shadowing effects – may give rise to morphological features of the spatial scale observed by *Rosetta*, we use a set of initial values for the thermophysical parameters, such that the same set can be used for all facets, on all our morphological features of interest, regardless of their location on the nucleus. These might not be representative of all the local conditions, for all features studied, but are a good-enough approximation to quantify local and global trends in the erosion rate. In the remainder of our study, we therefore consider the set of initial parameters used in Chapter 3 for the study of the specific pit located in the Seth region (Pit 5 in this chapter).

4.3.1 Energy received at the surface: general trends

The energy input at the surface is computed for the 380 studied facets, taking into account the effects of shadowing and self-heating on both local and global scale. We show in Figure 4.3 two quantities related to the energy input at the surface of 67P: the total energy integrated over one orbit, and the maximum energy flux received by each of the 380 facets. The maximum energy input is typically reached at perihelion for facets in the south, or just before perihelion for facets in the north. These two quantities were found to be essential to interpret the results of the thermal evolution model. Indeed, we see that the greatest amount of thermal processing – inducing substantial water ice sublimation and erosion – occurs during the perihelion passage, when the nucleus receives most of the direct solar energy on the southern hemisphere. As a result, the maximum energy is representative of this seasonal activity trend, and the maximum energy map does show the expected north-south dichotomy.

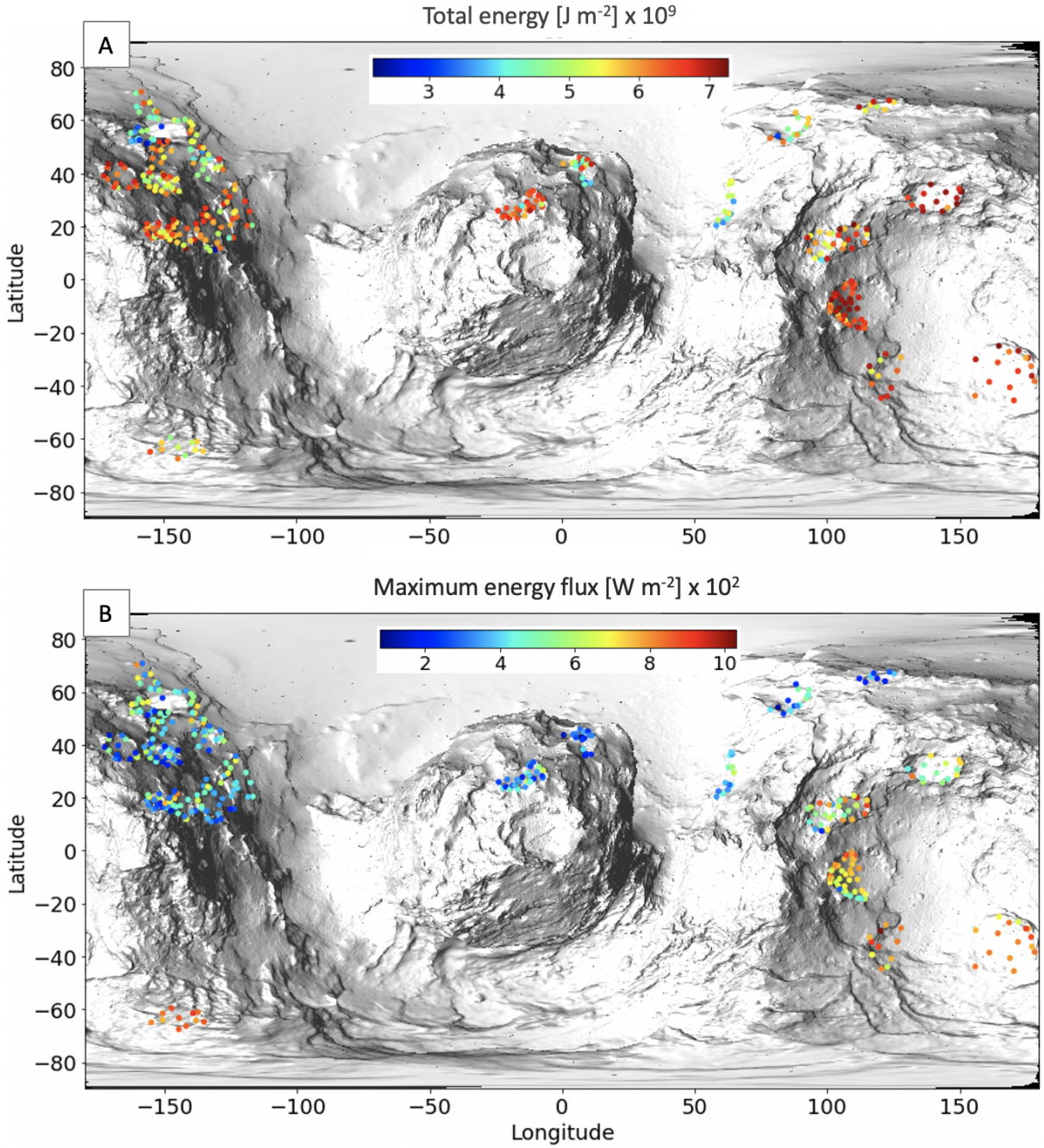

Figure 4.3: Energy flux received at the surface for all 380 facets, distributed over the 30 studied pits. Panel A gives the total quantity integrated over one complete orbit of 67P; panel B gives the maximum reached during the perihelion passage.

We categorized pits based on their location on the nucleus of 67P and identified distinct clusters in terms of surface energy input at perihelion and erosion. This allowed us to summarize the main latitudinal trends we observed, as shown in Figure 4.4. The southern hemisphere, which receives the highest peaks of energy during summer, exhibits the most erosion. The second highest erosion values are observed on facets situated near the equator, specifically at latitudes less than 20°. These regions receive significant energy

peaks. Lastly, high-latitude facets, whether on the large or small lobe, tend to erode the least and generally receive lower amounts of energy.

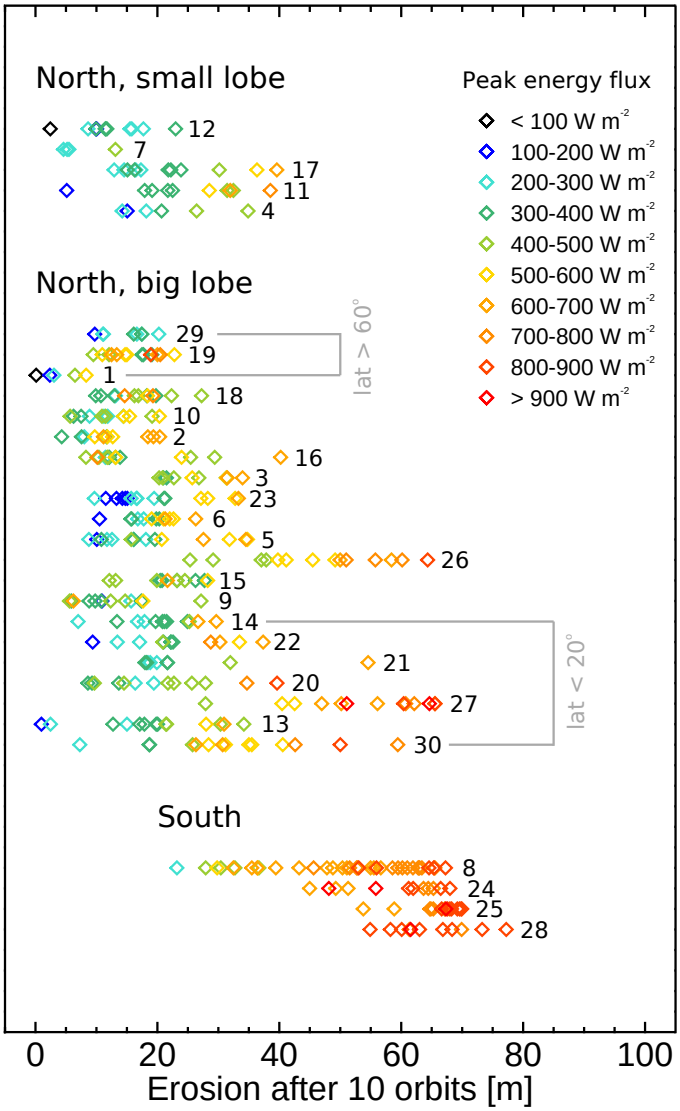

Figure 4.4: Erosion sustained by facets of all studied pits after 10 orbital revolutions.

However, we see from Figure 4.5 that a similar final amount of erosion can be achieved either by having a high amount of energy at or close to perihelion, or by having an increased amount of energy integrated over one orbit. As a result, we find facets in the north that can display some significant activity, out of the perihelion passage. This is due to the relatively high obliquity of the nucleus ($\sim 52°$, Sierks et al., 2015). For those facets, considering the amount of energy received over the whole orbit is usually necessary to describe their thermal behavior. This is reflected in the lack of clear north-south dichotomy in the integrated-energy map (see Figure 4.3), as the northern hemisphere receives direct solar energy outside of the perihelion passage. However, we also see that for the same value of the integrated energy, facets that receive the bulk of the energy at perihelion tend to erode more (Figure 4.5).

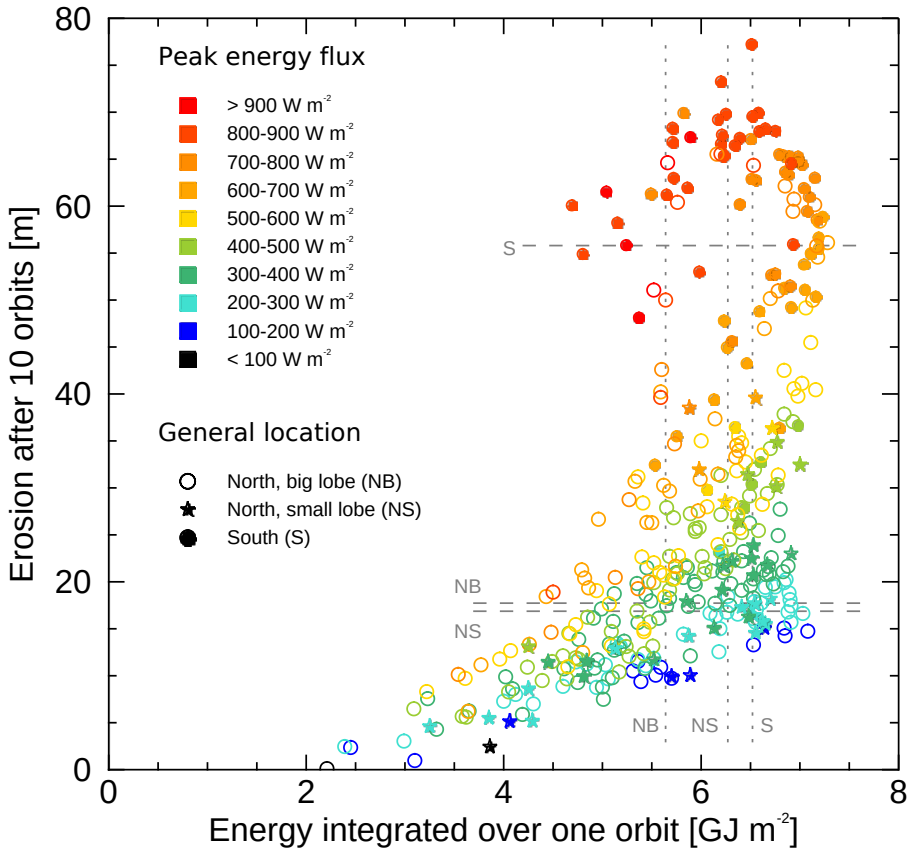

Figure 4.5: Erosion sustained at each facet as a function of the energy they receive, integrated over one orbit. Gray dotted lines show the median of this energy for the large regions, i.e., the small and big lobes on the northern hemisphere, and the southern hemisphere. Gray dashed lines show the median of erosion sustained by facets in these regions. The color code indicates the peak energy received at or close to perihelion.

These trends should be considered as a first order approximation rather than an absolute rule, as we can see from the complex erosional behavior resulting from the energy received at the surface (Figure 4.5). Furthermore, while the peak of surface temperature, shown in Figure 4.6, aligns with the north-south dichotomy trend, the differences between the northern and southern hemispheres are not significant, as surface temperature is greatly influenced by physical processes and sublimation occurring in the subsurface. This emphasizes the importance of accounting for the physical processes occurring at depths in the nucleus subsurface layers. Therefore, it is necessary to use a full subsurface thermophysical model, as we do below, rather than simply assessing the thermal behavior from surface energy balance maps.

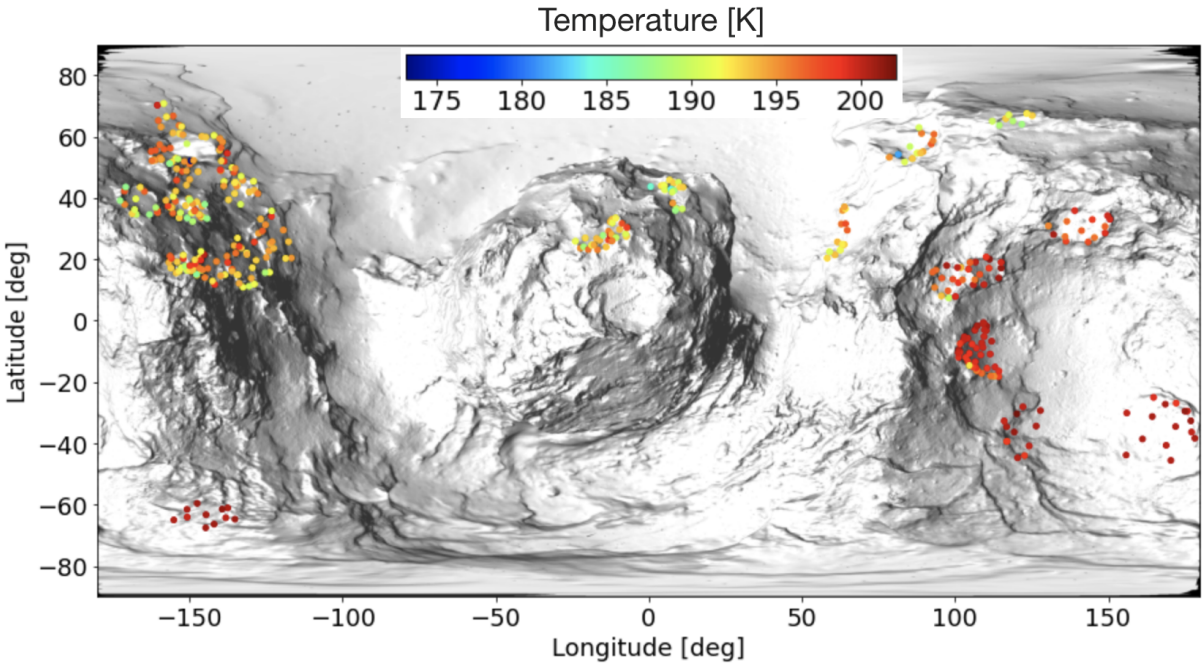

Figure 4.6: Maximum surface temperature reached at the surface for the 380 facets, distributed over the 30 studied pits.

Seasonal variations are the primary driver for the energy distribution on 67P's surface. Due to the high obliquity of the nucleus, its southern hemisphere receives more energy than the northern hemisphere. Both the total energy received over the orbit and the energy peak are crucial information for understanding the local behavior in terms of erosion.

4.3.2 Effects of local topography and global shape

Seasonal effects largely dominate the distribution of energy at the first order, whether it is in the form of the integrated amount or the maximum rates. However, we observe some variations at the level of specific latitudes and within individual morphological features, which can be attributed to shadowing and self-heating effects. Shadows are cast at the surface of 67P on a large scale (e.g., the neck area between the two lobes), as well as on a small, topographic scale (e.g., the bottom or part of the walls of deep circular pits), as we can see in Figure 4.7. Facets in the pits depths receive very low energy compared to the ones situated at the surrounding plateaus. Shadowing effect can induce a significant decrease of the energy input, by as much as 70% depending on the facets' location and orientation.

The effect of shadows can however be slightly offset by self-heating from neighboring facets (Figure 4.8). For most pits, self-heating contributes to less than 20% of the total energy received at the surface. Thus, direct insolation dominates the energy input, and self-heating is not the main activity driver. However, for several complex topographic configurations, where facets are not easily reached by direct insolation, self-heating can

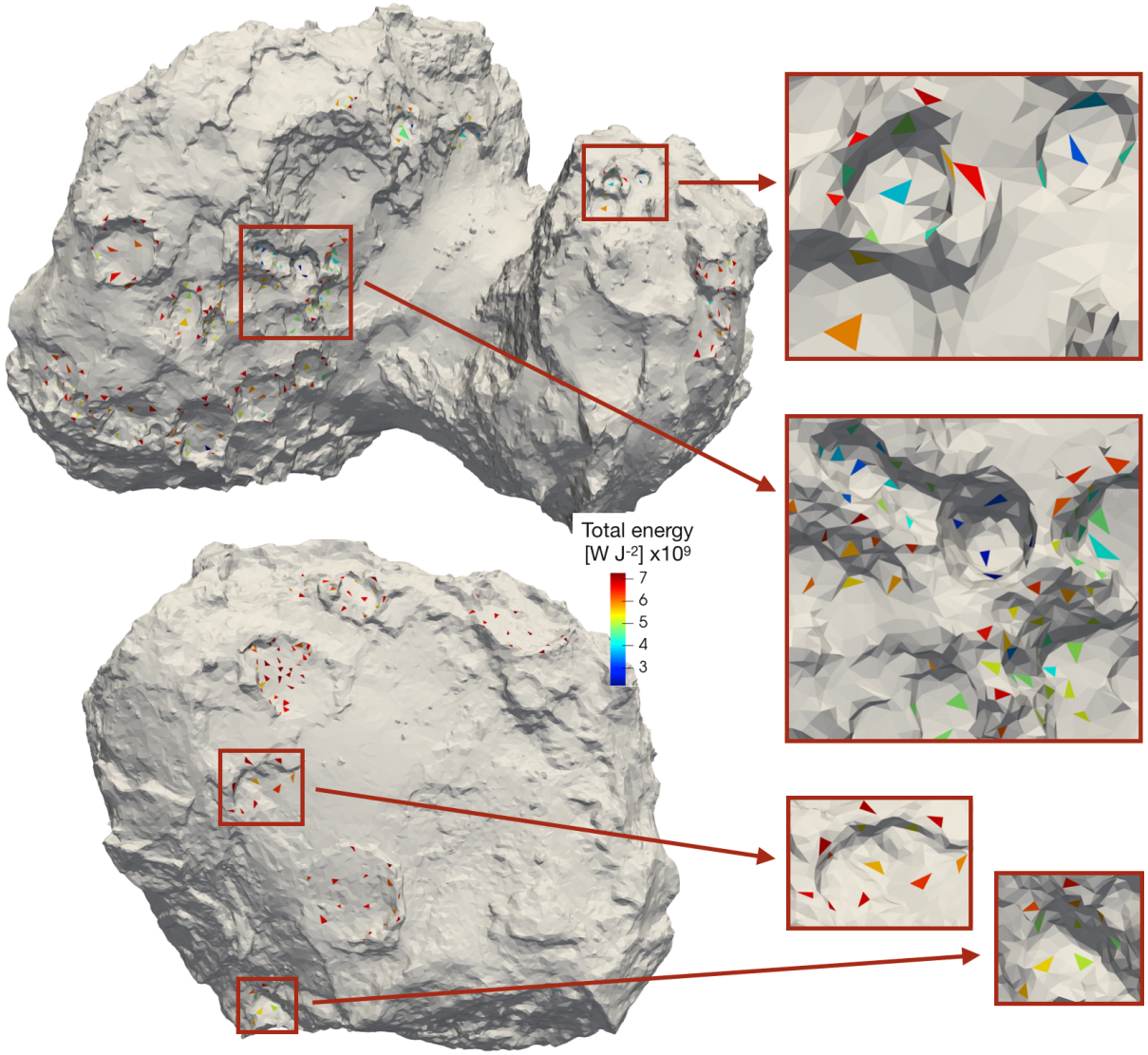

Figure 4.7: Total energy integrated over one orbit received by all facets of the 30 pits.

exceed the contribution from direct insolation. For these specific facets, the contribution of self-heating can reach more than 60% of the total energy received at the surface (Figure 4.8). They are typically located on the walls and at the bottom of deep circular pits. On a larger spatial scale, we also find such facets on alcoves close to the neck region, which are periodically in the shadow of the small lobe, and thus receive self-heating from it.

For the sake of completeness, we seek to quantify the relative contributions of the local topography vs. global morphology of the nucleus to the amount of self-heating. We thus compare the energy input for some facets of the shape model, and the energy input of the same facets when we numerically remove the small lobe from the shape model. This comparison is most informative for features 18 and 19 (a.k.a. Seth_05 and Seth_04 respectively). These are two alcoves located close to the neck area, whose evolution is extremely affected by the presence of the small lobe. The integrated energy received over

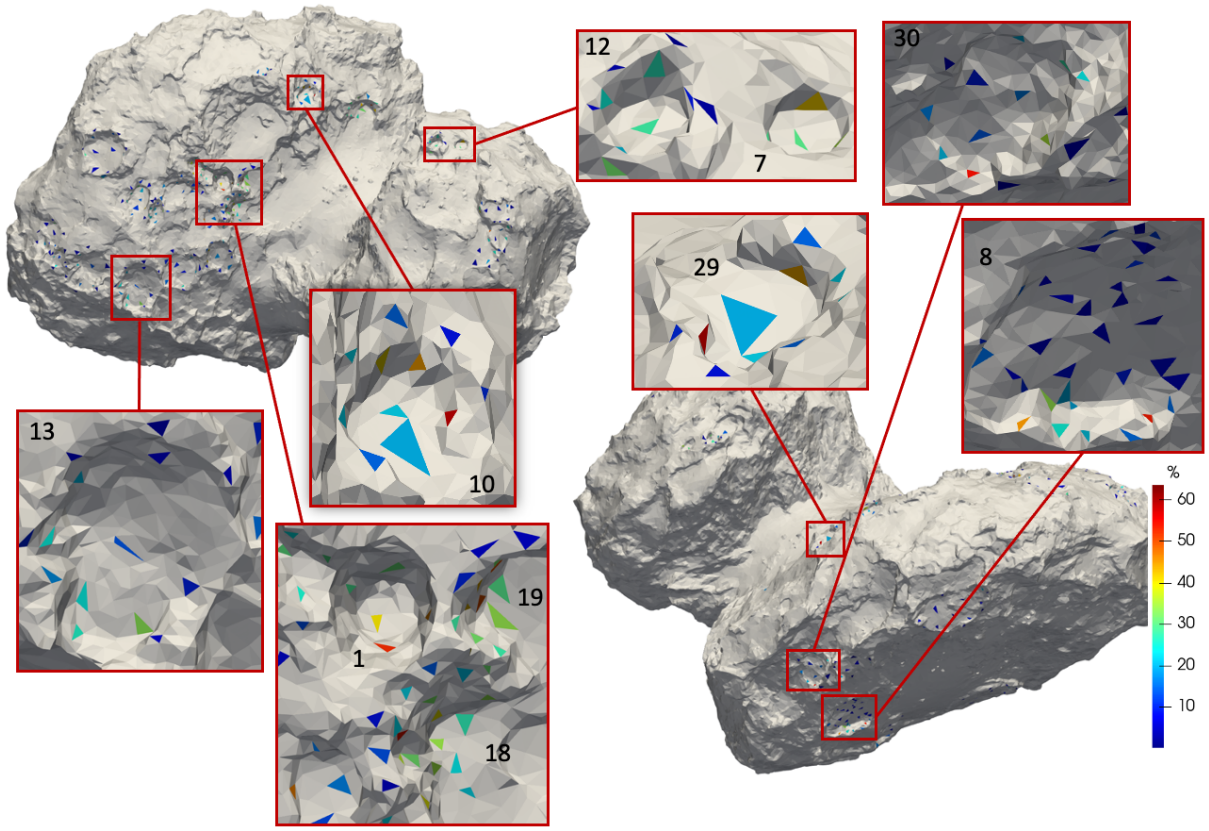

Figure 4.8: Fraction of energy input from self-heating relative to the total energy received. We highlight some examples where the self-heating contribution is significant.

one orbit, with and without the small lobe in the shape model, is given in Figure 4.9 (panels A and B). Facets on the alcoves receive up to 70% more energy when the small lobe is absent, due to the direct insolation reaching them. A detailed look at the various energy contributions informs us that the decrease in energy input from self-heating is not as significant as expected. For facets located at the bottom of those alcoves, direct insolation becomes the dominant source of energy as expected, though self-heating does not drop to 0. For one facet, there is even a slight increase in the self-heating contribution (∼7%). This is due to the fact that surrounding facets receive much more direct insolation, hence can transmit more energy. Overall, the contribution of the small lobe (vs. local topography) to the input of self-heating is not dominant (see Figure 4.9). The small lobe contributes to up to ∼22% of the total energy received by features 18 and 19. This is almost half of the total self-heating contribution for these alcoves, located in a region of the nucleus where the global contribution is maximum. However, in other regions, local topography is the major source of self-heating.

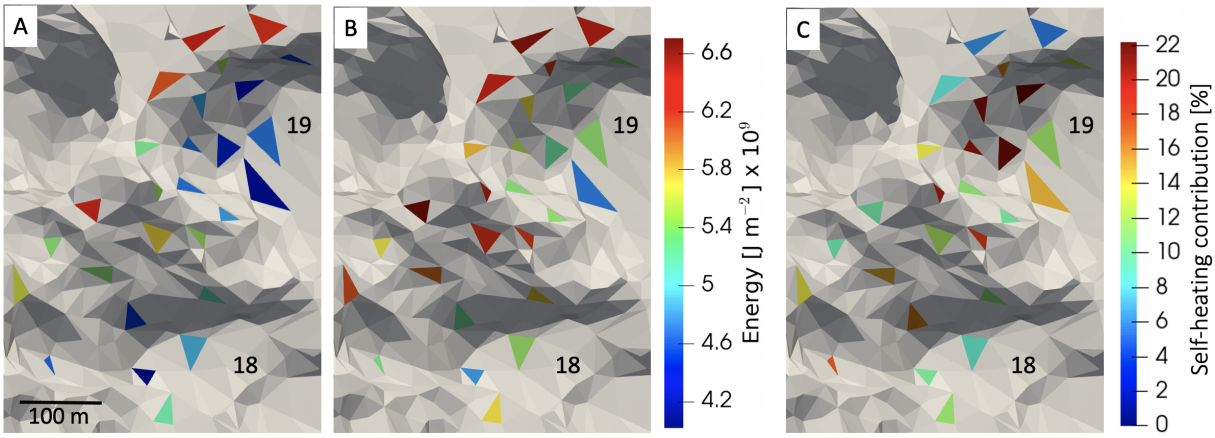

Figure 4.9: A and B: energy received at the surface of alcoves 18 and 19 integrated over one complete orbit with and without the small lobe in the shape model, respectively. C: contribution of self-heating received from the small lobe only to the total energy received at the surface of alcoves 18 and 19.

Direct insolation remains the dominant heat source, affecting the energy distribution and thus the surface erosion, despite occasional variations due to global shape and local topography effects. In specific cases, shadowing can reduce illumination by up to 70%, and self-heating may contribute up to 60% of the total energy received by a facet.

4.3.3 Thermal evolution simulations and surface erosion

The energy received at the surface of each facet, with the global distribution and trends described above, is the boundary condition for thermal evolution simulations performed over 10 full orbital revolutions. This energy input is used to quantify the activity for each facet: phase transition, gas and dust production, dust mantling, and erosion. To keep our model relatively simple: we use a uniform set of initial parameters for each facet, and we do not account for any influence of shape evolution on the illumination conditions during the thermal simulations, i.e., erosion sustained at each time step is not used to modify the geometry of the morphological features of the shape model. Instead, erosion after 10 cometary orbits is assessed from the current shape of 67P's nucleus, as observed by *Rosetta*.

The behavior of surface temperature, gas and dust production rates through the orbits, is consistent with what has been discussed during the study of the Pit 5 in Chapter 3. As such, this chapter will solely focus on the end result of the pits activity. Our main interest lies in the final erosion and the speed at which these features evolve, and whether they could have formed under the given conditions, through this process. Global results of the erosion achieved after the 10 orbits, obtained for the 380 facets across 30 pits and alcoves on the surface of 67P, are represented in Figure 4.10.

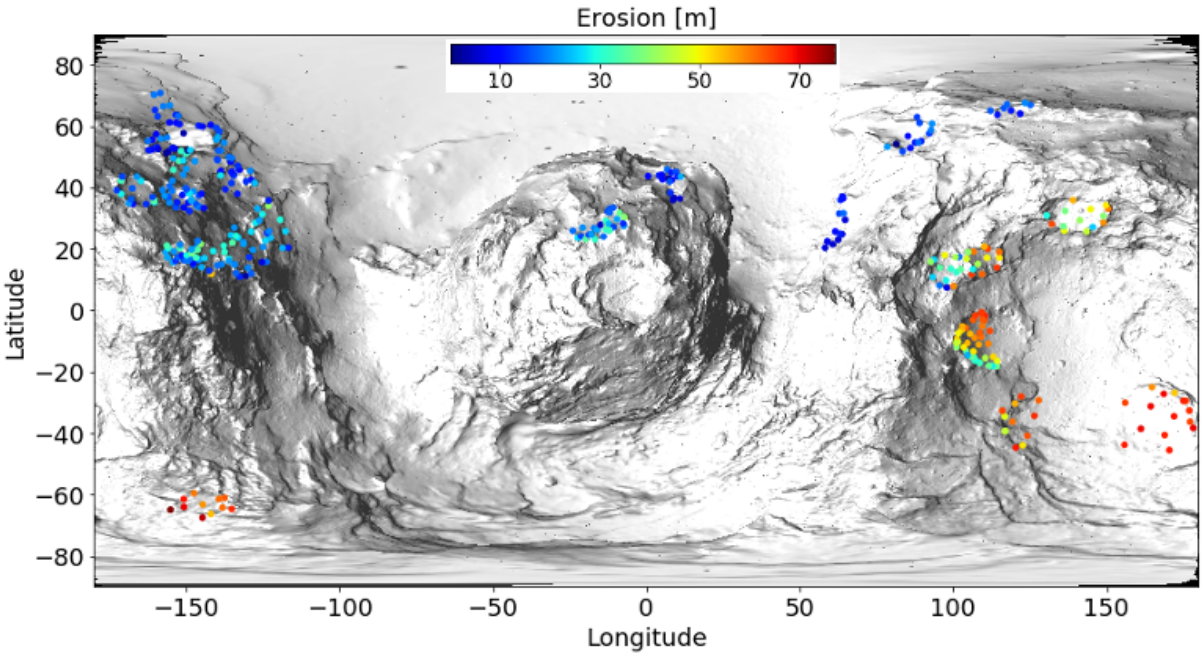

Figure 4.10: Erosion sustained after 10 revolutions on 67P's current orbit for all the 380 facets.

4.3.3.1 Latitudinal variations

We see from Figures 4.3 and 4.10 that erosion at the surface is mostly correlated with the energy received at or close to perihelion. A stark contrast is observed between both northern and southern hemispheres. After 10 orbital revolutions, erosion can reach up to ∼77 m in the most active, southern regions in our study. In contrast, it does not exceed ∼30 m for most northern features. We see that facets directed towards the equator, while in the northern hemisphere, sustain enhanced erosion compared to other facets at the same latitude. For those, it can reach the same level of erosion as seen in the southern hemisphere. As a consequence of the trends in the surface energy distribution described previously, the pattern of latitudinal variations for erosion is clearly observed. Indeed, the amount of erosion after 10 orbits decreases as the facets are located closer to the north pole. In the northern hemisphere, facets sustaining the most erosion are those closest to the equator, or perpendicular to the equatorial plane, as they receive direct insolation around successive perihelion passages.

It is also observed to be highly correlated with both the total amount of water flux generated by the activity throughout the 10 orbital revolutions and the peak rates (reached close to perihelion), as we can see from Figures 4.10 and 4.11. This highlights the direct link between the high outgassing episode, that is observed to consistently occur at one episode close to perihelion (largest amounts), and the main part of erosion, which is also observed to suddenly occur with important amounts at the same period (see Chapter 3).

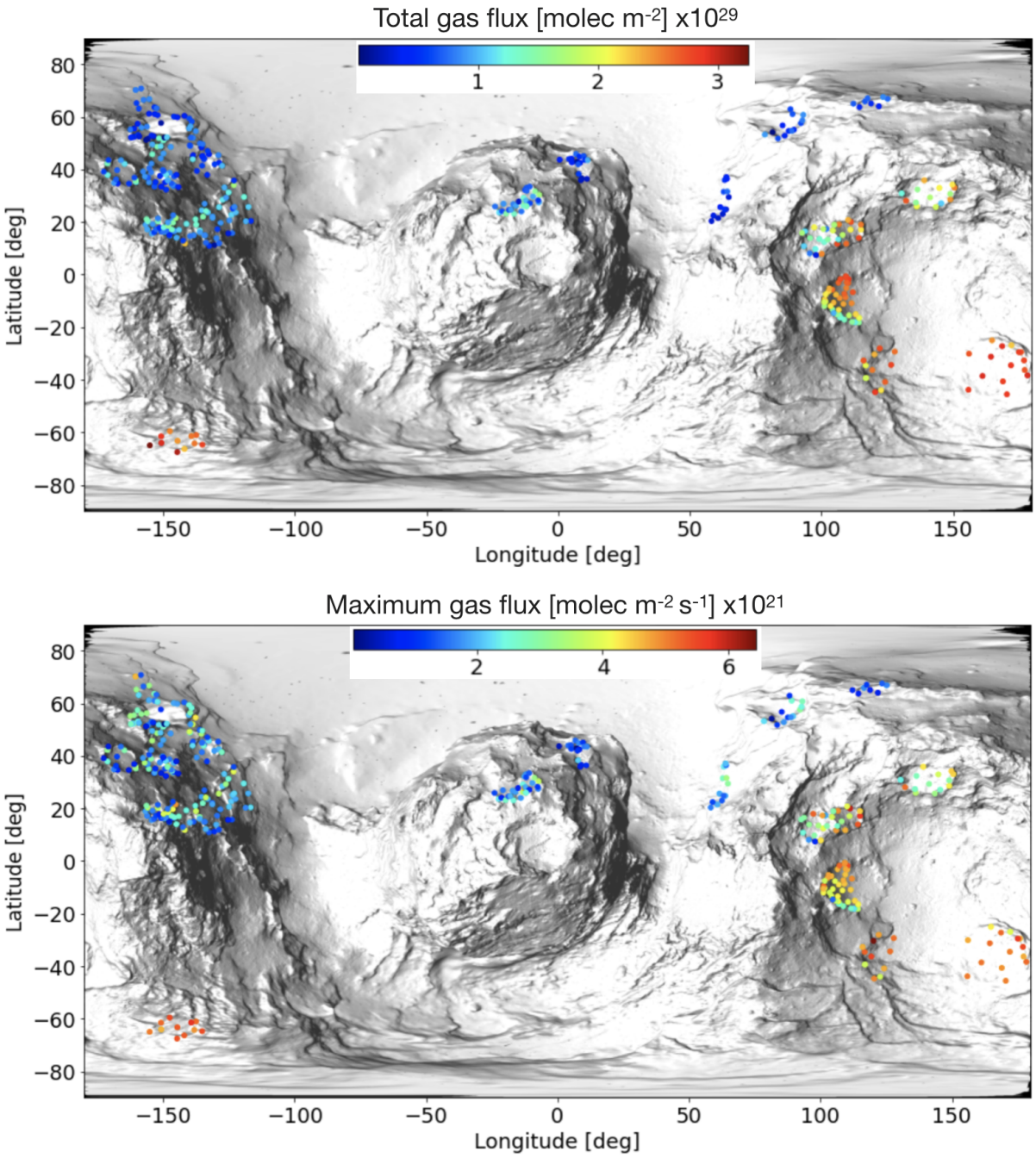

Figure 4.11: Water production rates of the 380 facets of the 30 studied pits. Upper panel: total water gas quantity integrated over one complete orbit of 67P; lower panel: maximum production rate achieved near the perihelion passage.

The total amount of dust integrated over the 10 orbital revolution displays the north south dichotomy as well, but the peak of dust flux does not show the same trend (Figure 4.12). Some facets in the northern hemisphere and near the equator exhibit the highest dust flux peaks, while these facets are not the most highly eroded ones. In fact, this observation is consistent with results in Chapter 3, where dust peaks can occur at

different times of the orbit. This illustrates the complex interplay between sublimation and dust mantling: dust may accumulate at the surface while subsequent activity may result in the removal of this recently build dust mantle. Peaks of dust activity may not result in significant net erosion.

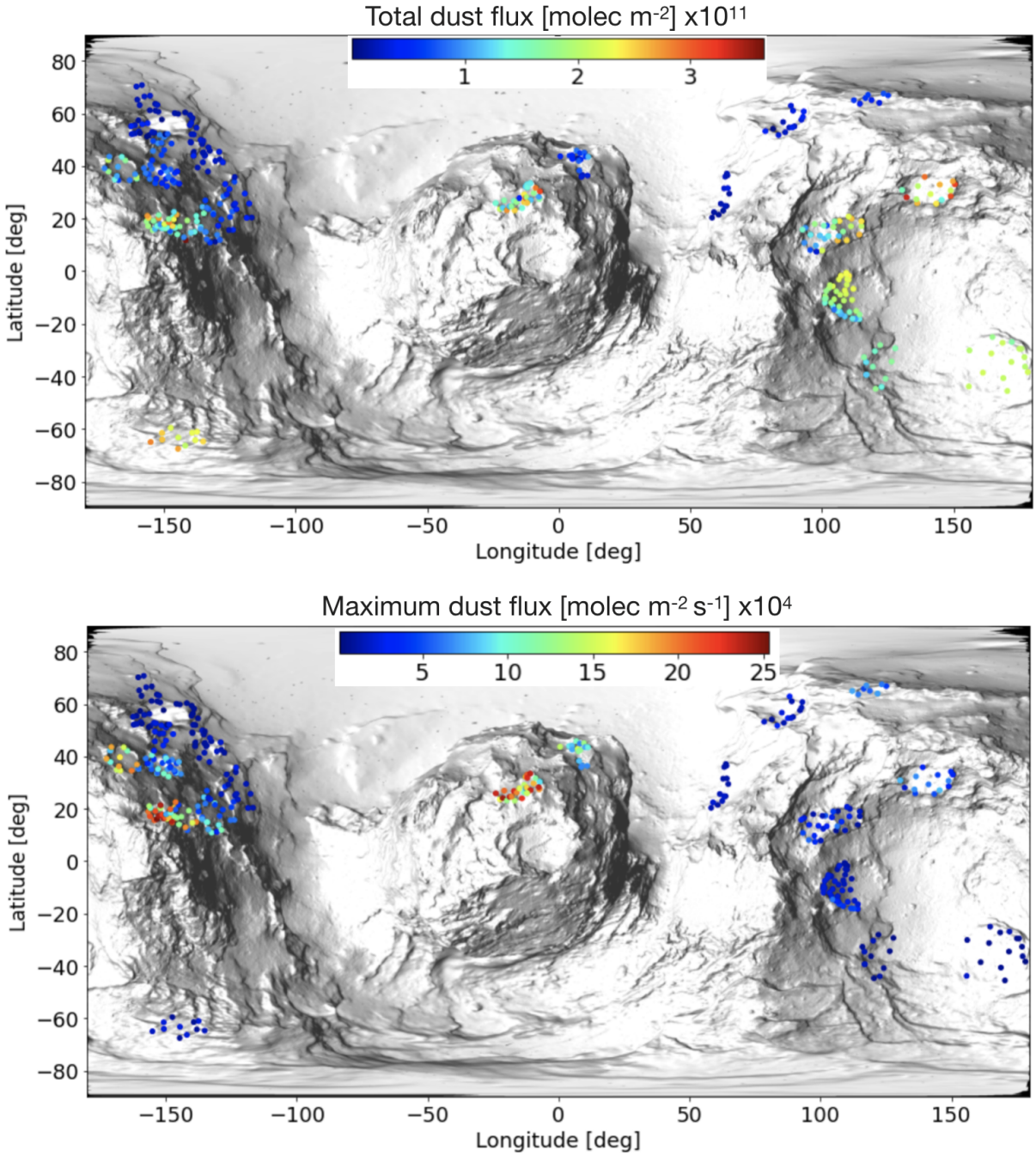

Figure 4.12: Dust production rates of the 380 facets of the 30 studied pits. Upper panel: total amount of ejected dust, integrated over one complete orbit of 67P; lower panel: maximum production rate achieved near the perihelion.

Erosion achieved after 10 orbital revolution displays a clear north-south dichotomy, which is strongly correlated with the seasonal patterns of energy distribution and outgassing.

4.3.3.2 Local variations

At the first order, the latitudinal pattern of erosion dominates, which is a direct result of seasonal trends described above. However, these trends are mitigated in some parts due to the complex topographic shape of 67P's nucleus, which induces local shadowing and self-heating. Furthermore, at the scale of each studied feature, there are some local trends, that appear to be similar across the surface.

The first trend observed at the scale of a pit is that erosion is generally more intense on the plateaus surrounding the pits that are exposed to the Sun (except when they are subject to shadowing on a larger scale). In contrast, the bottoms of these pits do not sustain as much erosion, even after 10 full orbital revolutions. This is especially true for circular pits with high depth/diameter ratio (e.g., pits 1 or 2, a.k.a. Seth_01 and Seth_02 with Seth_03 combined, respectively, and pit 12, a.k.a. Ma'at_01). This general behavior tends to erase the local topography and leads to shallower features, as those observed in the southern hemisphere. Also, in general, the walls of the pits experience some differential processing, with erosion enhanced along a specific direction (e.g., features 1 or 5 in Figure 4.13). This is directly related to the asymmetric distribution of the input energy, especially when some facets receive direct insolation while others mostly get only a self-heating contribution. This suggests that, if we account for the shape evolution due to erosion, elongated pits as observed today are more thermally-processed than small circular ones. As a consequence, our results are consistent with deep, circular or quasi-circular pits, such as labeled 1 (Seth_01 on the big lobe) and 12 (Ma'at_01 on the small lobe) in our study, being the least processed of pits, or the best preserved under current illumination conditions.

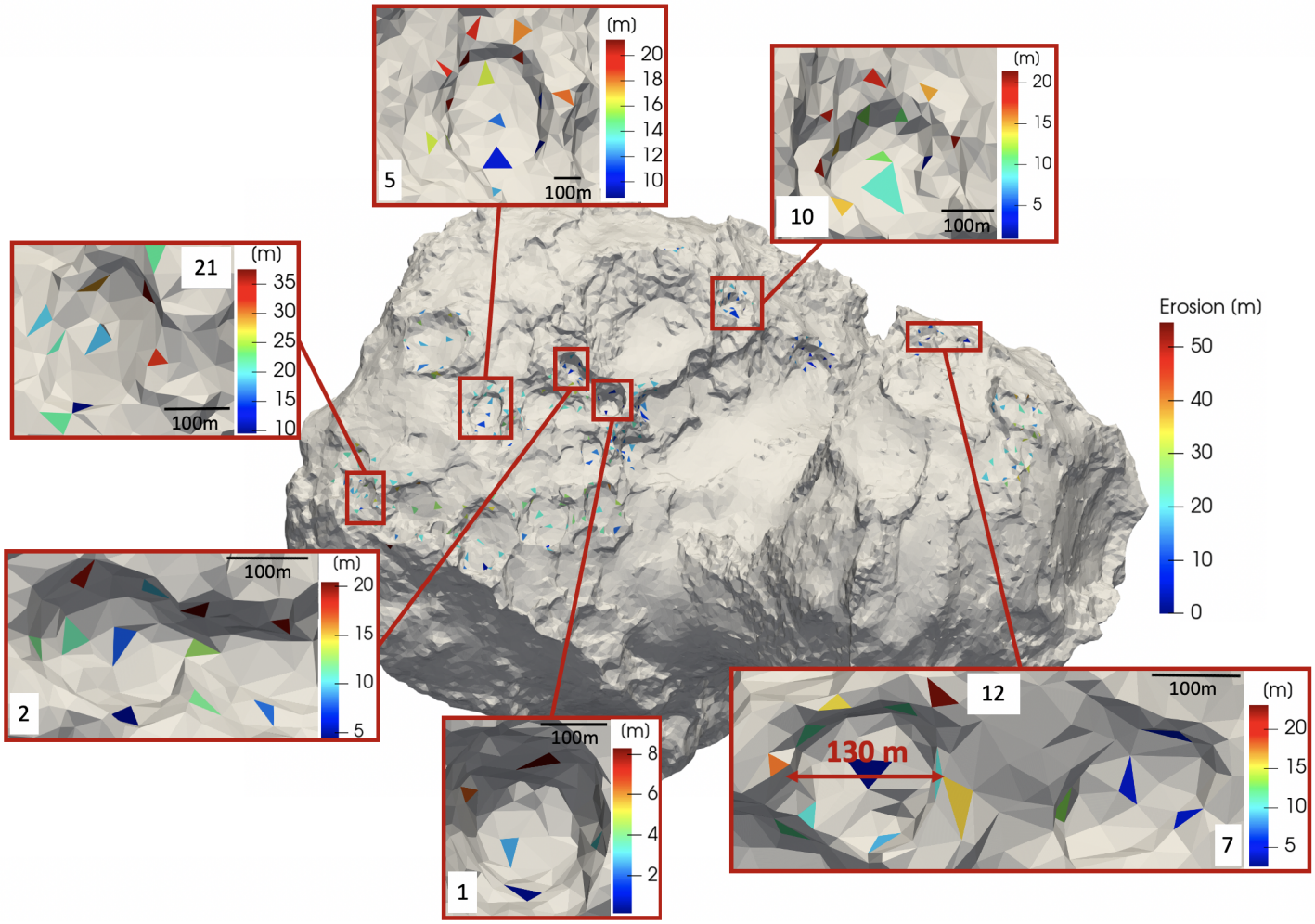

Figure 4.13: Local examples of erosion achieved after ten orbits on the surface of all the facets of the 30 studied pits, highlighting differential erosion (e.g., 5, 21) and flattening patterns (e.g., 10, 5, 12).

Figure 4.14 provides a detailed representation of the local erosion trends for the 30 studied features.

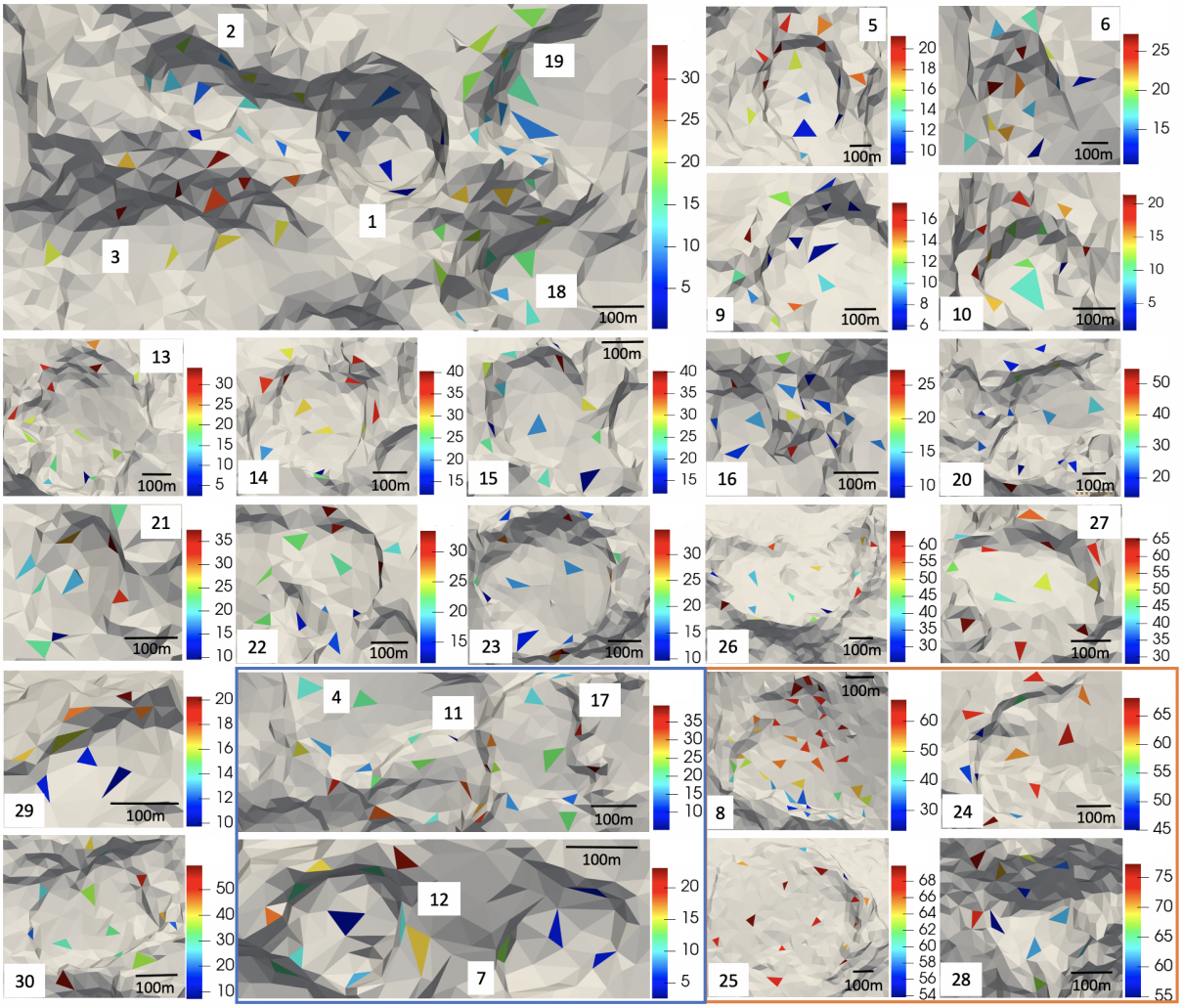

Figure 4.14: Erosion [m] achieved after 10 orbital revolutions, for all facets of studied depressions. The blue box contains depressions located in the small lobe, the orange box contains the big lobe's southern depressions, and the remaining features are located in the northern hemisphere of the big lobe.

> Throughout their evolution, pits and alcoves generally become shallower and larger rather than deeper, and exhibit an elongation trend rather than maintaining a circular shape.

4.3.3.3 Can erosion be at the origin of pits?

Following the thermal evolution of pits over 10 orbits (the estimated duration of the comet's exposure to current illumination conditions, Maquet, 2015), we found that the final erosion achieved is significantly lower than the dimensions of the morphological

structures. In fact, erosion did not reach the observed dimensions of any of the identified features. For instance, the smallest feature in our study: pit 12, also known as Ma'at_01, has an average size of ∼130 m (see Table 4.1) and would only experience a diameter increase of 10 to 15 m after 10 orbits as a result of erosion. Erosion does not exceed ∼77 m even in the most active facets, located in the southern hemisphere. Furthermore, it has been observed that the erosion of pit plateaus, which receive the most direct sunlight, is more significant compared to the walls and bottom of the pits, which are more prone to shadowing. As a result, the plateaus erode more quickly, followed by the walls, and then the bottom. This sequence of erosion makes the pits on comet 67P become progressively shallower and wider over time, as a result of activity, rather than deeper.

From these results, we confirm that progressive erosion alone cannot account for pit formation on 67P's surface. While it is clear that erosion plays a role in shaping the surface, other processes are likely involved as well.

> Erosion resulting from thermal activity under current illumination conditions is largely insufficient to carve pits observed on 67P's surface. Moreover, erosion tends to make pits shallower and larger over time: eventually, cometary activity tends to erase them.

4.4 Discussion

4.4.1 Shape effects on local and global scale

Despite the clear seasonal trends, our results show that the local topography, and the complex global shape of the nucleus, can considerably impact the energy balance at the surface (Section 4.3.2). This is particularly true when considering the different sides of a given pit. As a result, some walls and bottoms of pits are not as easily reached by insolation as the corresponding exposed plateaus, making the onset of activity in the inner parts of these morphological features more difficult. It is thus necessary to take into account the effects of both shadowing and self-heating at the scale of such features. These processes are also important at the scale of 67P's nucleus, because its specific bilobate shape leads to the neck region being highly shadowed during the northern day. While self-heating is found to be mostly negligible compared to direct insolation for most facets we studied, it can be an important energy source in some cases, especially at the bottom of pits and around the neck region, where direct insolation is limited. In such locations, the contribution of self-heating to the local energy balance can reach up to 60%. These results are consistent with earlier studies. For instance, Keller et al. (2015a) showed that self-heating could reach 50% of the total energy received in some areas of the neck region. Macher et al. (2019) also showed that, even though the average contribution of self-heating in the regions they studied was evaluated to 1% of the direct insolation, it can be enhanced in rough areas not reached by direct insolation. In these locations, it could reach as much as 50% of the direct insolation contribution. The important contribution of self-heating was also emphasized by Tosi et al. (2019), for deriving the temperature map at high spatial resolution (<15 m) from VIRTIS-M (the Visible InfraRed Thermal

Imaging Spectrometer) data. The aforementioned studies have been performed using various resolutions of 67P's shape model, which suggests that shadowing and self-heating are important at all scales. Therefore, the results of our study are not very sensitive to the choice of spatial resolution for the shape model: using the 125k-facet shape model, with an average distance between nodes of about 20 m (Marshall et al., 2018), allows to sample morphological features without increasing the computation time required if smaller facets were chosen. Overall, a detailed knowledge of the energy balance at the surface on a local scale is thus a necessary condition to quantify the effect of thermally-induced processes on the evolution of the cometary surface. However, as discussed below, we find that it is not sufficient to understand the evolution of the surface, since the energy input does not translate into phase transitions and erosion in a straightforward manner.

4.4.2 Erosion trends on 67P's surface

Our results show a strong correlation between the energy amount received close to perihelion, the outgassing peak, and the final erosion, with the southern hemisphere being the most actively eroded region. Indeed, the highest rate of erosion occurs during the peak of degassing, which is driven by the significant increase in energy near perihelion. Erosion reaches up up to ∼77 m (Figure 4.10) in the most eroded southern facets. The facets located near the equator experience moderate erosion, while the northern pits erode the least, with erosion depths of up to ∼30 m, which is less than the half of erosion values achieved in the south. This implies that, at first order, it is the obliquity that shapes the cometary surface. This results reaffirms results from (Keller et al., 2015a) which showed a distinct north-south dichotomy in the erosion of 67P (see Figure 11 of their paper).

At the local scale, we have shown that plateaus erode more than walls and bottoms since they are more exposed to solar illumination. Therefore, cometary activity tends to erase surface features, so that deep, circular pits are likely the least processed morphological structures on the surface. This result reinforces the findings by (Vincent et al., 2015a), which, through an analysis of pits morphology on 67P, suggest pits expand gradually after their formation. Additionally, a differential erosion in a lateral direction is observed, causing pits to get elongated as a result of sublimation-driven erosion. Clearly, these pits could not have been formed by sublimation-driven erosion. We have investigated very different illumination conditions across 67P's surface. Under these conditions, the patterns of differential erosion, and the preference for eroding plateaus rather than bottoms of pits, are maintained. Therefore, we can extrapolate that different illumination conditions on a different orbit would have led to similar trends. Furthermore, even if the southern hemisphere is obviously more processed than the northern hemisphere, traces of larger depressions can be found, and there is no clear latitudinal dependence of the distribution of depressions (Vincent et al., 2015a). Stretching on our results, we could argue that pits were initially present on a global scale, and they likely evolved due to sublimation-driven erosion at various degrees on the surface of 67P.

4.4.3 Erosion with non-uniform properties

The erosion rates are considerably low compared to the pits dimensions. In the southern regions, where sublimation-driven erosion is most effective, erosion does not even reach ~80 m (Figure 4.10), while the pits diameters range from 130 m to more than 500 m (see Table 4.1). This demonstrates that the current illumination conditions are unable to account for the formation of deep circular pits, such as observed by *Rosetta*. But how would initial structural and compositional parameters used in our thermal evolution model influence this outcome?
For instance, an increased porosity could result in larger amounts of erosion, as much as 50% for facets that receive the most energy as seen in the previous chapter. However, it is unlikely that the bulk material in the uppermost layers has a porosity greater than 75% (Ciarletti et al., 2015). An increased dust-to-ice mass ratio may have a similar effect (result from Chapter 3), although we identified that this was actually more due to the resulting increase in thermal conductivity than the composition itself. Therefore, local variations in composition or thermophysical properties could also induce different amounts of local erosion of the pits. The inclusion of super volatiles such as CO and CO_2 would contribute by up to 20% changes in the erosion as seen in the previous chapter.
Such local heterogeneities have indeed been identified at the surface of 67P, with a spatial scale of tens of meters, sometimes associated with the local exposure of volatile ices (e.g., Filacchione et al., 2016; Fornasier et al., 2016). On a global scale, differences between the small and the big lobes have been inferred from variations in their mechanical properties (El-Maarry et al., 2016), and physical characteristics. For instance, the small lobe has larger goose-bump features, fewer morphological changes, and less frequent and smaller frost areas than the big lobe (Fornasier et al., 2021). From these, the authors inferred that the small lobe might have a lower volatile content than the big lobe. Instead, we have chosen to apply a uniform set of initial parameters. Thus, our erosion rates could vary if we accounted for the actual heterogeneity of the nucleus. Based on the outcomes of simulations performed in Chapter 3 prior to the selection of this set of initial parameters, we can estimate that the final erosion would change by about 20% at most due to local changes of porosity, composition, or thermal properties as observed by the suite of instruments onboard *Rosetta*.

Nonetheless, our general trends, should not be sensitive to these initial conditions. As a consequence, our quantitative study validates the qualitative trend suggested by Vincent et al. (2017): that sublimation-driven erosion leads to shallower and larger depressions, effectively erasing sharp geological features with time.

4.4.4 Implications for the evolution and origin of pits

Our results provide a quantitative confirmation for several earlier studies since no quantification of the erosion through all the recent orbits of 67P has been performed before.

On the formation of pits, Ip et al. (2016) performed a morphological and dynamical study, by which they found that pits on JFCs were likely formed prior to acquiring their current orbital elements. Mousis et al. (2015) tested the formation of pits with three

phase transitions (sublimation, amorphous water ice crystallization, and clathrate destabilization) and found that each of these processes would require a period of time much longer than the time spent by the comet in the inner Solar System to form the observed pits. Guilbert-Lepoutre et al. (2016) also attested that it is very unlikely to form 200 m pits under current illumination conditions. Such conditions are however prone to the formation of smaller-scale geological features, such as shallow depressions of several meters in depth, probably formed due to progressive seasonal erosion (Bouquety et al., 2021a,b). Our study confirms that erosion occurring as a result of cometary activity under the current illumination conditions is not sufficient to create such features of few hundreds of meters.

When it comes to the evolution of pits, Belton (2010) proposed an evolutionary sequence of their morphology where pits are erased through cometary activity: initially found as acute depressions seen on 81P/Wild 2, they would progressively become shallower depressions as observed on 103P/Hartley 2 which is relatively older in terms of the sublimation process (Ip et al., 2016). Vincent et al. (2017) studied the global topography of comets observed by spacecrafts and reaffirmed this trend.
Interestingly, the more preserved features have been unambiguously pointed as the source of thin dust jets, arising from the edges of these depressions, which indicates that activity and erosion are currently occurring (Sierks et al., 2015). More generally, Vincent et al. (2015a) identified two trends in the depth-to-diameter ratio (d/D) of pits at the surface of 67P: active pits have a high d/D (>0.3), while pits with no observed activity have a much smaller d/D. From our results, we cannot exclude that large, relatively shallow pits could be active, as erosion is efficiently erasing the structures, especially in the southern regions (Section 4.3). Overall, our results of pits getting shallower with the activity supports the hypothesis that the deep, circular pits are less processed (or better preserved) than the large, or elongated ones.
Therefore, when it comes to understanding the origin of pits, we argue that feature 1 (Seth_01) on the big lobe, and 12 (Ma'at_01) on the small lobe, are the least processed. Notwithstanding local heterogeneity giving rise to various pit sizes, these features are thus likely representative of pits as they were formed. This needs to be kept in mind when we seek to constrain the thermal or physical processes that carve these structures, and which remains to be identified: any process invoked needs to be able to excavate a significant volume of material in a quasi-circular shape.

In conclusion, this study provides a quantification of the erosion rates sustained at the level of the pits during all the time that 67P spent as a JFC in the inner Solar System, which notably reaffirms the results of the previous studies, at least for 67P.
In the next chapter, we will confront the trends established in our study by constraining the sublimation-driven erosion sustained by other cometary nuclei where pits have also been observed: 103P/Hartley 2 (Syal et al., 2013), 81P/Wild 2 (Brownlee et al., 2004), and 9P/Tempel 1 (Thomas et al., 2013b).

Chapter 5

Evolution of pits on other JFCs: 81P, 9P, and 103P

Pits have been observed on all the Jupiter-family comets (JFCs) visited by spacecraft (see Figure 5.1). Continuing our study on pits observed on comet 67P, this chapter examines pits and alcoves observed on the surface of comets 81P/Wild 2 (Brownlee et al., 2004), 9P/Tempel 1 (Belton et al., 2013a), and 103P/Hartley 2 (Belton et al., 2013b; Syal et al., 2013). The origin of these pits, much like those on 67P, remains a subject of debate.

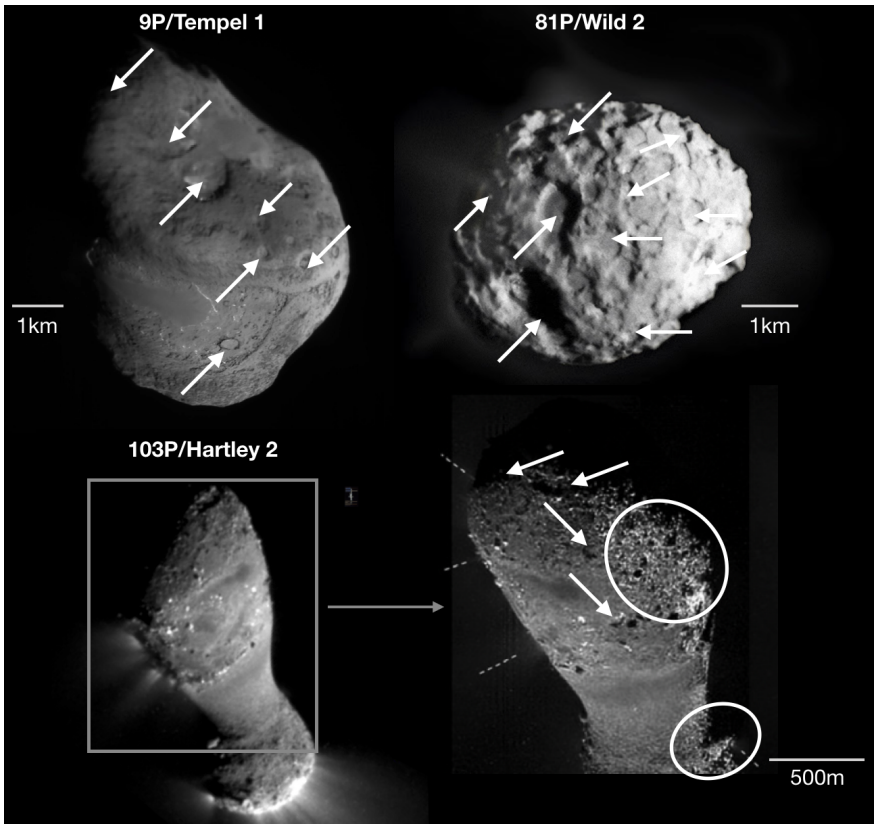

Figure 5.1: Images showing pits and alcoves on the surfaces of comets 81P, 9P, and 103P. Specific examples are highlighted. Pitted terrains on 103P are delineated with circles.

Pits on 81P, as revealed by *Stardust* images, greatly vary in size and shape, with some reaching up to ∼2 km in diameter. Brownlee et al. (2004) identified two types of pits: circular and irregular-shaped. Circular pits further exhibit two primary morphologies: pit-halo and flat-floored. Supported by laboratory experiments, these are theorized to result from impacts, possibly combined with sublimation and ablation processes. Indeed, hypervelocity impact experiments have successfully replicated pit-halo and flat-floor craters by impacting resin-coated sand with differing levels of porosity (Brownlee et al., 2004). In that framework, the lack of small impact structures (with sizes <0.5 km), would be attributed to surface erosion, or a limited number of impactors within this size range. Additionally, 81P exhibits non-circular depressions, like Mayo, which according to Brownlee et al. (2004) may have been formed by alternative processes such as sublimation, mass wasting, ablation, or a combination thereof. Brownlee et al. (2004) do not rule out the possibility of distinct processes, such as internal explosions driven by phase changes, to account for the observed depressions.

Observations by *Deep Impact* and *Stardust/NExT* revealed that 9P has a very pitted surface (Belton et al., 2013a), with 380 pits ranging in diameter from tens to hundreds of meters (up to ∼900 m) and a depth of up to 25 m. Two of these depressions are considered as plausible impact craters (Thomas et al., 2007). Belton et al. (2013a) inferred that Jupiter Family Comets enter the inner Solar System lacking "primitive" craters formed through intense collisional bombardment. Given their abundance and concentration in areas prone to outbursts, Belton et al. (2013a) suggests that most of these pits would likely result from volatile outbursts and sublimation erosion. Indeed, mini-outbursts could account for the formation of 96% of them, and the process could contribute a significant portion of total mass loss, in addition to sublimation. The authors further suggest, based on terrestrial experience and observations of pits at known mini-outburst locations, that pits are the geological features resulting from outbursts of activity. Finally, they propose that a few acute depressions may have resulted from sinkhole collapse, as the evolutionary timescale for these surface features substantially exceeds the sublimation timescale.

Similarly to 9P, comet 103P also displays depressions indicative of a formation process other than impact craters: (Bruck Syal et al., 2013) propose that most surface features, including circular depressions, are the products of evolving jets arising from vents active for several orbits. During low outgassing process, cometary material located on the periphery of the vent falls into the pit or cracks, which brings the warmer material into contact with the colder, icy material located at the bottom of the vent. This process likely applies to material tumbling from scarps and ridges, and might apply to both 103P and 9P (Farnham et al., 2013). The ongoing evolution of activity should alter the cylindrical vent or pit into a shallow depression. Thomas et al. (2013c) support the aforementioned correlation between jets and pits, as collimated jets seem to be linked with these pits. They also investigated the hypothesis of subsurface cavities collapsing.

Taken altogether, these observations suggest that pits may be ubiquitous on cometary surfaces, and that a link with cometary activity may exist. The pits (defined as in Chapter 3) observed on 9P, 81P, 103P and 67P display some geomorphic resemblances in terms of shape and dimensions (Vincent et al., 2015a; Ip et al., 2016). Thus, similarly to our study of of 67P's pits, we can attempt to understand how cometary activity may modify the morphology of pits at the surface of these other comets. Indeed, 3D shape

models of the comet nuclei are available, reconstructed from high-resolution images, with spatial resolutions of a few tens m/pixel Vincent et al. (2015b), taken by spacecraft that have visited them. The goal here is to explore whether the pits on these comets may have evolved similarly to those analyzed on 67P in Chapter 4. Specifically, we aim to investigate if the erosion sustained during their recent orbital evolution – in particular due to current illumination conditions – is sufficient to account for the formation of the observed pits and alcoves, or if these structures are gradually eroding, as observed for 67P in our results in Chapter 4.

5.1 Inputs for thermal evolution models

5.1.1 Orbital considerations for each comet

We run our calculations to study the impact of current illumination conditions. However, each comet "acquired" its current orbit following a distinct orbital evolution, and has been located on its current orbit for a different time. We thus use a different number of orbital revolutions for each comet, depending on their past history (see Figure 5.2): 6 orbits for comet 81P, 13 orbits for comet 9P, and 20 orbits for comet 103P (Ip et al., 2016).

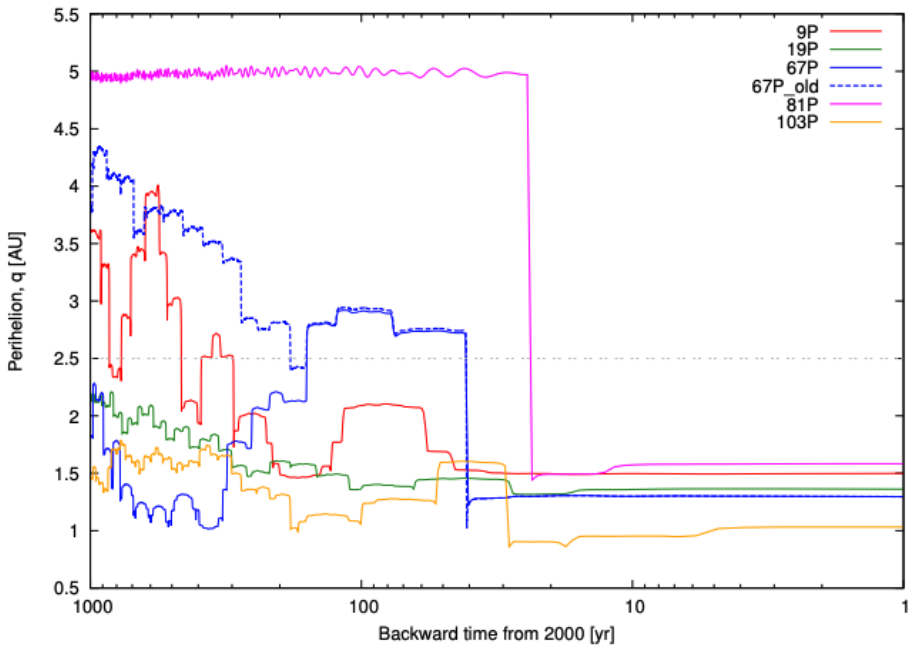

Figure 5.2: Orbital evolution of several short-period comets over one thousand years, including 9P, 81P, and 103P, shown as variations in perihelion distance: q over time. Sharp variations in q are due to close encounters with Jupiter. Credits: Ip et al. (2016)

For each orbital revolution, we use SPICE kernels available for each comet nucleus in order to compute the energy balance at the surface. We use timestep of 8 minutes for these calculations, which guarantee a good sampling of both diurnal and seasonal processes. The total energy received at the surface is used as the boundary condition of

the same 1D thermal evolution model described in Chapter 4, which accounts for heat diffusion, phase transitions (sublimation of various ices and crystallization of amorphous water ice), gas diffusion, erosion, and dust mantling (Lasue et al., 2008). Same thermophysical parameters are used as inputs to this model.

5.1.2 Shape models for comets 9P, 81P and 103P

For each studied comet – 81P, 9P, and 103P – we use the highest resolution shape model available to capture both the global shape and local topography of each nucleus as accurately as possible. Indeed, we need to account for an adequate number of plausible pits on their surfaces. The shape models are taken from: Farnham and Thomas (2013b) for 103P, derived from the images of the comet obtined by *EPOXI* mission; Farnham and Thomas (2013a) for 9P, derived from the images obtained by the *Deep Impact* spacecraft and by the *Stardust* spacecraft; and Farnham et al. (2005) for 81P, derived from the *Stardust* Navcam images. All images were obtained around the time of closest approach to the comets. The different shape models used are represented in Figure 5.3.

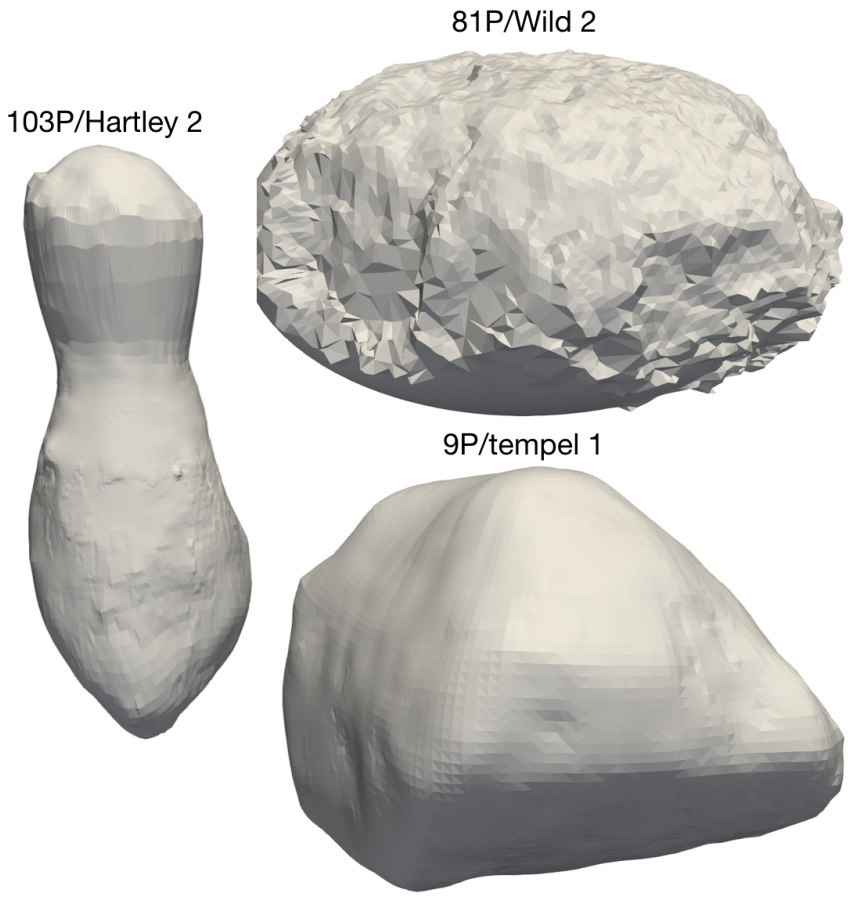

Figure 5.3: Shape models used for the study of pits on: 103P/Hartley 2 (32,040 facets), 81P/Wild 2 (17,518 facets), and 9P/Tempel 1 (32,040 facets). The shape models are oriented with respect to their rotation axes. The scale is not respected in this representation.

Shape models for comets 81P, 9P, and 103P are not as spatially-resolved as those available for comet 67P. This lower quality (for our purpose) is to be expected, as these were derived from limited observations during flyby missions, whereas 67P was followed during the 2 years of an orbiting mission. We note that for these reasons, we had to exclude 19P from our study, as no good shape model was available. Specifically, the shape models of 103P and 9P do not show distinct features as deep as the features which are observed on the images. For comet 81P, the southern hemisphere was not actually observed by the *Stardust* mission, resulting in a completely smooth representation of the hemisphere in the shape model. Despite these limitations, we were able to identify a number of pits and alcoves from the shape models, and select facets similarly to those of 67P, located on the plateaus, walls and bottoms of each feature, to the best of your ability and the local resolution of these shape models.

It is important to mention that the smoother appearance of depressions on the surfaces of the studied comets is not solely due to the comparatively lower resolution of their shape models relative to 67P, but also because the pits observed on these comets exhibit a lower depth-to-diameter (d/D) ratio compared to 67P. In particular the observed average d/D values are 0.1 for 9P (Thomas et al., 2013a) and 0.2 for 81P (Kirk et al., 2005; Vincent et al., 2015a). Also, the surface aspect of comet 103P closely looks like that of 9P, exhibiting a smooth appearance with no evident deep pits (Ip et al., 2016).

5.1.3 Selection of pits on each comet

For the three nuclei, we select a minimum of 10 surface features (i.e. pits or alcoves) with criteria similar to our selection criteria for 67P: we want to sample the nuclei in latitude as much as possible, to assess the influence of seasonal mechanisms, and we focus on larger depressions, which possess steep walls and flat bottoms and have sizes ranging from tens to hundreds of meters. Indeed, feature ranging from ∼150 m to ∼1 km exhibit a size-frequency distribution similar between 67P to those observed on comets 9P and 81P (Ip et al., 2016). On the corresponding shape models, we select multiple facets on different sides of each feature (plateaus, bottom and walls) and consider the complete thermal environment for each facet, including self-heating and shadowing, either by neighboring facets or due to the complex global morphology of the nucleus.

Considering the smooth appearance of the shape models, especially for the comets 9P and 103P, we endeavored to identify pits visible in images and pinpoint their location on the shape models. However, due to either the limited resolution of the images, or the challenges in localizing the pits on the shape model, we opted to select some depressions directly observed within the models. Nevertheless, since the primary objective of this study was to conduct a comprehensive analysis of the diverse illumination conditions present across the surface of the nuclei, by selecting depressions from shape models, we could explore various geometrical forms and potential evolutionary scenarios of such features.

The pits selected on the surface of comet 81P are necessarily located in the northern hemisphere, as there is no direct observation of the southern smooth hemisphere (see Figure 5.4). Despite this, we have also selected a group of facets within the reconstructed smooth southern hemisphere with the objective of comparing erosion rates between both hemispheres, which would allow us to gain insights into potential seasonal trends that may be present on the comet's surface. Furthermore, this comparison can help us understand how the pits might appeared or evolved at these latitudes.

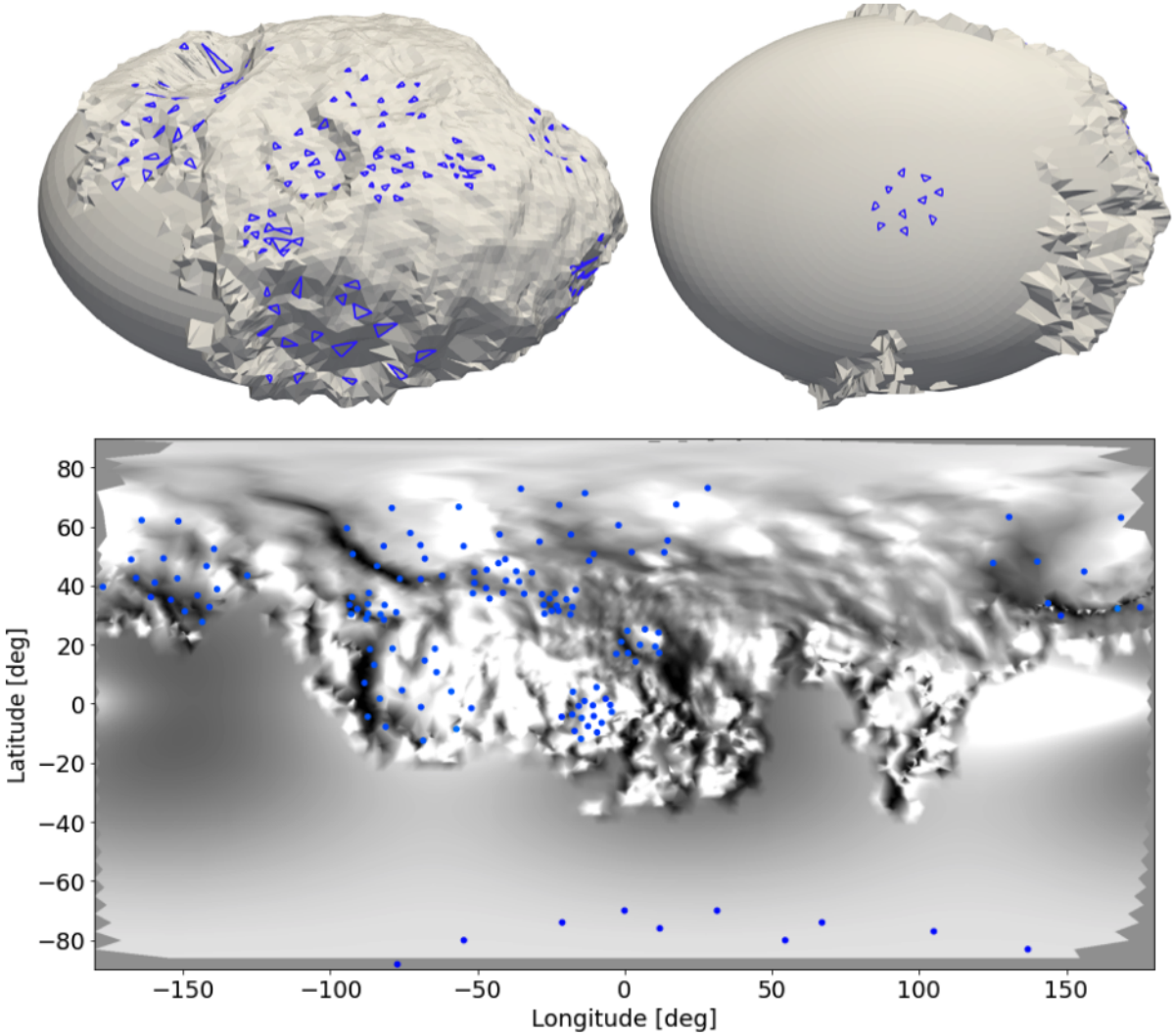

Figure 5.4: Facets selected for study on the surface of 81P. Due to the lack of information in the completely smooth southern hemisphere of the shape model, only a group of facets were selected for comparison.

Facets chosen for the study of pits on the surface of 9P are shown in Figure 5.5.

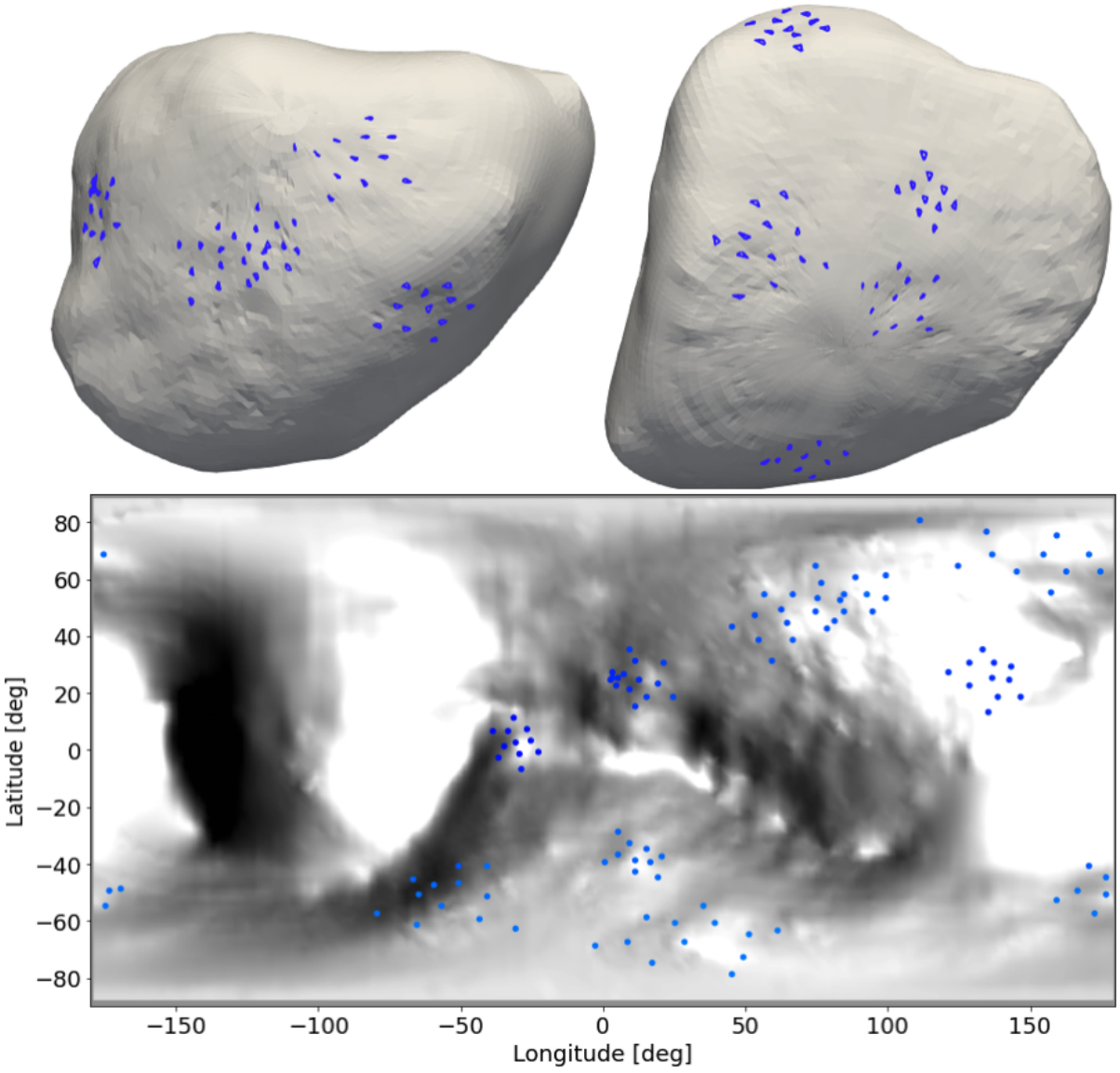

Figure 5.5: Facets selected for study on the surface of 9P.

Finally, we selected several pits across the entire surface of 103P (Figure 5.6). Given the nucleus' unique elongated shape and intricate spin axis parameters, and to thoroughly analyze the maximum latitudinal coverage assuring different illumination conditions, we incorporated additional facets all across the surface.

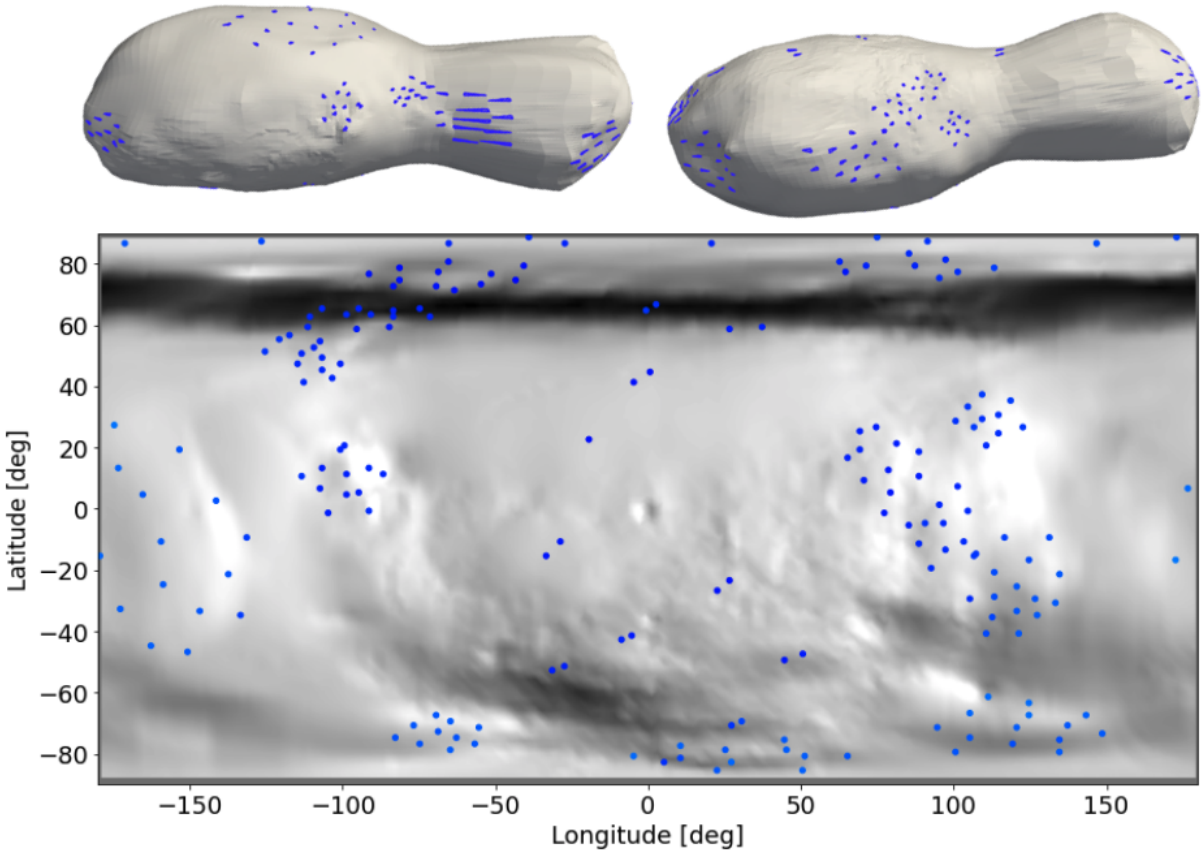

Figure 5.6: Facets selected for study on the surface of 103P.

5.2 Thermal evolution of selected pits

5.2.1 81P/Wild 2

The energy integrated over one orbit of 81P for each facet is presented in Figure 5.7. We see a nearly uniform distribution of total energy across all facets on the surface, with the southern hemisphere receiving the most of the energy integrated over one orbit. This is explained by the rotational properties of 81P, which make the subsolar point cross a large range of latitudes near the perihelion passage, as we can see from Figure 5.8. The nucleus is thus exposed almost entirely to direct insolation at perihelion. This results in almost similar amounts of energy received by all facets, as the most of the energy received across the orbit is actually received during this period. Only a few facets located in the walls of some pits receive lower amounts of energy, reaching less than half of the maximum amounts, as a result of the shadowing by neighboring facets.

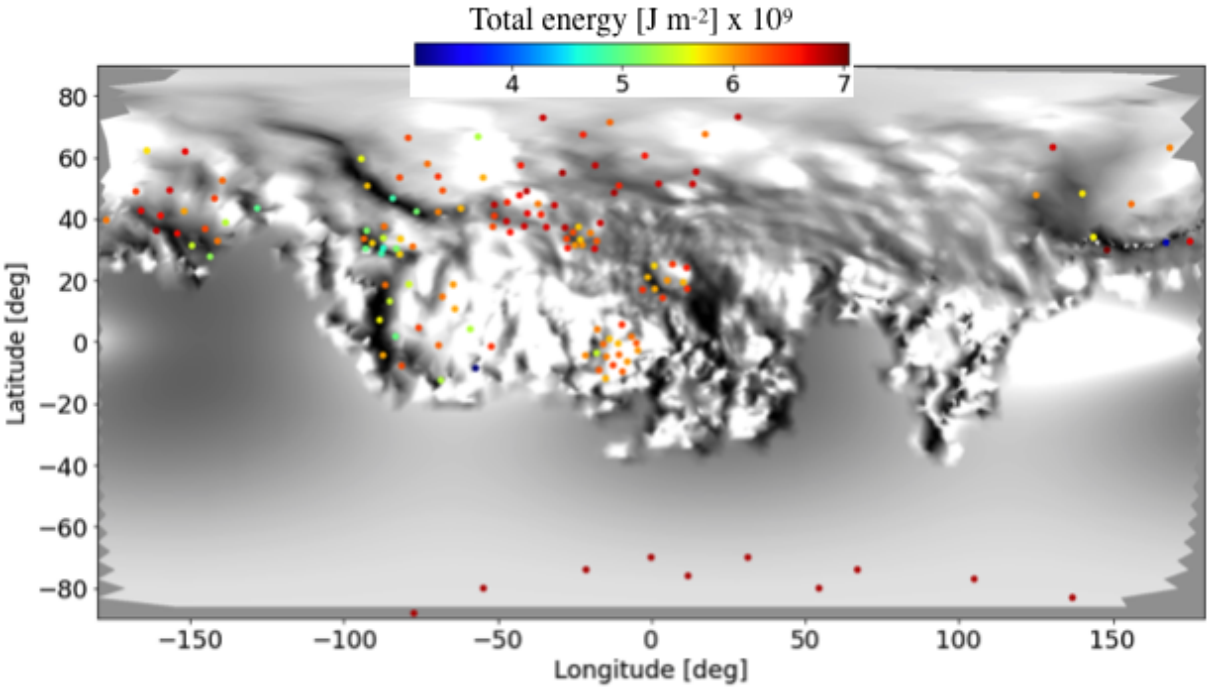

Figure 5.7: Total energy received at the surface of studied facets on 81P, integrated over one full orbit.

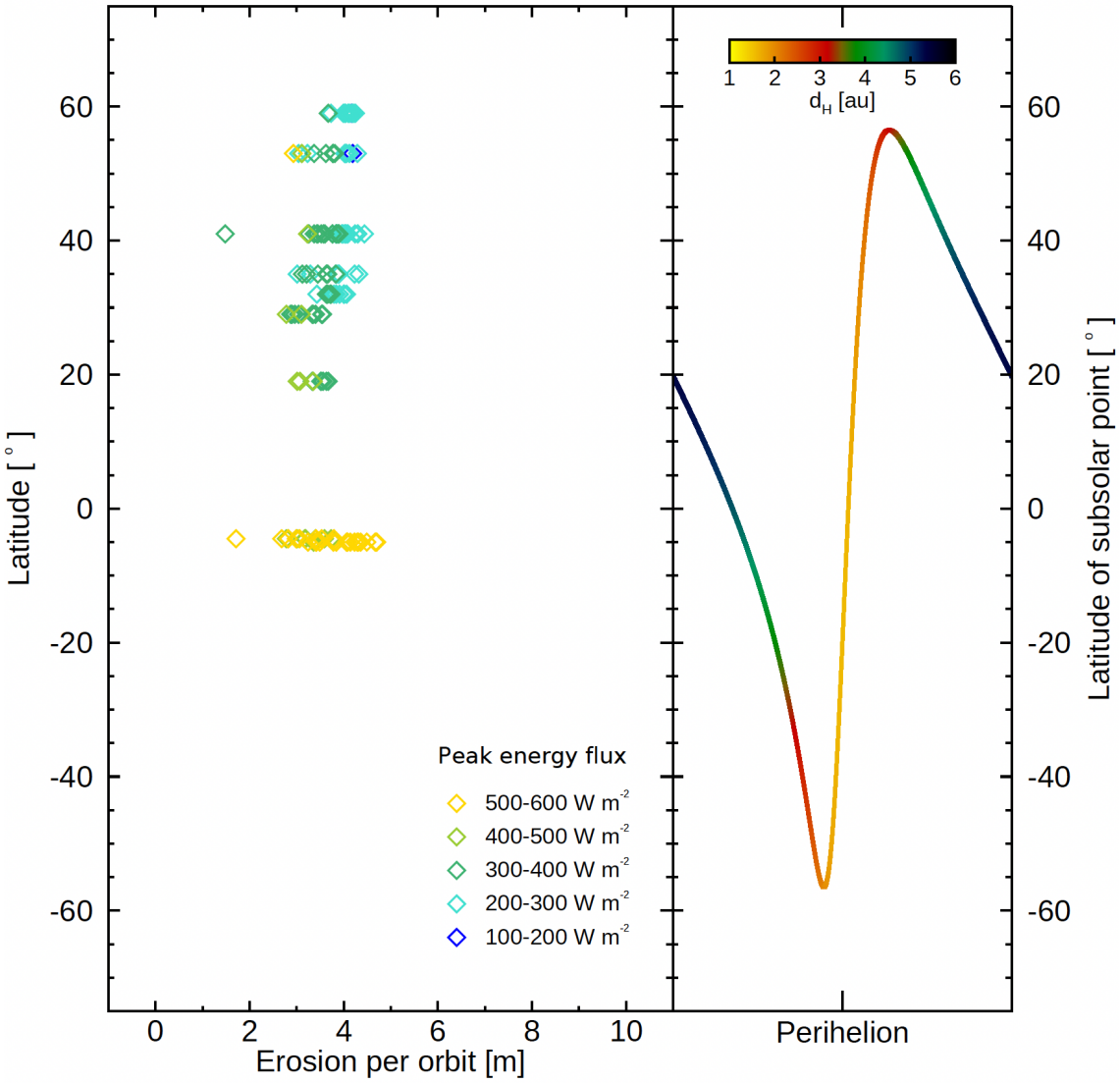

Figure 5.8: Left: erosion of all the studied facets of 81P as a function of latitude and energy peak. Right: subsolar latitude variation through the orbit of 81P, as a function of heliocentric distance.

As for 67P (Chapter 4), the latitudinal effects (i.e. seasonal) dominate the energy distribution at the surface of 81P, but the local shape can also play a key role. Figure 5.9 demonstrates how shadowing affects a few wall facets, highlighting the significance of considering shape when analyzing the thermal evolution of deep and acute pits, such as those observed on 67P and 81P.

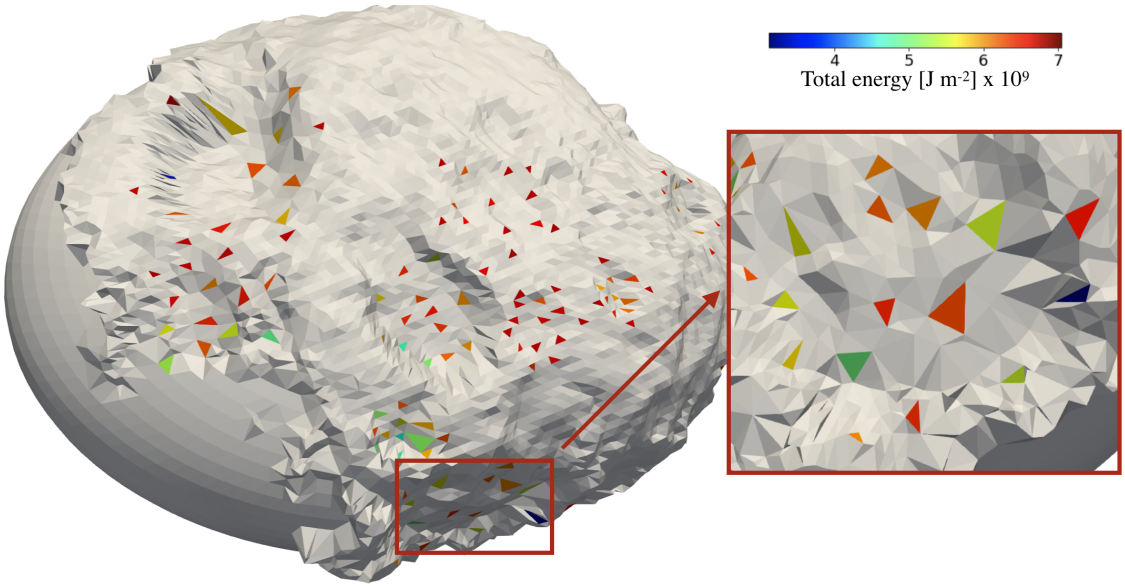

Figure 5.9: Total energy received at the surface of 81P's studied pits during one full orbit, as distributed over the 3D shape model. We zoom in on one pit for more visibility.

The self-heating contribution can account for up to 30% of the total energy in the shadowed regions where direct insolation is weak (see Figure 5.10). It should be noted, however, that due to the large size of the pits observed on 81P, i.e. ∼2 km for the largest one (Brownlee et al., 2004), most of the facets are exposed to direct insolation: the global shape does not have a high influence on them.

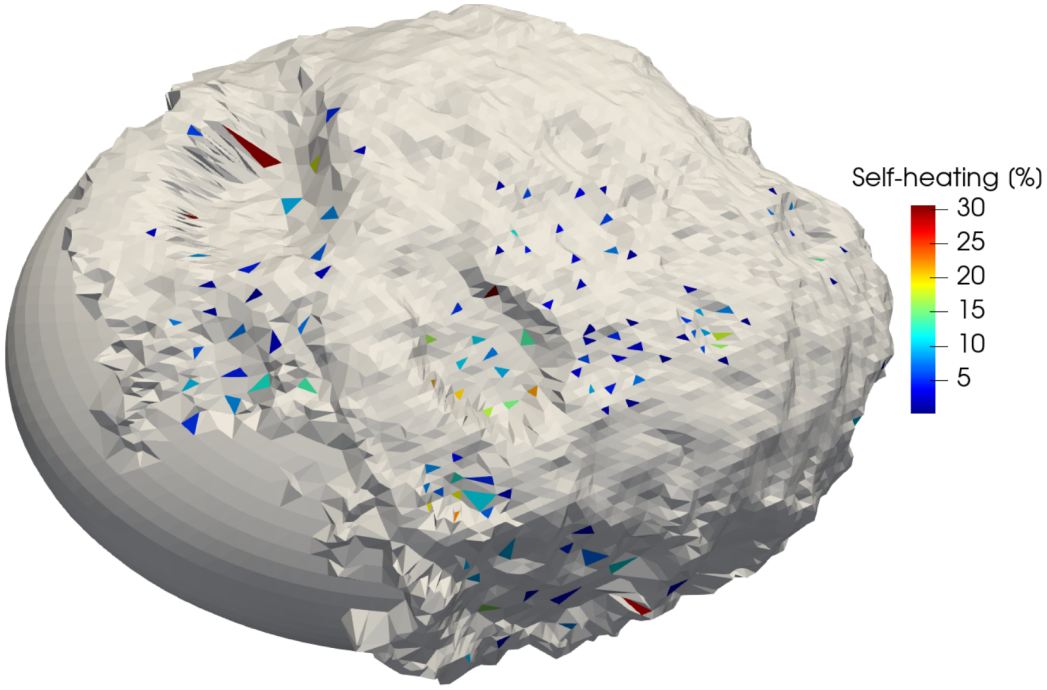

Figure 5.10: Self-heating contribution to total energy for the pits of 81P.

The highest peaks of energy are received by the equatorial regions, as illustrated in Figure 5.11, which is attributed to the subsolar point being located around these latitudes during the perihelion passage (Figure 5.8).

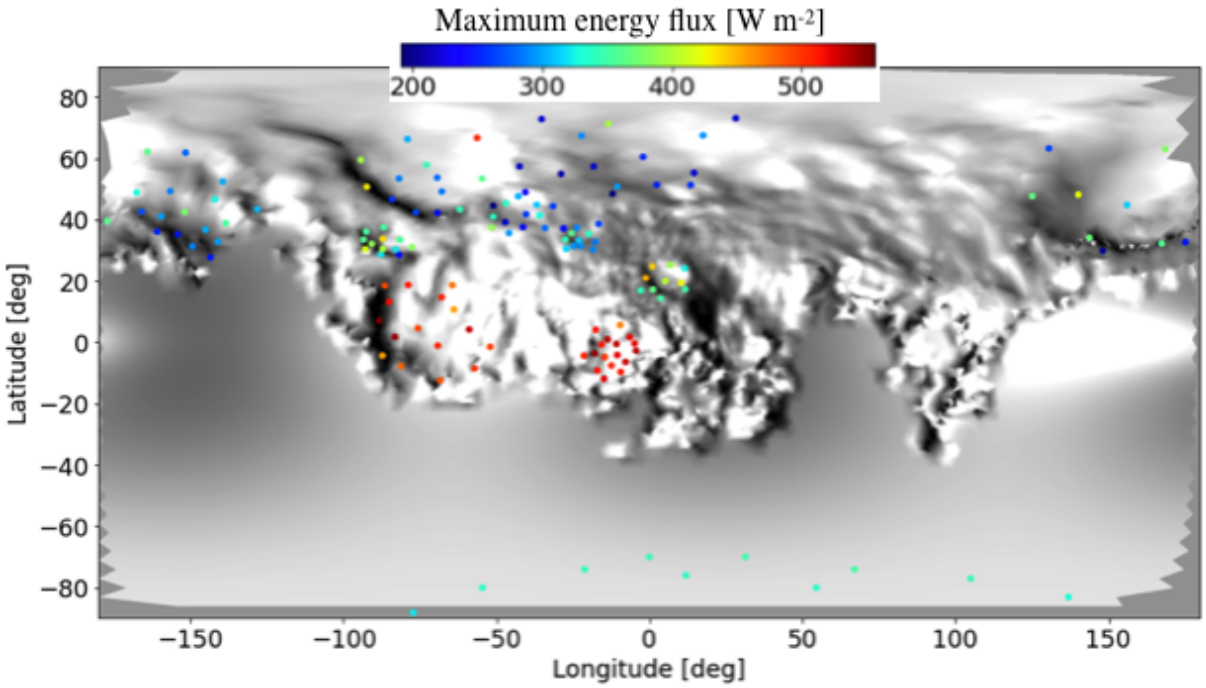

Figure 5.11: Peak energy received at the surface of all studied facets on 81P.

Because insolation is nearly uniform, erosion rates across for northern facets of 81P is also almost uniform, excluding some facets located in the walls of acute pits (Figure 5.12). Erosion rates of most northern facets typically range from ∼15 to 30 m after 6 orbital revolutions. The southern facets we have taken for comparison are actually the ones that erode the most. Figures 5.7 and 5.11 show that erosion on 81P's surface is better correlated with the total energy received over the orbit. As we noted earlier, this could be attributed to the strong variation of the the subsolar point's latitude during the perihelion passage, which results in a nearly uniform distribution of peak energy. The most active facets exhibit erosion rates that do not exceed ∼30 meters, after 6 orbital revolutions. These results indicate that erosion is not the primary process responsible for the formation of the kind of pits studied here, with diameters reaching up to 2 km.

Finally, we mention that in general, pits on 81P are large enough for facets located at the bottom of these surface morphological features to behave similarly to facets located on the surrounding plateaus. Both "parallel" plans thus erode in the same way, so that the depth of these features remains relatively constant (Figure 5.13). The irregular shape of these pits contributes to the non-uniform distribution of energy within the pit, which can influence the simulated erosion patterns.

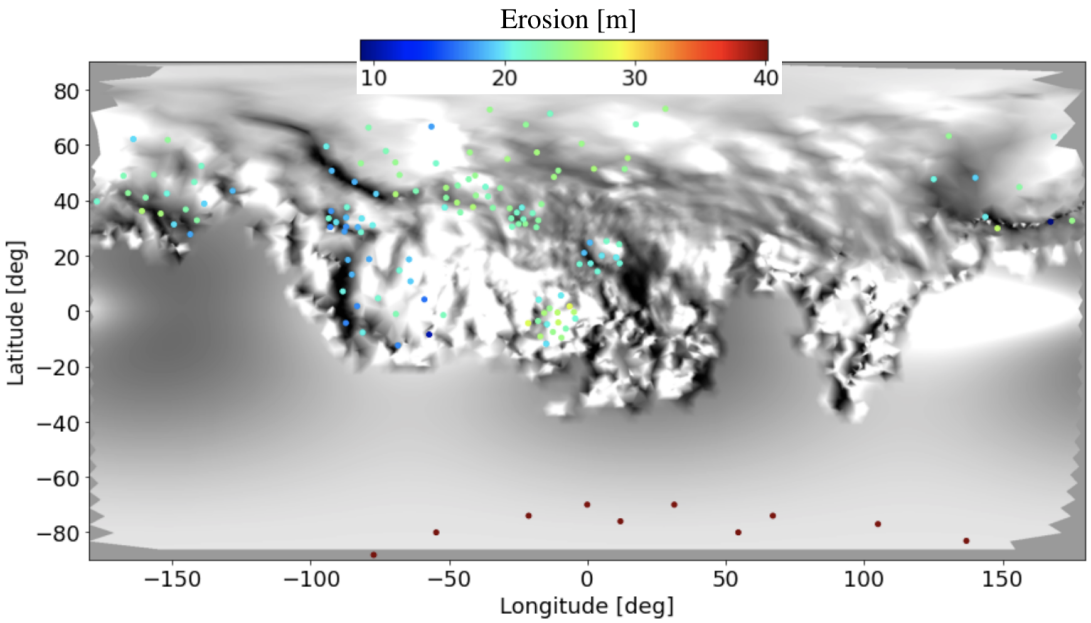

Figure 5.12: Erosion achieved at the facets of 81P after a thermal evolution of 6 orbits.

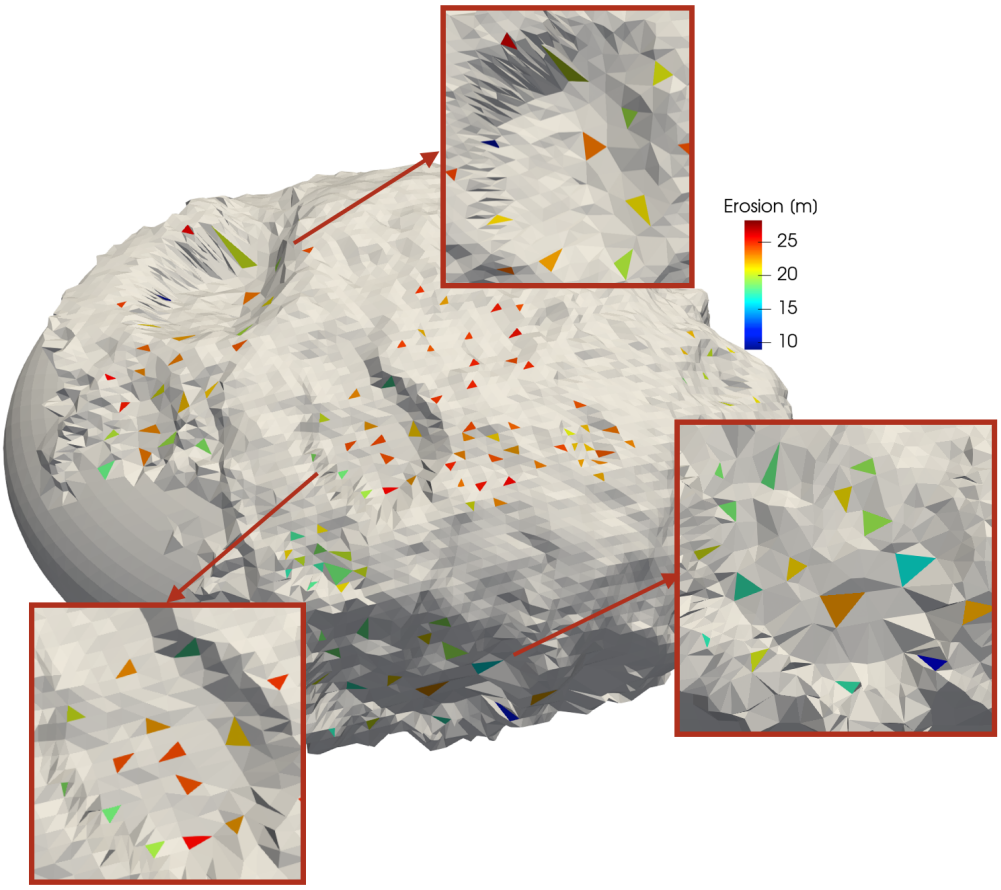

Figure 5.13: Erosion achieved on 81P's pits after a thermal evolution of 6 orbits.

5.2.2 9P/Tempel 1

Due to its low obliquity, the highest amounts of energy received at the surface of 9P are located near the equator. This is observed on both the integrated energy and the peak maps presented in Figures 5.14 and 5.15.

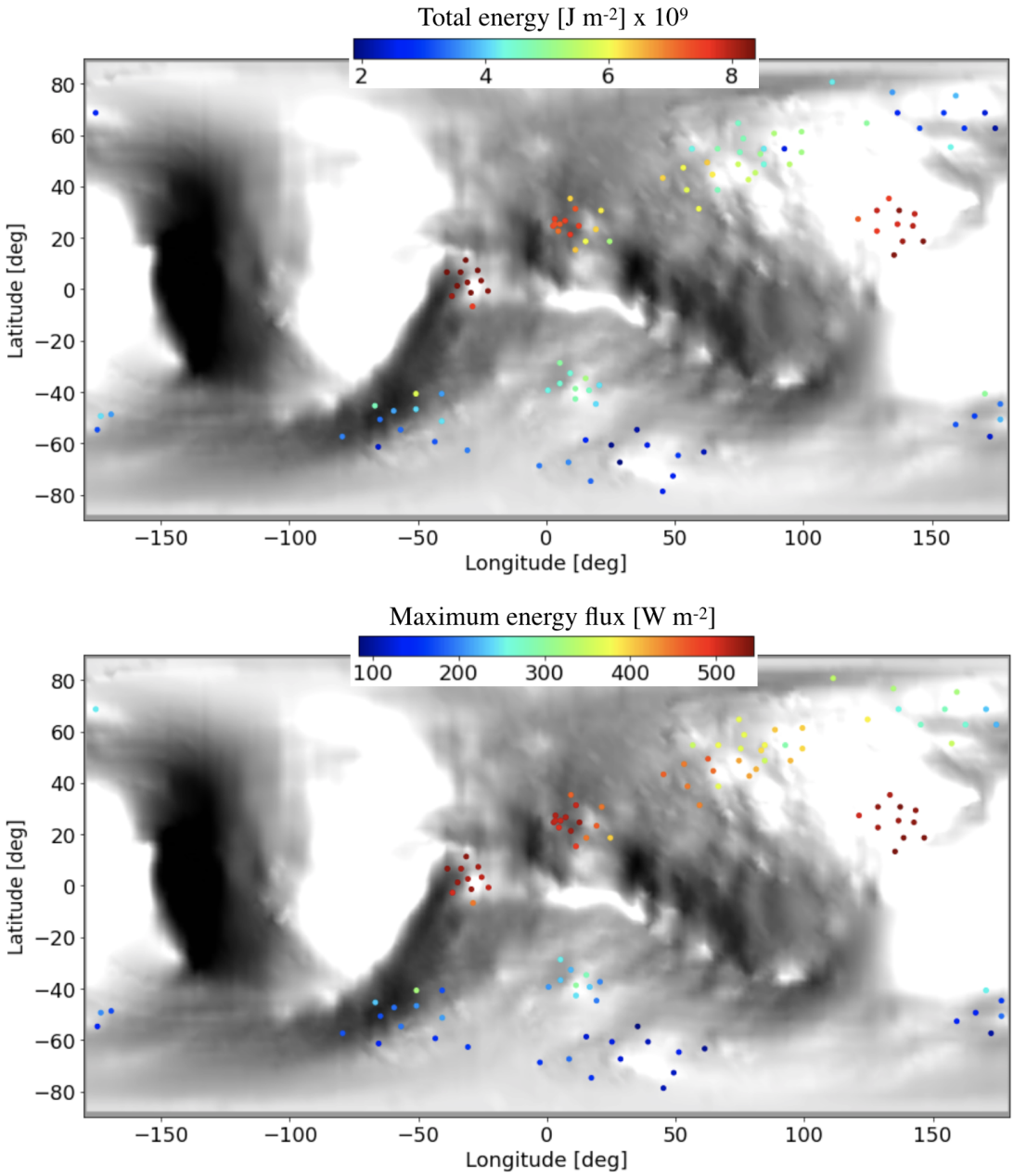

Figure 5.14: Top: total energy received at the surface of 9P's studied pits over one full orbit. Bottom: energy peak received close to perihelion.

The seasonal trend of energy received induces the most erosion in equatorial regions, followed by mid- and low-latitudes (Figures 5.15 and 5.16).

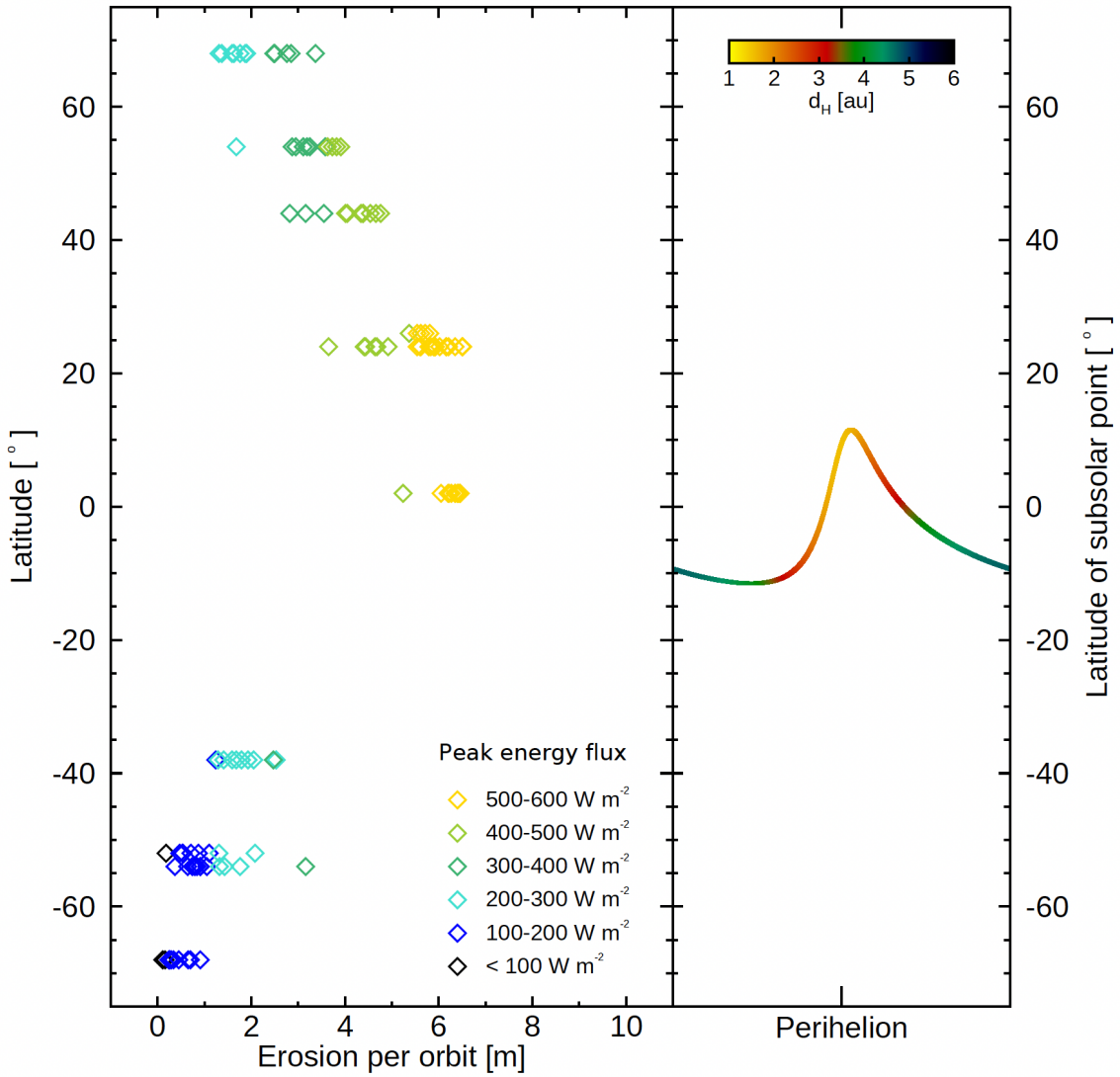

Figure 5.15: Left: erosion of all the studied facets of 9P as a function of latitude and energy peak. Right: subsolar latitude variation through the orbit of 9P, as a function of heliocentric distance. Facets close to equator exhibit the highest amounts of energy and erosion.

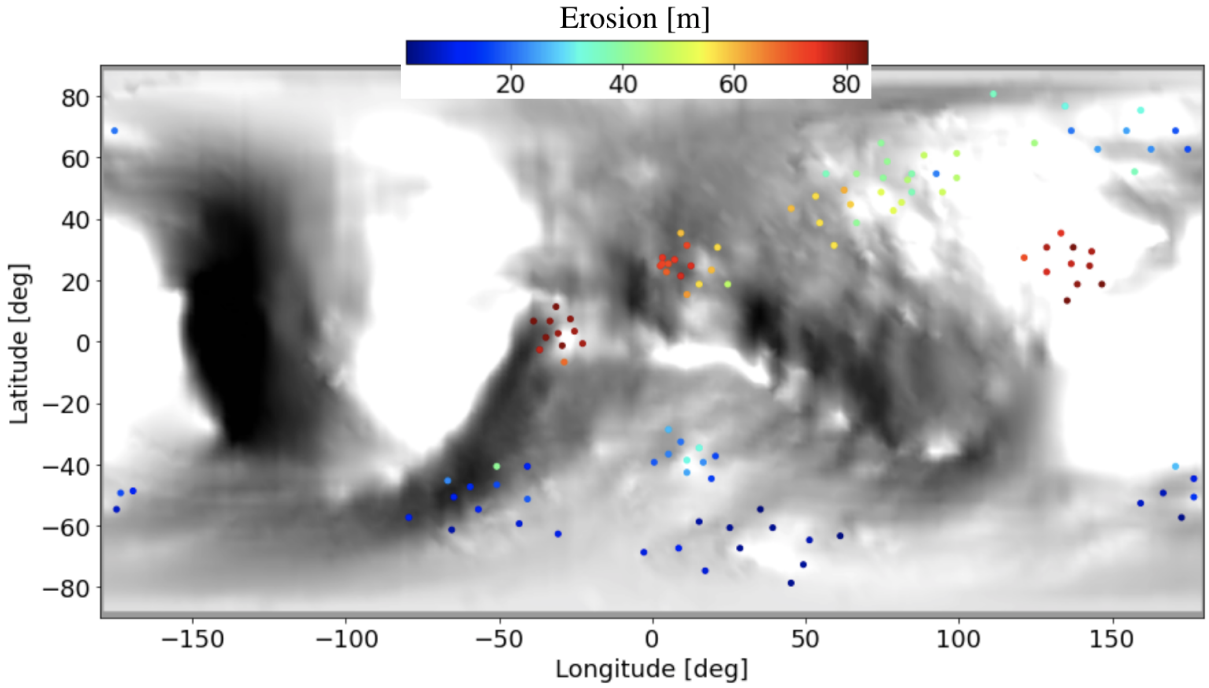

Figure 5.16: Erosion achieved at the surface of all studied facets on 9P after a thermal evolution of 13 orbits.

Erosion caused by water-driven outgassing over 13 orbital revolutions remains relatively low. It does not exceed a hundred meters in total, whereas the observed dimension of pits can reach several hundred meters across for the largest ones (Thomas et al., 2013b).

5.2.3 103P/Hartley 2

Comet 103P is characterized by an extremely complex rotation. The rotational properties are, in fact, so complex that the SPICE kernels have a limited range of validity around the flyby of the nucleus by *EPOXI* (around that perihelion passage), and that propagating coordinates for the subsolar points to the whole orbit is not necessarily possible. This is nonetheless the best we can do at this point, to assess the influence of activity on the evolution of surface features. We must thus keep in mind to interpret our results. The nucleus spins in an excited long-axis mode (LAM), with its rotational angular momentum per unit mass, and rotational energy per unit mass, slowly decreasing while the degree of excitation in the spin increases through perihelion passage (Belton et al., 2013b). In addition, the nucleus has a very elongated shape. These characteristics are reflected in the complex distribution of energy received by the nucleus' surface, which exhibits not only a latitudinal trend (as observed for the other comet nuclei), but also strong variations across longitude, especially around the equator region, as shown in Figures 5.17. Overall, equatorial regions and nearby northern latitudes receive a substantial amount of energy around perihelion, while the southern and extreme western equatorial regions receive the least energy during this period.

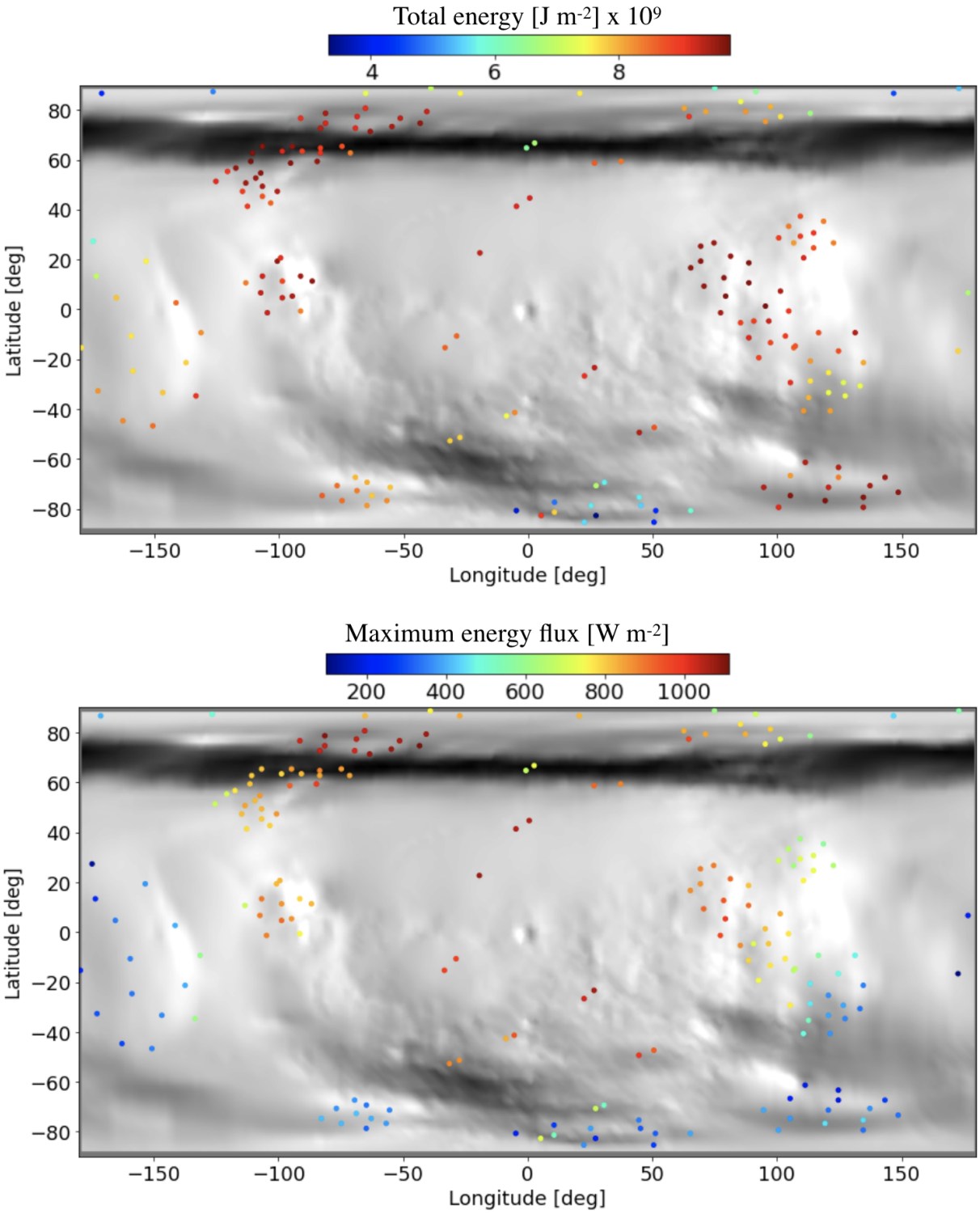

Figure 5.17: Top: total energy received over one orbit at the surface of 103P's studied pits. Bottom: peak energy received close to perihelion.

Erosion on 103P's surface is strongly correlated with the peak of energy received at perihelion (see Figures 5.18 and 5.19). This correlation can be attributed to the fact that erosion on 103P occurs predominantly during brief periods of intense heating, outside of which, the energy is insufficient to cause facets to erode. This is in contrast to 81P, where energy is more consistently distributed throughout the entire perihelion period instead of occurring in brief peaks. This behavior is primarily linked to the orbital and rotational characteristics of each comet (Figure 5.20). At perihelion, 103P is also closer to the Sun, at a distance of ∼1.05 AU, compared to 81P, which is at a distance of ∼1.59 AU. Additionally, the orbit of 81P is more circular, with an eccentricity of ∼0.5, compared to 103P's more elliptical orbit with an eccentricity of ∼0.7, so seasonal effects are stronger for 103P.

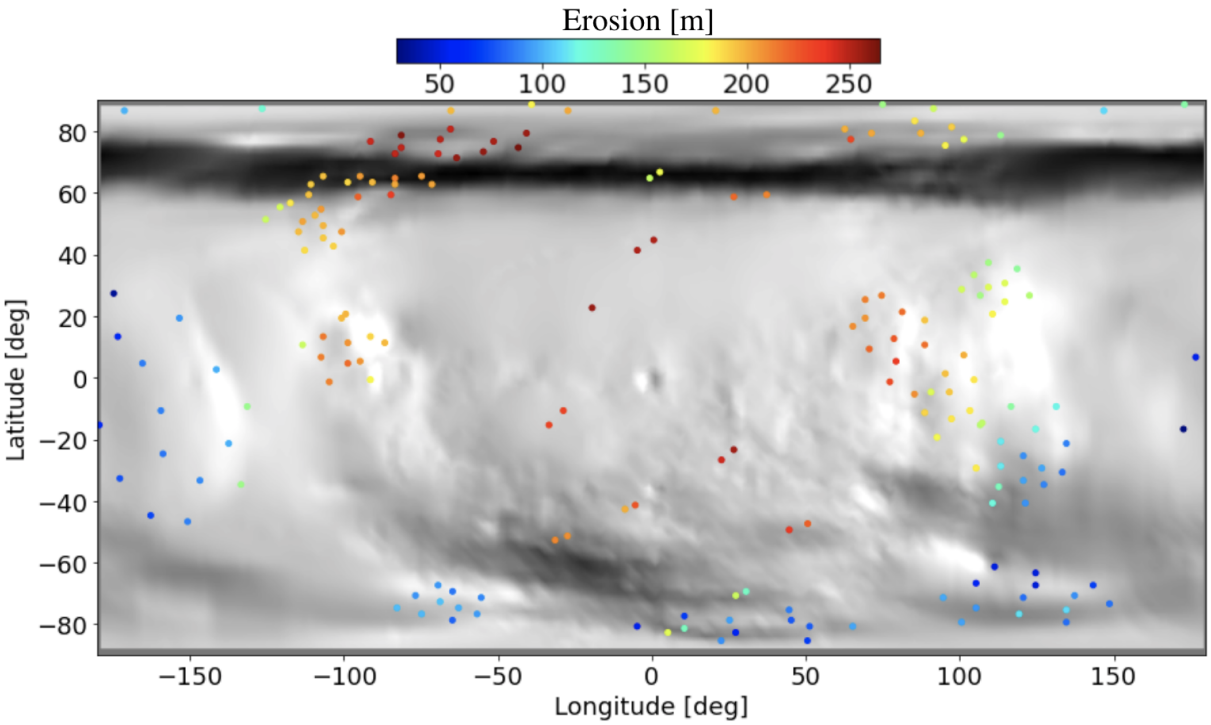

Figure 5.18: Erosion achieved at the surface of all studied facets on 103P after a thermal evolution of 20 orbits.

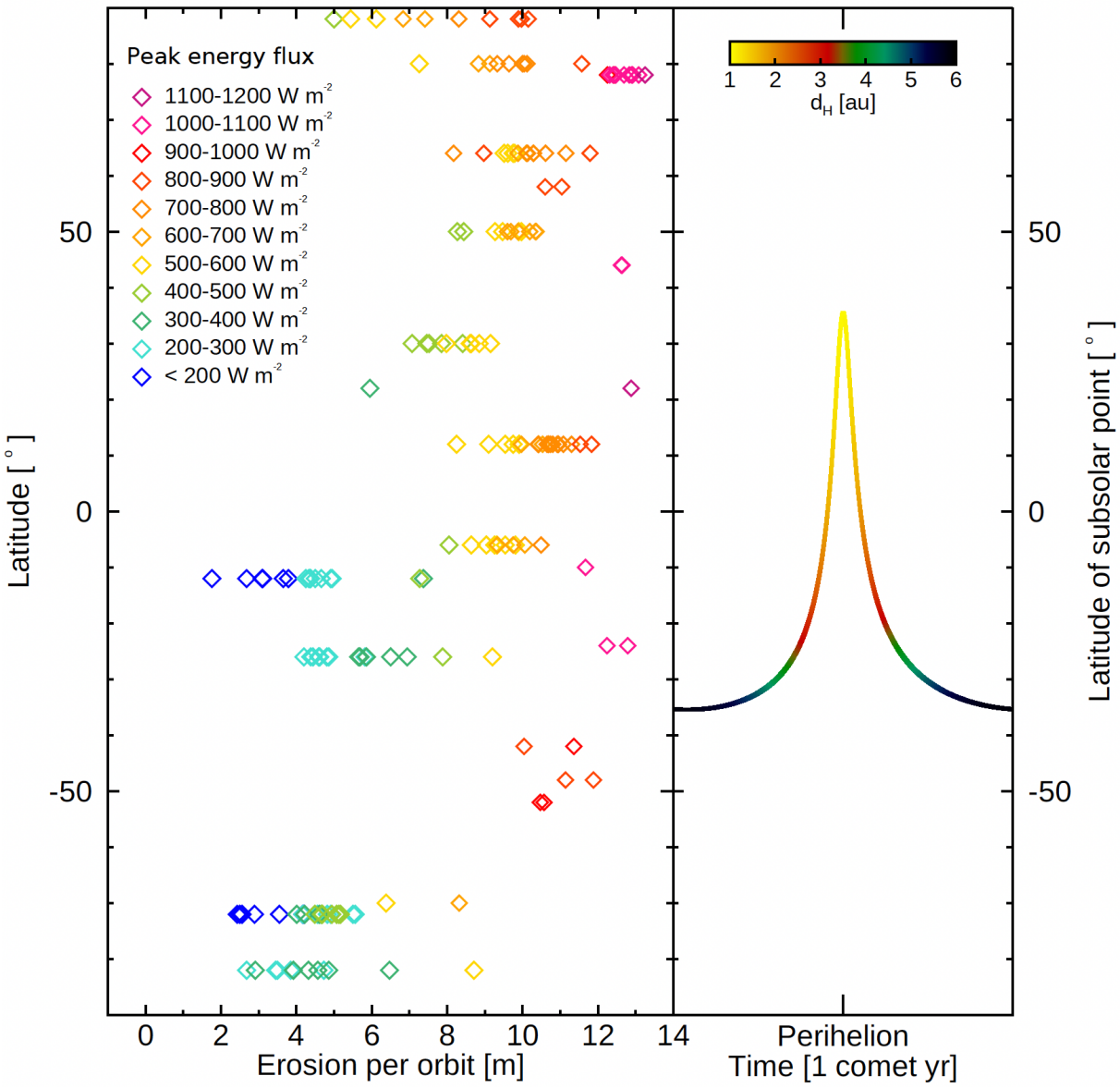

Figure 5.19: Left: erosion of all the studied facets of 103P as a function of latitude and energy peak. Right: subsolar latitude variation through the orbit of 103P, as a function of heliocentric distance. There is a strong correlation between the energy peak and erosion.

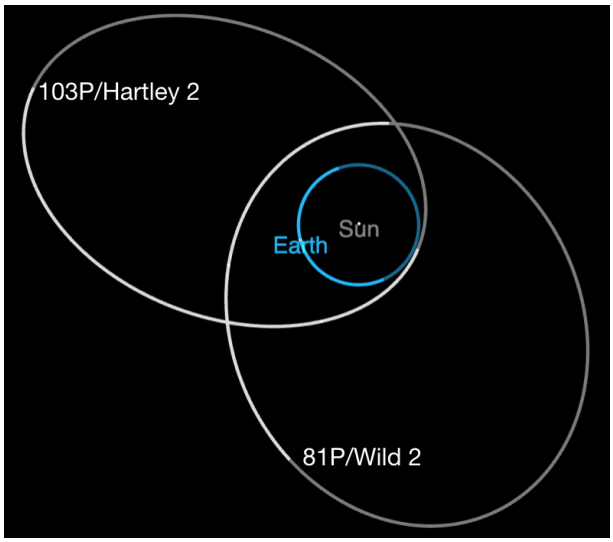

Figure 5.20: Orbits of comets 81P/Wild 2 and 103P/Hartley 2, illustrating the closer perihelion distance of 103P and the more circular trajectory of 81P.

In our simulations, the small northern lobe of the nucleus is very active and experiences the most erosion as a result of its preferential exposure to the Sun at perihelion. The northern lobe was indeed observed to be active during the *EPOXI* flyby. More precisely, jets are clustered in the rough topography of the small northern lobe and mid- to northern part of the big lobe (A'Hearn et al., 2011). Nevertheless, the observed high activity may not be only due to insolation, but may be enhanced by an important abundance of volatiles in specific regions of the small lobe. A'Hearn et al. (2011) indeed determined that different material was coming from the different parts of the nucleus, with H_2O vapor coming primarily from the waist and CO_2, H_2O ice, and CO_2 and organics coming primarily from the end of the small lobe. Taking into account a higher abundance of volatiles in the small lobe for thermal models would increase erosion compared to results from a homogeneous nucleus assumption. This would further emphasize the contrast with the southern big lobe. *EPOXI* revealed distinctly different terrains on the nucleus, with a smooth "waist" connecting two rougher lobes (A'Hearn et al., 2011; Knight and Schleicher, 2013b; Thomas et al., 2013b), but no pronounced differences in pits concentration or appearance between the two lobes were noted. If the surface roughness is primarily determined by outgassing erosion, then the waist region would have likely been the most active area during the comet's recent dynamical period, contributing to its current smooth appearance. The consequences of activity sustained during the comet's 20 recent orbits results in an erosion of more than 250 m, which would also significantly contribute to the removal of surface depressions as sharp and deep as those of a few hundred meters observed on other comets (67P, 81P, and 9P), if they were initially present on its surface.

Finally, the contribution of self-heating to the total energy measured for 9P and 103P is minimal, accounting for less than 10% of the total energy. This contribution is low compared to the cases of 67P or 81P, primarily due to the fact that the surface depressions on these comets have a low d/D (depth-to-diameter) ratio compared to 67P or 81P. Additionally, the low spatial resolution of the shape models may play a role in limiting the ability to effectively reproduce shadowing and self-heating effects.

5.3 Discussion

5.3.1 Seasonal control and shape effects

For all studied comets, activity and erosion are primarily controlled by direct insolation and display seasonal patterns. For comets 9P, 103P, and 81P, no global shape effects are expected due to the lack of significant shape irregularities on a global scale, unlike the pronounced bilobate shape of 67P. The unique shape of comet 67P, for instance, makes the pits located near the neck more susceptible to shadowing by the smaller lobe, as discussed in Chapter 4. However, we found that local shape effects (i.e. linked to local topography) can be significant at the scale of a given pit. Self-heating can contribute with important amounts to the total energy in deep pits and steep cliffs of 81P and 67P, accounting for 30% and 60% (respectively) of total energy input. In contrast, it is minimal for 9P and 103P (<10%), where surface features are shallower. Thus, it is crucial to take into account the shape effects in thermal evolution models when "significant roughness" can be observed at the surface. The term "significant roughness" refers to features deep and sharp enough for the walls or bottom areas to be substantially shadowed, as observed in pits of 67P and 81P (with d/D ratios of 0.3 and 0.2, respectively, Vincent et al., 2015a). However, incorporating the shadowing and self-heating geometry might make the model more time-consuming, while its relevance may not be as significant. Therefore, deciding whether to include shape effects in a model can be challenging. Rezac and Zhao (2020) tested various methods for numerical optimization of self-view factor calculation, showing that finding a trade-off between the accuracy of the surface's geometrical definition and computational speed is difficult to determine.

5.3.2 The role of erosion in pits evolution

Facets located at the bottom and on the wall of circular depressions can be affected by shadowing, compared to exposed plateau facets. Consequently, if these depressions are deep enough, they tend to become shallower over time due to water-driven erosion. This is due to the combination of two effects. First, plateaus tend to erode more than bottoms, so that pits tend to become shallower with time. In addition, walls sustain some differential erosion, which is clearly observed on 67P, and most walls erode more than bottoms. Over several perihelion passages, deep and small depressions become shallower but also wider over time. This trend is not observed for all pits we studied though. The reason for this is that either the pits are not deep enough compared to their diameter, as seen in most of the pits on 9P and 103P, or the pits are sufficiently large that the bottom parts of pits are directly exposed to the Sun, as in the case of the large pits of 81P. Overall, these pits have a depth-to-diameter (d/D) that seems to prevent any further change. Future studies could explore critical d/D thresholds in different lighting conditions, determining when pits are able to evolve and become shallower.
Ip et al. (2016) suggested that the d/D ratios of the large pits are mostly within the range of 0.1–0.3. In comparison, active pits studied by Vincent et al. (2015a) have a large d/D ratio (>0.3) and a small diameter (<300 m). This statistical result coupled with orbital integration studies suggests that large circular depressions could have outgrown from the

small and deep ones via erosive mass wasting of the surrounding areas (Cheng et al., 2013; Vincent et al., 2015a, 2016b). On 9P and 103P, erosion is more uniform since depressions are already shallow (as in the southern hemisphere of 67P). Overall, we find that sharp depressions are likely erased by cometary activity.

Erosion sustained after the multiple perihelion passages is not able to carve large depressions with the observed size and shape, on any of the comets we studied. Of course, some limitations arise from methodology, mainly form the fact that we have assumed a uniform thermal and physical characteristics for all pits we have studied. Local heterogeneities could have actually enhanced the local erosion. However, within the range of plausible parameters (as studied in Chapter 4), erosion could be increased by up to 20-30% at most: this does not affect our general trends, and the general conclusion that cometary activity tends to erase sharp surface features. We summarize our interpretations as follows: it is unlikely that current illumination conditions were able to carve such features, because: a) total erosion remains low compared to the observed dimensions of large and deep pits, b) tends to create elongated features due to differential erosion, and c) tends to erase the sharp features present at the surface (they become shallower and larger with time). From our simulations, we infer that current illumination conditions could have modified pits quite significantly, but not created them.

5.3.3 Implications

If sharp features are indeed erased by erosion, driven in our simulations by the sublimation of water ice, then as a corollary, we can infer that the deepest, most circular pits are likely the most primitive, or the best preserved pits. From the results of our thermal evolution model, we can try to "rank" the primitiveness of these surface features observed on these four comet nuclei: 81P would have the least processed pits (or best preserved), followed by the northern hemisphere of 67P (Chapter 4), its southern hemisphere, then 9P, and 103P. This result is primarily driven from the time each comet has spent on its current orbit, its perihelion distance, and rotational properties at a second level. When considering only the current orbit, 103P is expected to be the most processed, because it has already performed around 20 revolutions under these current illumination conditions, which are tougher at the closer perihelion distance this orbit yields. In addition, its very complex rotation distributes a large amount of energy at perihelion across the surface and throughout the orbit.

At the other end of the spectrum, 81P has probably performed ∼6 orbital revolutions under its current illumination conditions. Comets 9P and 67P could represent an intermediate state in surface alteration. Dynamical simulations for a longer historical period (100,000 years, Ip et al., 2016, see Figure 5.2) suggest that 81P and 9P might overall be less thermally-processed than 67P and 103P. If, as our simulations suggest, deep pits and sharp features are suggestive of surfaces unaltered by cometary activity (driven by the sublimation of water ice), then these dynamical simulations support our interpretation that 81P should have the least processed surface, and 103P the most processed one. Table 5.1 summarizes different characteristics of pits on 9P, 81P, 67P, and 103P: these illustrate the link between these comets' orbits, their modeled activity and its expected consequences on the surface. The maximum water production rates at the most active

facet of each comet, is highly influenced by the perihelion distance (q). Comet 103P having the smallest q produces more than 2 times the peak of water production rates at perihelion. Erosion occurs mostly as a result of highest degassing. Combined with the number of each comet's orbital revolutions, this leads to the most significant erosion for 103P, while 81P exhibits the least final erosion. The erosion values reached at the surface of the comets are relatively low compared to the dimensions of large pits.

Table 5.1: Orbital characteristics, activity outputs, and approximate pit size for the four studied comets, including 67P (studied in Chapter 4)

comet	orbits [#]	q [AU]	max H_2O [molec.s^{-1}]	max erosion [m]	pits diameter [m]	pits depth [m]
81P	6	1.59	$3.21x10^{21}$	28.25	[100s-1000s]	[10s-100s]
67P	10	1.24	$6.44x10^{21}$	77.23	100s	[10s-100s]
9P	13	1.54	$3.20x10^{21}$	83.81	[10s-100s]	[few,10s]
103P	20	1.06	$7.01x10^{21}$	265.10	[10s-100s]	[few,10s]

q: perihelion distance; max H_2O: the maximum values of production rates reached at the pits of each comet; and max erosion: the maximum erosion reached at the pits of each comet.

Vincent et al. (2017) have performed a statistical analysis of the distribution of large-scale topographic features on 67P, and found that cliff height, which correlate with surface erosion rates, follow a power law with an average cumulative power index of -1.69. Topography can be used to trace a comet's erosional history. Large cliffs characterize primordial surfaces, while eroded surfaces have smaller blocks. The power law of topography's cumulative height distribution can indicate how primitive a comet nucleus is. They performed the same analysis on surface features of 81P, 9P and 103P (see Table 2 of Vincent et al., 2017). They found that 67P and 81P have experienced similar levels of erosion, while comets such as 9P and the hyperactive 103P are more eroded, which aligns with the comets' dynamical histories, (see Figure 11 of Vincent et al., 2017). They concluded that a comet recently entering the inner Solar System will have a p-index of topographic height around -1.5. Older comets show larger power indices, up to about -2.3. A higher boundary indicates a primordial cometary surface, indicating original topographical shaping events such as small impactor' size and velocity distribution in the primordial Kuiper Belt or early cometary outbursts. The lower boundary is related to cometary material's intrinsic properties, outlining the erosion limit where a topographic feature breaks apart into smaller pieces as boulders and dust.

Kelley et al. (2021) examined several outbursts observed on comet 46P/Wirtanen and found that mass estimates were similar to or an order of magnitude larger than the mini-outbursts observed at comets 9P and 67P. They hypothesized that mini-outbursts on comets are associated with steep terrain features like cliffs and scarps, based on observations linking mini-outbursts of comet 67P to these terrain features, and even their collapse (Vincent et al., 2019). Using this assumption, they analyzed the differing frequencies of outbursts among comets 67P, 9P, 46P, and 103P, suggesting that these differences may be related to their varied terrains. Comets 67P and 9P displayed significantly higher outburst frequencies compared to 46P and 103P. Interestingly, comet 46P appears to be in an

evolutionary state between 103P and 9P in terms of surface topography and erosion. This hypothesis is in line with the evolutionary sequence proposed by Vincent et al. (2017) and Kokotanekova et al. (2018), which is based on a correlation between surface topography and insolation.

Our results are confirm these studies: different observational constraints thus seem to converge toward a possible way to estimate the relative age of a cometary surface.

5.4 Comment on the origin of pits

Various formation scenarios have been proposed in the literature to explain the origin of these depressions. Characterized by steep walls and flat bottoms, they differ from the bowl shape structure of impact craters found on the Moon and asteroids (Brownlee et al., 2004; Ip et al., 2016), and thus should be a signature of some process related to cometary activity rather than the result of collisions. However, it is important to consider that some of the pits may still be associated to impact events. Belton et al. (2013a) conducted a study on 9P and found that the evolutionary timescale for surface features is much longer than the sublimation timescale. They suggest that most pits on 9P's surface are likely due to outburst activity, accounting for 96% of them. They also attest that the pits are the most common features corresponding to expected outbursts, and terrestrial experience also supports this observation, where pits are observed at known mini-outburst locations. Moreover, they argue that geometric arrangements of pits might reflect aspects of the outburst process, with larger pits loosely confined to the highest terrain areas. Pozuelos et al. (2014) is also suggesting cometary outbursts as the origin of pits observed on 81P. Vincent et al. (2015a), Kossacki and Czechowski (2018), and Leliwa-Kopystynski (2018) propose the formation of pits by sinkhole collapse due to subsurface cavities, either primitive or formed as a result of subsurface depletion of volatiles by ice sublimation. However, Thomas et al. (2015b) argue that mechanisms such as ice sublimation or sinkhole collapse would not likely lead to the material structure giving rise to the quasi-circular aspect of pits.

Ip et al. (2016) maintain that these structures could either be quite ancient, originating from the early history in the Trans-Neptunian region, or they might have formed before crossing the water snow line. In the latter situation, sublimation erosion processes driven by more volatile ices, such as CO and CO_2, could be significant. This idea is supported by the detection of persistent coma activity in several Jupiter-family comets well beyond 3 AU (Kelley et al., 2013; Wierzchos and Womack, 2020). The dynamical past of each comet in our study (Ip et al., 2016) implies that previous orbits likely had greater perihelion distances. It is thus reasonable to think that these comet nuclei are currently experiencing the most processing that ever sustained at (any) perihelion, and that preserved morphological surface features have been preserved for some time. Now turning to the origin of these pits: we can infer from all the discussion above, that pits cannot be formed by erosion.

The circular aspect of the pits suggests that a likely scenario should involve a rather explosive mechanism, able to carve a large amount of cometary material in a short period

of time, in a region of the Solar System where water ice is not sublimating (or we would face the fate discussed above, with progressive elongation and erosion of the created features). The Centaur phase of each JFC may be key here to understand the origin of surface features.
In the Centaur region, sudden thermal events such as clathrate destabilization and the crystallization of amorphous ice could explain important explosions at the surface of the comet (Miles, 2016; Wierzchos and Womack, 2020), that could lead to the pits formation. Thermal simulations by Mousis et al. (2015) show that both of these mechanisms are plausible at the depths consistent with those observed in the Seth region pits.
Many Centaurs indeed exhibit important, recurrent sporadic outburst activity. For instance, 29P/Schwassmann-Wachmann is a Centaur that regularly undergoes significant CO gas and dust outbursts (Wierzchos and Womack, 2020), possibly resulting from amorphous ice crystallization when the temperature reaches around 120 K, even though Wierzchos and Womack (2020) conclude not finding any evidence of an existing straightforward relationship between outbursts of dust and gas. Recurrent outbursts are also observed on the Centaur 174/P Echeclus, even though the CO amount present within its nucleus is 40 times lower than that of 29P (Kareta et al., 2019). Ip et al. (2016) found that such features with steep walls and flat bottoms, with sizes between 150 m and 1 km on 67P, have the same size frequency distribution as those on 81P and 9P. This suggests that they might share the same origin and formation mechanism. If the formation mechanism is indeed the same for these JFCs, it likely occurred in the Centaur phase.

Nevertheless, we cannot rule out the possibility that these depressions may have formed during cometary stages before the Centaur phase. In this regard, Comet Interceptor mission could provide further insights. This mission is designed to encounter a long-period comet. If such a comet is found to have pits on its surface, it would suggest the intriguing possibility that these pits formed in early stages of the comet, either during the comet's formation or in later stages but still prior to the Centaur phase.

In conclusion, pits observed on the surface of JFCs are unlikely to have formed as a result of outgassing erosion, neither in the comets' recent orbits under current illumination conditions, nor in older phases of the comets. Instead, these features are more likely being elongated and erased with time. The pits' enigmatic origin, possibly arising from older dynamical stages of the comets, possibly from the Centaur phase, calls for further investigation into various potential formation scenarios.

Chapter 6

Impact of shape on cometary activity observed from the ground

6.1 Context for a case study of 67P, 9P, and 103P

Cometary activity is characterized by relatively well-understood patterns, driven by phase transitions triggered at various heliocentric distances. However, each comet remains intrinsically unpredictable. For instance, the peak production of water does not always occur at perihelion and can take place before or after. Additionally, many comets exhibit discrete emission areas, that can be active only at certain times during their orbit, such as comets 9P and 103P (Farnham and Thomas, 2013a; A'Hearn et al., 2011). The water production rates can also be either symmetric or asymmetric around perihelion, as observed for comets Hale-Bopp and 67P, respectively (Sekanina, 1981). The rate of change of the activity curve, or the slopes, also vary between comets mainly because of the spin axis orientation and shape (Marschall et al., 2019).
In fact, the production of dust and gas from comet nuclei as they orbit around the Sun is driven by various factors, including their composition and structure, rotational properties or shape. Skorov et al. (2023) analyzed the impact of different parameters, including microstructures and thermophysical characteristics, on gas production of comets. They showed that the influence of structural parameters (e.g., porosity and dust layer thickness) was small or moderate at perihelion but increases with the heliocentric distance, and that when the bulk thermal conductivity decreases (as if the comet was far from perihelion), the role of the structural characteristics increases. They also found that thermophysical characteristics highly depend on thermal conductivity, the uncertainty around which leads to significant uncertainties in gas production. De Sanctis et al. (2010b) argues that differently shaped nuclei can have different internal structures, leading to different activity patterns, and that the orientation of the rotation axis plays a strong role in determining seasonal effects on the observed gas fluxes. Marshall et al. (2019) found that the illuminated cross-section of known nuclei can vary by as much as 50% over an orbit due to shape and obliquity, and conclude that it is difficult to determine the nature of cometary outgassing solely from heliocentric production rates without prior knowledge of basic parameters such as shape, spin axis orientation, and active regions.
In this chapter, we aim to understand the relative influence of a nucleus shape, surface

and internal properties on the water production rates for comets 67P, 103P and 9P. For those comets, a large sample of data is available from ground-based observations and from spacecraft missions that have visited them, and their shapes have been modeled with sufficient resolution. We want to assess whether the information of the shape leaves a signature in ground-based observations, and whether our interpretation of these curves can be biased by a possible complex shape behind. Ultimately, we want to assess whether such nucleus characteristics could be retrieved from ground-based observations for other nuclei.
To achieve this, we first calculate the energy received by each facet of the shape model for each comet, taking into consideration both direct insolation and the impact of the nucleus' overall shape. This energy serves as the surface condition for a 1D thermal evolution model (Lasue et al., 2008), which in turn yields theoretical water production rates as a function of heliocentric distance. We use the same methodology for describing the surface energy model, accounting for the shape model, and the thermal evolution model as detailed in Chapter 2. We apply this method using different initial parameters for the nuclei, such as porosity, dust-to-ice ratio, dust mantle, and Hertz factor. We then compare the simulated water production rates, obtained from different sets of simulations, to observed water or OH production rates observed in the past.

6.2 Some elements of methodology

6.2.1 Observational datasets

6.2.1.1 67P: H_2O production rates observed by Rosetta

For comet 67P, we use water production rates from Läuter et al. (2020b), derived from data collected by *ROSINA* observations (Figure 6.1). COPS and DFMS provided in-situ densities of 14 gas species. They were collected during the comet mission from August 2014 to September 2016 and were fitted to an inverse coma model. Surface emissions were retrieved for a cometary shape, and production rates were determined for each gas (see more details in Läuter et al., 2020b). In this study we focus exclusively on H_2O.

These data can effectively act as a proxy for ground-based production rate observations. Indeed, Figure 6.2, from Hansen et al. (2016) presents the water production of 67P as a function of heliocentric distance, as observed by *Rosetta*'s various instruments, in conjunction with scaled ground-based dust measurements. In the figure, a strong correlation between ROSINA water production rate measurements and scaled ground-based dust measurements is observed, implying a nearly constant ratio of dust surface area to water production during the perihelion passage (see more details in Hansen et al., 2016).

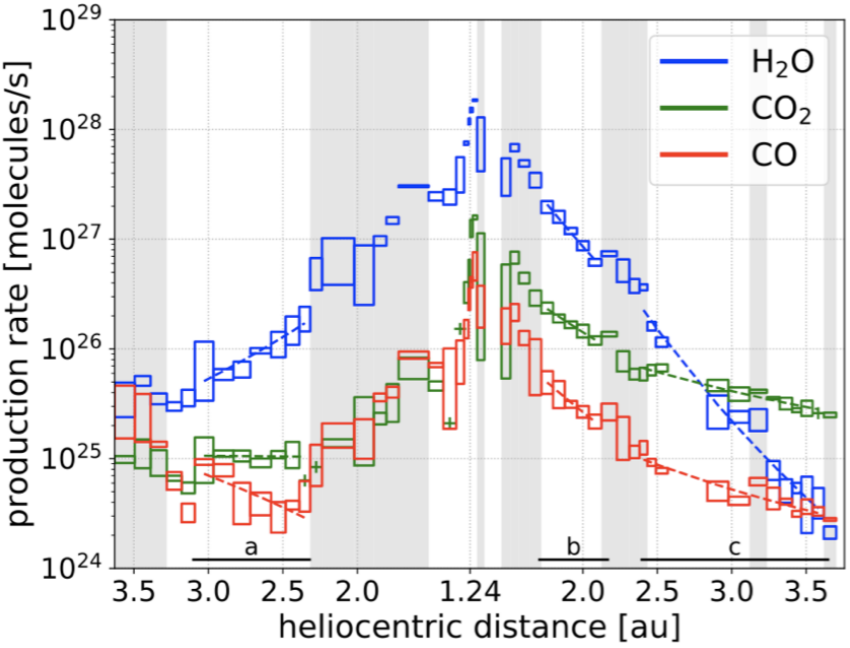

Figure 6.1: Production rates of H_2O, CO_2 and CO as a function of heliocentric distance of comet 67P/C-G from Läuter et al. (2020b). The boxes indicate the uncertainties, presented in the paper.

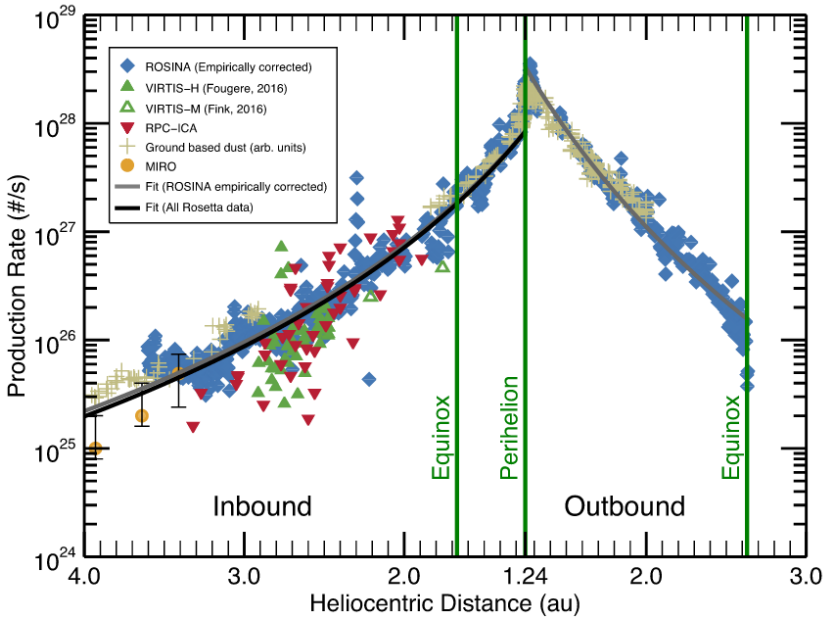

Figure 6.2: H_2O production rate of 67P as determined by multiple instruments: ROSINA, VIRTIS, RPC/ICA, MIRO, and ground-based telescopes. The ground-based data are not water productions and have been scaled using an arbitrary factor for comparative purposes. Grey and black lines represent the fits to the ROSINA and all inbound *Rosetta* data, respectively. Credits: Hansen et al. (2016).

6.2.1.2 103P: H_2O and OH data collected over several perihelion passages

In the case of comet 103P, we consider H_2O data presented in Knight and Schleicher (2013a). The authors computed a vectorial-equivalent water production rate using the Haser model for OH production rates, measured at Lowell Observatory from 1991 to 2011 and presented in Figure 6.3. The photometry was carried out on two nights in 1991, four nights in 1997/98, and 13 nights in 2010/11. We will also place our results in the context of water data from various other sources, all summarized in (Knight and Schleicher, 2013a, see Figure 6.4).

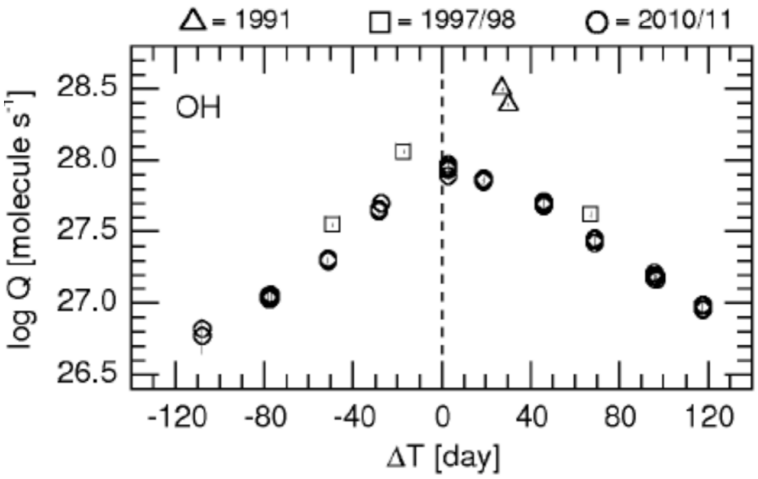

Figure 6.3: Log-scaled OH production rates of 103P/Hartley 2 as a function of time from perihelion, based on data from Lowell Observatory for three distinct perihelion passages: 1991, 1997/98, and 2010/11. Credits: Knight and Schleicher (2013a).

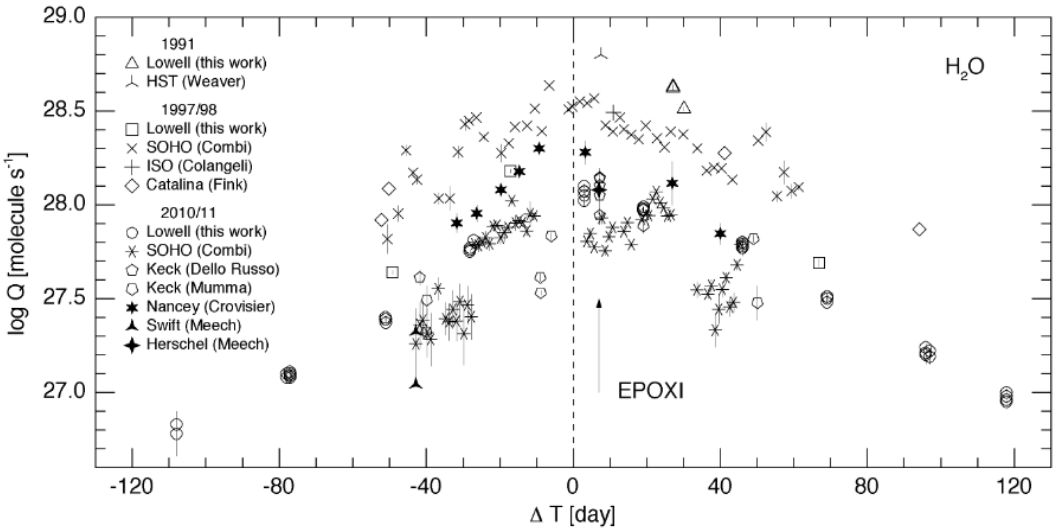

Figure 6.4: H_2O production rates of 103P as a function of time from perihelion, derived from various data including the OH data of Figure 6.3. A large dispersion is observed in the different water rates of the different studies. Credits: Knight and Schleicher (2013a).

6.2.1.3 9P: H_2O and OH data during the Deep Impact mission

For comet 9P, we rely on data from (Biver et al., 2007, see Figure 6.5). H_2O production rates are either based on Nançay observations of the OH radical or Odin observations of the H_2O line at 557 GHz.

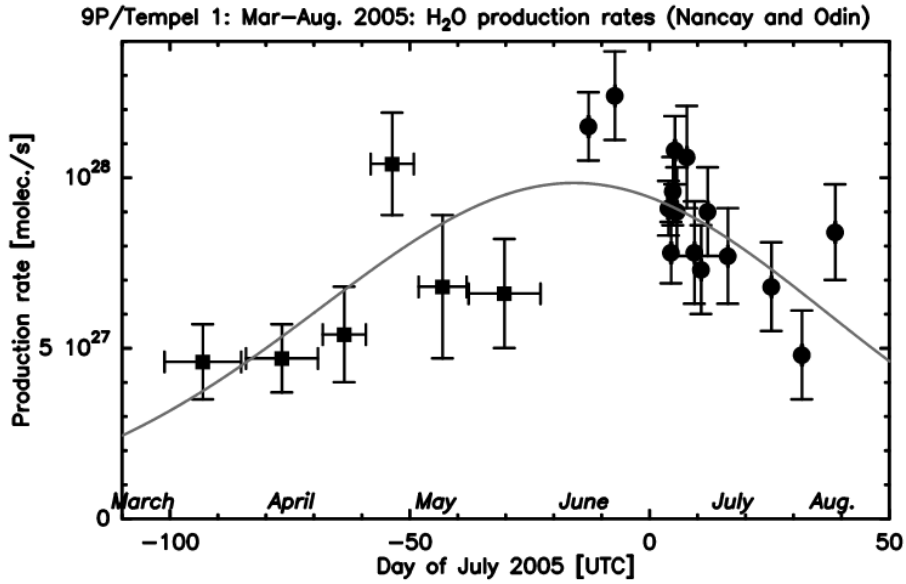

Figure 6.5: Molecular "apparent" production rates of comet 9P/Tempel 1, based on either Nançay observations of the OH radical (squares) or Odin observations of the H_2O line at 557 GHz (circles). Credits: Biver et al. (2007).

Comet 9P was observed both before and after the *Deep Impact* mission. The Nançay radio telescope monitored the comet's outgassing of OH for four months from March to June, while the Odin satellite observed H_2O emissions from June to August. Following the impact on July 4th, the Odin satellite continuously monitored the H_2O line at 557 GHz for 38 hours and continued weekly monitoring thereafter. The impact occurred during a period of naturally increasing outgassing, which reached its peak a few hours after the impact (Biver et al., 2007).

All aforementioned data of the three comets were collected during the time period surrounding each comet's perihelion, when their respective activities reach peak levels.

6.2.2 Shape models used for the three comets

For each studied comet (67P, 9P, and 103P), we reduced the resolution of the shape models to a maximum of 500 facets to optimize computation time while still accounting for the overall shape of the nucleus. This resolution does not incorporate local topography, which was deemed unnecessary for the purposes of this work. We show the different shape models used in this study in Figure 6.6 . For each comet nucleus, a spherical model with the same surface area was created, in order to compare the performance of both shapes in reproducing the observed water production rates over the orbit, and assess whether a

signature of the actual shape can be inferred.

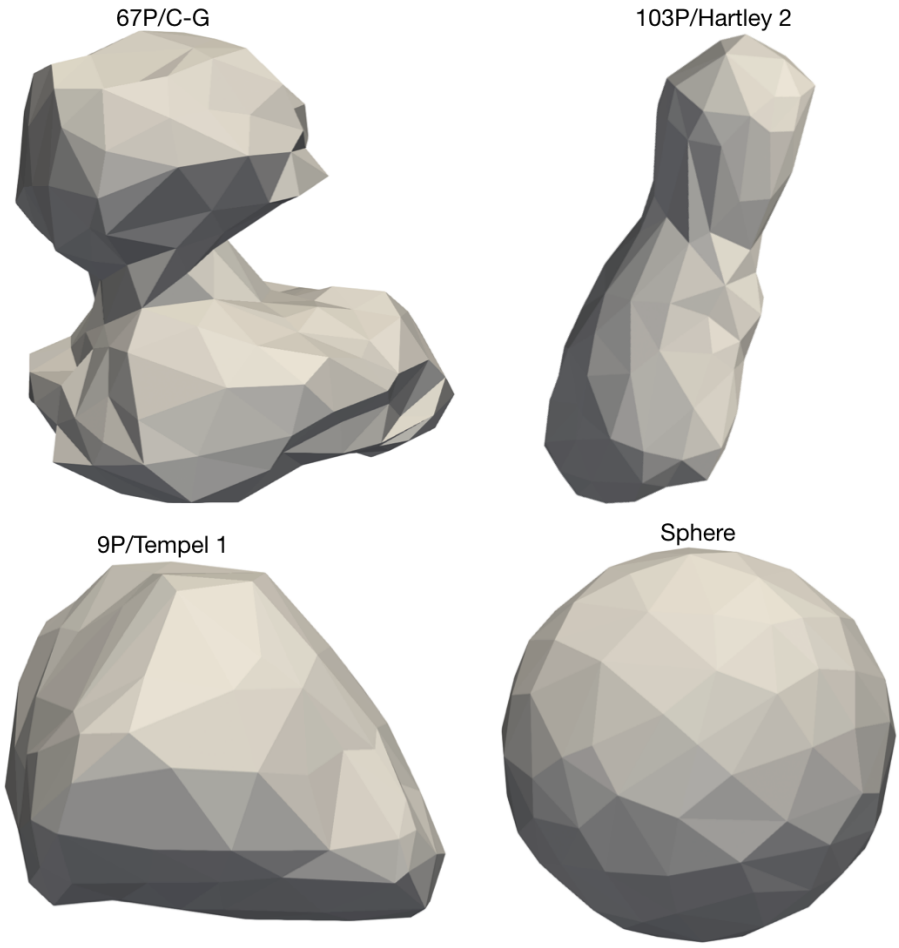

Figure 6.6: Shape models used in our thermal simulations for the comets of 67P, 103P, and 9P, as well as a spherical nucleus. Note that the representations are not to scale.

6.3 Influence of nucleus shape on water production rates

In this section, we aim to investigate the influence of the nucleus shape on the secular production of water. To achieve this, we conducted thermal simulations using both the shape and sphere models of each comet during each observation period. Our objective is to compare the predicted production rates obtained using the shape model with those obtained using the sphere, and to compare both sets of results to the observed dataset. As previously noted in Chapters 2 and 3, our simulations assume a homogeneous comet composed of dust and H_2O ice, with a dust/ice mass ratio of 1 and a porosity of 75% for the reference simulations. The reference initial parameters used in our simulations are summarized in Table 2.2 of Chapter 2. We note that these initial parameters are subject

to variation in our simulations, as we tested the influence of several of them: such changes will be specified where relevant.

The production rates of 67P obtained from our simulations are presented in Figure 6.7.

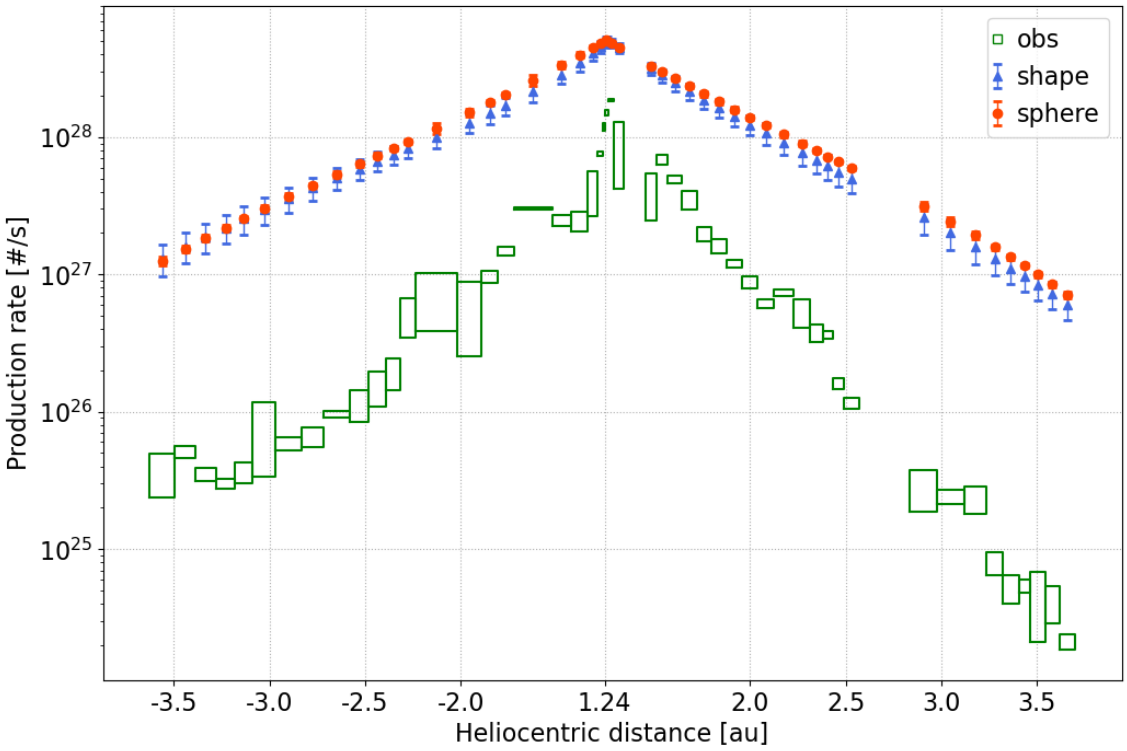

Figure 6.7: Water production rates of comet 67P. Green boxes: observed production rates from Läuter et al. (2020b), shown in Figure 6.1; blue and red points: production rates generated using the shape model and the sphere, respectively. Error bars of all our theoretical data represent the standard deviation during each time interval. The complex shape of the nuclei leads to variations in production rates during each time interval, leading to larger error bars for the shape model compared to the sphere.

The production rates of both the shape model and the sphere are strikingly similar, with only minimal differences, compared to the differences with the observations, despite the complex bilobate shape of the nucleus. The spherical model yields slightly higher magnitudes, exceeding the shape model's production rates by a maximum of 20% occurring far from perihelion (∼2 AU), but this discrepancy still falls within their error bars. This suggests that the illuminated cross-section is almost unchanged throughout the observation period, and is nearly equivalent to that of the sphere, as all other characteristics of the nucleus remain the same for both models (spin axis, structure, and composition). This result was anticipated by Marshall et al. (2019, see Figure 1), who reported a variation of less than 5% in the cross-section of 67P throughout its orbit. Somehow, it was also anticipated by Lamy et al. (2007), who missed the bilobate shape of 67P due to a complex interplay between shape and rotational axis of the nucleus, leading to the roundish

potato-like shape anticipated in the pre-*Rosetta* era. This result suggests that information on the shape would not be present in 67P's production rates observed from the ground.

The production rates, from both the shape and sphere, match the overall trends of the observed data, taking into account the associated measurement uncertainties. The water flux decreases as a function of heliocentric distance but does not follow the heliocentric distance dependence r_h^{-2} and, rather, presents an asymmetry between pre- and post-perihelion that we observe on both the theoretical and observation curves. This asymmetry is mainly due to the tilted spin axis (obliquity of $\sim$52°). As attested by Marshall et al. (2019), the heliocentric dependence of water production rate remains unchanged for different nucleus shapes as long as the rotation axis is perpendicular to the orbital plane. Obliquity of the spin axis can lead to arbitrary deviations from the expected inverse square law dependence of water. However, we notice that in the observations, the asymmetry is accentuated, indicating that other factors besides the spin axis are likely interfering.
In terms of magnitude, the theoretical production rates exceed the observations by approximately half an order of magnitude during perihelion, and at large distances from perihelion, they exceed one order of magnitude.

We conducted simulations of production rates using a shape model composed of 1000 facets to evaluate the influence of the 500-facet model in representing cometary activity influenced solely by the global shape. The 1000-facet model indeed displays some high-level, large local topography (of the order of a few hundred meters, see Figure 6.8).

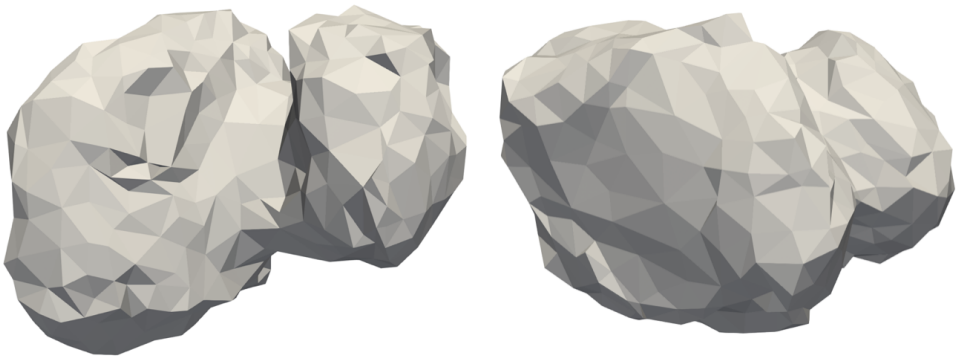

Figure 6.8: 1000-facet shape model of 67P, derived from the SHAP7 SPG (Preusker et al., 2017).

As shown in Figure 6.9, the production rates obtained using both 500-facet and 1000-facet models are consistent. This indicates that surface features at a scale of a few hundred meters do not significantly impact the activity of the comet, at least at the perihelion period. However, it is noteworthy that during this time, it is primarily the southern hemisphere that contributes to activity since it is facing the sun, and since it is relatively smoother compared to the north, the activity would not change much in comparison to the smooth 500-facet shape. The slight differences observed between the two models are probably due to the difference in surface area between the two models, resulting from the simplification process used to create them.

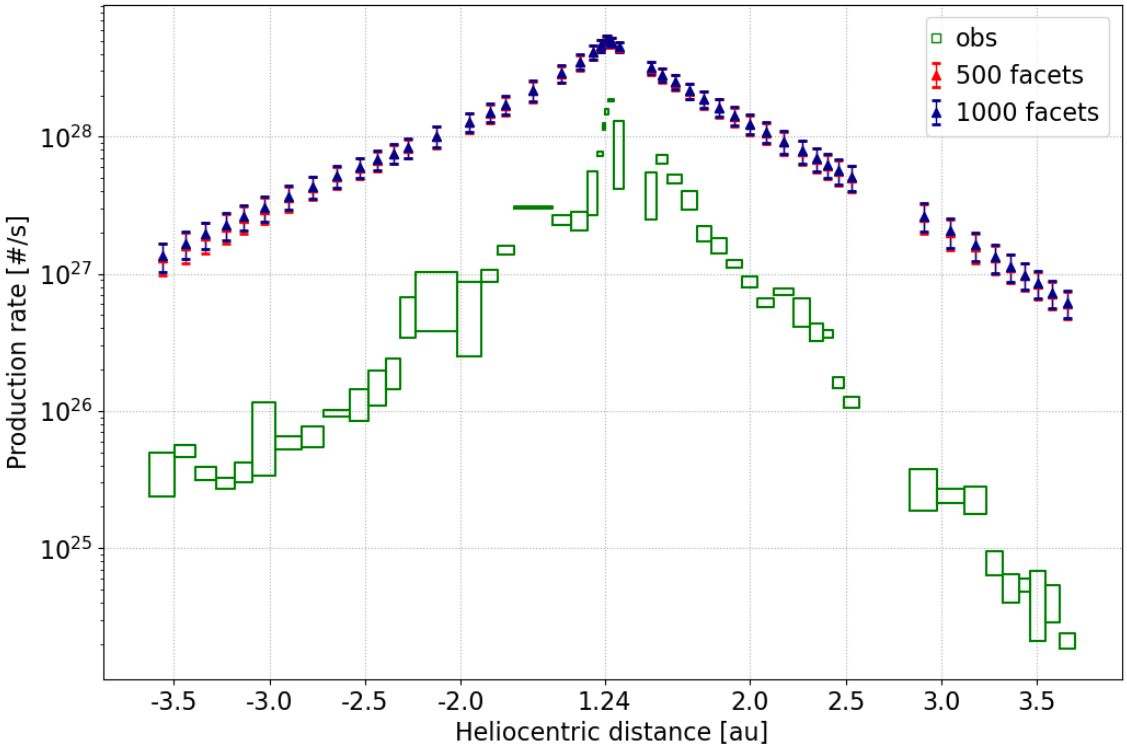

Figure 6.9: Water production rates of comet 67P. Green boxes: observed production rates from Läuter et al. (2020b), blue and red points: the production rates generated using a shape model of 500 facets and a shape model of 1000 facets, respectively. Error bars of the theoretical data represent the standard deviation during each time interval.

Comet 9P exhibits a behavior similar to 67P, with both the sphere and shape following the observation global trend (Figure 6.10), with more than one order of magnitude difference between simulated and observed production rates. The sphere produces higher rates throughout the observation period, reaching up double the production rates by the shape few days after the perihelion. This contrasts with 67P's case, where such discrepancies were notably smaller and reached at greater distances from perihelion. This highlights the impact of the shape, combined with the spin axis, on the activity of this comet. This may be counter-intuitive, as 9P's shape resembles more a sphere than 67P's, but the varying position of the comet in relation to the Sun during observation results in variations in its cross-section, reaching ∼10% throughout its orbits when considering the obliquity of 9P, following Marshall et al. (2019). We point out that our study period only encompasses a few months around perihelion. The differences between the production rates could be higher further from perihelion, between 0 and 2 AU, as indicated by the variations of the cross-section (Marshall et al., 2019). Nonetheless, the time around perihelion, when the comet's activity is at its peak, remains the most observationally compelling period.

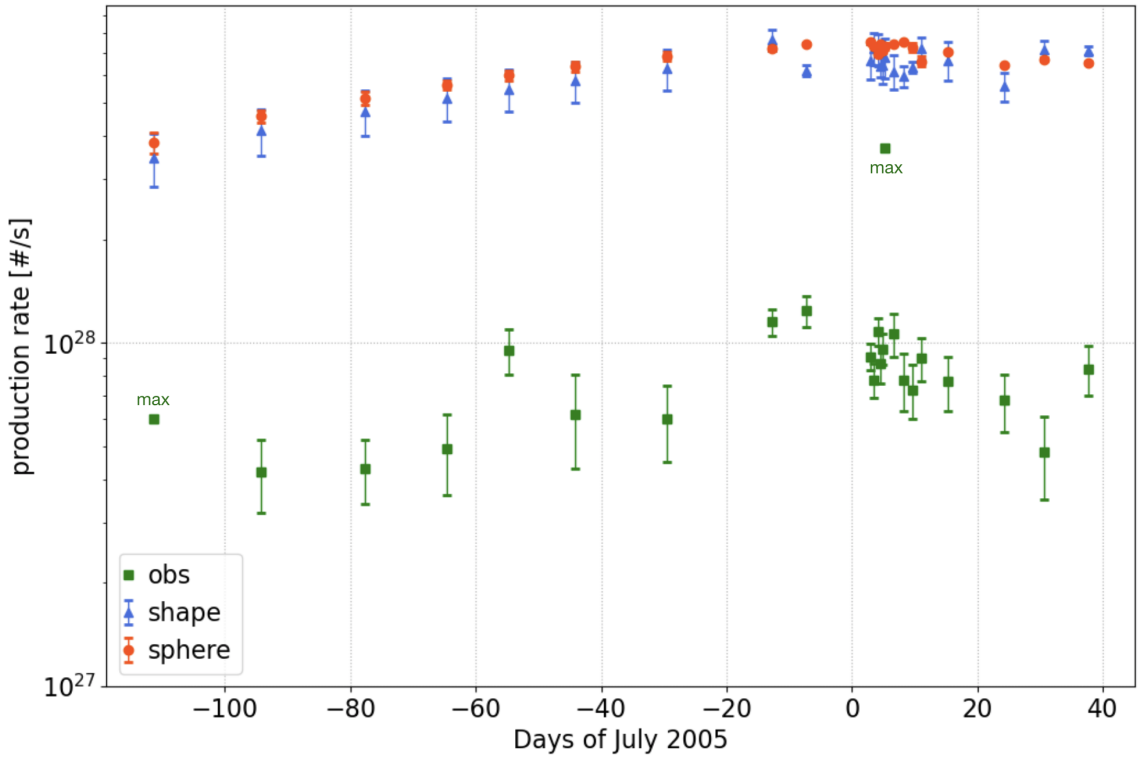

Figure 6.10: Water production rates of comet 9P. Green points: observed production rates from Biver et al. (2007), shown in Figure 6.5, blue and red points: production rates generated using the shape model and the sphere, respectively. Error bars of the theoretical data represent the standard deviation during each time interval.

For comet 103P, both the spherical and shape models yield water production rates that are relatively similar to observations during the few days around perihelion (Figure 6.11), which differs from the results seen with comets 67P and 9P where the model-derived production rates were significantly higher than the observations. The disparity between the production rates of the shape and sphere models can amount to up to 30%. Indeed, during the perihelion period, the variation in the cross-section of 103P's nucleus can reach around 15% for an obliquity value similar to that of 103P, as a result of the combination of its spin axis and shape (Marshall et al., 2019).
However, both the sphere and shape models exhibit consistently similar trends throughout the studied time frame, and deviate from the observations outside the perihelion, similar to what we observed for 67P.

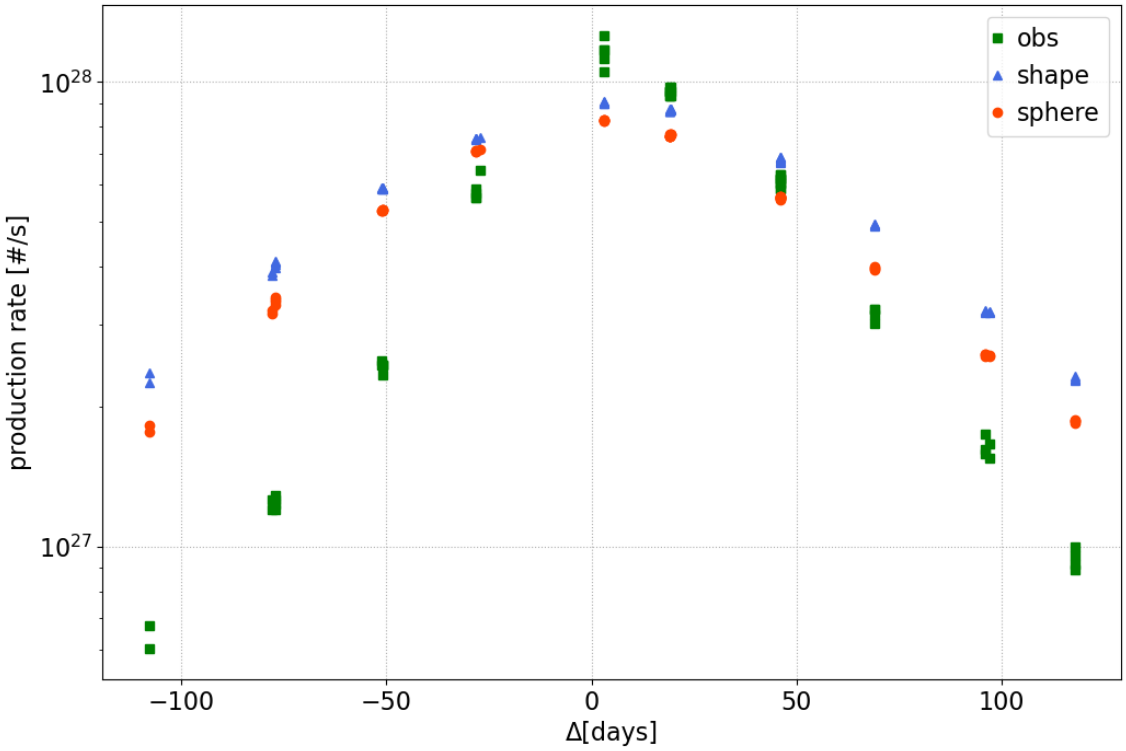

Figure 6.11: Water production rates of comet 103P. Green points: observed production rates from Knight and Schleicher (2013a), shown in Figure 6.3, blue and red points: the production rates generated using the shape model and the sphere, respectively.

The notable differences in the slopes between the simulated and observed production rates for both 67P and 103P, as well as the discrepancies observed between the simulated absolute water production, for both the shape and sphere models, and the observed data for all three comets indicate that the shape may have some influence on water production rates, but it is not the dominant factor. Rather, other factors such as composition and internal structure may play a more crucial role in influencing water production rates, which we will explore further in the subsequent section.

6.4 Role of composition and structure

With the aim to investigate how the composition and internal structure of nuclei may influence their observed volatile production rates, we conducted thermal simulations by varying these parameters of the model. We used different initial parameters in our simulation, within the range of values typically observed for comets in general. Specifically, we test different values of porosity ϕ, dust mantle's initial thickness, dust/ice mass ratio, and the thermal conductivity through variations of the Hertz factor (h) while keeping all else constant. The results of these simulations were relatively consistent for all three comets: we present results for comet 67P in Figures 6.12 and 6.13.

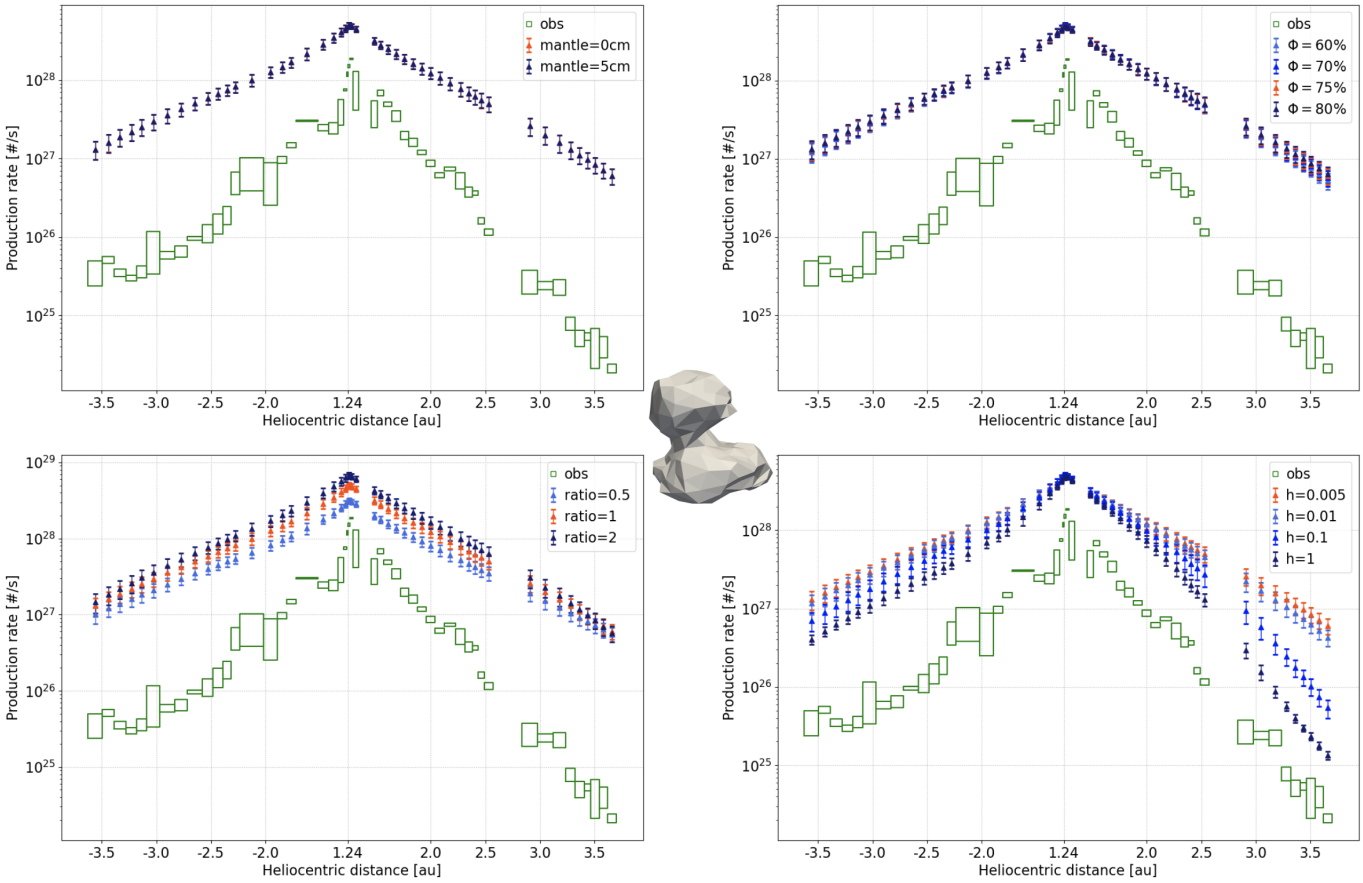

Figure 6.12: Influence of key parameters: initial dust mantle, bulk porosity, dust/ice mass ratio, and Hertz factor, on the production rates of 67P, and comparison to observed ones (Läuter et al., 2020b) represented in green boxes.

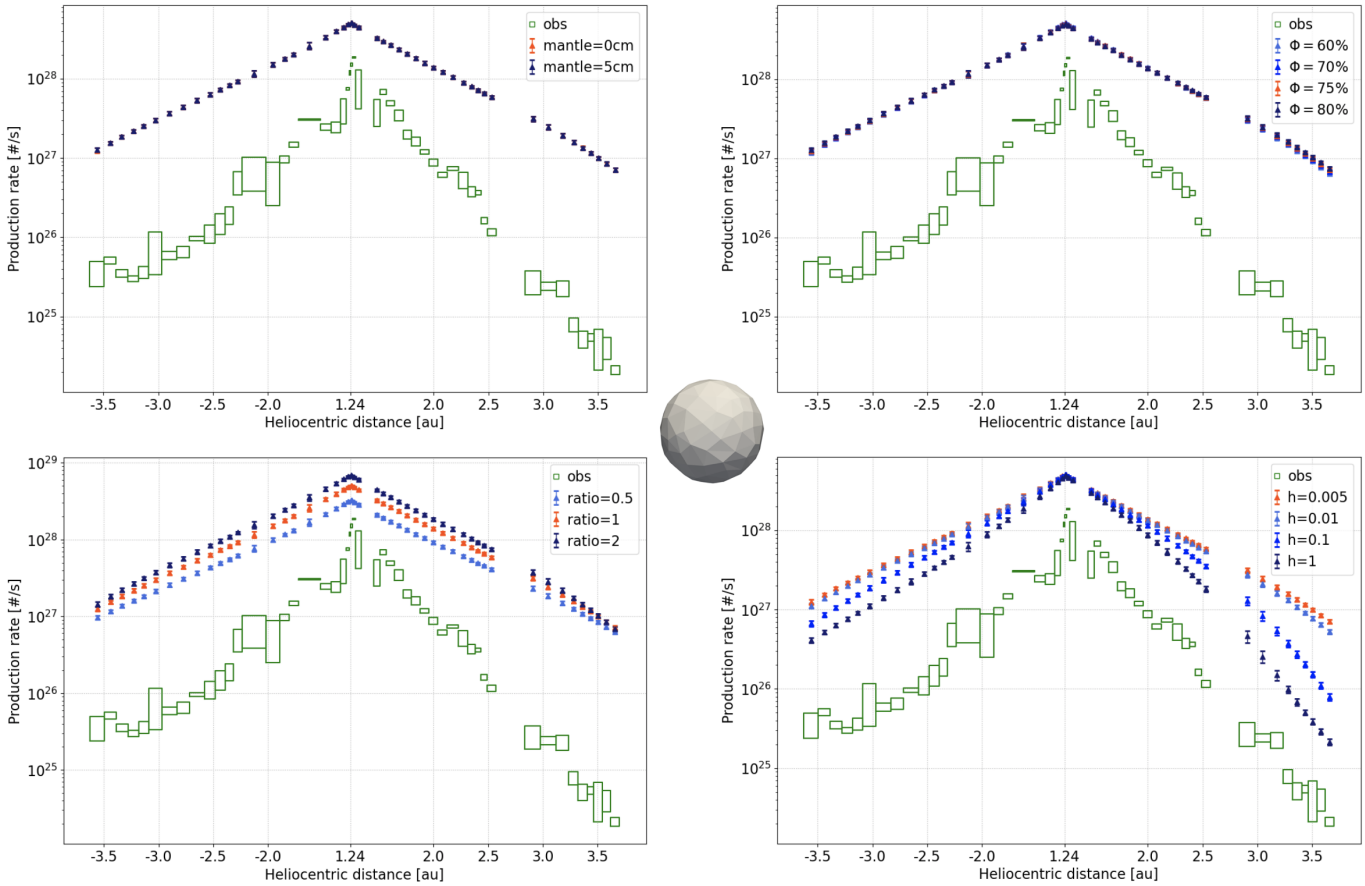

Figure 6.13: Influence of key parameters: initial dust mantle, porosity, dust/ice ratio, and Hertz factor, on the production rates using a sphere instead of the shape model of 67P (see Figure 6.12), and comparison to observed ones (Läuter et al., 2020b) represented in green boxes.

Simulations with both varying internal porosity and initial dust mantle thickness, within the range typically observed in comets (60%, 70%, 75%, and 80% for porosity, and 0 cm or 5 cm for dust mantle thickness), and while keeping other initial parameters at their reference values, show that these parameters do not have a significant impact on the simulated production rates, either when using the actual shape or the sphere for the nucleus. Changing the dust/ice ratio, however, leads to considerable changes in the production rates during the period of highest activity, where a higher ratio leads to higher outgassing (Benseguane et al., 2022). We notice that this effect decreases with increasing heliocentric distance. The parameter with the most influence is the thermal conductivity, which we tested by considering different values of Hertz factor h. We observe that varying h, and thus conductivity, directly and notably influences the production rates as a function of heliocentric distance. This leads to different slopes of the pre- and post-perihelion gas production curves: they are steeper with higher values of conductivity. As a result, for 67P, we obtain a better qualitative fit to the post-perihelion curve if we consider a larger thermal conductivity than in our reference simulation. Additionally, the shape model shows a slightly improved post-perihelion fit compared to the sphere model

for high values of the conductivity.

Contrary to the effect of the initial dust/ice ratio, the effect of varying conductivity is not only insignificant during the closest approach, but also becomes increasingly significant further from perihelion, where the amount of production rates with h=1 drop by more than one order of magnitude compared to the case with h=0.005. Therefore, there is a complex interplay between the dust to ice ratio, which results in a larger value for the effective thermal conductivity of the material, and the composition of the material "available" to be sublimated. A higher thermal conductivity implies a higher thermal inertia: with a higher thermal inertia, the nucleus takes longer to heat up. As a result, the heat is absorbed more slowly and distributed deeper within the nucleus. This slower heating can influence the production rates. At this point of our tests, we note that using a different thermal conductivity can better adjust the slopes from a qualitative point of view, but the simulated production rates remain overestimated compared to the observations. This suggests that taking into account surface heterogeneity may be essential for more accurate predictions.

6.5 Influence of surface heterogeneity

To investigate the influence of surface heterogeneities, such as the presence of partial activity due to compositional heterogeneities or the presence of dust mantle on specific regions of the surface, and whether they can get simulations closer to observations, we conducted tests using known characteristics of partial activity in the studied comets, or by simply reducing the fraction of the overall production rate.

By only including the regions of 67P derived from Läuter et al. (2019b, see Figure 6.14) as the most active during the perihelion phase, we were able to obtain production rates that closely match observations for both the shape and sphere, as shown in Figure 6.15.

However, the post-perihelion period, in contrast to the pre-perihelion, does not fit as well with the observations. There remains an overproduction of water in our simulations when compared to the actual observations. By increasing the conductivity and still considering solely active regions, the post-perihelion slope can be adjusted qualitatively, resulting in a better fit with observational data, especially when considering the actual shape vs the sphere (Figure 6.16). The observed production rates are within the simulated data corresponding to the range of Hertz factor commonly used in cometary models. These results indicate that, within the bounds of validity of the previous assumptions, during this perihelion passage, 67P would have required different conductivity values before and after perihelion. It is likely that the structure or composition of the comet was affected by the sustained activity during this period, or simply that distinct regions of the nucleus with distinct conductivities contribute to the observed activity. They also demonstrate the necessity of combining information about both the shape and large scale heterogeneities, whether on the subsurface or the surface, in order to accurately fit the data. This highlights the complexity of the observable and the importance of considering multiple factors when analyzing cometary activity and behavior.

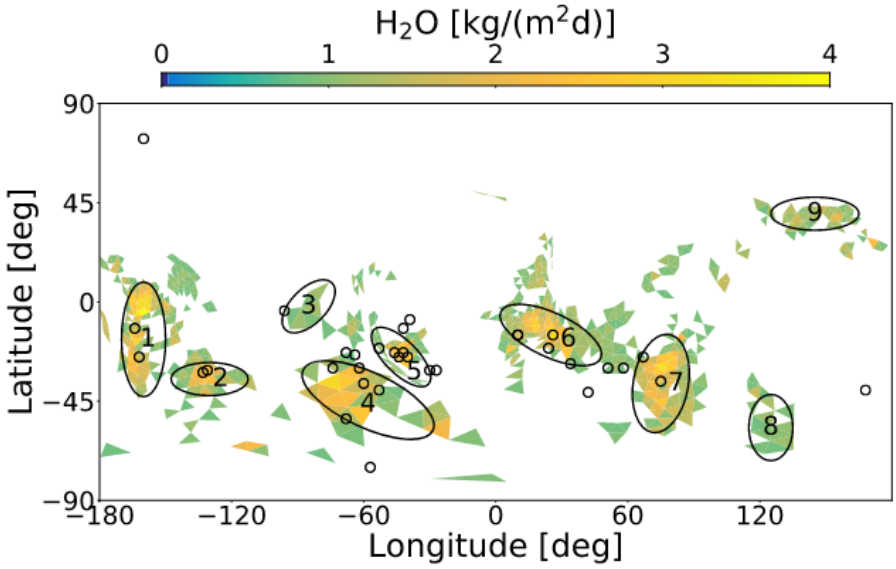

Figure 6.14: Surface H_2O emission rates for the most active regions of 67P, accounting for 50% of the total emission within [-50, 50] days of perihelion. Short-lived outbursts are indicated by circles. Credits: Läuter et al. (2019b).

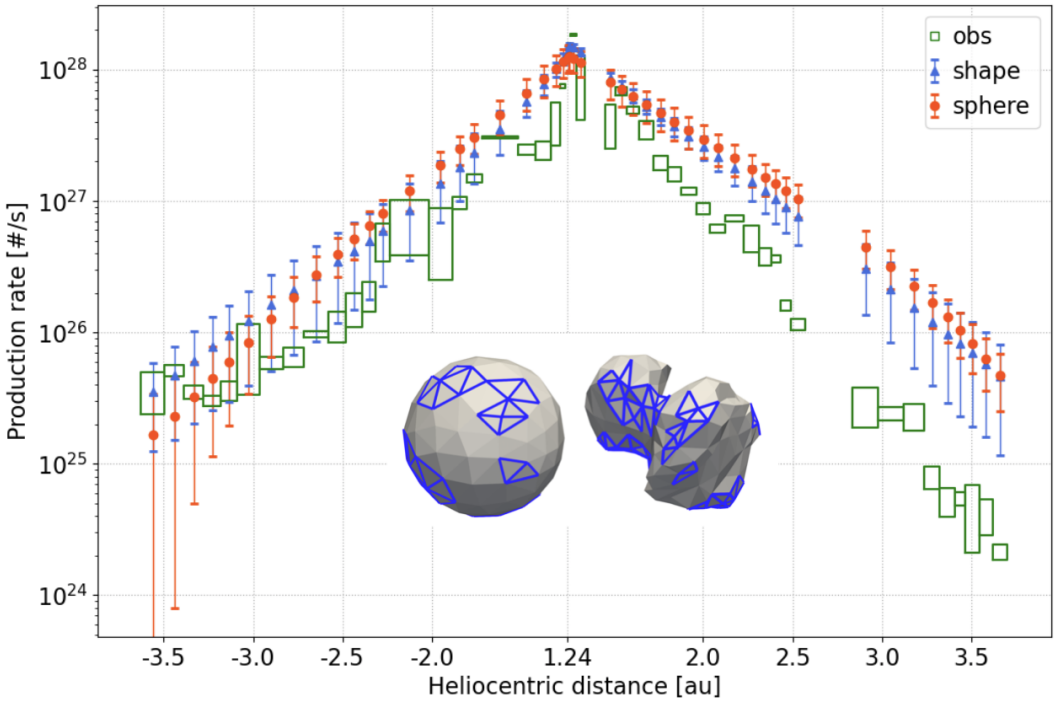

Figure 6.15: Water production rates generated considering only active regions of 67P proposed by Läuter et al. (2019b), for the shape model and the sphere, and comparison to observed water production rates from Läuter et al. (2020b). The active facets on the sphere were localized based on their latitude and longitude positions on the comet's surface.

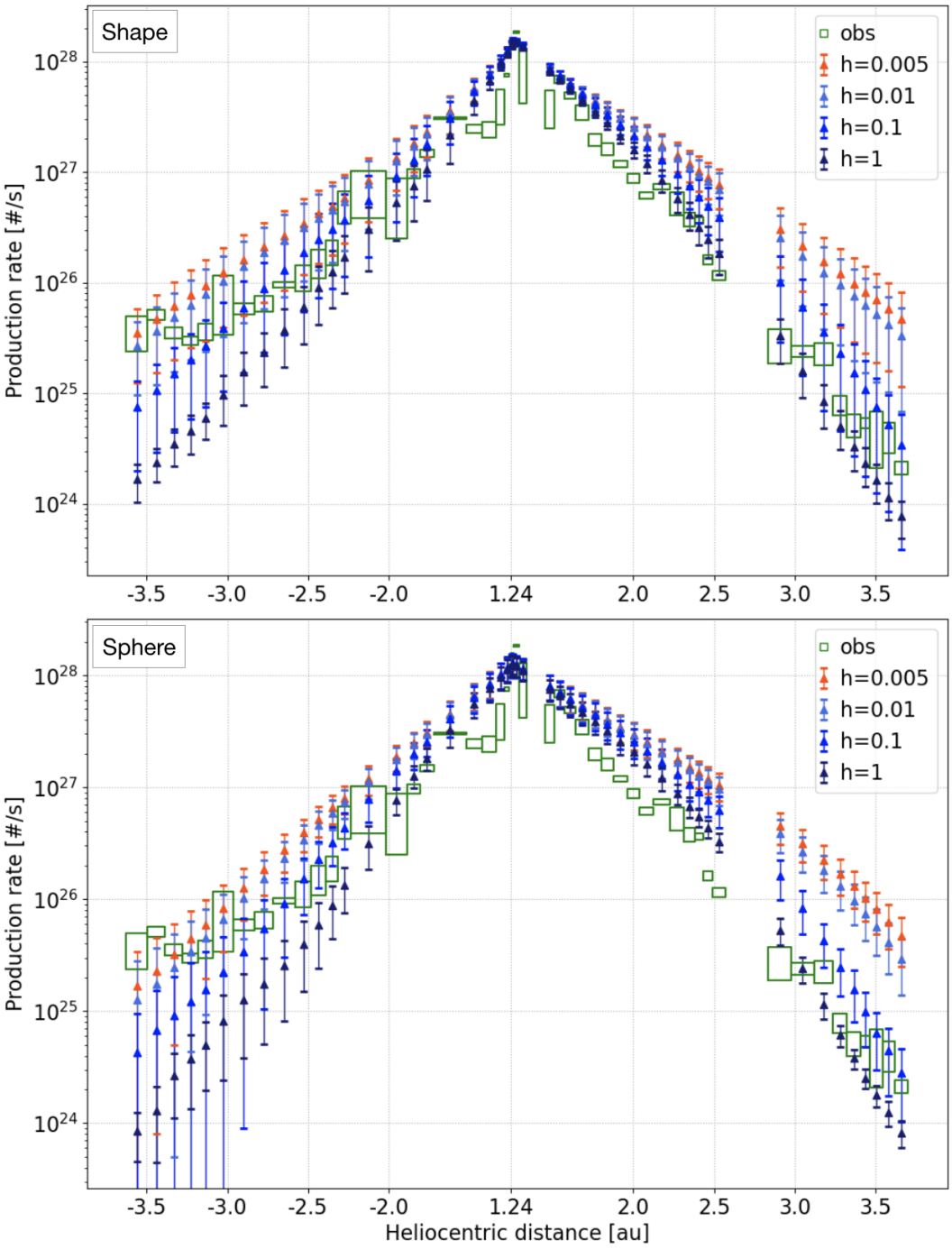

Figure 6.16: Water production rates generated using active regions of 67P (Läuter et al., 2019b) for different values of Hertz factor, and comparison to observed water production rates from Läuter et al. (2020b), using the shape and sphere up and down respectively.

It is important to note that, according to Läuter et al. (2019b), the nine active regions are thought to account for about 50% of the total activity, with H_2O emissions observable around the entire nucleus during the perihelion period. Despite this, our simulations align closely with the full observed activity, notably pre-perihelion, indicating that our model

overestimates water production. This overestimation could be marginally influenced by overstepping the region boundaries in our lower resolution shape model. Nonetheless, achieving such alignment using only these active regions and their immediate surroundings suggests that the remaining activity across the nucleus is likely homogeneous.

We constrained the activity to specific regions of 103P's nucleus (Figure 6.17), as activity has been observed to be heterogeneous between the two lobes of the nucleus (Syal et al., 2013). Our results indicate that restricting activity to solely one of the lobes or the neck is inadequate for reproducing the observed activity. This implies that activity likely originates from more extensive surface areas. Additionally, the slopes do not improve with these tests, reinforcing the hypothesis that they could be due to different thermal or mechanical properties.

Overall, as already seen for 67P, varying the Hertz factor helped slightly adjust the slopes of the simulated curves, with a value of 0.01 providing a better fit (Figure 6.18).

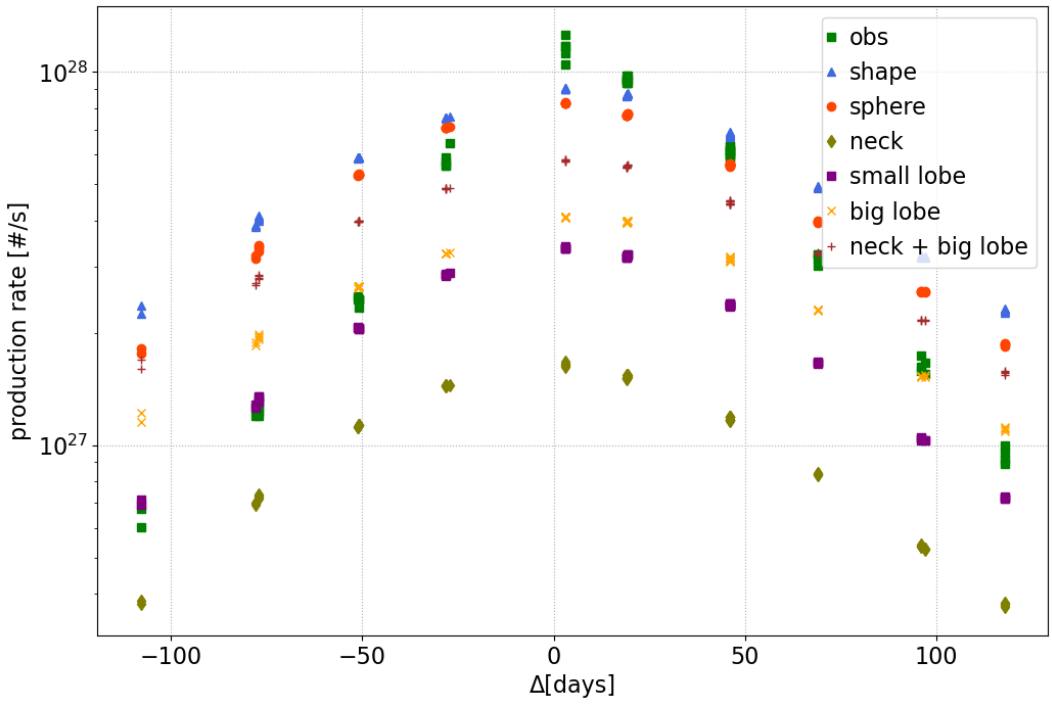

Figure 6.17: Water production rates resulting from considering partial activity of comet 103P, and comparison to observed production rates from Knight and Schleicher (2013a).

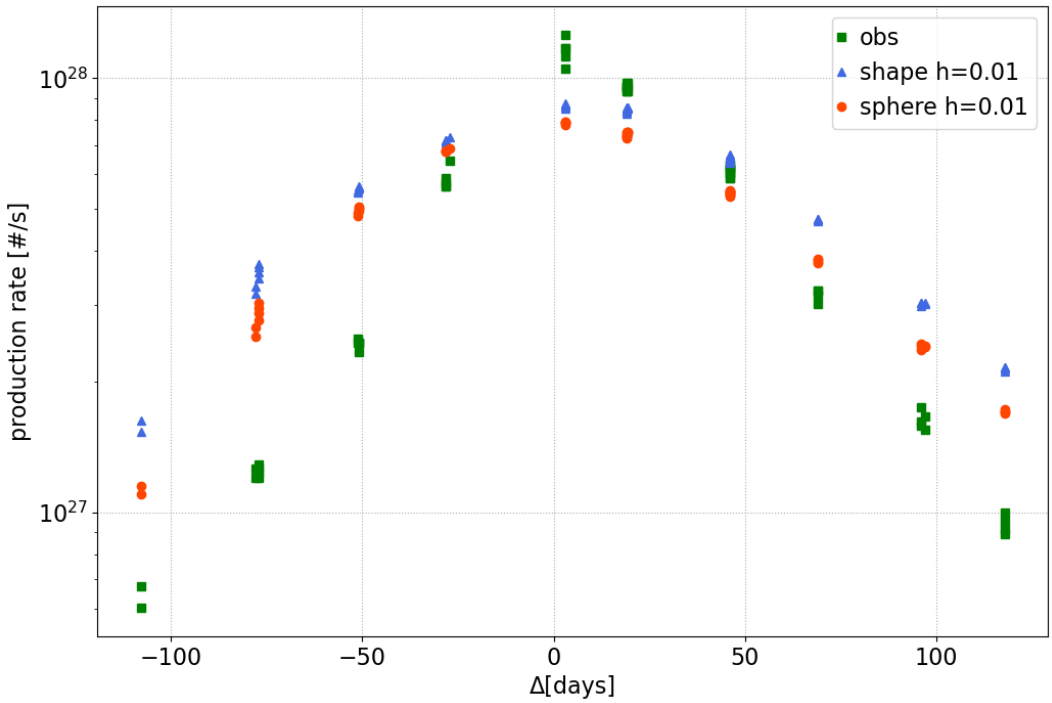

Figure 6.18: Water production rates of comet 103P. Green: observed production rates from Knight and Schleicher (2013a). Blue: production rates generated using the shape model, considering h=0.01. Red: production rates calculated by accounting for only 10% of the sphere's activity, also considering h=0.01.

For comet 9P, considering 10% of the activity for both the sphere and the shape model leads to a good qualitative fit to observations, when considering h=0.005 (Figure 6.19). However, small discrepancies between the simulated data and the observations may still be attributed to shape-linked uncertainties, thermal or compositional heterogeneities, or complex rotation properties that were not accounted for in the simulations.

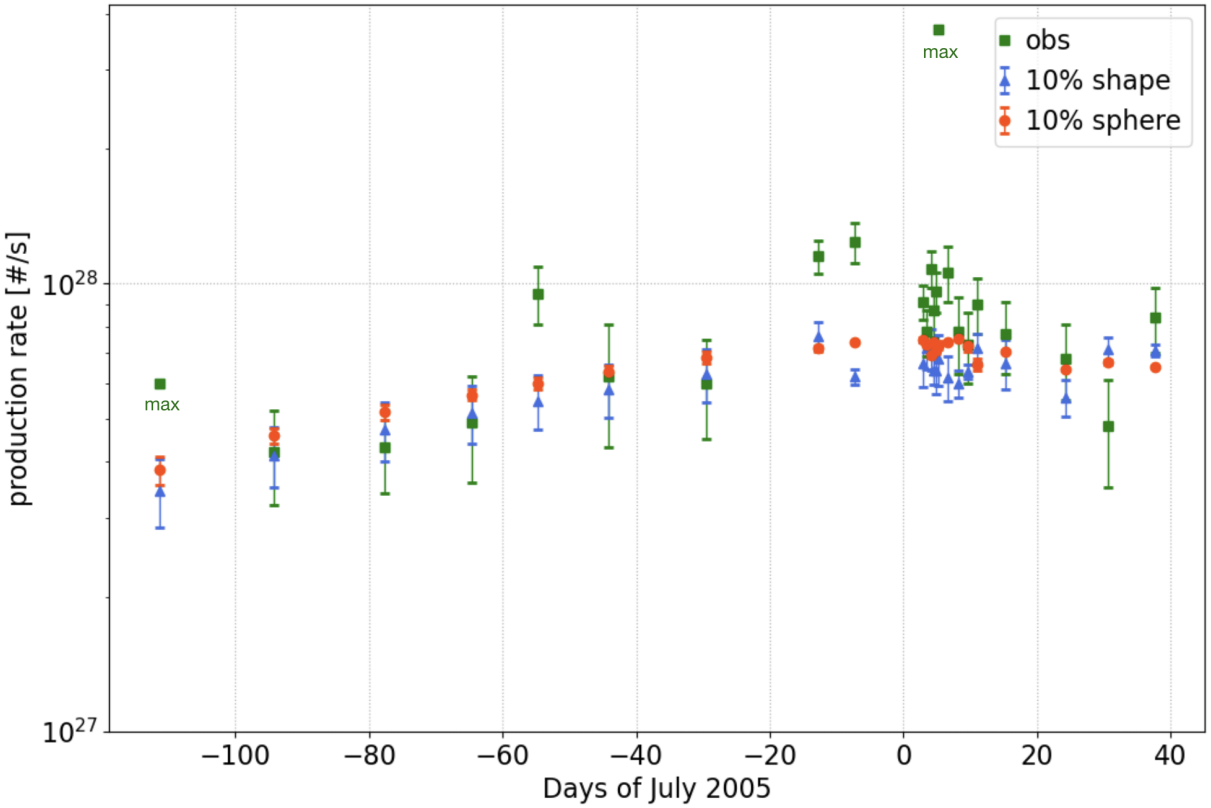

Figure 6.19: Water production rates resulting from considering partial activity of both the shape model and sphere for comet 9P, and comparison to observed production rates from Biver et al. (2007).

Restricting activity to the few regions surrounding the jets spots reported in Farnham and Thomas (2013a, see Figure 6.20), within the limits of the spatial precision of the used shape model, still gives higher amounts of water flux than the observations, for both the sphere and shape models (Figure 6.21). This may be due to spatial and temporal uncertainties linked to the origins of jets, to our selection of the regions, and possibly to other heterogeneities within the nucleus.

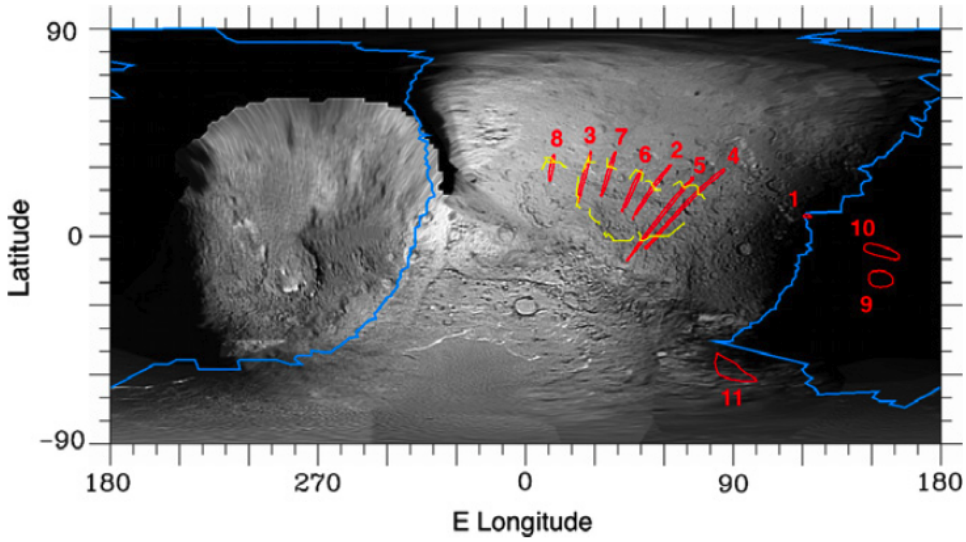

Figure 6.20: Surface map of comet 9P, with red ellipses indicating jet sources. The yellow bounding positions represent observed features crossing the horizon. The blue line indicates the terminator derived from the shape model. Credits: Farnham and Thomas (2013a).

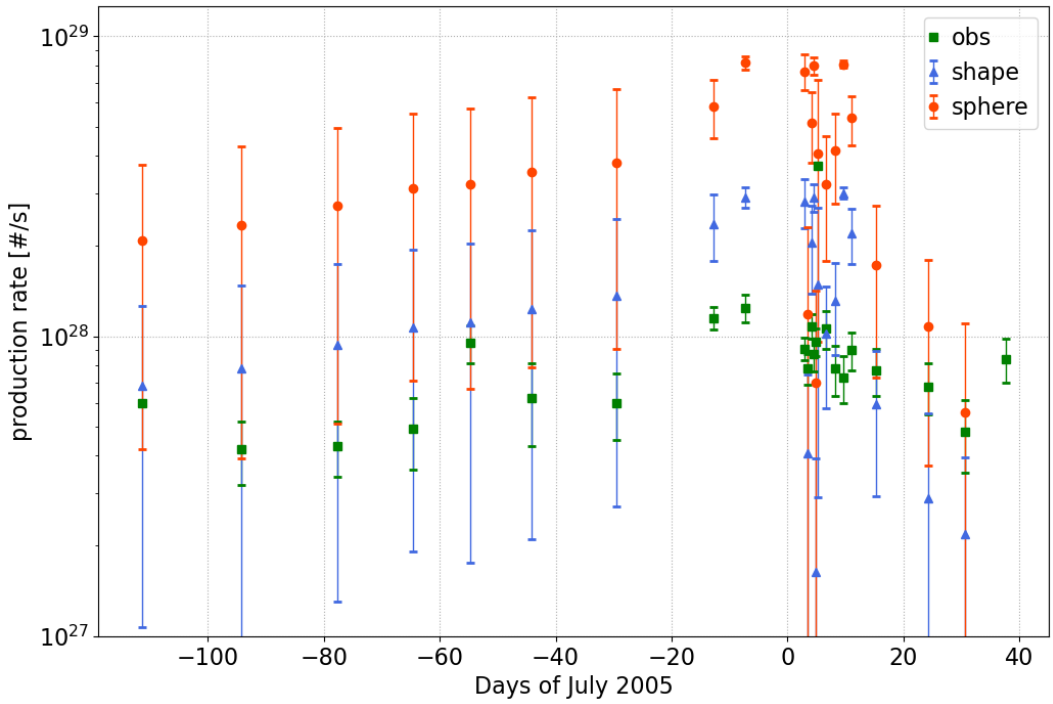

Figure 6.21: Water production rates resulting from partial activity of comet 9P corresponding to the jets spots retrieved from Farnham and Thomas (2013a), and comparison to the observed production rates from Biver et al. (2007). Error bars are important since we only consider few regions of the comet for which the production rate vary significantly during each time interval.

6.6 Discussion

We conducted a study examining the impact of shape, composition, and structural properties on the water production rates of cometary nuclei as observed from the ground or spacecraft. Our focus was on three Jupiter-family comets with the required available data (production rates and sufficiently resolved shape models): 67P, 9P, and 103P. We ran simulations with various initial configurations, considering the shape model, treating the comet as a sphere, and varying parameters such as porosity, dust-to-ice mass ratio, the presence of a thin dust mantle, and thermal conductivity (expressed through the Hertz factor) within plausible ranges for comet nuclei. The goal was to determine the extent to which shape and other parameters influence the observed curves, and their importance when analyzing observational data, as well as to assess the limitations in inferring such characteristics from ground-based observations.

Our study reveals that the shape of the nucleus affects secular water production rates; however, this influence does not dominate the patterns of activity:
For the three comets studied, the discrepancies between the production rates generated using the shape model and the sphere are considerably low when compared to the differences with the actual observations. Therefore, it is fair to attest that both the sphere and the shape models provide good qualitative fits of the observed secular water production rates, within the associated measurement uncertainties. For 67P, the differences are negligible during the period of highest activity around perihelion. This is consistent with Marshall et al. (2019), who reported a change of less than 5% in the cross-section of 67P throughout its whole orbit, and affirmed that the dependence on shape, spin axis orientation, and activity distribution is weak when the illuminated cross-section of the nucleus is invariant. Similarly, Davidsson et al. (2022a) found that the discrepancy in production rates between the shape and sphere models for 67P is minor compared to the variation in measurements. Additionally, using a shape model with 1,000 facets, that contains surface features on the scale of few hundred m, results in no substantial differences in production rates compared to the 500-facets model accounting solely for the global shape. This suggests that local roughness at this scale has a minimal impact on overall production rates, and that seasonal changes is the primary driver of outgassing. For 9P and 103P, the differences between the production rates using the sphere and the shape are higher than 67P, reaching up to 30% for 103P, and even the double for 9P during certain periods close to perihelion, highlighting the variable effect of shape in the observed production rates. Indeed, Marshall et al. (2019) showed that the cross-section area of 9P and 103P show higher changes around perihelion, which contributes to the observed difference in flux between the shape and sphere models. However, these differences do not always correspond to a better fit to observations by the shape model. For example, outside the perihelion, the sphere of 103P provides a closer qualitative fit to the observations, highlighting the interference of other characteristics in the activity.

The minimal influence of the shape on the observed water production rates, along with the notable discrepancies between simulations (using both sphere and shape models) and observations for both 67P and 9P, which are an order of magnitude apart, suggests that

surface and subsurface heterogeneities, of compositional or thermal/mechanical origin plays a major role in the observed outgassing. Taking into account the activity from only 9 active regions of 67P, as proposed by Läuter et al. (2019b), substantially improves the simulated production rates, improving both the magnitude and the pre-perihelion trend. Likewise, accounting for 10% of 9P's activity results in simulated production rates that are more closely aligned with observations, either with the shape or the sphere. The remaining minor discrepancies can be ascribed to shape-related uncertainties, time-varying thermal heterogeneities, or complex rotation properties not considered in the simulations. Researches have long recognized the need to consider a smaller active surface area on comets, varying from few to 10% in order to accurately fit the water activity (Huebner et al., 2006; Weissman et al., 2002). Additionally, varying thermal conductivity can improve the qualitative fit of the slopes of the the pre- and post-perihelion production curves. This may stem from an uneven distribution of water activity, leading to distinct thermal properties. Alternatively, shifts in conductivity might occur due to the activity itself, particularly the heightened activity at perihelion, causing thermal or structural modifications in the surface layers. The substantial importance of conductivity in comet activity aligns with the findings of Skorov et al. (2023), who emphasize the significance of thermal conductivity for the accuracy of cometary activity simulations, compared to structural properties such as porosity or dust mantle which have a marginal impact, which is consistent with our findings as well. However, it is worth noting that the asymmetry in the slopes before and after perihelion is not solely due to heterogeneities; it is partially attributed to the shape and spin axis properties (Sekanina, 1981). As evidence, for 67P and 103P for instance, we obtain a slightly asymmetrical simulated curve when considering a homogeneous nucleus, even before adjusting conductivity to better fit the post-perihelion part. This result is consistent with the findings of Marshall et al. (2019), who also concluded that irregularly shaped comets with non-zero obliquity can lead to asymmetric water production rate curves. An asymmetry is also observed in the sphere cases, indicating that it is not solely due to shape. Rotation properties alone and other factors can contribute as well. For instance, the complex rotation of 103P could potentially have effects that impact not only diurnal activity, but also propagate over a larger time scale. Given that the rotation properties used in our simulations concern only the few days around perihelion, their extrapolation over longer periods may induce effects observable for both the sphere and shape cases. Additionally, the lag in activity during perihelion or an asymmetry in the orbit, may also be contributing to this asymmetry for both the sphere and shape model.

Turning our attention back to heterogeneities, the case of 103P stands out as particularly interesting. Near perihelion, both the shape and the spherical models yield production rates comparable to the observed ones. Interestingly, considering the entire comet as active did not result in overproduction of water during the perihelion despite the nucleus's very complex shape. However, outside of the perihelion period, activity generated by a sphere fits the observation even better than with the shape, which emphasizes the assumption that heterogeneities are a crucial factor in the cometary production rates. The persisting discrepancies in slopes between the simulated and observed curves may be attributable to intricate rotational spin properties that are not fully known or considered in our analysis. It is important to note that these results are based on comparisons

with data solely from Knight and Schleicher (2013a), and that 103P's activity has been observed to change significantly between the different perihelion passages, as illustrated in Figure 6.4. This highlights the challenge in making assumptions about the structure, composition, and rotational properties of the comet, especially as the theoretical production rates with different values of initial parameters encompasses the different data from the past orbits. On top of that comet 103P is classified as hyper-active, exhibiting extended gas production during the perihelion period, including the production of icy grains in the coma (Lisse et al., 2009). Our model does not account for this additional water production source. This could potentially explain the discrepancies between our simulations' production rates and observations during the perihelion moment. However, while the presence of an icy grain halo, as suggested by Lisse et al. (2009) to explain the high water production rate of comet 103P seems plausible, it is challenging to provide quantitative justification (Protopapa et al., 2014).

In conclusion, our results suggest that heterogeneities (chemical, thermal or mechanical) are more important than the shape when it comes to understanding the secular activity of comets as observed from the ground. As a corollary, the shape of a nucleus does not leave a unique fingerprint in the observed secular water production rates. Moreover, the degeneracy between all the studied characteristics, including the shape, is impossible to lift with secular lightcurves alone. Therefore, from a modeling point of view, assuming that comet nuclei are spheres remains good enough to broadly understand their observed activity from the ground.

Conclusions and Perspectives

Our study of pits revealed interesting insights into their origin and evolution:

Influence of initial parameters on thermal activity
Our initial work probed the effect of several structural and thermal parameters integral to our model. The dual aim of this was to evaluate their respective importance within our simulations and to accurately determine the relative importance of the influence of local shape on the pit's evolution later on. A porosity of 80% generates almost double the erosion compared to a porosity of 60%. This shows that compact and dusty regions on the surface of a comet are expected to react differently to activity. The dust-to-ice ratio significantly influences activity, with higher ratios causing increased activity and erosion. The presence of CO and CO_2 into the initial composition of the nucleus has a negligible effect on the overall activity and erosion, that is mainly due to water sublimation. The thickness of the dust mantle plays a crucial role in thermally-driven activity and erosion: a mantle of less than 5 cm is rapidly removed, as a direct consequence of ice sublimation and gas drag of dust particle. A mantle of 10 cm or more can reduce or quench it. These first results showed the evidence that certain initial parameters can substantially influence a comet's overall activity and models outcomes.

Seasonal induced activity
A strong correlation exists between the energy received near perihelion, the peak of outgassing, and the surface erosion rates. For instance, the southern hemisphere of 67P/C-G stands as the most actively eroded area, with erosion reaching $\sim$77 m on the most active facets after evolving over 10 orbits. The rates of erosion tend to diminish as we approach the northern latitudes. Thus, obliquity, especially when it is high (as in the case of 67P, with 52°), plays a significant role in shaping the cometary surface. Findings on 81P/Wild 2, 9P/Tempel 1, and 103P/Hartley 2 corroborated the results of 67P. Activity and erosion of all three comets are the most intense as a result of the direct insolation during perihelion.

Role of shape in pits evolution
While seasonal trends are evident, our findings highlight that both local topography and the complex global shape of the nucleus play significant roles in influencing the energy distribution on the surface. At the level of individual pits, plateaus can receive up to twice the energy compared to the walls and floors of the highly shadowed pits, especially when the depth-to-diameter (d/D) ratio is adequately high. Self-heating is these cases can represent a significant energy source. For 67P, self-heating accounts for up to 60% of

the total energy within the pit in certain instances. For this comet, shape effects carry substantial significance across all scales. For instance, shadowing by the smaller lobe can curtail the energy experienced by the facing cliffs by over 70%. We also found an asymmetrical energy distribution corresponding to the orientation of the facets in relation to the Sun. Shape effects are less important for 9P and 103P due to the shallow aspect of their pits, adding to that the low resolution of their shape models. Overall, our results underline the imperative of considering shape effects when carrying studies of pit-like features.

Assessing erosion as a primary mechanism for pits' formation on JFCs
With our study, we provide a quantification of the erosion experienced over the different sides of the pits throughout the recent inner Solar System orbits, a period of intense activity. Intesrestingly, the erosion endured after several orbits is comparatively low relative to the large pits, which span several tens to hundreds of meters, implying it is insufficient to explain their formation. For instance, in southern regions of 67P where erosion is the highest, it does not surpass 80 m, while pit diameters vary between 130 m and more than 500 m. The same applies for all studied pits of 81P. These can be up to 2 km in diameter and several hundred meters in depth, yet the maximum erosion does not surpass 80 m. On the surfaces of 9P and 103P, pits may be considerably shallower, but those extending to several hundred meters cannot be formed by this process. Our results confirm several earlier studies, notably that erosion due to current thermally-driven activity is insufficient to create features of several hundred meters (Mousis et al., 2015; Guilbert-Lepoutre et al., 2016).

Pit evolution aligns with energy trends, leading to more erosion on plateaus than walls and bottoms. This pattern causes pit widening and erasure, particularly for those with high d/D ratios where the bottoms are predominantly shadowed. These findings support the hypothesis that deep and circular pits are less evolved, or better preserved, than their larger or elongated counterparts (Vincent et al., 2015a). One might question how smaller pits can persist on the surfaces of 9P and 103P, given their extensive erosion over their long presence in current orbits (13 and 20 orbits respectively). The longevity of these smaller pits may be due to a low d/D ratio, which results in less shadowing in pits depths, thereby leading to similar levels of erosion on both the plateaus and bottoms. Future works could explore determining a critical d/D threshold in different illumination conditions, above which pits become shallower.

Considering the erosion rates and patterns, it's unlikely that the formation of pits, ranging from several tens to hundreds of meters, can be attributed to the erosion stemming from the recent thermal activity of comets in their current orbits, suggesting the involvement of other processes.

As per our thermal evolution simulations on the surfaces of the four comets under their existing illumination conditions, the levels of depression erosion can be ranked from low to high as follows: 81P, 67P(N), 67P(S) and 9P, then 103P. The erosion amount attained is intrinsically associated with the period of evolution. We can notice a direct correlation between the time spent during the active period and their surface characteristics, especially pits. 67P and 81P, the comets that are dynamically newer than 9P and then 103P, exhibit the most acute depressions. When considering the d/D ratio, 67P's pits have the

highest values: 0.3, followed by 0.2 for 81P (Kirk et al., 2005; Vincent et al., 2015a), and 0.1 for 9P (Thomas et al., 2013a). The surface appearance of 103P is reported to resemble that of 9P (Ip et al., 2016). This further emphasizes the hypothesis that pits are gradually erased over time, following the evolving surface characteristics from 81P/67P to 103P. Finally, steep pits with flat bottoms, ranging from 150 m to 1k m, present a similar size frequency distribution on 67P, 9P, and 81P (Ip et al., 2016), which suggests that these depressions would be formed by the same mechanism across the different comets.

We explored the impact of nucleus morphology on its activity, and how this compares to the influence of thermal and compositional characteristics:

While shape affects overall cometary activity, it is not the prevailing factor
Our research revealed that while the overall shape of a comet nucleus affect global outgassing, this impact is not significant. For comet 67P, the disparity in production rates between the shape and spherical approximation models was minimal, aligning with Marschall et al. (2019)'s finding that its cross-section does not undergo considerable change throughout its orbit, due to the combination of its rotation axis and shape. This suggests that seasons relatively predominate global production rates. We also found that difference between production rates produced by models with 500 and 1000 facets was minimal, implying that roughness on the scale of several hundred meters contributes minimally to a nucleus's global activity. For comets 9P and 103P, the influence of shape is more important, particularly during the perihelion period, where the peak of activity occurs. In the case of 9P, the actual amounts of production rates predicted by shape models are closer to observations than spherical models during the observation period. Conversely, for 103P, the production rates predicted by the sphere are marginally closer to the observations, even though both the sphere and shape models accurately capture the order of magnitude of the production rates. However, the slopes of the activity curve consistently differ from modeled curves, regardless of the shape model employed. Therefore, while comet shape can significantly influence global activity as observed from Earth, it should not be considered the primary determinant.

Composition and heterogeneity are key
The significant disparities observed between simulated and observed production rates, both in terms of amounts and trends, can be attributed to the substantial heterogeneity present on their surface and subsurface. Varying the thermal conductivity helps improve the trends of pre- and post-perihelion activity curve, underscoring the importance of thermal conductivity in comet activity compared to factors such as porosity or dust mantle already outlined by Skorov et al. (2023). Furthermore, when considering only the most active regions of 67P as proposed by Läuter et al. (2020a), the production rates derived from both the shape model and the spherical model align more closely with the observed data. Similarly, by considering only 10% of the activity from both the spherical and shape models, a better match to the observed production rates of comet 9P is achieved. For 103P, both the shape and the spherical models gave production rates almost similar to the observed values at the perihelion moment, but relatively overestimated outside of this period, underscoring the significant role played by heterogeneities in the production

processes of comets.

In conclusion, heterogeneity (chemical, thermal, or mechanical) is as important, if not more, than shape for understanding the overall activity of comets. From a modeling perspective, assuming comet nuclei as spheres is sufficient to understand their secular activity as observed from Earth.

Perspectives

In our study, we assumed a homogeneous nucleus when investigating the pits evolution. However, this assumption does not capture the actual heterogeneities in physical, thermal, and compositional characteristics across the comet's surface (Elmaarry et al., 2017; Fornasier et al., 2019). These variations, such as differences in dust mantle thickness or the presence of ice patches, could lead to substantial localized activity and differential pit evolution, potentially explaining the disparate dimensions observed. A more accurate modeling of pits evolution would necessitate considering such heterogeneity. Still, even in scenarios involving maximum variations of key parameters, such as doubling the erosion rates as seen in the porosity case, the resulting erosion appears modest compared to the size of large pits. Anyhow, future research should explore these potential heterogenities and their impact on pit formation and evolution.

Furthermore, the enigmatic origin of the pits, which could be linked to earlier phases of comets' evolution, calls for further investigations to explore different potential scenarios of their formation. The Centaur phase of JFCs may provide critical insights into the origin of pits. Notably, abrupt thermal events in this phase, such as clathrate destabilization or amorphous ice crystallization, could result in explosive surface activity that forms pits (Mousis et al., 2015; Wierzchos and Womack, 2020) . Evidence of such activity is seen in the frequent and substantial outbursts exhibited by several Centaurs, such as 29P/Schwassmann-Wachmann and 174P Echeclus (Wierzchos and Womack, 2020; Kareta et al., 2019). Future works should explore this mechanism as potential contributors to the formation of pits.

Concerning larger-scale activity, future studies would benefit from integrating more detailed shape models that include small-scale topography, like the deep, acute pits found on 67P. Although these features constitute only limited areas on the nucleus surface, their presence could significantly decrease activity levels at a regional scale. Consequently, production rates obtained in our study from low-resolution shape models should be viewed as upper limit approximations.

Additionally, our simulations did not consider several thermal mechanisms that, if numerically feasible, could be intriguing to incorporate, given their substantial potential impact on activity outcomes. For instance, our model did not simulate phenomena such as outburst activity or hyperactivity, similar to what was observed on 103P. These events could significantly contribute to the observed activity, leading to a more accurate alignment with observed data. A better understanding of these phenomena would provide valuable insights into the role of heterogeneities or other complex processes in cometary activity.

Bibliography

M. F. A'Hearn, D. G. Schleicher, R. L. Millis, P. D. Feldman, and D. T. Thompson. Comet bowell 1980b. *The Astronomical Journal*, 89:579–591, 1984.

M. F. A'Hearn, R. C. Millis, D. G. Schleicher, D. J. Osip, and P. V. Birch. The ensemble properties of comets: Results from narrowband photometry of 85 comets, 1976-1992. *Icarus*, 118(2):223–270, 1995.

M. F. A'Hearn, M. J. S. Belton, W. A. Delamere, J. Kissel, Kp. Klaasen, L. A. McFadden, K. J. Meech, H. J. Melosh, P. H. Schultz, and J. M. Sunshine. Deep impact: Excavating comet Tempel 1. *science*, 310(5746):258–264, 2005.

M. F. A'Hearn, M. J. Belton, W. A. Delamere, L. M. Feaga, D. Hampton, J. Kissel, K. P. Klaasen, L. A. McFadden, K. J. Meech, and H. J. Melosh. EPOXI at comet Hartley 2. *Science*, 332(6036):1396–1400, 2011.

K. Altwegg, H. Balsiger, A. Bar-Nun, J.-J. Berthelier, A. Bieler, P. Bochsler, C. Briois, U. Calmonte, M. Combi, and J. De Keyser. 67P/Churyumov-Gerasimenko, a Jupiter family comet with a high D/H ratio. *Science*, 347(6220):1261952, 2015.

K. Altwegg, H. Balsiger, A. Bar-Nun, J.-J. Berthelier, A. Bieler, P. Bochsler, C. Briois, U. Calmonte, M. R. Combi, and H. Cottin. Prebiotic chemicals—amino acid and phosphorus—in the coma of comet 67P/Churyumov-Gerasimenko. *Science advances*, 2 (5):e1600285, 2016.

K. Altwegg, H. Balsiger, N. Hänni, M. Rubin, M. Schuhmann, I. Schroeder, T. Sémon, S. Wampfler, J.-J. Berthelier, and C. Briois. Evidence of ammonium salts in comet 67P as explanation for the nitrogen depletion in cometary comae. *Nature astronomy*, 4(5): 533–540, 2020.

E. I. Asphaug and J. Thangavelautham. Conference on Spacecraft Reconnaissance of Asteroid and Comet Interiors: January 8-10, 2015, Tempe, Arizona, 2015.

N. Attree, L. Jorda, O. Groussin, S. Mottola, N. Thomas, Y. Brouet, E. Kührt, M. Knapmeyer, F. Preusker, and F. Scholten. Constraining models of activity on comet 67P/Churyumov-Gerasimenko with Rosetta trajectory, rotation, and water production measurements. *Astronomy & Astrophysics*, 630:A18, 2019.

M. N. Barrington, S. P. D. Birch, A. Jindal, A. Hayes, P. Corlies, and J.-B. Vincent. Geomorphologic Evolution of Smooth Terrains of Comet 67P/Churyumov-Gerasimenko. *LPI Contributions*, 2678:1702, 2022.

M. A. Barucci, A. Doressoundiram, and D. P. Cruikshank. Surface characteristics of transneptunian objects and Centaurs from photometry and spectroscopy. *Comets II*, 647, 2004.

M. A. Barucci, M. Fulchignoni, J. Ji, S. Marchi, and N. Thomas. The flybys of asteroids (2867) Šteins,(21) Lutetia, and (4179) Toutatis. *Asteroids IV*, 433:448, 2015.

M. A. Barucci, GIANRICO. Filacchione, S. Fornasier, A. Raponi, J. D. P. Deshapriya, F. Tosi, C. Feller, M. Ciarniello, H. Sierks, and FABRIZIO. Capaccioni. Detection of exposed H2O ice on the nucleus of comet 67P/Churyumov-Gerasimenko-as observed by Rosetta OSIRIS and VIRTIS instruments. *Astronomy & Astrophysics*, 595:A102, 2016.

A. T. Basilevsky and H. U. Keller. Comet nuclei: Morphology and implied processes of surface modification. *Planetary and Space Science*, 54(8):808–829, 2006.

J. M. Bauer, Y. R. Fernández, S. Protopapa, and L. M. Woodney. Comet Science With Ground Based and Space Based Surveys in the New Millennium. *arXiv preprint arXiv:2210.09400*, 2022.

M. J. Belton. Cometary activity, active areas, and a mechanism for collimated outflows on 1P, 9P, 19P, and 81P. *Icarus*, 210(2):881–897, 2010.

M. J. Belton, P. Thomas, B. Carcich, A. Quick, J. Veverka, H. J. Melosh, M. F. A'Hearn, J.-Y. Li, D. Brownlee, and P. Schultz. The origin of pits on 9P/Tempel 1 and the geologic signature of outbursts in Stardust-NExT images. *Icarus*, 222(2):477–486, 2013a.

M. J. Belton, P. Thomas, J.-Y. Li, J. Williams, B. Carcich, M. F. A'Hearn, S. McLaughlin, T. Farnham, L. McFadden, and C. M. Lisse. The complex spin state of 103P/Hartley 2: Kinematics and orientation in space. *Icarus*, 222(2):595–609, 2013b.

J. Benkhoff and D. C. Boice. Modeling the thermal properties and the gas flux from a porous, ice-dust body in the orbit of P/Wirtanen. *Planetary and space science*, 44(7): 665–673, 1996.

J. Benkhoff and W. F. Huebner. Influence of the vapor flux on temperature, density, and abundance distributions in a multicomponent, porous, icy body. *Icarus*, 114(2): 348–354, 1995.

S. Benseguane, A. Guilbert-Lepoutre, J. Lasue, S. Besse, C. Leyrat, A. Beth, M. C. Sitjà, B. Grieger, and M. T. Capria. Evolution of pits at the surface of 67P/Churyumov-Gerasimenko. *Astronomy & Astrophysics*, 668:A132, 2022.

S. B. Besse, A. Guilbert-Lepoutre, J.-B. Vincent, D. Bodewits, and M. Pajola. Circular depressions on 67P/Churyumov-Gerasimenko observed by the OSIRIS instrument. In *European Planetary Science Congress*, pages EPSC2015–114, 2015.

J. Biele, S. Ulamec, M. Maibaum, R. Roll, L. Witte, E. Jurado, P. Muñoz, W. Arnold, H.-U. Auster, and C. Casas. The landing (s) of Philae and inferences about comet surface mechanical properties. *Science*, 349(6247):aaa9816, 2015.

A. Bieler, K. Altwegg, H. Balsiger, A. Bar-Nun, J.-J. Berthelier, P. Bochsler, C. Briois, U. Calmonte, M. Combi, and J. De Keyser. Abundant molecular oxygen in the coma of comet 67P/Churyumov–Gerasimenko. *Nature*, 526(7575):678–681, 2015.

S. P. Birch, Y. Tang, A. G. Hayes, R. L. Kirk, D. Bodewits, H. Campins, Y. Fernandez, R. de Freitas Bart, N. W. Kutsop, and H. Sierks. Geomorphology of comet 67P/Churyumov–Gerasimenko, 2017.

N. Biver, D. Bockelée-Morvan, J. Boissier, J. Crovisier, P. Colom, A. Lecacheux, R. Moreno, G. Paubert, D. C. Lis, and M. Sumner. Radio observations of Comet 9P/Tempel 1 before and after Deep Impact. *Icarus*, 191(2):494–512, 2007.

N. Biver, D. Bockelée-Morvan, M. Hofstadter, E. Lellouch, M. Choukroun, S. Gulkis, J. Crovisier, F. P. Schloerb, L. Rezac, and P. Von Allmen. Long-term monitoring of the outgassing and composition of comet 67P/Churyumov-Gerasimenko with the Rosetta/MIRO instrument. *Astronomy & Astrophysics*, 630:A19, 2019.

N. Biver, N. D. Russo, C. Opitom, and M. Rubin. Chemistry of comet atmospheres. *arXiv preprint arXiv:2207.04800*, 2022.

D. Bockelée-Morvan. Cometary science with ALMA. *Astrophysics and Space Science*, 313:183–189, 2008.

D. Bockelée-Morvan and N. Biver. The composition of cometary ices. *Philosophical Transactions of the Royal Society A: Mathematical, Physical and Engineering Sciences*, 375(2097):20160252, 2017.

J. Boissier, D. Bockelée-Morvan, N. Biver, J. Crovisier, R. Moreno, E. Lellouch, and R. Neri. Present and future cometary science with the IRAM Plateau de Bure interferometer. *Earth, Moon, and Planets*, 105:89–93, 2009.

B. P. Bonev, N. D. Russo, M. A. DiSanti, E. C. Martin, G. Doppmann, R. J. Vervack, G. L. Villanueva, H. Kawakita, E. L. Gibb, and M. R. Combi. First Comet Observations with NIRSPEC-2 at Keck: Outgassing Sources of Parent Volatiles and Abundances Based on Alternative Taxonomic Compositional Baselines in 46P/Wirtanen. *The Planetary Science Journal*, 2(2):45, 2021.

A. Bouquety, O. Groussin, L. Jorda, A. Séjourné, F. Costard, and S. Bouley. Evidence for scalloped terrains on 67P. Technical report, Copernicus Meetings, 2021a.

A. Bouquety, L. Jorda, O. Groussin, A. Sejourné, S. Bouley, and F. Costard. Ancient and present surface evolution processes in the Ash region of comet 67P/Churyumov-Gerasimenko. *Astronomy & Astrophysics*, 649:A82, 2021b.

A. Bouquety, O. Groussin, L. Jorda, A. Sejourné, F. Costard, and S. Bouley. Evidence for thermokarst depressions on comet 67P/Churyumov-Gerasimenko: An interplanetary comparison. 2022.

J. C. Brandt, R. W. Farquhar, S. P. Maran, M. B. Niedner, and T. Von Rosenvinge. The International Cometary Explorer (ICE) mission to comet Giacobini-Zinner (G/Z). In *International Astronomical Union Colloquium*, volume 83, pages 405–414. Cambridge University Press, 1985.

R. Brasser and A. Morbidelli. Oort cloud and Scattered Disc formation during a late dynamical instability in the Solar System. *Icarus*, 225(1):40–49, 2013.

D. E. Brownlee, F. Horz, R. L. Newburn, M. Zolensky, T. C. Duxbury, S. Sandford, Z. Sekanina, P. Tsou, M. S. Hanner, and B. C. Clark. Surface of young Jupiter family comet 81P/Wild 2: View from the Stardust spacecraft. *Science*, 304(5678):1764–1769, 2004.

M. Bruck Syal, P. H. Schultz, J. M. Sunshine, M. F. A'Hearn, T. L. Farnham, and D. S. Dearborn. Geologic control of jet formation on Comet 103P/Hartley 2. *Icarus*, 222(2): 610–624, 2013.

M. J. Burchell, S. A. Fairey, P. Wozniakiewicz, D. E. Brownlee, F. Hörz, A. T. Kearsley, T. H. See, P. Tsou, A. Westphal, and S. F. Green. Characteristics of cometary dust tracks in Stardust aerogel and laboratory calibrations. *Meteoritics & Planetary Science*, 43(1-2):23–40, 2008.

F. Capaccioni, A. Coradini, G. Filacchione, S. Erard, G. Arnold, P. Drossart, M. C. De Sanctis, D. Bockelee-Morvan, M. T. Capria, and F. Tosi. The organic-rich surface of comet 67P/Churyumov-Gerasimenko as seen by VIRTIS/Rosetta. *Science*, 347(6220): aaa0628, 2015.

C. Capanna, L. Jorda, P. L. Lamy, and G. Gesquiere. A new multiresolution method applied to the 3D reconstruction of small bodies. In *AGU Fall Meeting Abstracts*, volume 2012, pages P23B–1937, 2012.

M. T. Capria, F. Capaccioni, A. Coradini, M. C. De Sanctis, S. Espinasse, C. Federico, R. Orosei, and M. Salomone. AP/Wirtanen evolution model. *Planetary and space science*, 44(9):987–1000, 1996.

M. T. Capria, A. Coradini, M. C. De Sanctis, and M. I. Blecka. P/Wirtanen thermal evolution: Effects due to the presence of an organic component in the refractory material. *Planetary and Space Science*, 49(9):907–918, 2001.

M. T. Capria, D. Turrini, and M. C. De Sanctis. The buried snow line: Where ice could still be found in the inner Solar System. In *European Planetary Science Congress 2012*, pages EPSC2012–841, 2012.

A. Carusi, L. Kresák, E. Perozzi, and G. B. Valsecchi. Long-term evolution of short-period comets. *Bristol: Hilger*, 1985.

A. F. Cheng, C. M. Lisse, and M. A'Hearn. Surface geomorphology of Jupiter Family Comets: A geologic process perspective. *Icarus*, 222(2):808–817, 2013.

M. Choukroun, K. Altwegg, E. Kührt, N. Biver, D. Bockelée-Morvan, J. Drążkowska, A. Hérique, M. Hilchenbach, R. Marschall, and M. Pätzold. Dust-to-gas and refractory-to-ice mass ratios of comet 67P/Churyumov-Gerasimenko from Rosetta observations. *Space science reviews*, 216(3):1–38, 2020.

V. Ciarletti, A. C. Levasseur-Regourd, J. Lasue, C. Statz, D. Plettemeier, A. Hérique, Y. Rogez, and W. Kofman. CONSERT suggests a change in local properties of 67P/Churyumov-Gerasimenko's nucleus at depth. *Astronomy & Astrophysics*, 583:A40, 2015.

M. Cohen, D. Prialnik, and M. Podolak. A quasi-3D model for the evolution of shape and temperature distribution of comet nuclei—application to Comet 46P/Wirtanen. *New Astronomy*, 8(3):179–189, 2003.

M. Combi, Y. Shou, N. Fougere, V. Tenishev, K. Altwegg, M. Rubin, D. Bockelée-Morvan, F. Capaccioni, Y.-C. Cheng, and U. Fink. The surface distributions of the production of the major volatile species, H2O, CO2, CO and O2, from the nucleus of comet 67P/Churyumov-Gerasimenko throughout the Rosetta Mission as measured by the ROSINA double focusing mass spectrometer. *Icarus*, 335:113421, 2020.

J. J. Cowan and M. F. A'Hearn. Vaporization of comet nuclei: Light curves and life times. *the Moon and the Planets*, 21(2):155–171, 1979.

B. J. Davidsson. Thermophysical evolution of planetesimals in the primordial disc. *Monthly Notices of the Royal Astronomical Society*, 505(4):5654–5685, 2021.

B. J. Davidsson, S. Birch, G. A. Blake, D. Bodewits, J. P. Dworkin, D. P. Glavin, Y. Furukawa, J. I. Lunine, J. L. Mitchell, and A. N. Nguyen. Airfall on Comet 67P/Churyumov–Gerasimenko. *Icarus*, 354:114004, 2021a.

B. J. Davidsson, S. Birch, G. A. Blake, D. Bodewits, J. P. Dworkin, D. P. Glavin, Y. Furukawa, J. I. Lunine, J. L. Mitchell, and A. N. Nguyen. Airfall on Comet 67P/Churyumov–Gerasimenko. *Icarus*, 354:114004, 2021b.

B. J. Davidsson, N. H. Samarasinha, D. Farnocchia, and P. J. Gutiérrez. Modelling the water and carbon dioxide production rates of Comet 67P/Churyumov–Gerasimenko. *Monthly Notices of the Royal Astronomical Society*, 509(2):3065–3085, 2022a.

B. J. Davidsson, N. H. Samarasinha, D. Farnocchia, and P. J. Gutiérrez. Modelling the water and carbon dioxide production rates of Comet 67P/Churyumov–Gerasimenko. *Monthly Notices of the Royal Astronomical Society*, 509(2):3065–3085, 2022b.

B. J. Davidsson, F. P. Schloerb, S. Fornasier, N. Oklay, P. J. Gutiérrez, B. J. Buratti, A. B. Chmielewski, S. Gulkis, M. D. Hofstadter, and H. U. Keller. CO2-driven surface changes in the Hapi region on Comet 67P/Churyumov–Gerasimenko. *Monthly Notices of the Royal Astronomical Society*, 516(4):6009–6040, 2022c.

B. J. R. Davidsson, H. Sierks, C. Güttler, F. Marzari, MAURIZIO. Pajola, H. Rickman, M. F. A'Hearn, A.-T. Auger, M. R. El-Maarry, and S. Fornasier. The primordial nucleus of comet 67P/Churyumov-Gerasimenko. *Astronomy & Astrophysics*, 592:A63, 2016.

M. C. De Sanctis, F. Capaccioni, M. T. Capria, A. Coradini, C. Federico, R. Orosei, and M. Salomone. Models of P/Wirtanen nucleus: Active regions versus non-active regions. *Planetary and space science*, 47(6-7):855–872, 1999.

M. C. De Sanctis, M. T. Capria, and A. Coradini. Thermal evolution model of 67P/Churyumov-Gerasimenko, the new Rosetta target. *Astronomy & Astrophysics*, 444(2):605–614, 2005.

M. C. De Sanctis, J. Lasue, and M. T. Capria. Seasonal effects on comet nuclei evolution: Activity, internal structure, and dust mantle formation. *The Astronomical Journal*, 140 (1):1, 2010a.

M. C. De Sanctis, J. Lasue, M. T. Capria, G. Magni, D. Turrini, and A. Coradini. Shape and obliquity effects on the thermal evolution of the Rosetta target 67P/Churyumov-Gerasimenko cometary nucleus. *Icarus*, 207(1):341–358, 2010b.

M. C. De Sanctis, FABRIZIO. Capaccioni, M. Ciarniello, GIANRICO. Filacchione, M. Formisano, S. Mottola, A. Raponi, F. Tosi, D. Bockelée-Morvan, and S. Erard. The diurnal cycle of water ice on comet 67P/Churyumov–Gerasimenko. *Nature*, 525 (7570):500–503, 2015.

A. H. Delsemme and D. C. Miller. The continuum of Comet Burnham (1960 II): The differentiation of a short period comet. *Planetary and Space Science*, 19(10):1229–1257, 1971.

M. R. El-Maarry, N. Thomas, L. Giacomini, M. Massironi, MAURIZIO. Pajola, R. Marschall, A. Gracia-Berná, H. Sierks, C. Barbieri, and P. L. Lamy. Regional surface morphology of comet 67P/Churyumov-Gerasimenko from Rosetta/OSIRIS images. *Astronomy & Astrophysics*, 583:A26, 2015.

M. R. El-Maarry, N. Thomas, A. Gracia-Berná, MAURIZIO. Pajola, J.-C. Lee, M. Massironi, B. Davidsson, S. Marchi, H. U. Keller, and S. F. Hviid. Regional surface morphology of comet 67P/Churyumov-Gerasimenko from Rosetta/OSIRIS images: The southern hemisphere. *Astronomy & Astrophysics*, 593:A110, 2016.

M. R. El-Maarry, O. Groussin, H. U. Keller, N. Thomas, J.-B. Vincent, S. Mottola, MAURIZIO. Pajola, K. Otto, C. Herny, and S. Krasilnikov. Surface morphology of comets and associated evolutionary processes: A review of Rosetta's observations of 67p/Churyumov–Gerasimenko. *Space science reviews*, 215(4):1–33, 2019.

M. R. Elmaarry, O. Groussin, N. Thomas, M. Pajola, A.-T. Auger, B. J. R. Davidsson, X. Hu, S. F. Hviid, K. Joerg, and C. Güttler. How do the surfaces of comets evolve with time?: Insights from Rosetta's two-year journey with 67P/Churyumov-Gerasimenko. In *AGU Fall Meeting Abstracts*, volume 2017, pages P51D–2638, 2017.

A. Enzian, H. Cabot, and J. Klinger. A 2 1/2 D thermodynamic model of cometary nuclei. I. Application to the activity of comet 29P/Schwassmann-Wachmann 1. *Astronomy and Astrophysics*, 319:995–1006, 1997.

A. Enzian, J. Klinger, G. Schwehm, and P. R. Weissman. Temperature and gas production distributions on the surface of a spherical model comet nucleus in the orbit of 46P/Wirtanen. *Icarus*, 138(1):74–84, 1999.

S. Espinasse, J. Klinger, C. Ritz, and B. Schmitt. Modeling of the thermal behavior and of the chemical differentiation of cometary nuclei. *Icarus*, 92(2):350–365, 1991.

S. Espinasse, A. Coradini, M. T. Capria, F. Capaccioni, R. Orosei, M. Salomone, and C. Federico. Thermal evolution and differentiation of a short-period comet. *Planetary and space science*, 41(6):409–427, 1993.

T. Farnham and P. Thomas. PLATE SHAPE MODEL OF COMET 9P/TEMPEL 1 V2.0, DIF-C-HRIV/ITS/MRI-5-TEMPEL1-SHAPE-MODEL-V2.0, 2013a.

T. Farnham, T. Duxbury, and J.-Y. L. SHAPE MODELS OF COMET WILD 2, SDU-C-NAVCAM-5-WILD2-SHAPE-MODEL-V2.1, 2005.

T. L. Farnham and P. C. Thomas. Plate shape model of comet 103P/Hartley 2 V1.0, DIF-C-HRIV/MRI-5-HARTLEY2-SHAPE-V1.0, 2013b.

T. L. Farnham, D. Bodewits, J.-Y. Li, J. Veverka, P. Thomas, and M. J. S. Belton. Connections between the jet activity and surface features on Comet 9P/Tempel 1. *Icarus*, 222(2):540–549, 2013.

I. Ferrín. Atlas of secular light curves of comets. *Planetary and Space Science*, 58(3): 365–391, 2010.

G. Filacchione, M. Ciarniello, S. Fornasier, and A. Raponi. Comet nuclei composition and evolution. *arXiv preprint arXiv:2210.02741*, 2022.

GIANRICO. Filacchione, A. Raponi, FABRIZIO. Capaccioni, M. Ciarniello, F. Tosi, M. T. Capria, M. C. De Sanctis, A. Migliorini, GIUSEPPE. Piccioni, and P. Cerroni. Seasonal exposure of carbon dioxide ice on the nucleus of comet 67P/Churyumov-Gerasimenko. *Science*, 354(6319):1563–1566, 2016.

U. Fink and M. Rubin. The calculation of Afρ and mass loss rate for comets. *Icarus*, 221 (2):721–734, 2012.

S. Fornasier, P. H. Hasselmann, M. A. Barucci, C. Feller, S. Besse, C. Leyrat, L. Lara, P. J. Gutierrez, N. Oklay, and C. Tubiana. Spectrophotometric properties of the nucleus of comet 67P/Churyumov-Gerasimenko from the OSIRIS instrument onboard the ROSETTA spacecraft. *Astronomy & Astrophysics*, 583:A30, 2015.

S. Fornasier, S. Mottola, H. U. Keller, M. A. Barucci, B. Davidsson, C. Feller, J. D. P. Deshapriya, H. Sierks, C. Barbieri, and P. L. Lamy. Rosetta's comet 67P/Churyumov-Gerasimenko sheds its dusty mantle to reveal its icy nature. *Science*, 354(6319):1566–1570, 2016.

S. Fornasier, C. Feller, P. H. Hasselmann, M. A. Barucci, J. Sunshine, J.-B. Vincent, X. Shi, H. Sierks, G. Naletto, and P. L. Lamy. Surface evolution of the Anhur region on comet 67P/Churyumov-Gerasimenko from high-resolution OSIRIS images. *Astronomy & Astrophysics*, 630:A13, 2019.

S. Fornasier, J. B. de Micas, P. H. Hasselmann, H. V. Hoang, M. A. Barucci, and H. Sierks. Small lobe of comet 67P: Characterization of the Wosret region with ROSETTA-OSIRIS. *Astronomy & Astrophysics*, 653:A132, 2021.

S. Fornasier, H. V. Hoang, M. Fulle, E. Quirico, and M. Ciarniello. Volatile exposures on the 67P/Churyumov-Gerasimenko nucleus. *arXiv preprint arXiv:2302.11424*, 2023.

N. Fougere, K. Altwegg, J.-J. Berthelier, A. Bieler, D. Bockelée-Morvan, U. Calmonte, F. Capaccioni, M. R. Combi, J. De Keyser, and V. Debout. Direct simulation Monte Carlo modelling of the major species in the coma of comet 67P/Churyumov-Gerasimenko. *Monthly Notices of the Royal Astronomical Society*, 462(Suppl_1):S156–S169, 2016.

M. Fulle, VINCENZO. Della Corte, A. Rotundi, S. F. Green, M. Accolla, L. Colangeli, MARCO. Ferrari, S. Ivanovski, R. Sordini, and VLADIMIR. Zakharov. The dust-to-ices ratio in comets and Kuiper belt objects, 2017.

R. W. Gaskell, J. Gillis-Davis, and A. L. Sprague. Topography of Mercury from imaging data. In *AAS/Division for Planetary Sciences Meeting Abstracts# 40*, volume 40, pages 51–05, 2008.

J. A. Ghormley. Enthalpy changes and heat-capacity changes in the transformations from high-surface-area amorphous ice to stable hexagonal ice. *The Journal of Chemical Physics*, 48(1):503–508, 1968.

A. Gkotsinas, A. Guilbert-Lepoutre, S. N. Raymond, and D. Nesvorny. Thermal Processing of Jupiter-family Comets during Their Chaotic Orbital Evolution. *The Astrophysical Journal*, 928(1):43, 2022.

K.-H. Glassmeier, H. Boehnhardt, D. Koschny, E. Kührt, and I. Richter. The Rosetta mission: Flying towards the origin of the solar system. *Space Science Reviews*, 128: 1–21, 2007.

B. Grieger. Quincuncial adaptive closed Kohonen (QuACK) map for the irregularly shaped comet 67P/Churyumov-Gerasimenko. *Astronomy & Astrophysics*, 630:A1, 2019.

E. Grün, A. Bar-Nun, J. Benkhoff, A. Bischoff, H. Düren, H. Hellmann, P. Hesselbarth, P. Hsiung, H. U. Keller, and J. Klinger. Laboratory simulation of cometary processes:

Results from first KOSI experiments. In *International Astronomical Union Colloquium*, volume 116, pages 277–297. Cambridge University Press, 1989.

E. Grün, J. Gebhard, A. Bar-Nun, J. Benkhoff, H. Düren, G. Eich, R. Hische, W. F. Huebner, H. U. Keller, and G. Klees. Development of a dust mantle on the surface of an insolated ice-dust mixture: Results from the KOSI-9 experiment. *Journal of Geophysical Research: Planets*, 98(E8):15091–15104, 1993.

A. Guilbert-Lepoutre and D. Jewitt. Thermal shadows and compositional structure in comet nuclei. *The Astrophysical Journal*, 743(1):31, 2011.

A. Guilbert-Lepoutre, J. Lasue, C. Federico, A. Coradini, R. Orosei, and E. D. Rosenberg. New 3D thermal evolution model for icy bodies application to trans-Neptunian objects. *Astronomy & Astrophysics*, 529:A71, 2011.

A. Guilbert-Lepoutre, R. Schulz, A. Rożek, S. C. Lowry, G. P. Tozzi, and J. A. Stüwe. Pre-perihelion activity of comet 67P/Churyumov-Gerasimenko. *Astronomy & Astrophysics*, 567:L2, 2014.

A. Guilbert-Lepoutre, E. D. Rosenberg, D. Prialnik, and S. Besse. Modelling the evolution of a comet subsurface: Implications for 67P/Churyumov–Gerasimenko. *Monthly Notices of the Royal Astronomical Society*, 462(Suppl_1):S146–S155, 2016.

S. Gulkis, M. Allen, P. von Allmen, G. Beaudin, N. Biver, D. Bockelée-Morvan, M. Choukroun, J. Crovisier, B. J. Davidsson, and P. Encrenaz. Subsurface properties and early activity of comet 67P/Churyumov-Gerasimenko. *Science*, 347(6220), 2015a.

S. Gulkis, M. Allen, P. Von Allmen, G. Beaudin, N. Biver, D. Bockelée-Morvan, M. Choukroun, J. Crovisier, B. J. Davidsson, and P. Encrenaz. Subsurface properties and early activity of comet 67P/Churyumov-Gerasimenko. *Science*, 347(6220): aaa0709, 2015b.

P. J. Gutiérrez, J. L. Ortiz, R. Rodrigo Montero, and J. J. López-Moreno. A study of water production and temperatures of rotating irregularly shaped cometary nuclei. 2000.

P. J. Gutiérrez, L. Jorda, N. H. Samarasinha, and P. Lamy. Outgassing-induced effects in the rotational state of comet 67P/Churyumov—Gerasimenko during the Rosetta mission. *Planetary and Space Science*, 53(11):1135–1145, 2005.

C. Güttler, T. Mannel, A. Rotundi, S. Merouane, M. Fulle, D. Bockelée-Morvan, J. Lasue, A. C. Levasseur-Regourd, J. Blum, and G. Naletto. Synthesis of the morphological description of cometary dust at comet 67P/Churyumov-Gerasimenko. *Astronomy & Astrophysics*, 630:A24, 2019.

K. C. Hansen, K. Altwegg, J.-J. Berthelier, A. Bieler, N. Biver, D. Bockelée-Morvan, U. Calmonte, FABRIZIO. Capaccioni, M. R. Combi, and J. De Keyser. Evolution of

water production of 67P/Churyumov–Gerasimenko: An empirical model and a multi-instrument study. *Monthly Notices of the Royal Astronomical Society*, 462(Suppl_1): S491–S506, 2016.

M. Hässig, K. Altwegg, H. Balsiger, A. Bar-Nun, J.-J. Berthelier, A. Bieler, P. Bochsler, C. Briois, U. Calmonte, and M. Combi. Time variability and heterogeneity in the coma of 67P/Churyumov-Gerasimenko. *Science*, 347(6220):aaa0276, 2015.

A. Hérique, B. Agnus, E. Asphaug, A. Barucci, P. Beck, J. Bellerose, J. Biele, L. Bonal, P. Bousquet, and L. Bruzzone. Direct observations of asteroid interior and regolith structure: Science measurement requirements. *Advances in Space Research*, 62(8): 2141–2162, 2018.

A. Herique, W. Kofman, S. Zine, J. Blum, J.-B. Vincent, and V. Ciarletti. Homogeneity of 67P/Churyumov-Gerasimenko as seen by CONSERT: Implication on composition and formation. *Astronomy & Astrophysics*, 630:A6, 2019.

C. Herny, O. Mousis, R. Marschall, N. Thomas, M. Rubin, O. Pinzón-Rodríguez, and I. P. Wright. New constraints on the chemical composition and outgassing of 67P/Churyumov-Gerasimenko. *Planetary and Space Science*, 200:105194, 2021.

K. Hirao and T. Itoh. *The Sakigake/Suisei Encounter with Comet p/Halley*. Springer, 1988.

M. Hoang, P. Garnier, J. Lasue, H. Rème, M. T. Capria, K. Altwegg, M. Läuter, T. Kramer, and M. Rubin. Investigating the Rosetta/RTOF observations of comet 67P/Churyumov-Gerasimenko using a comet nucleus model: Influence of dust mantle and trapped CO. *Astronomy & Astrophysics*, 638:A106, 2020.

K. A. Holsapple and K. R. Housen. A crater and its ejecta: An interpretation of Deep Impact. *Icarus*, 191(2):586–597, 2007.

E. Howell, P. Taylor, M. Nolan, A. Springmann, L. Benner, M. Brozovic, J. Giorgini, M. Busch, J. Margot, and S. Naidu. Radar characterization of asteroids and comets. *Asteroids, Comets, Meteors 2014*, page 222, 2014.

X. Hu, X. Shi, H. Sierks, M. Fulle, J. Blum, H. U. Keller, E. Kührt, B. Davidsson, C. Güttler, and B. Gundlach. Seasonal erosion and restoration of the dust cover on comet 67P/Churyumov-Gerasimenko as observed by OSIRIS onboard Rosetta. *Astronomy & Astrophysics*, 604:A114, 2017.

W. F. Huebner. über die Gasproduktion der Kometen. *Zeitschrift fur Astrophysik*, 63:22, 1965.

W. F. Huebner, J. Benkhoff, M.-T. Capria, A. Coradini, C. De Sanctis, R. Orosei, and D. Prialnik. *Heat and Gas Diffusion in Comet Nuclei*, volume 133. International Space Science Institute Bern, 2006.

W.-H. Ip, I.-L. Lai, J.-C. Lee, Y.-C. Cheng, Y. Li, Z.-Y. Lin, J.-B. Vincent, S. Besse, H. Sierks, and C. Barbieri. Physical properties and dynamical relation of the circular depressions on comet 67P/Churyumov-Gerasimenko. *Astronomy & Astrophysics*, 591: A132, 2016.

D. Jewitt. Color systematics of comets and related bodies. *The Astronomical Journal*, 150(6):201, 2015.

L. Jorda, P. Lamy, S. Besse, C. Capanna, B. Carry, G. Faury, R. Gaskell, G. Gesquière, O. Groussin, and M. Kaasalainen. Shape and physical properties of asteroid (21) Lutetia from OSIRIS images. In *AAS/Division for Planetary Sciences Meeting Abstracts*, volume 42, page 1043, 2010.

L. Jorda, P. L. Lamy, R. W. Gaskell, M. Kaasalainen, O. Groussin, S. Besse, and G. Faury. Asteroid (2867) Steins: Shape, topography and global physical properties from OSIRIS observations. *Icarus*, 221(2):1089–1100, 2012.

L. Jorda, R. Gaskell, C. Capanna, S. Hviid, P. Lamy, J. Ďurech, G. Faury, O. Groussin, P. Gutiérrez, and C. Jackman. The global shape, density and rotation of Comet 67P/Churyumov-Gerasimenko from preperihelion Rosetta/OSIRIS observations. *Icarus*, 277:257–278, 2016.

N. A. Kaib and T. Quinn. Reassessing the source of long-period comets. *Science*, 325 (5945):1234–1236, 2009.

P. Kamoun, P. L. Lamy, I. Toth, and A. Herique. Constraints on the subsurface structure and density of the nucleus of Comet 67P/Churyumov-Gerasimenko from Arecibo radar observations. *Astronomy & Astrophysics*, 568:A21, 2014.

T. Kareta, B. Sharkey, J. Noonan, K. Volk, V. Reddy, W. Harris, and R. Miles. Physical characterization of the 2017 December outburst of the Centaur 174P/Echeclus. *The Astronomical Journal*, 158(6):255, 2019.

B. A. Keeney, S. A. Stern, P. D. Feldman, M. F. A'Hearn, J.-L. Bertaux, L. M. Feaga, M. M. Knight, R. A. Medina, J. Noonan, and J. W. Parker. Stellar Occultation by Comet 67P/Churyumov–Gerasimenko Observed with Rosetta's Alice Far-ultraviolet Spectrograph. *The Astronomical Journal*, 157(5):173, 2019.

H. U. Keller, W. A. Delamere, W. F. Huebner, H. J. Reitsema, H. U. Schmidt, F. L. Whipple, K. Wilhelm, W. Curdt, R. Kramm, and N. Thomas. Comet P/Halley's nucleus and its activity. In *Exploration of Halley's Comet*, pages 807–823. Springer, 1988.

H. U. Keller, S. Mottola, B. Davidsson, S. E. Schröder, Y. Skorov, E. Kührt, O. Groussin, M. Pajola, S. F. Hviid, and F. Preusker. Insolation, erosion, and morphology of comet 67P/Churyumov-Gerasimenko. *Astronomy & Astrophysics*, 583:A34, 2015a.

H. U. Keller, S. Mottola, Y. Skorov, and L. Jorda. The changing rotation period of comet 67P/Churyumov-Gerasimenko controlled by its activity. *Astronomy & Astrophysics*, 579:L5, 2015b.

H. U. Keller, S. Mottola, S. F. Hviid, J. Agarwal, E. Kührt, Y. Skorov, K. Otto, J.-B. Vincent, N. Oklay, and S. E. Schröder. Seasonal mass transfer on the nucleus of comet 67P/Chuyumov–Gerasimenko. *Monthly Notices of the Royal Astronomical Society*, 469 (Suppl_2):S357–S371, 2017.

M. S. Kelley, Y. R. Fernández, J. Licandro, C. M. Lisse, W. T. Reach, M. F. A'Hearn, J. Bauer, H. Campins, A. Fitzsimmons, and O. Groussin. The persistent activity of Jupiter-family comets at 3–7 AU. *Icarus*, 225(1):475–494, 2013.

M. S. Kelley, T. L. Farnham, J.-Y. Li, D. Bodewits, C. Snodgrass, J. Allen, E. C. Bellm, M. W. Coughlin, A. J. Drake, and D. A. Duev. Six Outbursts of Comet 46P/Wirtanen. *The Planetary Science Journal*, 2(4):131, 2021.

R. L. Kirk, T. C. Duxbury, F. Horz, D. E. Brownlee, R. L. Newburn, and P. Tsou. Topography of the 81/P Wild 2 nucleus derived from Stardust stereoimages. *Lunar and Planetary Science XXXVI, Part 11*, 2005.

J. Klinger. Some consequences of a phase transition of water ice on the heat balance of comet nuclei. *Icarus*, 47(3):320–324, 1981.

M. M. Knight and D. G. Schleicher. The highly unusual outgassing of Comet 103P/Hartley 2 from narrowband photometry and imaging of the coma. *Icarus*, 222(2):691–706, 2013a.

M. M. Knight and D. G. Schleicher. The highly unusual outgassing of Comet 103P/Hartley 2 from narrowband photometry and imaging of the coma. *Icarus*, 222(2):691–706, 2013b.

M. M. Knight, R. Kokotanekova, and N. H. Samarasinha. Physical and Surface Properties of Comet Nuclei from Remote Observations. *arXiv preprint arXiv:2304.09309*, 2023.

H. Kobayashi and H. Kawakita. Water Production Rate of the Jupiter-Family Comet 46P/Wirtanen in the 2008 Apparition with the Subaru Telescope/IRCS. *Publications of the Astronomical Society of Japan*, 62(4):1025–1033, 2010.

W. Kofman, A. Herique, Y. Barbin, J.-P. Barriot, V. Ciarletti, S. Clifford, P. Edenhofer, C. Elachi, C. Eyraud, and J.-P. Goutail. Properties of the 67P/Churyumov-Gerasimenko interior revealed by CONSERT radar. *Science*, 349(6247), 2015.

W. Kofman, S. Zine, A. Herique, Y. Rogez, L. Jorda, and A.-C. Levasseur-Regourd. The interior of Comet 67P/C–G; revisiting CONSERT results with the exact position of the Philae lander. *Monthly Notices of the Royal Astronomical Society*, 497(3):2616–2622, 2020.

R. Kokotanekova, C. Snodgrass, P. Lacerda, and S. F. Green. Physical properties of Jupiter-family comets and KBOs from ground-based lightcurve observations. In *AAS/Division for Planetary Sciences Meeting Abstracts# 49*, volume 49, pages 403–03, 2017.

R. Kokotanekova, C. Snodgrass, P. Lacerda, S. F. Green, P. Nikolov, and T. Bonev. Implications of the small spin changes measured for large Jupiter-family comet nuclei. *Monthly Notices of the Royal Astronomical Society*, 479(4):4665–4680, 2018.

K. J. Kossacki and L. Czechowski. Comet 67p/Churyumov–Gerasimenko, possible origin of the depression Hatmehit. *Icarus*, 305:1–14, 2018.

K. J. Kossacki and A. Jasiak. The evolution of gently sloping mantled deposits on Comet 67P/Churyumov-Gerasimenko. *Icarus*, 319:381–391, 2019.

E. Kührt. Temperature profiles and thermal stresses in cometary nuclei. *Icarus*, 60(3): 512–521, 1984.

Y. G. Kwon, S. Bagnulo, J. Markkanen, J. Agarwal, L. Kolokolova, A.-C. Levasseur-Regourd, C. Snodgrass, and G. P. Tozzi. VLT spectropolarimetry of comet 67P: Dust environment around the end of its intense southern summer. *Astronomy & Astrophysics*, 657:A40, 2022.

P. L. Lamy, I. Toth, B. J. Davidsson, O. Groussin, P. Gutiérrez, L. Jorda, M. Kaasalainen, and S. C. Lowry. A portrait of the nucleus of comet 67P/Churyumov-Gerasimenko. *Space science reviews*, 128:23–66, 2007.

P. L. Lamy, I. Toth, H. A. Weaver, M. F. A'Hearn, and L. Jorda. Properties of the nuclei and comae of 13 ecliptic comets from Hubble Space Telescope snapshot observations. *Astronomy & Astrophysics*, 508(2):1045–1056, 2009.

P. L. Lamy, I. Toth, H. A. Weaver, M. F. A'Hearn, and L. Jorda. Properties of the nuclei and comae of 10 ecliptic comets from Hubble Space Telescope multi-orbit observations. *Monthly Notices of the Royal Astronomical Society*, 412(3):1573–1590, 2011.

J. Lasue, M. C. De Sanctis, A. Coradini, G. Magni, M. T. Capria, D. Turrini, and A. C. Levasseur-Regourd. Quasi-3-D model to describe topographic effects on non-spherical comet nucleus evolution. *Planetary and Space Science*, 56(15):1977–1991, 2008.

M. Läuter, T. Kramer, M. Rubin, and K. Altwegg. Surface localization of gas sources on comet 67P/Churyumov–Gerasimenko based on DFMS/COPS data. *Monthly Notices of the Royal Astronomical Society*, 483(1):852–861, 2019a.

M. Läuter, T. Kramer, M. Rubin, and K. Altwegg. Surface localization of gas sources on comet 67P/Churyumov–Gerasimenko based on DFMS/COPS data. *Monthly Notices of the Royal Astronomical Society*, 483(1):852–861, 2019b.

M. Läuter, T. Kramer, M. Rubin, and K. Altwegg. The gas production of 14 species from comet 67P/Churyumov–Gerasimenko based on DFMS/COPS data from 2014 to 2016. *Monthly Notices of the Royal Astronomical Society*, 498(3):3995–4004, 2020a.

M. Läuter, T. Kramer, M. Rubin, and K. Altwegg. The gas production of 14 species from comet 67P/Churyumov–Gerasimenko based on DFMS/COPS data from 2014 to 2016. *Monthly Notices of the Royal Astronomical Society*, 498(3):3995–4004, 2020b.

J. Leliwa-Kopystynski. Collapse-driven formation of depressions on comet 67P/Churyumov–Gerasimenko. *Icarus*, 302:266–272, 2018.

M. Leon-Dasi, S. Besse, B. Grieger, and M. Küppers. Mapping a duck: Geological features and region definitions on comet 67P/Churyumov-Gerasimenko. *Astronomy & Astrophysics*, 652:A52, 2021.

J.-Y. Li, M. F. A'Hearn, L. A. McFadden, and M. J. Belton. Photometric analysis and disk-resolved thermal modeling of Comet 19P/Borrelly from Deep Space 1 data. *Icarus*, 188(1):195–211, 2007.

M. Lippi, G. L. Villanueva, M. J. Mumma, and S. Faggi. Investigation of the Origins of Comets as Revealed through Infrared High-resolution Spectroscopy I. Molecular Abundances. *The Astronomical Journal*, 162(2):74, 2021.

C. M. Lisse, Y. R. Fernandez, W. T. Reach, J. M. Bauer, M. F. A'hearn, T. L. Farnham, O. Groussin, M. J. Belton, K. J. Meech, and C. D. Snodgrass. Spitzer Space Telescope observations of the nucleus of Comet 103P/Hartley 2. *Publications of the Astronomical Society of the Pacific*, 121(883):968, 2009.

C. M. Lisse, M. R. Combi, T. L. Farnham, N. D. Russo, S. Sandford, A. F. Cheng, U. Fink, W. M. Harris, J. McMahon, and D. J. Scheeres. Operating spacecraft around comets: Evaluation of the near-nucleus environment. *Acta Astronautica*, 2021.

A. Luspay-Kuti, O. Mousis, F. Pauzat, O. Ozgurel, Y. Ellinger, J. I. Lunine, S. A. Fuselier, K. E. Mandt, K. J. Trattner, and S. M. Petrinec. Dual storage and release of molecular oxygen in comet 67P/Churyumov–Gerasimenko. *Nature Astronomy*, 6(6): 724–730, 2022.

R. A. Lyttleton. On the origin of comets. *Monthly Notices of the Royal Astronomical Society*, 108(6):465–475, 1948.

W. Macher, N. Kömle, Y. Skorov, L. Rezac, G. Kargl, and P. Tiefenbacher. 3D thermal modeling of two selected regions on comet 67P and comparison with Rosetta/MIRO measurements. *Astronomy & Astrophysics*, 630:A12, 2019.

L. Maquet. The recent dynamical history of comet 67P/Churyumov-Gerasimenko. *Astronomy & Astrophysics*, 579:A78, 2015.

R. Marschall, L. Rezac, D. Kappel, C.-C. Su, S.-B. Gerig, M. Rubin, O. Pinzón-Rodríguez, D. Marshall, Y. Liao, and C. Herny. A comparison of multiple Rosetta data sets and 3D model calculations of 67P/Churyumov-Gerasimenko coma around equinox (May 2015). *Icarus*, 328:104–126, 2019.

R. Marschall, J. Markkanen, S.-B. Gerig, O. Pinzón-Rodríguez, N. Thomas, and J.-S. Wu. The dust-to-gas ratio, size distribution, and dust fall-back fraction of comet 67p/Churyumov-Gerasimenko: Inferences from linking the optical and dynamical properties of the inner comae. *Frontiers in physics*, 8:227, 2020.

D. Marshall, O. Groussin, J.-B. Vincent, Y. Brouet, D. Kappel, G. Arnold, M. T. Capria, GIANRICO. Filacchione, P. Hartogh, and M. Hofstadter. Thermal inertia and roughness of the nucleus of comet 67P/Churyumov–Gerasimenko from MIRO and VIRTIS observations. *Astronomy & Astrophysics*, 616:A122, 2018.

D. Marshall, L. Rezac, P. Hartogh, Y. Zhao, and N. Attree. Interpretation of heliocentric water production rates of comets. *Astronomy & Astrophysics*, 623:A120, 2019.

M. Massironi, G. Cremonese, LIVIA. Giacomini, MAURIZIO. Pajola, S. Marchi, S. Besse, N. Thomas, J. B. Vincent, M. A. Barucci, and I. Bertini. First geological mapping of 67P/Churyumov-Gerasimenko nucleus from Rosetta mission. In *European Planetary Science Congress*, volume 9, pages EPSC2014–595, 2014.

M. Massironi, E. Simioni, F. Marzari, G. Cremonese, L. Giacomini, M. Pajola, L. Jorda, G. Naletto, S. Lowry, and M. R. El-Maarry. Two independent and primitive envelopes of the bilobate nucleus of comet 67P. *Nature*, 526(7573):402–405, 2015.

K. J. Meech, O. R. Hainaut, and B. G. Marsden. Comet nucleus size distributions from HST and Keck telescopes. *Icarus*, 170(2):463–491, 2004.

S. Merouane, B. Zaprudin, O. Stenzel, Y. Langevin, N. Altobelli, V. Della Corte, H. Fischer, M. Fulle, K. Hornung, and J. Silén. Dust particle flux and size distribution in the coma of 67P/Churyumov-Gerasimenko measured in situ by the COSIMA instrument on board Rosetta. *Astronomy & Astrophysics*, 596:A87, 2016.

R. Miles. Heat of solution: A new source of thermal energy in the subsurface of cometary nuclei and the gas-exsolution mechanism driving outbursts of Comet 29P/Schwassmann–Wachmann and other comets. *Icarus*, 272:356–386, 2016.

S. Mottola, S. Lowry, C. Snodgrass, P. L. Lamy, I. Toth, A. Rożek, H. Sierks, M. F. A'Hearn, F. Angrilli, and C. Barbieri. The rotation state of 67P/Churyumov-Gerasimenko from approach observations with the OSIRIS cameras on Rosetta. *Astronomy & Astrophysics*, 569:L2, 2014.

O. Mousis, A. Guilbert-Lepoutre, B. Brugger, L. Jorda, J. S. Kargel, A. Bouquet, A.-T. Auger, P. Lamy, P. Vernazza, and N. Thomas. Pits formation from volatile outgassing on 67P/Churyumov–Gerasimenko. *The Astrophysical Journal Letters*, 814(1):L5, 2015.

D. Nesvornỳ, D. Vokrouhlickỳ, L. Dones, H. F. Levison, N. Kaib, and A. Morbidelli. Origin and evolution of short-period comets. *The Astrophysical Journal*, 845(1):27, 2017.

J. Oberst, B. Giese, E. Howington-Kraus, R. Kirk, L. Soderblom, B. Buratti, M. Hicks, R. Nelson, and D. Britt. The nucleus of Comet Borrelly: A study of morphology and surface brightness. *Icarus*, 167(1):70–79, 2004.

L. O'rourke, P. Heinisch, J. Blum, S. Fornasier, G. Filacchione, H. Van Hoang, M. Ciarniello, A. Raponi, B. Gundlach, and R. A. Blasco. The Philae lander reveals low-strength primitive ice inside cometary boulders. *Nature*, 586(7831):697–701, 2020.

M. Pajola, J.-B. Vincent, M. R. El-Maarry, and A. Lucchetti. Cometary nuclei morphology and evolution. page 41.

R. L. Palma, R. O. Pepin, A. J. Westphal, E. Füri, D. J. Schlutter, Z. S. Gainsforth, and D. R. Frank. Helium and neon in comet 81P/Wild 2 samples from the NASA Stardust mission. *Meteoritics & Planetary Science*, 54(1):3–53, 2019.

F. P. Panale and J. R. Salvail. An idealized short-period comet model: Surface insolation, H2O flux, dust flux, and mantle evolution. *Icarus*, 60(3):476–511, 1984.

M. Pätzold, T. Andert, M. Hahn, S. W. Asmar, J.-P. Barriot, M. K. Bird, B. Häusler, K. Peter, S. Tellmann, and E. Grün. A homogeneous nucleus for comet 67P/Churyumov–Gerasimenko from its gravity field. *Nature*, 530(7588):63–65, 2016.

M. Pätzold, T. P. Andert, M. Hahn, J.-P. Barriot, S. W. Asmar, B. Häusler, M. K. Bird, S. Tellmann, J. Oschlisniok, and K. Peter. The Nucleus of comet 67P/Churyumov–Gerasimenko–Part I: The global view–nucleus mass, mass-loss, porosity, and implications. *Monthly Notices of the Royal Astronomical Society*, 483(2):2337–2346, 2019.

F. J. Pozuelos, F. Moreno, F. Aceituno, V. Casanova, A. Sota, J. J. López-Moreno, J. Castellano, E. Reina, A. Climent, and A. Fernández. Dust environment and dynamical history of a sample of short-period comets-II. 81P/Wild 2 and 103P/Hartley 2. *Astronomy & Astrophysics*, 571:A64, 2014.

F. Preusker, F. Scholten, K.-D. Matz, T. Roatsch, R. Jaumann, C. A. Raymond, and C. T. Russell. Topography of Vesta from Dawn FC stereo images. 2012.

F. Preusker, F. Scholten, K.-D. Matz, T. Roatsch, K. Willner, S. F. Hviid, J. Knollenberg, L. Jorda, P. J. Gutiérrez, and E. Kührt. Shape model, reference system definition, and cartographic mapping standards for comet 67P/Churyumov-Gerasimenko–Stereo-photogrammetric analysis of Rosetta/OSIRIS image data. *Astronomy & Astrophysics*, 583:A33, 2015.

F. Preusker, F. Scholten, K.-D. Matz, T. Roatsch, S. F. Hviid, S. Mottola, J. Knollenberg, E. Kührt, M. Pajola, and N. Oklay. The global meter-level shape model of comet 67P/Churyumov-Gerasimenko. *Astronomy & Astrophysics*, 607:L1, 2017.

D. Prialnik. Modelling gas and dust release from Comet Hale–Bopp. *Earth, Moon, and Planets*, 77(3):223–230, 1997.

D. Prialnik. What makes comets active? In *Asteroids, Comets, Meteors*, volume 229, pages 153–170, 2006.

D. Prialnik and A. Bar-nun. The formation of a permanent dust mantle and its effect on cometary activity. *Icarus*, 74(2):272–283, 1988.

D. Prialnik and AKIVA. Bar-Nun. On the evolution and activity of cometary nuclei. *The Astrophysical Journal*, 313:893–905, 1987.

D. Prialnik and D. Jewitt. Amorphous ice in comets: Evidence and consequences. *arXiv preprint arXiv:2209.05907*, 2022.

D. Prialnik and M. Podolak. Radioactive heating of porous comet nuclei. *Icarus*, 117(2): 420–430, 1995.

D. Prialnik, J. Benkhoff, and M. Podolak. Modeling the structure and activity of comet nuclei. *Comets II*, 1:359–387, 2004.

S. Protopapa, J. M. Sunshine, L. M. Feaga, M. S. Kelley, M. F. A'Hearn, T. L. Farnham, O. Groussin, S. Besse, F. Merlin, and J.-Y. Li. Water ice and dust in the innermost coma of comet 103P/Hartley 2. *Icarus*, 238:191–204, 2014.

R. Reinhard. The Giotto encounter with comet Halley. *Nature*, 321(Suppl 6067):313–318, 1986.

L. Rezac and Y. Zhao. Accuracy of view factor calculations for digital terrain models of comets and asteroids. *Astronomy & Astrophysics*, 642:A167, 2020.

H. Rickman. The nucleus of comet Halley: Surface structure, mean density, gas and dust production. *Advances in Space Research*, 9(3):59–71, 1989.

H. Rickman. Origin and Evolution of Comets: Ten Years after the Nice Model and One Year after Rosetta, Volume 2. *Origin and Evolution of Comets: Ten Years after the Nice Model and One Year after Rosetta*, 2, 2018.

H. Rickman, J. A. Fernandez, and B. A. S. Gustafson. Formation of stable dust mantles on short-period comet nuclei. *Astronomy and Astrophysics*, 237:524–535, 1990.

E. D. Rosenberg and D. Prialnik. Fully 3-dimensional calculations of dust mantle formation for a model of Comet 67P/Churyumov–Gerasimenko. *Icarus*, 201(2):740–749, 2009.

N. X. Roth, D. Bodewits, B. Bonev, A. Cochran, M. Combi, M. Cordiner, N. D. Russo, M. DiSanti, S. Faggi, and L. Feaga. The Crucial Role of Ground-and Space-Based Remote Sensing Studies of Cometary Volatiles in the Next Decade (2023-2032). *arXiv preprint arXiv:2007.08568*, 2020.

M. Rubin, K. Altwegg, H. Balsiger, A. Bar-Nun, J.-J. Berthelier, C. Briois, U. Calmonte, M. Combi, J. De Keyser, and B. Fiethe. Krypton isotopes and noble gas abundances in the coma of comet 67P/Churyumov-Gerasimenko. *Science advances*, 4(7):eaar6297, 2018.

B.-K. Ruzicka. Layerings in the nucleus of comet 67P/Churyumov-Gerasimenko. *arXiv preprint arXiv:1912.06544*, 2019.

B.-K. Ruzicka, L. Penasa, H. Boehnhardt, A. Pack, B. Dolives, F. Souvannavong, and E. Remetean. Analysis of layering-related linear features on comet 67P/Churyumov–Gerasimenko. *Monthly Notices of the Royal Astronomical Society*, 482(4):5007–5011, 2019.

R. Z. Sagdeev, J. Blamont, A. A. Galeev, V. I. Moroz, V. D. Shapiro, V. I. Shevchenko, and K. Szeg\Ho. Vega spacecraft encounters with comet Halley. *Nature*, 321(Suppl 6067):259–262, 1986.

K. Sárneczky, G. M. Szabó, B. Csák, J. Kelemen, G. Marschalkó, A. Pál, R. Szakáts, T. Szalai, E. Szegedi-Elek, and P. Székely. Activity of 50 long-period comets beyond 5.2 au. *The Astronomical Journal*, 152(6):220, 2016.

B. Schmitt, S. Espinasse, R. J. A. Grim, J. M. Greenberg, and J. Klinger. Laboratory studies of cometary ice analogues. In *Physics and Mechanics of Cometary Materials*, volume 302, 1989.

P. H. Schultz, B. Hermalyn, and J. Veverka. The deep impact crater on 9P/Tempel-1 from Stardust-NExT. *Icarus*, 222(2):502–515, 2013.

M. E. Schwamb. Stranded in no-man's-land. *Nature*, 507(7493):435–436, 2014.

S. R. Schwartz, P. Michel, M. Jutzi, S. Marchi, Y. Zhang, and D. C. Richardson. Catastrophic disruptions as the origin of bilobate comets. *Nature astronomy*, 2(5):379–382, 2018.

G. Schwehm and R. Schulz. Rosetta goes to comet Wirtanen. *Space Science Reviews*, 90 (1-2):313–319, 1999.

D. W. Sears, H. W. Kochan, and W. F. Huebner. Laboratory simulation of the physical processes occurring on and near the surfaces of comet nuclei. *Meteoritics & Planetary Science*, 34(4):497–525, 1999.

K. J. Seidensticker and H. Kochan. Gas Dynamics of Sublimating Ice/Dust Samples. In *AAS/Division for Planetary Sciences Meeting Abstracts# 24*, volume 24, pages 38–12, 1992.

Z. Sekanina. Rotation and precession of cometary nuclei. *Annual Review of Earth and Planetary Sciences*, 9(1):113–143, 1981.

O. Shubina, V. Kleshchonok, O. Ivanova, I. Luk'yanyk, and A. Baransky. Photometry of comet 29P/Schwassmann–Wachmann 1 in 2012–2019. *Icarus*, 391:115340, 2023.

H. Sierks, C. Barbieri, P. L. Lamy, R. Rodrigo, D. Koschny, H. Rickman, H. U. Keller, J. Agarwal, M. F. A'hearn, and F. Angrilli. On the nucleus structure and activity of comet 67P/Churyumov-Gerasimenko. *Science*, 347(6220), 2015.

J. B. Simon, J. Blum, T. Birnstiel, and D. Nesvornỳ. Comets and Planetesimal Formation. *arXiv preprint arXiv:2212.04509*, 2022.

Y. Skorov, V. Reshetnyk, M. Küppers, M. S. Bentley, S. Besse, and P. Hartogh. Sensitivity of modelled cometary gas production on the properties of the surface layer of the nucleus. *Monthly Notices of the Royal Astronomical Society*, 519(1):59–73, 2023.

C. Snodgrass, L. Feaga, G. H. Jones, M. Kueppers, and C. Tubiana. Past and Future Comet Missions. *arXiv preprint arXiv:2208.08476*, 2022.

L. A. Soderblom, T. L. Becker, G. Bennett, D. C. Boice, D. T. Britt, R. H. Brown, B. J. Buratti, C. Isbell, B. Giese, and T. Hare. Observations of Comet 19P/Borrelly by the miniature integrated camera and spectrometer aboard Deep Space 1. *Science*, 296 (5570):1087–1091, 2002.

M. Solontoi, Ž. Ivezić, M. Jurić, A. C. Becker, L. Jones, A. A. West, S. Kent, R. H. Lupton, M. Claire, and G. R. Knapp. Ensemble properties of comets in the Sloan Digital Sky Survey. *Icarus*, 218(1):571–584, 2012.

T. Spohn, J. Knollenberg, A. J. Ball, M. Banaszkiewicz, J. Benkhoff, M. Grott, J. Grygorczuk, C. Hüttig, A. Hagermann, and G. Kargl. Thermal and mechanical properties of the near-surface layers of comet 67P/Churyumov-Gerasimenko. *Science*, 349(6247): aab0464, 2015.

R. E. Squires and D. B. Beard. Physical and Orbital Behavior of Comets. *The Astrophysical Journal*, 133:657, 1961.

J. K. Steckloff, G. Sarid, K. Volk, T. Kareta, M. Womack, W. Harris, L. Woodney, and C. Schambeau. P/2019 LD2 (ATLAS): An Active Centaur in Imminent Transition to the Jupiter Family. *The Astrophysical Journal Letters*, 904(2):L20, 2020.

G. Steiner, N. I. Kömle, and E. Kührt. Theoretical modelling of comet simulation experiments. *VOAW, Graz*, page 11, 1991.

A. Stinson, S. Bagnulo, H. Böhnhardt, G. Tozzi, S. Fornasier, and K. Muinonen. Broadband FORS/VLT polarimetry of comet nuclei: 9P/Tempel 1, 19P/Borrelly, 67P/Churyumov-Gerasimenko, 74P/Smirnova-Chernykh, and 152P/Helin-Lawrence. *Asteroids, Comets, Meteors 2014*, page 513, 2014.

P. J. Stooke. Cartography of asteroids and comet nuclei from low resolution data. *Lunar and Planetary Inst., Asteroids, Comets, Meteors 1991*, 1992.

M. B. Syal, P. H. Schultz, J. M. Sunshine, M. F. A'Hearn, T. L. Farnham, and D. S. Dearborn. Geologic control of jet formation on Comet 103P/Hartley 2. *Icarus*, 222(2): 610–624, 2013.

MGGT. Taylor, N. Altobelli, B. J. Buratti, and M. Choukroun. The Rosetta mission orbiter science overview: The comet phase. *Philosophical Transactions of the Royal Society A: Mathematical, Physical and Engineering Sciences*, 375(2097):20160262, 2017.

N. Thomas, B. Davidsson, M. R. El-Maarry, S. Fornasier, L. Giacomini, A. G. Gracia-Berná, S. F. Hviid, W.-H. Ip, L. Jorda, and H. U. Keller. Redistribution of particles across the nucleus of comet 67P/Churyumov-Gerasimenko. *Astronomy & Astrophysics*, 583:A17, 2015a.

N. Thomas, H. Sierks, C. Barbieri, P. L. Lamy, R. Rodrigo, H. Rickman, D. Koschny, H. U. Keller, J. Agarwal, and M. F. A'Hearn. The morphological diversity of comet 67P/Churyumov-Gerasimenko. *Science*, 347(6220):aaa0440, 2015b.

P. Thomas, M. A'Hearn, M. J. S. Belton, D. Brownlee, B. Carcich, B. Hermalyn, K. Klaasen, S. Sackett, P. H. Schultz, and J. Veverka. The nucleus of Comet 9P/Tempel 1: Shape and geology from two flybys. *Icarus*, 222(2):453–466, 2013a.

P. C. Thomas, J. Veverka, M. J. Belton, A. Hidy, M. F. A'Hearn, T. L. Farnham, O. Groussin, J.-Y. Li, L. A. McFadden, and J. Sunshine. The shape, topography, and geology of Tempel 1 from Deep Impact observations. *Icarus*, 187(1):4–15, 2007.

P. C. Thomas, M. F. A'Hearn, J. Veverka, M. J. Belton, J. Kissel, K. P. Klaasen, L. A. McFadden, H. J. Melosh, P. H. Schultz, and S. Besse. Shape, density, and geology of the nucleus of Comet 103P/Hartley 2. *Icarus*, 222(2):550–558, 2013b.

P. C. Thomas, M. F. A'Hearn, J. Veverka, M. J. Belton, J. Kissel, K. P. Klaasen, L. A. McFadden, H. J. Melosh, P. H. Schultz, and S. Besse. Shape, density, and geology of the nucleus of Comet 103P/Hartley 2. *Icarus*, 222(2):550–558, 2013c.

F. Tosi, FABRIZIO. Capaccioni, M. T. Capria, S. Mottola, A. Zinzi, M. Ciarniello, GIANRICO. Filacchione, M. Hofstadter, S. Fonti, and M. Formisano. The changing temperature of the nucleus of comet 67P induced by morphological and seasonal effects. *Nature Astronomy*, 3(7):649–658, 2019.

J.-B. Vincent, D. Bodewits, S. Besse, H. Sierks, C. Barbieri, P. Lamy, R. Rodrigo, D. Koschny, H. Rickman, and H. U. Keller. Large heterogeneities in comet 67P as revealed by active pits from sinkhole collapse. *Nature*, 523(7558):63–66, 2015a.

J.-B. Vincent, N. Oklay, S. Marchi, S. Höfner, and H. Sierks. Craters on comets. *Planetary and Space Science*, 107:53–63, 2015b.

J.-B. Vincent, M. F. A'Hearn, Z.-Y. Lin, M. R. El-Maarry, M. Pajola, H. Sierks, C. Barbieri, P. L. Lamy, R. Rodrigo, and D. Koschny. Summer fireworks on comet 67P. *Monthly Notices of the Royal Astronomical Society*, 462(Suppl_1):S184–S194, 2016a.

J.-B. Vincent, N. Oklay, M. Pajola, S. Höfner, H. Sierks, X. Hu, C. Barbieri, P. L. Lamy, R. Rodrigo, and D. Koschny. Are fractured cliffs the source of cometary dust jets? Insights from OSIRIS/Rosetta at 67P/Churyumov-Gerasimenko. *Astronomy & Astrophysics*, 587:A14, 2016b.

J.-B. Vincent, S. F. Hviid, S. Mottola, E. Kührt, F. Preusker, F. Scholten, H. U. Keller, N. Oklay, D. de Niem, and B. Davidsson. Constraints on cometary surface evolution

derived from a statistical analysis of 67P's topography. *Monthly Notices of the Royal Astronomical Society*, 469(Suppl_2):S329–S338, 2017.

J.-B. Vincent, T. Farnham, E. Kührt, Y. Skorov, R. Marschall, N. Oklay, M. R. El-Maarry, and H. U. Keller. Local manifestations of cometary activity. *Space Science Reviews*, 215:1–27, 2019.

P. R. Weissman, M. F. A'Hearn, L. A. McFadden, and H. Rickman. Evolution of comets into asteroids. *Asteroids III*, 1:669, 2002.

F. L. Whipple. A comet model. I. The acceleration of Comet Encke. *The Astrophysical Journal*, 111:375–394, 1950.

K. Wierzchos and M. Womack. CO gas and dust outbursts from centaur 29P/Schwassmann–Wachmann. *The Astronomical Journal*, 159(4):136, 2020.

Y. Zhao, L. Rezac, Y. Skorov, and J.-Y. Li. The phenomenon of shape evolution from solar-driven outgassing for analogues of small Kuiper belt objects. *Monthly Notices of the Royal Astronomical Society*, 492(4):5152–5166, 2020.

M. E. Zolensky, T. J. Zega, H. Yano, S. Wirick, A. J. Westphal, M. K. Weisberg, I. Weber, J. L. Warren, M. A. Velbel, and A. Tsuchiyama. Mineralogy and petrology of comet 81P/Wild 2 nucleus samples. *Science*, 314(5806):1735–1739, 2006.

List of Figures

List of Tables

Appendices

Resumé

Les noyaux cométaires manifestent une complexité considérable, tant à l'échelle locale que globale. Des dépressions circulaires, appelées "pits", ont été observées sur toutes les Comètes de la Famille de Jupiter visitées, suscitant un intérêt pour leur formation et évolution induites par l'activité générée par des processus thermiques et l'érosion dans les conditions actuelles d'illumination. De plus, l'irrégularité globale de ces noyaux nous a conduit à examiner son impact potentiel sur l'activité cométaire globale et l'importance des données de forme du noyau pour une meilleure compréhension des courbes d'activité observées depuis la Terre.

Cette thèse s'est concentrée sur l'impact de la forme complexe locale et globale sur l'activité thermique des comètes. Nous avons étudié en profondeur les changements thermiques et morphologiques des pits, en tenant compte des effets des paramètres structuraux et thermiques initiaux. Nous avons aussi exploré comment la forme d'un noyau cométaire influence sa courbe d'activité. L'influence de la composition de surface et interne d'une comète a également été investiguée, visant à déchiffrer les liens entre les propriétés du noyau d'une comète et son comportement observable depuis le sol.

Nous avons développé un modèle qui permet l'incorporation de la forme du noyau cométaire, afin de prendre en compte sa morphologie locale et globale, dans le calcul du bilan d'énergie en surface. Cette énergie représente la condition de surface d'un modèle thermique, que l'on utilise afin de simuler les taux de production et l'érosion dûs à l'activité thermique. Pour ce faire, nous utilisons un modèle de forme 3D pour chaque comète (Preusker et al., 2017; Farnham and Thomas, 2013b,a; Farnham et al., 2005, pour 67P/C-G, 103P/Hartley 2, 9P/Tempel 1, et 81P/Wild 2, respectivement). Nous considérons la géométrie du shadowing et du self-heating – l'énergie reçue par réflexion ou émission depuis des facettes voisines. Nous calculons le bilan énergétique pour chacune de ces facettes avec un pas de temps de 8 minutes sur une révolution orbitale récente complète de la comète. Ce bilan d'énergie est la condition aux limites (à la surface) d'un modèle d'évolution thermique 1D (Lasue et al., 2008). Ce modèle résout simultanément les équations de conservation de la masse et de l'énergie pour chaque facette du modèle de forme. Il prend en compte la cristallisation de la glace amorphe, ainsi que la sublimation et la recondensation des glaces d'H_2O, de CO et de CO_2. L"éjection de grains de poussière dûe à la pression exercée par le flux de gaz est également calculée, tout comme l'érosion

de surface et le redépôt de poussière. Pour simuler l'évolution thermique des noyaux cométaires sous les conditions d'illumination actuelles, il faut considérer leur trajet de la ceinture de Kuiper vers le Système Solaire interne via quelques orbites d'injection. Cela permet de modéliser une composition de sous-surface plus réaliste, en tenant compte du retrait des fronts de sublimation des glaces sous la surface.

Pour l'étude des pits, nous faisons tourner les simulations pendant le nombre d'orbites que la comète a parcouru dans les conditions actuelles d'illumination. Pour 67P, cela correspond à environ 10 orbites depuis son dernier changement orbital significatif (Maquet, 2015), et jusqu'à ce qu'elle ait été visitée par la sonde Rosetta. Pour l'étude des effets globaux, les calculs sont réalisés en correspondance avec les observations des taux de production d'eau ou de poussière. La résolution du modèle de forme utilisé change en fonction du but de l'étude (plus de 20,000 facettes pour l'étude des pits et jusqu'à 500 facettes pour l'étude de l'activité globale).

Étude détaillée d'un pit sur 67P, et effet des paramètres initiaux

Nous avons examiné l'évolution thermique d'un pit spécifique sur 67P afin de comprendre son évolution thermique et morphologique. En outre, nous avons étudié l'influence de la forme locale sur cette activité, en intégrant les effets d'ombre et de self-heating dans notre modèle de comète. En effet, la topographie complexe des comètes joue un rôle crucial dans leur bilan énergétique et leur évolution thermique. Toutefois, l'évolution de structures profondes telles que les pits sur une longue durée, en tenant compte des effets de forme, n'a pas été quantifiée auparavant. Par ailleurs, nous avons également exploré l'influence des paramètres physiques du modèle sur l'activité thermique. Des paramètres tels que la porosité, le rapport poussière/glace, l'abondance relative de CO et de CO_2 par rapport à H_2O, et la présence d'un manteau de poussière initial peuvent impacter l'activité thermique des comètes. Chaque paramètre a été évalué de manière indépendante pour en isoler les effets. Notre étude vise à approfondir la compréhension de ces effets sur l'activité et la morphologie de la surface sur une longue période afin d'essayer de retracer les caractéristiques originelles des pits pour identifier leur mécanisme de formation.

Nous avons trouvé que la topographie locale influence de manière significative la distribution d'énergie dans les pits: les plateaux peuvent recevoir plus du double d'énergie par rapport aux murs et aux fonds. Une distribution asymétrique de l'énergie est également observée, les facettes orientées vers l'équateur recevant davantage d'énergie. Le self-heating peut constituer une source d'énergie notable, pouvant représenter jusqu'à 60% de l'énergie totale dans le pit. Ces résultats soulignent l'importance de prendre en compte les effets de la forme dans les études à cette échelle spatiale. Une porosité de 80% engendre presque le double d'érosion par rapport à 60%, montrant que les régions compactes et poussiéreuses réagissent différemment. Le rapport poussière/glace influence significativement l'activité, les rapports plus élevés provoquant une activité et une érosion accrues. L'introduction de CO et CO_2 dans la composition initiale a un effet négligeable sur l'érosion, celle-ci étant principalement dûe à la sublimation de l'eau. L'épaisseur du manteau de poussière joue également un rôle crucial pour l'activité thermique et l'érosion: un manteau de moins de 5 cm est rapidement érodé par l'activité cométaire, tandis qu'un manteau de 10 cm ou plus peut considérablement la réduire, ce qui concorde avec la

présence d'un manteau cyclique de quelques centimètres (Davidsson et al., 2022b).

Enfin, l'érosion atteinte après 10 orbites ne suffit pas à expliquer la formation des pits, suggérant l'intervention d'autres processus. Bien que ce résultat soit intéressant pour comprendre l'origine des pits, la diversité de leurs formes, tailles et conditions d'illumination locales sur 67P nous conduit à étudier un plus grand échantillon. Nous maintiendrons les paramètres initiaux uniformes et ne modifierons que l'apport d'énergie.

Pour le reste des simulations, la porosité a été fixée à 75% et le rapport poussière/glace à 1. Le CO et CO_2 n'ont pas été inclus dans le mélange de glace pour éviter les instabilités numériques. De plus, un manteau de poussière initial n'a pas été pris en compte dans les simulations en raison de sa présence variable et de sa faible épaisseur.

Étude de 30 pits sur 67P

Nous avons choisi 30 pits pour notre étude. La variété des caractéristiques morphologiques locales de la surface de 67P peut illustrer les différentes conditions d'illumination de celle-ci. Notre attention se porte sur les grandes dépressions, de quelques dizaines à plusieurs centaines de mètres de diamètre. Par conséquent, nous n'incluons pas les dépressions de thermokarst cométaires, qui correspondent à un affaissement du sol causé par la fonte du permafrost initiée par la sublimation de la glace (Bouquety et al., 2022). Nous avons sélectionné des pits circulaires, allongés, des alcôves et des falaises, afin d'atteindre nos objectifs d'échantillonnage et d'étudier d'éventuels liens évolutifs entre ces caractéristiques. Nous notons également que certains des pits sélectionnés ont montré de l'activité, observée par Rosetta/OSIRIS (Vincent et al., 2015b). La plupart des pits se trouvent dans l'hémisphère nord, caractérisé par des pits profonds et des falaises abruptes. Les pits sont plus rares, généralement plus larges et moins profonds dans l'hémisphère sud. Cette dichotomie résulte de la forte obliquité du noyau (52°), provoquant de fortes saisons. L'hémisphère sud subit un chauffage et une érosion intensifs pendant l'été (Keller et al., 2015a).

Nos résultats montrent une forte corrélation entre la quantité d'énergie reçue près du périhélie, le pic de dégazage, et l'érosion. L'hémisphère sud est la zone la plus activement érodée, avec une érosion atteignant 77 m dans les facettes les plus actives: l'obliquité façonne la surface cométaire. En revanche, malgré les tendances saisonnières évidentes entraînant une érosion plus marquée au sud, la topographie locale et la forme du noyau influencent grandement la distribution énergétique. Le shadowing peut réduire l'énergie de 70%, et le self-heating contribuer jusqu'à 60% de l'énergie totale dans certains cas. En conséquence de la distribution locale de l'énergie, les plateaux érodent plus que les murs et les fonds des pits, suggérant que les pits ont tendance à s'élargir et à s'aplatir avec le temps. Aussi, les taux d'érosion sont nettement inférieurs par rapport aux dimensions des pits. Par exemple, dans les régions du sud où l'érosion est la plus prononcée, elle n'atteint pas plus de 80 m, alors que les diamètres des pits varient de 130 m à plus de 500 m. Il est toutefois crucial de considérer les hétérogénéités locales pouvant entraîner des variations d'érosion.

Nos résultats confirment plusieurs études antérieures, montrant notamment que l'érosion dûe à l'activité thermique actuelle est insuffisante pour créer des caractéristiques de quelques centaines de mètres (Mousis et al., 2015; Guilbert-Lepoutre et al., 2016). Con-

cernant l'évolution des pits, nos résultats soutiennent l'hypothèse que les pits profonds et circulaires sont moins évolués (ou mieux préservés) que les grands ou allongés (Vincent et al., 2015a).

Étude des pits sur 9P, 81P, et 103P

Afin de contextualiser nos conclusions sur l'étude des pits sur 67P et explorer des similitudes potentielles dans leur évolution, nous avons analysé l'érosion induite par la sublimation des pits sur d'autres noyaux de comètes. Nous avons etudié: 81P, 9P, et 103P, pour lesquels des modèles de forme à résolution suffisante sont disponibles.

Nous avons simulé l'activité thermique pendant 6 orbites pour 81P, 13 orbites pour 9P, et 20 orbites pour 103P. Pour chaque comète, nous avons utilisé le modèle de forme le plus détaillé disponible pour intégrer la forme locale et tenir compte d'un nombre adéquat de pits plausibles sur leurs surfaces. Les pits de ces comètes présentent un rapport profondeur-diamètre (d/D) généralement plus faible que les pits de 67P. Par exemple, les valeurs moyennes observées de d/D sont de 0.1 pour 9P (Thomas et al., 2013a) et de 0.2 pour 81P (Kirk et al., 2005; Vincent et al., 2015b). L'aspect de surface de 103P ressemble à celui de 9P, présentant une apparence lisse sans pits profonds évidents (Ip et al., 2016). Les pits abruptes avec des fonds plats et variant de 150 m à 1 km, présentent une distribution de fréquence de taille similaire sur 67P, 9P et 81P (Ip et al., 2016). Cela suggère que ces structures seraient formées par le même mécanisme sur les différentes comètes. Ainsi, dans cette étude, nous traitons des pits de l'ordre de plusieurs dizaines à plusieurs centaines de mètres. Pour chaque noyau, nous sélectionnons plus de 10 pits.

Nos résultats montrent que pour toutes les comètes étudiées, l'activité et l'érosion sont principalement contrôlées par l'insolation directe, et donc manifestent des tendances saisonnières. En raison de l'absence de complexité significative de la forme global de ces noyaux, aucun effet notable de la forme globale n'est observé. Cependant, les effets de forme peuvent être importants à l'échelle des pits, notamment pour les pits de 81P. De manière similaire à 67P, les pits marqués peuvent s'effacer ou s'élargir. De plus, l'érosion causée par les multiples passages au périhélie n'est pas suffisante pour former des pits de plusieurs centaines de mètres ni pour reproduire la forme creusée observée.

Selon nos simulations de l'évolution thermique induite par l'illumination actuelle, les niveaux d'érosion des dépressions, de faible à élevé, sont : 81P, 67P, 9P, puis 103P. Ceci concorde avec leur histoire dynamique et les résultats d'analyses de surface par Vincent et al. (2017).

En conclusion, la formation des pits ne peut être expliquée par l'érosion dûe à l'activité thermique récente des comètes dans leurs orbites actuelles. Au contraire, il est plus probable que les pits s'effacent avec le temps. L'origine énigmatique des pits, qui pourrait être liée à des phases dynamiques antérieures des comètes, appelle à des investigations supplémentaires pour explorer les différents scénarios potentiels de leur formation.

Influence de la forme du noyau cométaire sur l'activité globale

Nous nous sommes intéressés à l'étude de l'impact de la forme des noyaux cométaires sur les taux de production d'eau pour les comètes suivantes: 67P, 103P et 9P.

L'objectif était de déterminer si les courbes d'activité de ces comètes, obtenues à partir d'observations terrestres ou spatiales, contiennent des informations sur leur forme et si des formes complexes des noyaux pourraient influencer notre interprétation des données. De plus, nous avons étudié l'effet de différents paramètres de composition et de propriétés structurelles, tels que la porosité, le rapport poussière/glace et la présence d'une fine couche de poussière, la conductivité, ainsi que l'activité partielle, sur les taux de production. Notre objectif était d'évaluer l'influence de la forme du noyau sur l'activité, en comparaison à tous les autres facteurs, et de définir les limites de l'interprétation des caractéristiques des comètes à partir des observations.

Nouc avons simulé les taux de production sur toutes les facettes des modèles de forme, en variant les paramètres initiaux. Nous avons ensuite comparé les taux de production, intégrés sur toute la surface du modele de forme ainsi que de la sphère, obtenus à partir de différentes simulations, avec les données d'observations. Pour 67P, nous avons comparé nos résultats aux taux de production de l'H_2O dérivées des observations de ROSINA/Rosetta (Läuter et al., 2020a). Pour l'analyse de 103P, nous avons utilisé les données H_2O de Knight and Schleicher (2013a). Ces données ont été obtenues à partir du modèle de Haser pour les taux de production du OH, mesurés à l'observatoire de Lowell entre 1991 et 2011. Pour 9P, nous avons utilisé les taux de production d'H_2O de Biver et al. (2007). Ces taux sont basés sur les observations du OH effectuées avec le télescope de Nancay ainsi que sur les observations de la ligne H_2O à 557 GHz réalisées par le satellite Odin. Ces données ont été recueillies pendant la période entourant le périhélie de chaque comète, lorsque leur activité est à son apogée. Pour ces simulations, nous avons réduit la résolution des modèles de forme à un maximum de 500 facettes afin d'optimiser le temps de calcul tout en préservant la forme globale du noyau. Les modèles sphériques ont la même surface que les modèles de forme correspondants.

Que ce soit pour le modèle de forme ou bien la sphère, les taux de production globaux simulés suivent la tendence générale des observations pour les trois comètes étudiées. En revanche, la quantité dans l'absolue est surestimée par les simulations. La forme globale du noyau peut affecter les taux de production, mais son impact n'est pas primordial. Pour 67P, la différence dans les taux de production entre les modèles de forme et de sphère est minime. Ce résultat est en accord avec Marschall et al. (2019), qui ont constaté un changement inférieur à 5% de la section transversale de 67P le long de son orbite, affirmant que la dépendance à la forme et à l'orientation de l'axe de rotation est faible lorsque la section transversale éclairée du noyau reste constante. De plus, l'utilisation d'un modèle de forme à 1,000 facettes, qui intègre des caractéristiques de surface à l'échelle de quelques centaines de mètres, ne montre aucune différence significative dans les taux de production par rapport au modèle à 500 facettes qui représente uniquement la forme globale. Cela suggère que la rugosité locale à cette échelle a un impact négligeable sur les taux de production globaux, tandis que les variations saisonnières jouent un rôle majeur dans le dégazage. Cependant, pour les comètes 9P et 103P, la forme peut jouer un rôle plus important. Le modèle de forme de 9P produit des taux de production légèrement plus proches des observations que les modèles sphériques. Ces derniers surestiment la production d'eau, ce qui suggère une section transversale plus grande que celle des modèles de forme pendant la période d'observation. Pour 103P, bien que les deux modèles – la sphère et le modèle de forme – reproduisent le bon ordre de grandeur des taux de

production, la sphère fournit des taux de production légèrement meilleurs en dehors du perihelie.

Les hétérogénéités de surface et de sous-surface jouent un rôle crucial dans le dégazage cométaire observé. Cela est illustré par les différences significatives entre les taux de production d'eau simulés et observés pour les comètes 67P et 9P, qu'il s'agisse d'utiliser le modèle ou la sphère, ainsi que par les variations de pente avant et après le périhélie entre les modèles des trois comètes et la courbe observée. Inclure uniquement l'activité de neuf régions actives de 67P, tel que rapportées par Läuter et al. (2019b), améliore considérablement les taux de production simulés, tant en ce qui concerne l'amplitude que la tendance pré-périhélique. De même, inclure 10% de l'activité de 9P permet aux taux de production simulés de se rapprocher davantage des observations, que ce soit en utilisant le modèle de forme ou le modèle sphérique. De plus, nos modèles de forme ne prennent pas en compte la topographie à petite échelle, ce qui pourrait réduire les taux de production en raison du shadowing. Par conséquent, les taux de production fournis par notre modèle doivent être considérés comme une limite supérieure.

En outre, varier la conductivité thermique améliore les pentes des courbes d'activité pré- et post-périhélie, probablement en raison de la distribution hétérogène de l'activité de l'eau ou des changements de conductivité dûs à l'activité elle-même. Ce résultat est soutenue par Skorov et al. (2023), qui souligne l'importance de la conductivité thermique dans l'activité cométaire par rapport à la porosité ou au manteau de poussière. Cependant, il convient de noter que l'asymétrie des pentes n'est pas uniquement dûe aux hétérogénéités, mais aussi à la forme et aux caractéristiques de l'axe de rotation (Sekanina, 1981). Par exemple, pour 67P, nous obtenons une courbe légèrement asymétrique en considérant un noyau homogène, avant même d'ajuster la conductivité pour mieux correspondre à la partie post-périhélique. Cette observation est en accord avec (Marschall et al., 2019), qui ont également observé que les comètes irrégulières avec une obliquité non nulle peuvent entraîner des courbes asymétriques de production d'eau. Le cas de 103P est remarquable. Près du périhélie, le modèle de forme ainsi que la sphère donne des taux de production similaires aux observations. Cependant, la sphère donne une meilleure corrélation avec les observations en dehors du périhélie, ce qui met en évidence l'importance des hétérogénéités dans l'activité cométaire. Les divergences entre les pentes des courbes simulées et observées pourraient être dûes à des différences thermiques ou structurelles. De plus, des caractéristiques de rotation complexes, qui ne sont pas pleinement comprises ou prises en compte dans notre analyse, pourraient expliquer les différences globales observées. Il faut souligner tout de même que ces résultats reposent sur des comparaisons avec les données de (Knight and Schleicher, 2013a) uniquement, et l'activité de 103P varie significativement entre les différentes approches du périhélie. Cela met en évidence la difficulté de faire des suppositions sur la structure, la composition et la rotation de la comète à partir des observations.

En conclusion, les hétérogénéités, thermiques ou mécaniques, sont tout aussi, voire plus importantes que la forme pour comprendre l'activité séculaire des comètes observée depuis le sol. La dégénérescence entre toutes ces caractéristiques, y compris la forme, est donc impossible à lever uniquement avec des courbes d'activité observées depuis le sol. Par conséquent, supposer que les noyaux cométaires sont sphériques est suffisant, en première approximation, pour comprendre l'activité cométaire observée depuis le sol.

Publications

S. Benseguane, A. Guilbert-Lepoutre, J. Lasue, S. Besse, C. Leyrat, A. Beth, M. C. Sitjà, B. Grieger, and M. T. Capria. Evolution of pits at the surface of 67P/Churyumov-Gerasimenko. Astronomy & Astrophysics, 668, A132, 2022: **published**

A. Guilbert-Lepoutre, S. Benseguane, J. Lasue, A. Beth, M. C. Sitjà, and B. Grieger. Pits on Jupiter-family Comets and the Age of Cometary Surfaces. The Planetary Science Journal, 4:220 (10pp), 2023: **published**

S. Benseguane, A. Guilbert-Lepoutre, M. Knight, J. Lasue, A. Beth. Influence of a comet nucleus shape on its activity as observed from the ground. Astrophysical Journal: **in revision**.